



“CHANNELING THE GREEN DEAL FOR VENICE”
Action n. 2019-IT-TM-0096-S
CEF Connecting Europe Facility

HYDRODYNAMIC SIMULATIONS

**Numerical modelling study of the vessel
generated erosion along the Malamocco Marghera
Channel – present configuration**



Activity	Phase 2
Task	Numerical modelling study of the vessel generated erosion along the Malamocco Marghera Channel – present configuration
Authors	Grith Christoffersen Marco Guerrini Berry Elfrink, Project Manager Andrea Pedroncini, Project Manager
Dissemination Level	Restricted
Status	Final
Due date	
Document Date	17/05/2023
Version Number	1.2

Legal Disclaimer

CHANNELING THE GREEN DEAL FOR VENICE is co-funded by the European Commission, Connecting Europe Facility (CEF) programme under grant agreement No. INEA/CEF/TRAN/M2019/2112366 - Action No: 2019-IT-TM-0096-S. The information and views set out in this document are those of the author(s) and do not necessarily reflect the official opinion of the European Union.





LIST OF CONTENTS

1	CONTENT.....	6
2	HYDRODYNAMIC MODEL OF THE MALAMOCCO MARGHERA CHANNEL FOR QUANTIFICATION OF VESSEL GENERATED EFFECTS	7
2.1	Hydrodynamics of displacement waves	7
2.2	Numerical model domain for the modelling of displacement waves	8
2.2.1	Bathymetric datasets.....	10
2.2.2	Model bathymetry and computational mesh	13
2.3	Model forcing for the modelling of displacement waves.....	17
2.4	Model configuration.....	19
2.4.1	Computational Grid	19
2.4.2	Vessel	21
2.4.3	Test of Model Type.....	21
2.4.4	Resolution	25
2.6	Model parameters applied in the displacement wave model.....	27
2.7	Calibration of the hydrodynamic displacement wave model.....	29
2.7.1	Calibration data	29
2.7.1.1	The CNR Database.....	29
2.7.1.2	The HS Marine Dataset.....	30
2.7.2	Model calibration	32
2.7.2.1	Calibration against data from CNR Database.....	34
2.7.2.2	Calibration against data from HS Marine Dataset.....	41
2.8	Establishment of representative vessel traffic.....	47
2.8.1	Vessel geometry	48
2.8.2	Vessel speed.....	52
2.8.3	Production modelling of displacement waves	55
2.9	Kelvin Waves	57
2.9.1	Estimation of Kelvin wave properties.....	59





2.9.1.1	Wave direction and period.....	59
2.9.1.2	Wave height	60
2.9.2	Kelvin waves with time	63
2.9.2.1	Vessel speeds per category	63
2.9.2.2	Vessel frequency per category	64
2.9.2.3	Duration with diverging Kelvin waves per year	66
2.9.3	Bed shear stresses from diverging Kelvin waves.....	67
2.9.4	Sediment transport from diverging Kelvin waves	70
2.9.5	Conclusion summary.....	74
2.10	Propeller wash	76
2.10.1	The basics of a water jet	76
2.10.2	Bed shear stress from ship propeller	81
2.10.3	Importance of propellor generated bed shear stress and turbulence on sediment transport	85
2.10.4	Conclusion summary.....	88
3	SEDIMENT TRANSPORT MODEL OF THE MALAMOCCO MARGHERA CHANNEL	89
3.1	Numerical model details for the modelling of the sediment transport	89
3.1.1	Sedimentary conditions	89
3.1.2	Numerical model bed	94
3.1.3	Dispersion	98
3.2	Calibration of the displacement wave sediment transport model	101
3.2.1	Calibration data	101
3.2.2	Model calibration	105
4	PRODUCTION MODELLING OF EXISTING CHANNEL LAYOUT	113
4.1	Detailed run though of Con-S passage.....	115
4.2	Hydrodynamic results.....	120
4.3	Accumulated bed changes	128
5	DISPLACEMENT WAVES RELATIVE TO AMBIENT FORCING	134
5.1	Transport and fate of the vessel-induced sediment plume.....	135
5.2	Transport and fate of the “natural forcing generated” sediment plume.....	141





5.3	Conclusion summary.....	151
6	CONCLUSIONS.....	153
7	BIBLIOGRAPHY	156

APPENDICES

- APPENDIX A – TABULARIZED HYDRODYNAMIC AND SEDIMENT TRANSPORT RESULTS
- APPENDIX B – SHIP GENERATED WAVES AND CURRENT SPEED MEASUREMENTS CAMPAIGN AT MALAMOCCO-MARGHERA CHANNEL
- APPENDIX C - CRITICAL SHEAR STRESS DISTRIBUTION FOR THE MODEL'S SETUP
- APPENDIX D - CFD SIMULATIONS OF THE WAVE PATTERN GENERATED BY A SHIP HULL IN SHALLOW WATER



1 CONTENT

A series of comprehensive modelling activities was conducted to quantify the impact of maritime traffic on the Malamocco – Marghera Channel (abbreviated as MMC in the following) and surrounding areas. Possible solutions are identified aimed at minimizing the erosion processes that are now affecting the tidal flats surrounding the channel, thus achieving sustainable navigation conditions.

To match this ambitious goal, following Public Tender procedures, the Contract was awarded by Port of Venice to a Consortium led by DHI S.r.l. and formed by DHI A/S, Force Technology, HS Marine S.r.l., Cetena S.p.A. and Around Water di Andrea Zamariolo Ph.D. Geol.

The present document is concerned with the modelling of the vessel generated hydrodynamics and sediment transport along the MMC.

Section 2 focuses on setup and calibration of the hydrodynamic displacement wave model, the hydrodynamical aspects of Kelvin waves as well as propeller wash and provides a discussion of their significance to the sediment balance of the MMC and surrounding areas. Finally, the section presents an overview of the vessel traffic that will be used in the production modelling.

Section 3 focuses on the setup and calibration of the displacement wave sediment transport model.

Section 4 provides analyses and discussions of model results considering the existing channel layout.

Section 6 provides a comparison of the amount of sediment that is discharged out of the Malamocco mouth following the passage of vessels along the MMC and following a storm in the Lagoon.

With reference to the “*Capitolato Tecnico*” the present document includes the following deliverables:

13. *Relazione tecnica degli scenari clima-canale-nave da sottoporre a indagine mediante simulazioni idrodinamiche;*
14. *Relazione tecnica delle simulazioni idrodinamiche finalizzate allo studio degli scenari clima-canale-nave;*
15. *Relazione illustrativa dei risultati ottenuti dalle modellazioni idrodinamiche;*
16. *Elaborati grafici di sintesi per la rappresentazione dei risultati dei modelli idrodinamici.*



2 HYDRODYNAMIC MODEL OF THE MALAMOCCO MARGHERA CHANNEL FOR QUANTIFICATION OF VESSEL GENERATED EFFECTS

When vessels navigate through water, they create displacement (primary) waves and diverging (secondary) waves also known as Kelvin waves. In addition, the vessel propeller forms a jet which will impinge onto the bed contributing to the hydrodynamic forcing from the vessel generated waves. The present chapter will provide details on the hydrodynamical modelling approach and model calibration of displacement waves in Sections 2.1 through 2.7. The hydrodynamical aspects of Kelvin waves and propeller wash will be considered in Section 2.9 and Section 2.10 respectively.

2.1 Hydrodynamics of displacement waves

The primary wave (or displacement wave) is associated with acceleration of the flow under - and around the vessel hull. This flow acceleration generates a draw-down, which to a stationary observer, is seen as a long-period transient wave. This type of wave is especially important in narrow channels (such as the MMC) where the draw-down can become quite significant.

The formation of the primary waves follows the below principals:

- At the bow a stagnation point is formed due to the reduction in velocity relative to the vessel. This causes an increase in pressure seen as a local increase in water level travelling ahead of the vessel.
- Along the sides of the vessel the flow is re-accelerated causing a decrease in water level known as the draw-down.
- At the stern the flow decelerates again causing an increase in water level.

These water level changes are known as displacement waves and can be described by the Bernoulli equation:

$$\frac{v^2}{2g} + \frac{p}{\rho g} = c \quad \text{Eq. 2.1}$$

Here v is the flow velocity (m/s), g is the acceleration due to gravity (m/s^2), ρ is the water density (kg/m^3), p is the pressure (Pa) and c is a constant (m). The pressure variation along the hull is assumed hydrostatic and therefore follows Eq. 2.2.



$$p = -\rho \cdot g \cdot \eta + p_0 \quad \text{Eq. 2.2}$$

Here η is the surface elevation (m) and p_0 is the atmospheric pressure (Pa).

The draw down depends highly on three aspects which will be evaluated during the production modelling of the existing channel layout and the future channel layout:

- the speed of the vessel
- the vessel displacement stencil i.e., the hull geometry
- the channel geometry i.e., how restrictive is the channel cross section relative to the cross section of the vessel

The present report will focus on the existing channel layout.

Model simulations were carried out using DHI's hydrodynamic model MIKE 3 FM. This is a three-dimensional model based on the hydrostatic pressure assumption. The model thus solves the simplified version of the Navier Stokes equations known as the shallow water equations, see [1] for details.

In the following sections (2.2 to 2.6) the setup of the hydrodynamic displacement wave model will be provided.

2.2 Numerical model domain for the modelling of displacement waves

The extent of the model domain for the displacement wave modelling is shown in Figure 2.1. The domain contains the central part of the lagoon from the entrance to the MMC and onwards to the area of Fusina. The western shallow hinterland separated from the lagoon by extensive salt marsh areas is included only to incorporate the effect of the connecting channels.



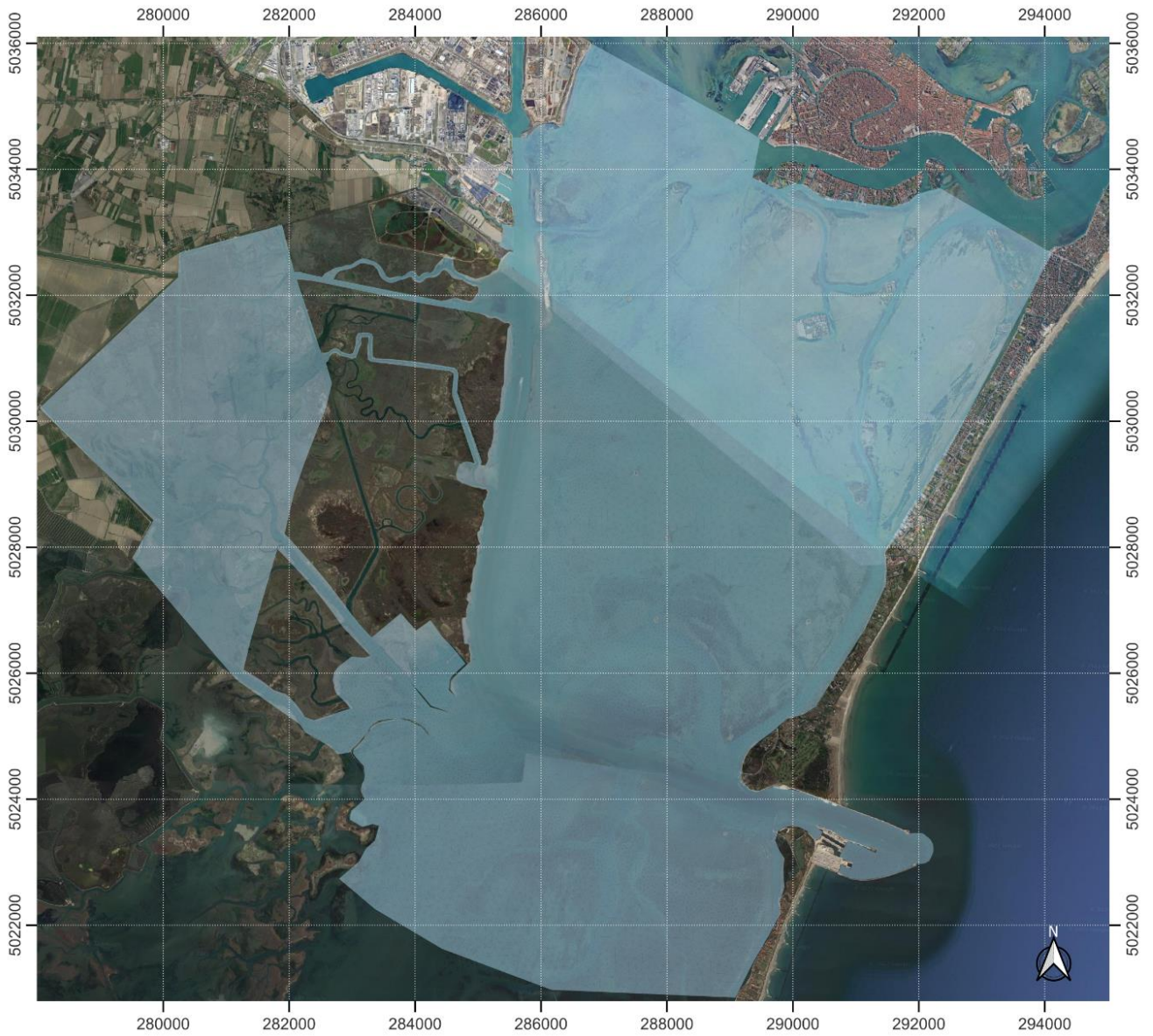


Figure 2.1. Extent of model domain for displacement wave modelling.



2.2.1 Bathymetric datasets

The bathymetry of the numerical model is based on the four datasets listed in Table 2-1. A single dataset covering the entire lagoon has not been available, hence several surveys carried out at different periods and related to different areas of the lagoon had to be used instead.

Table 2-1. List of bathymetric datasets used in the model

Source	Dataset no.	Time	Horizontal resolution [m]	Vertical datum	Area
Autorità di Sistema Portuale del Mare Adriatico Settentrionale [2]	1	2002	1	IGM42	Figure 2.2
Provveditorato (Ex Magistrato delle Acque) [3]	2	2018	~100	IGM42	Figure 2.3
Autorità di Sistema Portuale del Mare Adriatico Settentrionale [2]	3	2017 to 2021	1	IGM42	Figure 2.4
Consiglio Nazionale delle Ricerche [4]	4	2013	1	IGM42	Figure 2.5

The model bathymetry is mainly based on Dataset 2, 3 and 4. Dataset 2 and 4 provides the data for the central part of the lagoon and its channel network aside from the channels covered by Dataset 3. These channels are based only Dataset 3.

Dataset 1 has been cleaned up from overlaps with Dataset 2 in the central part of the lagoon and Dataset 4 wherever bathymetric data for channels were available.

Dataset 1 is used only for the shallow hinterland west of the MMC and some of the channels leading to this hinterland from the MMC-area (the channels not resolved by Dataset 2).

Dataset (3) is made of a number of surveys carried out between 2017 and 2021 including surveys taking place after 2021 dredging operations. The dataset stretches from the Malamocco Marghera channel, through Canale Vittorio Emanuele III, Canale della Giudecca up to Lido inlet.



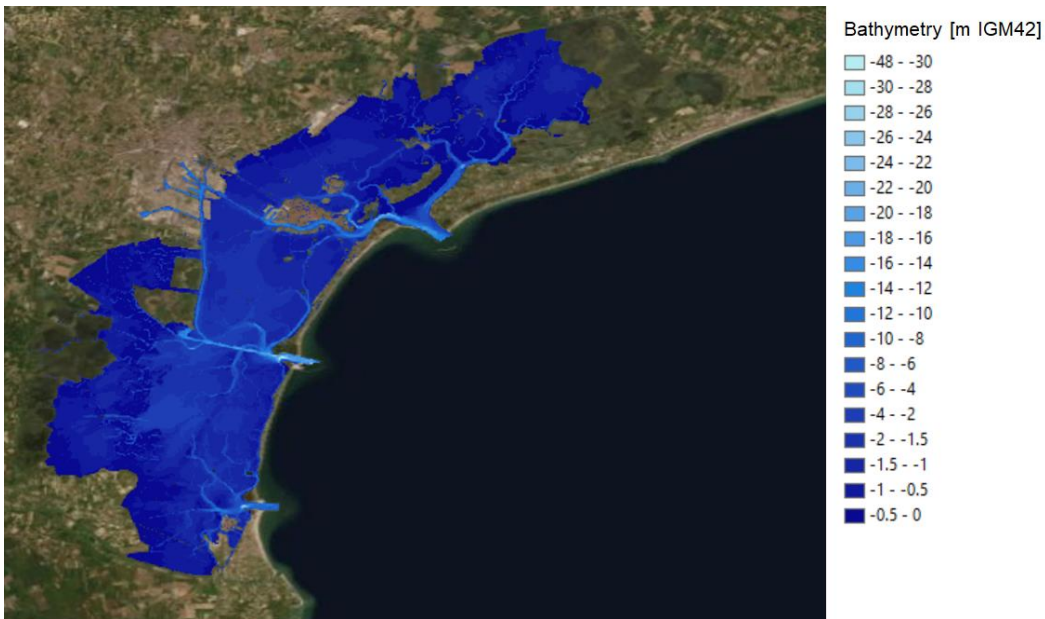


Figure 2.2. Bathymetry Dataset 1.

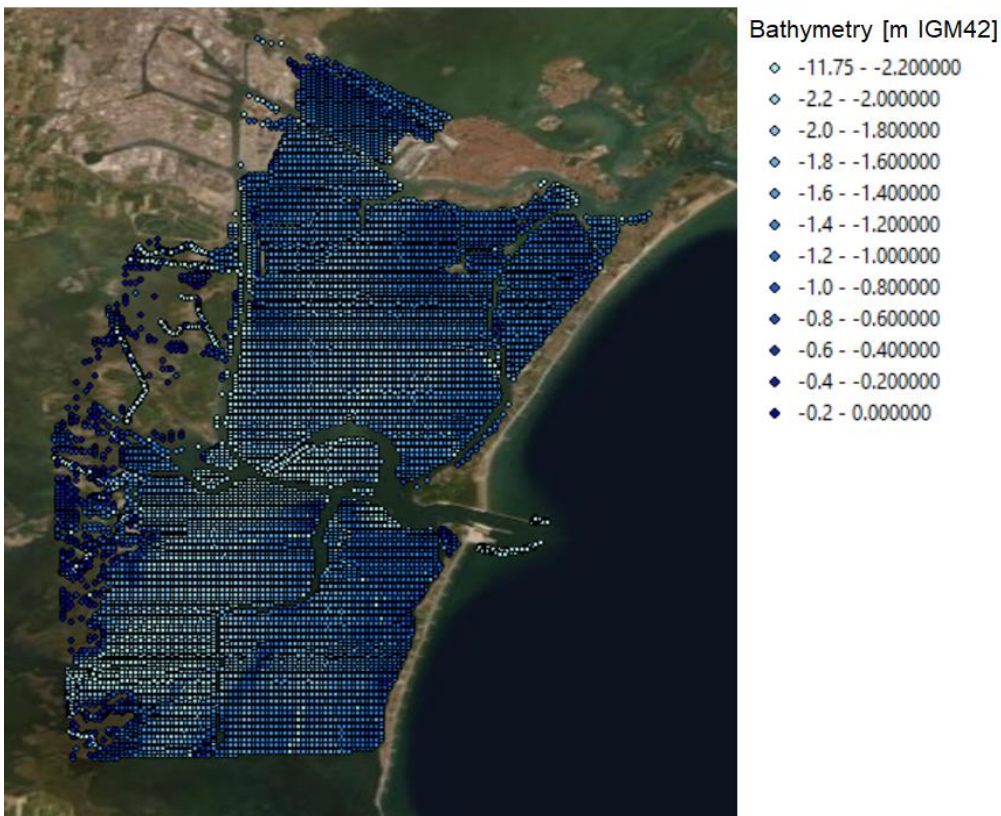
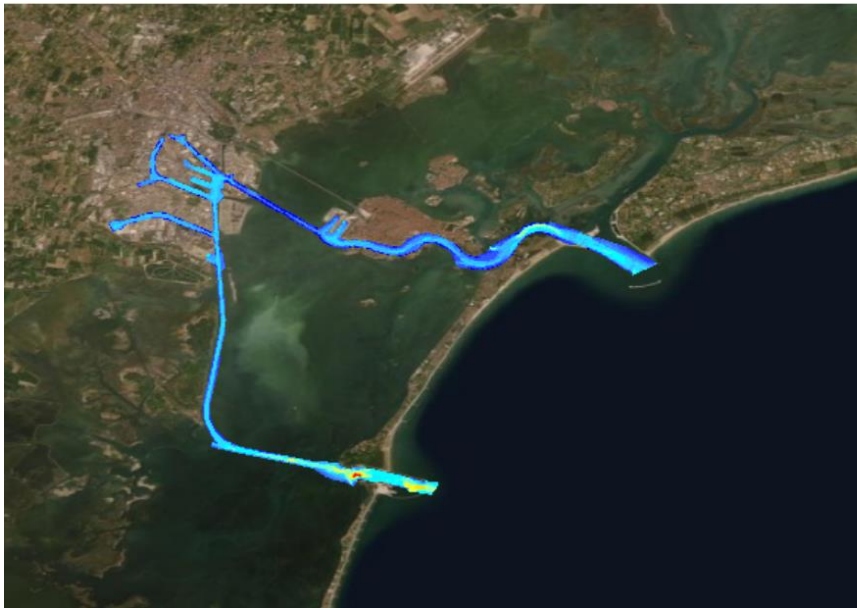


Figure 2.3. Bathymetry Dataset 2 (colour scale values were chosen to highlight shallower areas).





Bathymetry [m IGM42]

- -44 - -42
- -42 - -40
- -40 - -38
- -38 - -36
- -36 - -34
- -34 - -32
- -32 - -30
- -30 - -28
- -28 - -26
- -26 - -24
- -24 - -22
- -22 - -20
- -20 - -18
- -18 - -16
- -16 - -14
- -14 - -12
- -12 - -10
- -10 - -8
- -8 - -6
- -8 - -4
- -4 - -2
- -2 - 0

Figure 2.4. Bathymetry Dataset 3.



Bathymetry [m IGM42]

- -44 - -42
- -42 - -40
- -40 - -38
- -38 - -36
- -36 - -34
- -34 - -32
- -32 - -30
- -30 - -28
- -28 - -26
- -26 - -24
- -24 - -22
- -22 - -20
- -20 - -18
- -18 - -16
- -16 - -14
- -14 - -12
- -12 - -10
- -10 - -8
- -8 - -6
- -8 - -4
- -4 - -2
- -2 - 0

Figure 2.5. Bathymetry Dataset 4



2.2.2 Model bathymetry and computational mesh

An overview of the resulting model bathymetry and computational mesh is shown in Figure 2.8. The thin black lines in the view of the bathymetry indicates a few selected contours: -1, -3 and -10 m MSL. The thick black lines indicate implemented structures.

The structures along the MMC, identified from a Google Satellite image from March 2021, are illustrated in Figure 2.6 and Figure 2.7. They have been named as follows from the north along the eastern side of the channel Rubble-01 to Rubble-06. From north along the western side Seawall-01, Rubble-07a and Rubble-07b. These structures consist of three types:

- sheet wall
- rubble type structure
- morphological structure

Table 2-2 provides the relation of the structure type and structure names. The sea wall is excluded from the computational mesh i.e., considered as land by the model. The rubble type structures are implemented with a top level of 0.90 m MSL and a slope of 1:25. The morphological structures are implemented with a top level of 0.35 m MSL and a slope of 1:6. An example of the mesh implementation of these structures is provided in Figure 2.9.

Table 2-2. *Relation between structure type and structure name.*

Sheet Wall	Rubble Type Structure	Morphological Structure
Seawall-01	Rubble-01 Rubble-04 Rubble-05 Rubble-06 Rubble-07a and 07b	Rubble-02 Rubble-03



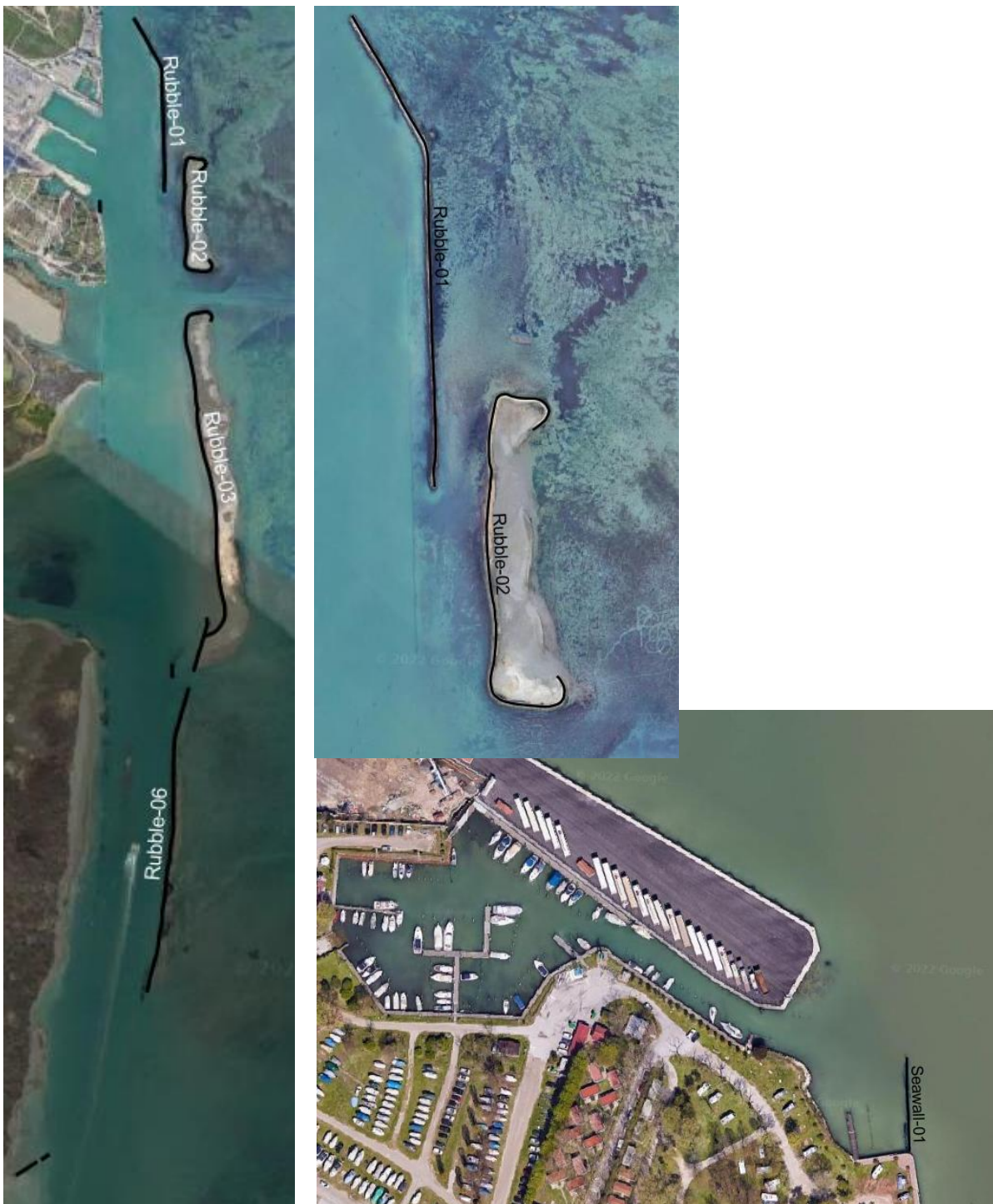


Figure 2.6. Structures along MMC, Part-I.



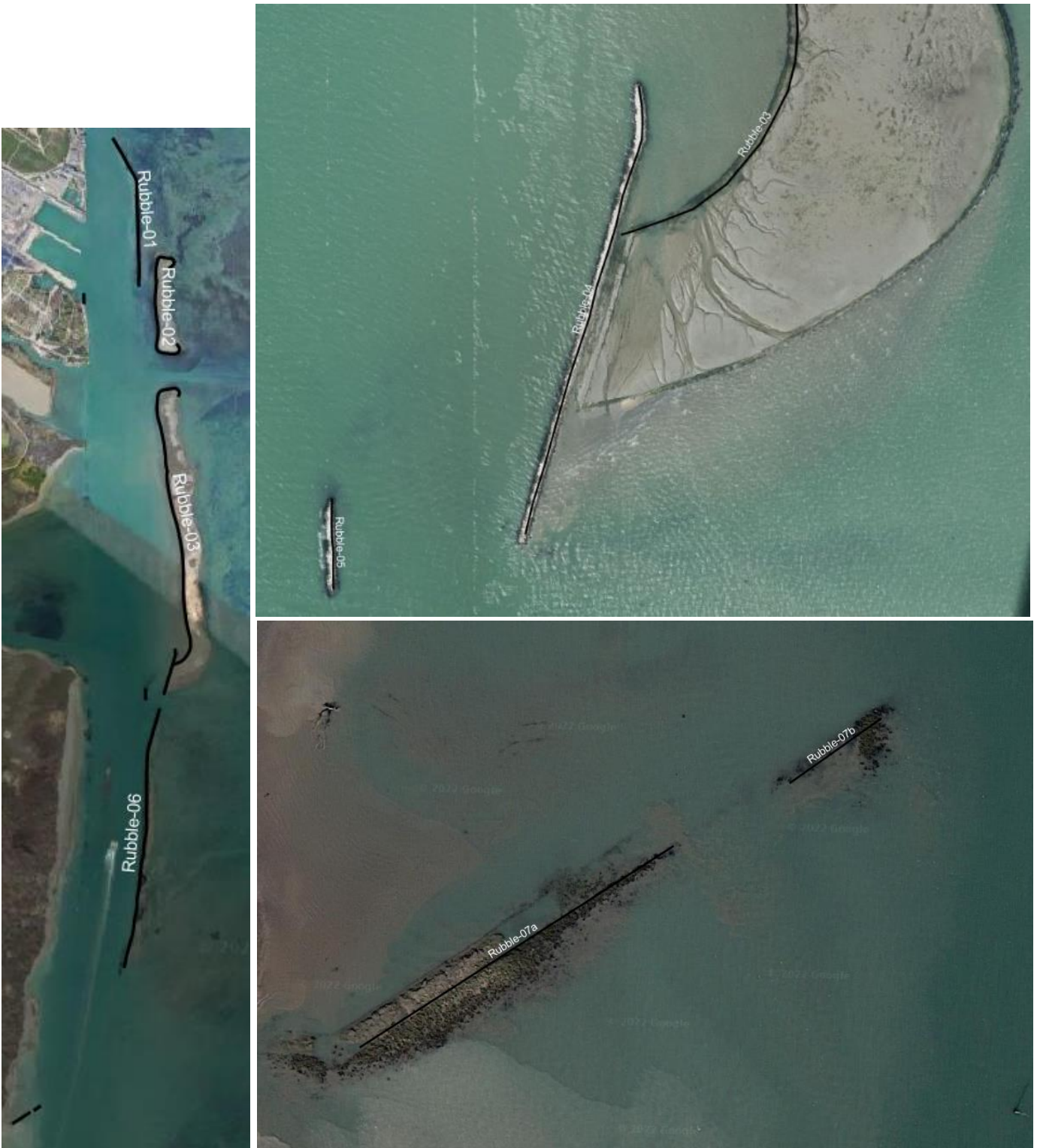


Figure 2.7. Structures along MMC, Part-II.



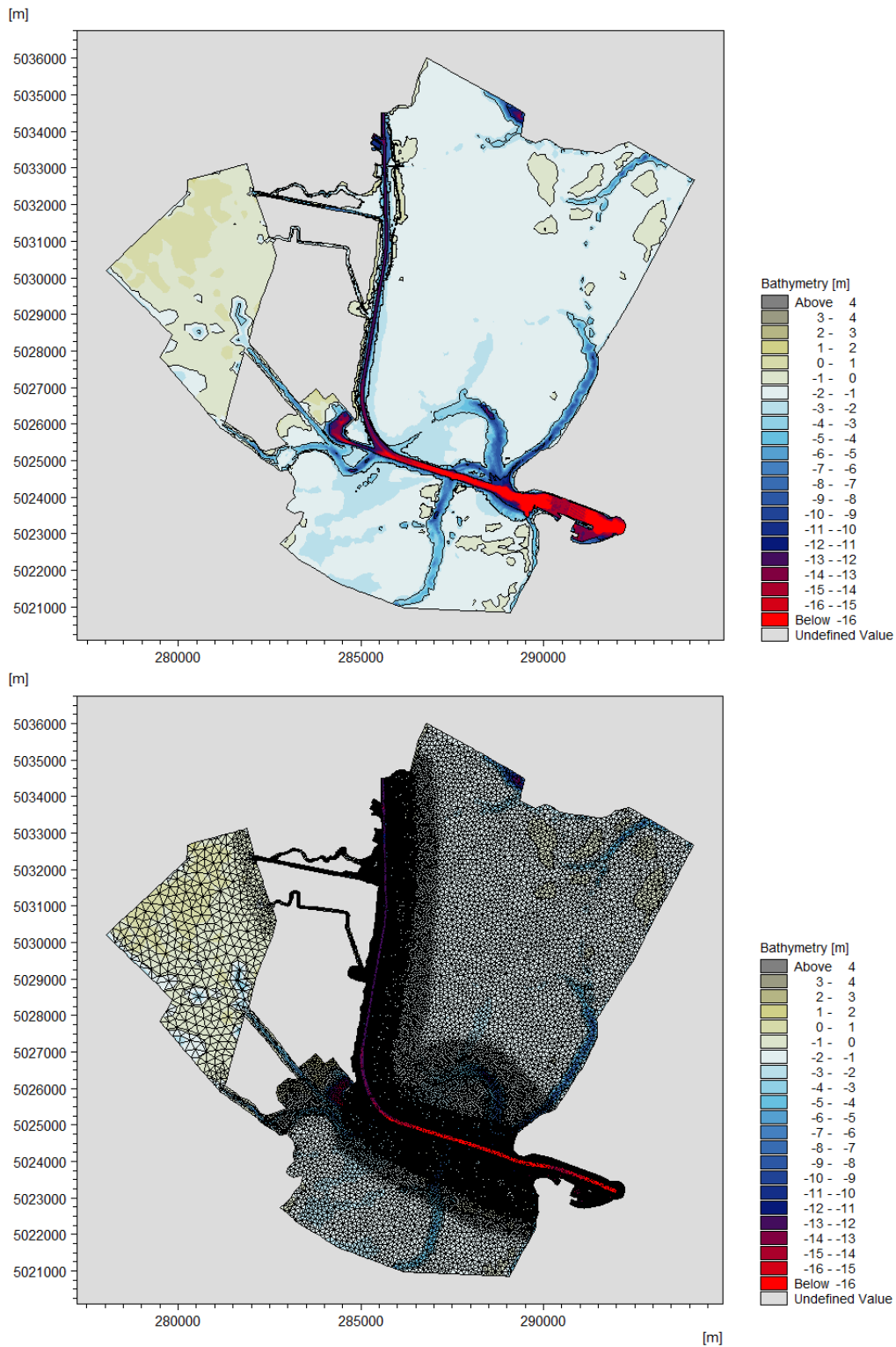


Figure 2.8. Full overview of model bathymetry (top) and computational mesh (bottom).



The computational mesh contains 820,463 elements. Most of which are used to resolve the MMC itself. This channel is resolved by 2x2 m quadrilateral elements over a cross sectional width of about 120 m. This very high resolution is required to provide a good representation of the moving vessel inside the channel. Moving away from the MMC, the computational mesh expands into triangular elements with 5 m resolution and then to about 10 m resolution. In the far field e.g., the central part of the lagoon, the resolution is about 150 m.

The vertical resolution of the domain consists of five equidistant sigma-layers, meaning that the water column consists of five vertical layers everywhere. In an area of 5 m water depth each layer will have a thickness of 1 m whereas in an area of 10 m water depth the layers will be 2 m thick. As such the layer thickness varies across the domain.

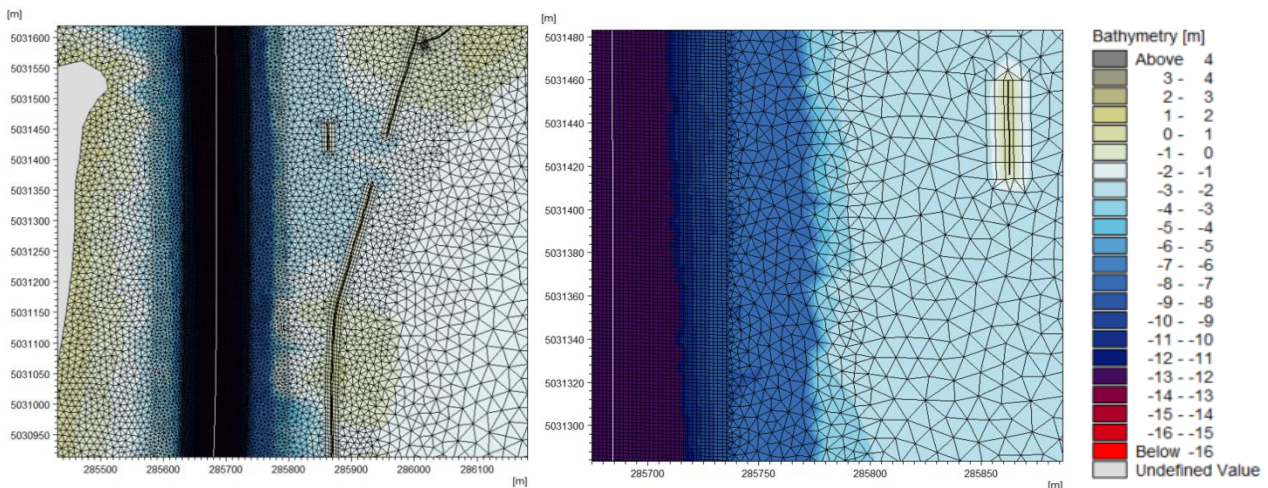


Figure 2.9. Zoomed view of computational mesh details.

2.3 Model forcing for the modelling of displacement waves

To isolate the effect from the displacement waves, all open boundaries of the model domain are considered as land and no wind forcing is included. Hence, the only forcing of the displacement wave model (aside from the Coriolis force) is the moving vessel. This vessel is implemented in the model as a moving surface pressure field such that η in Eq. 2.2 represents a water level offset equivalent to the three-dimensional vessel hull. This methodology provides a good approximation for the flow field around the vessel and thus the generation of the displacement waves. An example of a timestep in such a moving pressure field is shown in Figure 2.10.



It is noted that submerged 3D features such as a bulb keel and some stern features are not resolved with this methodology. Therefore, the details of the flow field in these areas, associated with these phenomena, will not be represented completely by the model. However, this is irrelevant relative to the modelling of the sediment transport along the banks of the MMC.

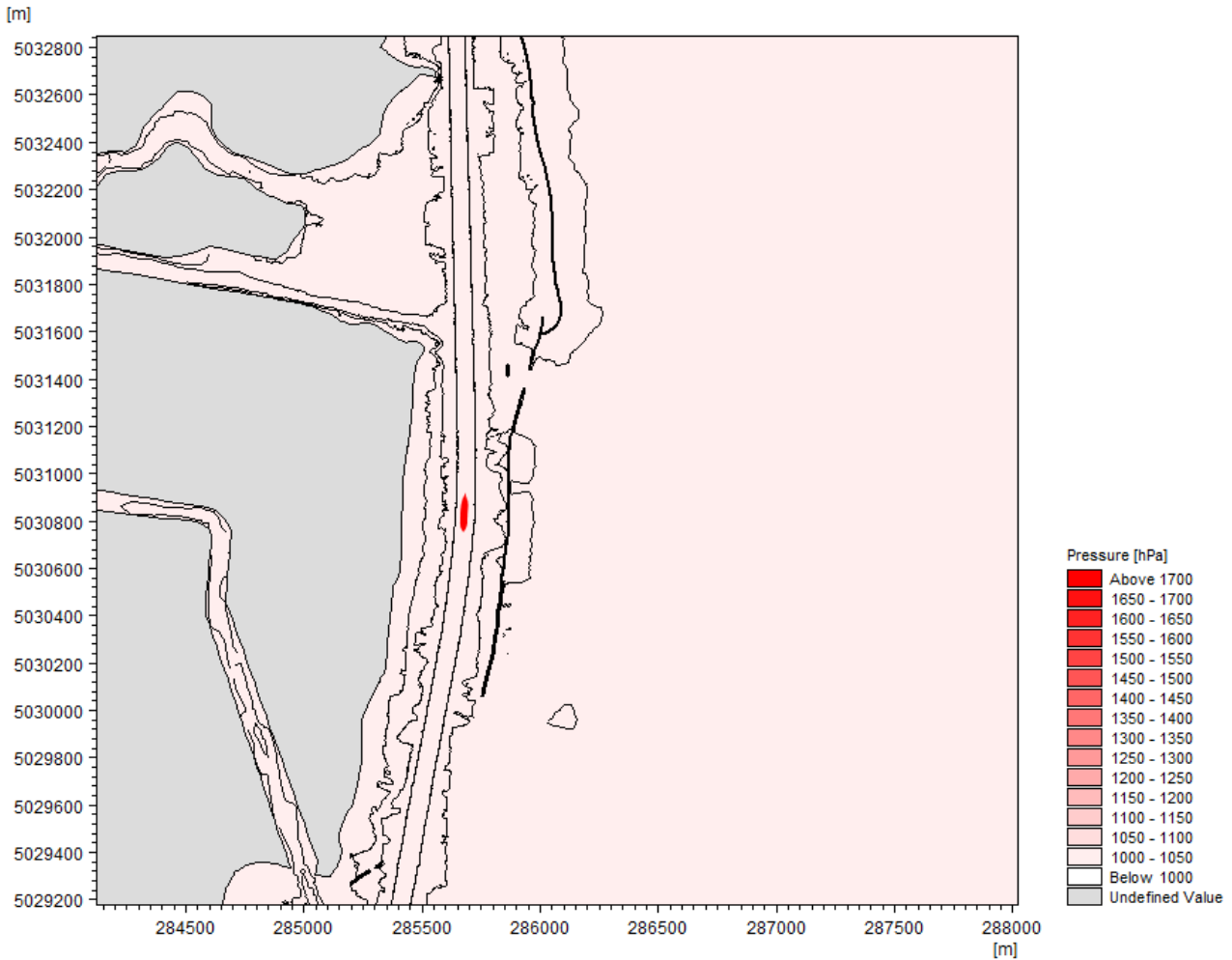


Figure 2.10. Example of a timestep in a moving pressure field.



2.4 Model configuration

To determine the optimal configuration for the modelling of the displacement waves a series of initial investigations was carried out. The modelling of displacement waves in MIKE FM can be done using a 2D or 3D model. In case of a 3D model there is an option to use a hydrostatic or non-hydrostatic description. The use of a full non-hydrostatic 3D model is considerably more demanding in terms of CPU than non-hydrostatic - or a 2D model. The advantage of a less-demanding model configuration is that a much higher spatial resolution in the computational mesh can be applied. In order to determine the optimal model configuration, the following set-ups were tested:

- 3D model (MIKE3 FM)
 - Non-hydrostatic
 - Hydrostatic
- 2D model (MIKE21 FM)

MIKE21 FM assumes hydrostatic pressure (similar to the hydrostatic version of MIKE 3 FM). Without the hydrostatic pressure assumption MIKE3 FM solves the three-dimensional set of Navier Stokes equations i.e., the model is similar to a Computational Fluid Dynamics (CFD) model.

2.4.1 Computational Grid

For the sake of numerical stability, the size of the computational grid cells in the channel itself must be comparable to the distance travelled by the ship within 1 s. Additionally, the cells must have a size capable of representing the vessel geometry, not only during straight parts of the channel but also in the bends. From experience this means that grid cells must have a dimension of around 1 by 1 m. The depth inside navigation channels is often relatively large, around 10 m water depth. The combination of small grid cells and large water depths gives rise to small time steps and thus long computation times. Given that the modelled part of the MMC-channel is about 15 km long, the aimed model resolution in the channel is around 2 x 2 to 3 x 3 m to reduce the computational effort. This would enable a larger number of model tests to be made, which gives a better representation of the traffic in the channel.

Initial tests were made using an idealized straight channel domain before the MMC bathymetric data became available, see Figure 2.11.



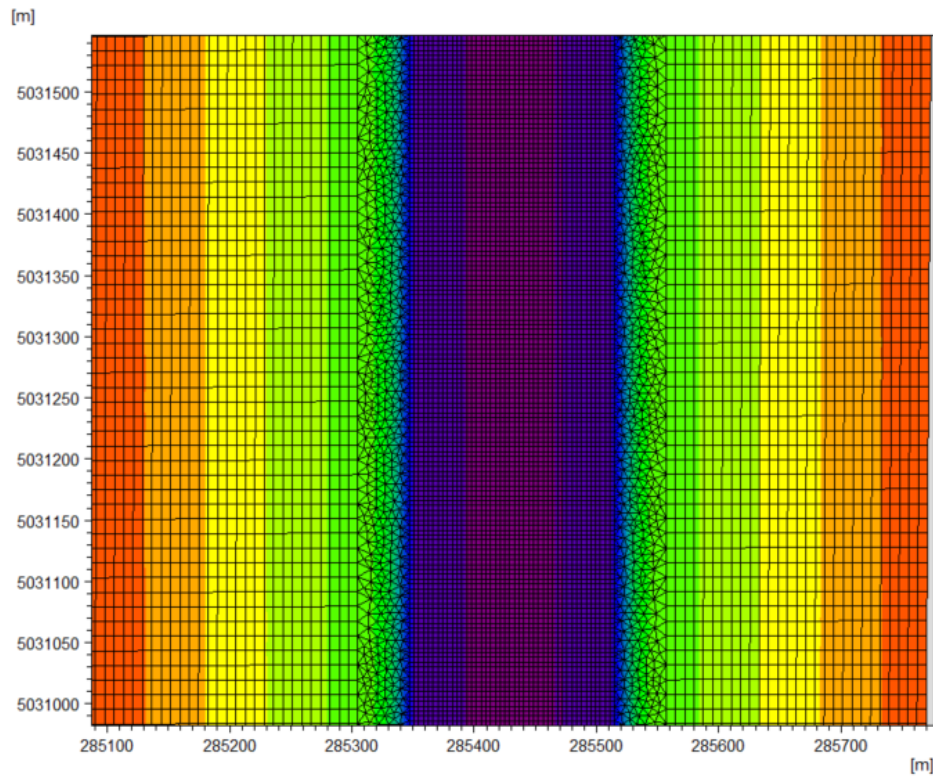
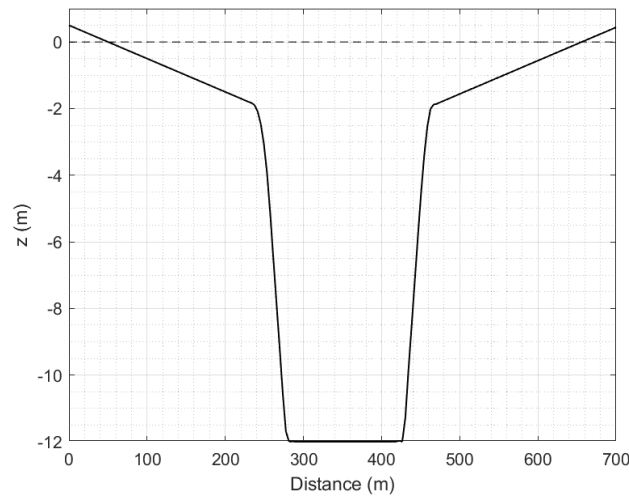


Figure 2.11 Computational grid and bathymetry of idealized channel used in initial model tests.

The channel is 3.6 km long and has a depth of 12 m, which is similar to the north-south oriented part of the MMC. The 12 m wide part of the channel is 152 m wide – about twice as large as the real channel. A slope of 1:3 is used to transit from -12 m MSL to -2 m MSL. Above -2 m MSL a slope of



1:100 is applied to represent a tidal flat region. The resolution in the deep part of the idealized channel is 4 x 4 m expanding to 12 x 8 m on the slope.

In reality, the slope towards the shallow banks west of the channel transits from steep (about 1:4 – 1:3) towards gentler (about 1:10) slopes already around -10 to -8 m MSL compared to -2 m MSL in the idealized channel. The slope towards the lagoon (east side) is generally relatively gentle (around 1:10) starting from the deep part of the channel and moving out. Though the real Malamocco-Marghera channel has a narrower deep section it is possible that the gentler slopes will make the real cross section less restrictive towards the primary ship generated wave – especially since the wave will be quite free to dissipate into the lagoon on the eastern side.

The idealized channel is resolved vertically by means of 12 equidistant (σ) layers, i.e. 1 m resolution in the deep part of the channel.

2.4.2 Vessel

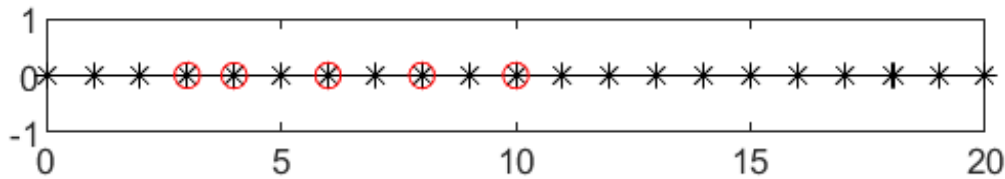
The considered vessel passage was chosen before any data on the traffic of the MMC was available. The dimensions have been based on an NCL Cruise Vessel which is fairly close to the large cruise ship modelled with the production model. The vessel hull used is a Ro-Ro ferry due to availability at the time:

- Length: 294 m
- Width: 38 m
- Draft: 8 m
- Speed: 8 knots

2.4.3 Test of Model Type

To evaluate the performance of the 3 selected model types a transect across the idealized channel was extracted at $y = 5030900$ m UTM-33. This corresponds to a central location in the model channel after the vessel has gained its full speed of 8 knots i.e., the vessel no longer accelerates. Timeseries of water level and bed shear stress at Points 3, 4, 6, 8 and 10 are investigated.





	Point 3	Point 4	Point 6	Point 8	Point 10
Water depth (m MSL)	0.47	0.83	1.54	10.99	12.00

Figure 2.12 Transect points for comparison of parameters from idealized channel tests.

Points 3, 4 and 6 are located on the slope of the mud flat whereas Point 8 and 10 are located in the deep channel – Point 10 just below the vessel center line. The erosion under investigation in the present project is the erosion of the channel banks. As such the main area of importance is covered by Points 3, 4, and 6. At these locations the modelled bed shear stresses should be well represented by the model. Inside the deep channel and close to the ship some discrepancies may be accepted.

Comparisons between MIKE3 FM non-hydrostatic and hydrostatic are shown in Figure 2.13 and between MIKE3 FM non-hydrostatic and MIKE21 FM in Figure 2.14. The MIK3 FM hydrostatic model is seen to give very similar results as the non-hydrostatic version whereas the MIKE21 FM model shows larger deviation from the 3D model inside the channel. On the banks the 2D and 3D models show similar performance.

The model tests indicate that the 3D – non-hydrostatic model configuration is optimal for this application because it resolves the details of the flow sufficiently accurate and allows for a fine spatial model resolution.



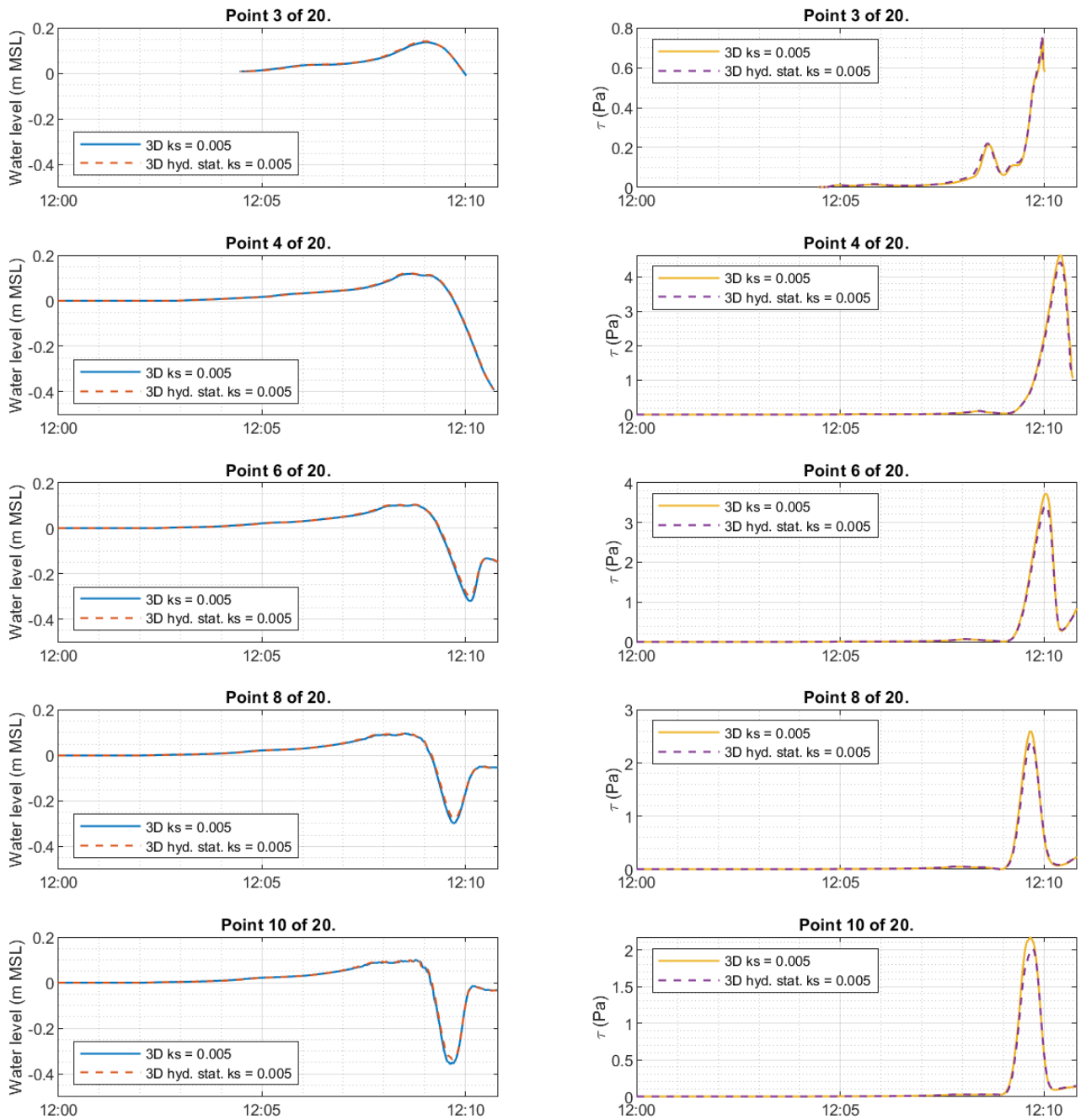


Figure 2.13 Water level and bed shear stress comparing non-hydrostatic to hydrostatic MIKE3 FM.



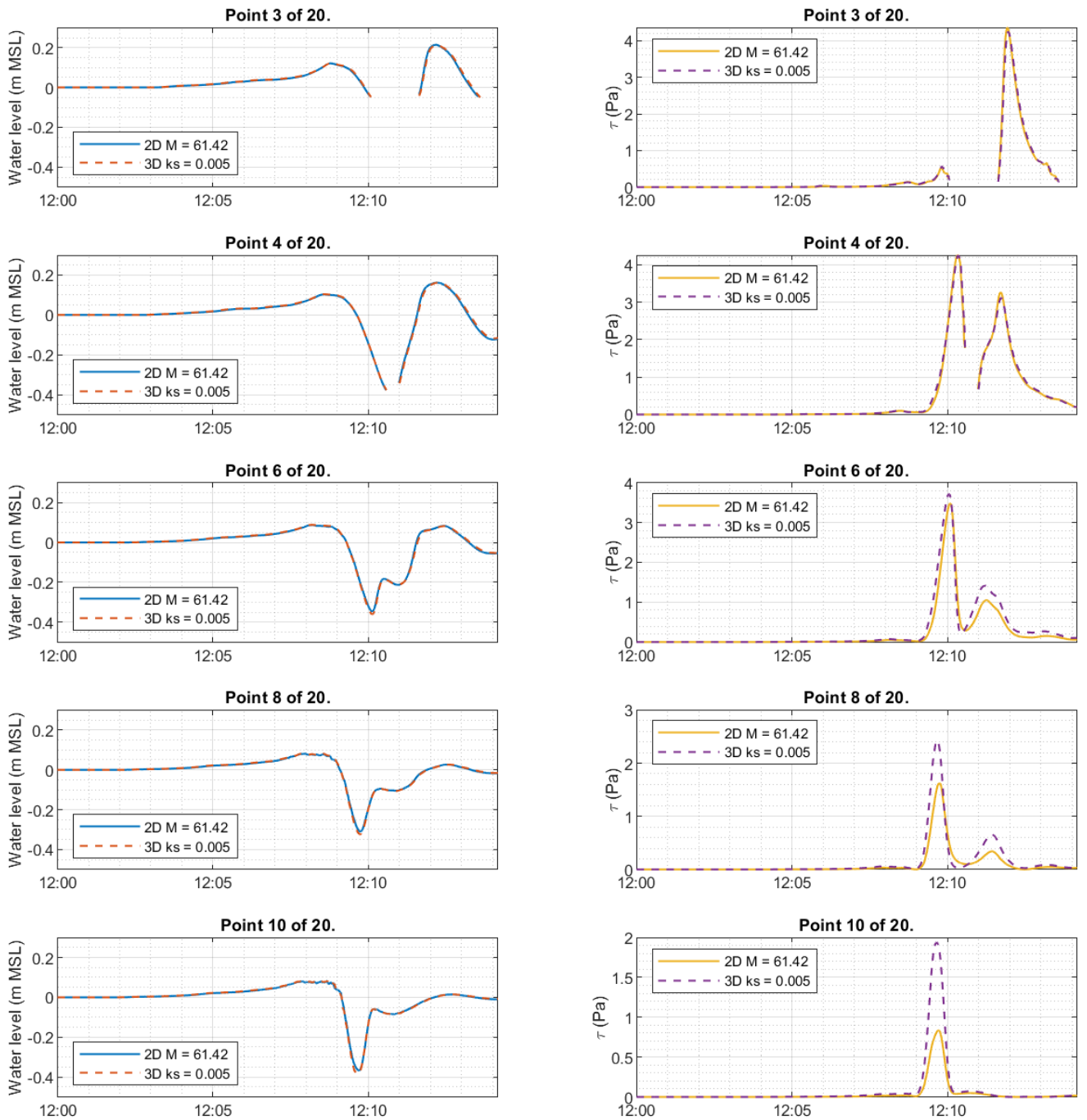


Figure 2.14 Water level and bed shear stress comparing non-hydrostatic MIKE3 FM to hydrostatic MIKE21 FM.



2.4.4 Resolution

In Table 2-3 the maximum modelled bed shear stresses at the three extraction points (Point 3, 4 and 6) are listed considering 3 different vertical resolutions (12, 6 and 3 equidistant sigma layers). In this context it is noted that the production model uses 5 vertical layers. At 3 vertical layers there starts to be a difference from the 12-layer case considering Point 6 (located in about 1.5 m water depth). The 6-layer case on the other hand gives quite similar results. Due to the high horizontal resolution needed in and along the channel of the large production domain, a vertical resolution of 5 layers has been chosen.

Table 2-3 Maximum modelled bed shear stress for varying vertical resolution at Points 3, 4 and 6 using MIKE3 FM hydrostatic.

	Point 3	Point 4	Point 6
Max shear stress (Pa) 12 layers	1.4	1.8	2.1
Max shear stress (Pa) 6 layers	1.3	1.7	1.9
Max shear stress (Pa) 3 layers	1.2	1.5	1.6

In Figure 2.15 the modelled bed shear stresses at extraction Point 3 are shown considering 2 different horizontal resolutions. The finer resolution gives rise to a higher modelled bed shear stress (~0.5 Pa higher) than the coarse resolution.

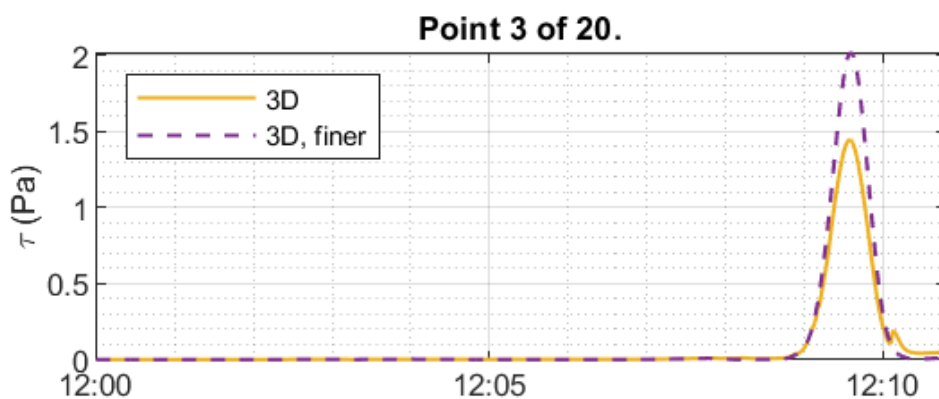


Figure 2.15 Bed shear stress, increasing horizontal resolution on the slopes from 16 to 8 m.





In the production model a resolution of 2 x 2 m is used inside the channel expanding to about 5 m on the slopes and 10 m on the flats, see Figure 2.9. The 5 m resolution used on the slopes of the channel banks in the production model is similar to the fine resolution tested above. As opposed to the simplified model domain considered during these initial tests, the flats of the lagoon are almost constant in depth – the simplified domain considers a constant slope. Additionally, the displacement wave can travel out into the lagoon east of the channel. As such the run-up and -down events from the displacement waves are less pronounced in the production model domain. Run-up and run-down of waves are of importance in shallow water and Point 3 is also described by only about 0.5 m water depth. At the other extraction points (Point 4 and 6, not plotted here) no changes to the bed shear stress are seen from changing the horizontal resolution. As such, the resolution of about 10 m used on the flats in the production model is considered adequate for the purpose of analysing the impact from the existing vessel traffic on the erosion of the channel banks and the effect from a changed channel design/vessel speed.



2.6 Model parameters applied in the displacement wave model

The bed roughness applied in the hydrodynamic model of the displacement waves was kept similar to that applied in the lagoon model. Hence the roughness height follows Table 2-4, see also Figure 2.16.

Table 2-4. Roughness of hydrodynamic model for displacement waves.

	Channels	Flats	Rubble Structure	Morphological Structure
Roughness (m)	0.049	0.014	1.5	0.75

In the model a computational cell is considered fully wet/dry when the total water depth is greater than 10 cm/smaller than 0.5 cm respectively. When a cell is in between wet and dry, only the mass fluxes are accounted for in the calculation and the momentum fluxes are set to zero. These flood and dry settings are chosen for stability reasons since unrealistically high flow velocities may otherwise occur in the model during the draw down event in shallow areas which will lead to numerical instability.

The horizontal eddy viscosity (v_t^h) i.e., the horizontal turbulence, is modelled using the Smagorinsky (1963) formulation with $c_s = 0.28$:

$$v_t^h = c_s^2 l^2 \sqrt{2S_{ij}S_{ij}} \quad \text{Eq. 2.3}$$

Here l is a characteristic length scale and S_{ij} is deformation rate:

$$S_{ij} = \frac{1}{2} \left(\frac{\partial u_i}{\partial x_j} + \frac{\partial u_j}{\partial x_i} \right) \quad , \quad (i, j = 1, 2) \quad \text{Eq. 2.4}$$

The vertical eddy viscosity (v_t^v , or vertical turbulence) is modelled using the two-equation (k - ϵ)-model, where k refers to the turbulent kinetic energy (TKE) and ϵ to the dissipation rate of TKE:

$$v_t^v = c_\mu \frac{k^2}{\epsilon} \quad \text{Eq. 2.5}$$

Here c_μ is an empirical constant taken as 0.09.



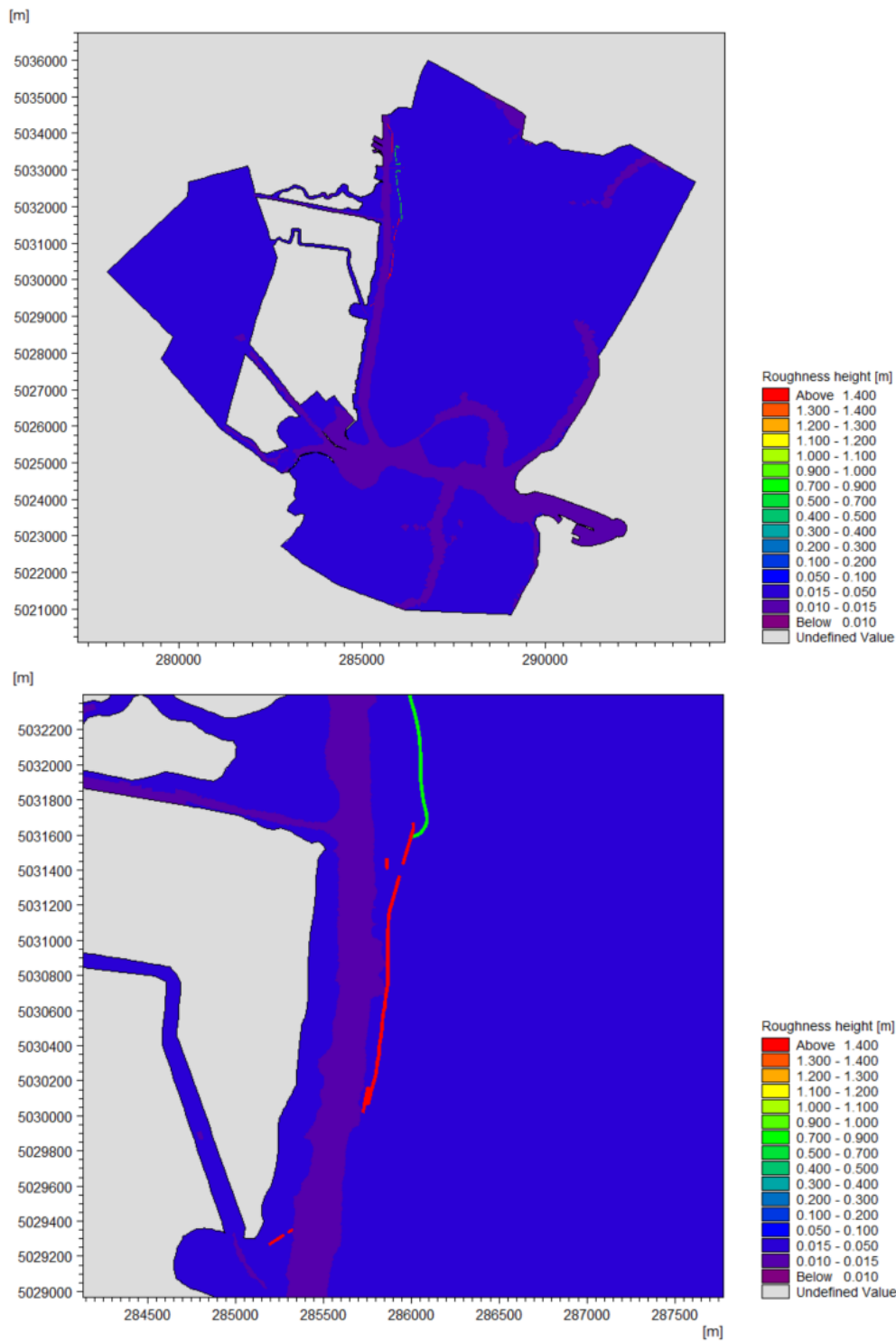


Figure 2.16. Illustration of roughness used in hydrodynamic displacement wave model.



2.7 Calibration of the hydrodynamic displacement wave model

2.7.1 Calibration data

Two calibration datasets have been available:

1. The CNR Database
 - a. Large database consisting of measurements of water depth related to vessel name, length, width and draft as well as speed.
2. The HS Marina Dataset
 - a. Measurements of water depth and flow velocity for a limited number of vessel passages

These datasets will be described in greater detail in the following.

2.7.1.1 The CNR Database

The CNR database considers timeseries of measured water depth at the location specified in Table 2-5, see also a map of the location in Figure 2.17.

The timeseries have been collected during the fall of 2019 (from mid-August to mid-December), see Table 2-5. Given the data collection period, no cruise vessels are included in the database.

The database correlates the maximum measured wave height (the draw down magnitude) to AIS data from the specific vessel passing the measurement location at that instance in time:

- Vessel name
- IMO number
- Vessel speed
- Sailing direction
- Overall length
- Overall breadth
- Draft
- Passage time

Based on this information it is possible to set up a moving pressure field once the vessel type i.e., the hull type, has been determined. This has been done via <https://www.marinetraffic.com>.



Table 2-5. Location and measurement periods of CNR database.

CNR Database	Longitude (°E)	Latitude (°N)	Period 1	Period 2	Period 3	Period 4
	12.2567	45.3764	14/08/2019 to 04/09/2019	09/09/2019 to 10/10/2019	10/10/2019 to 18/11/2019	18/11/2019 to 17/12/2019

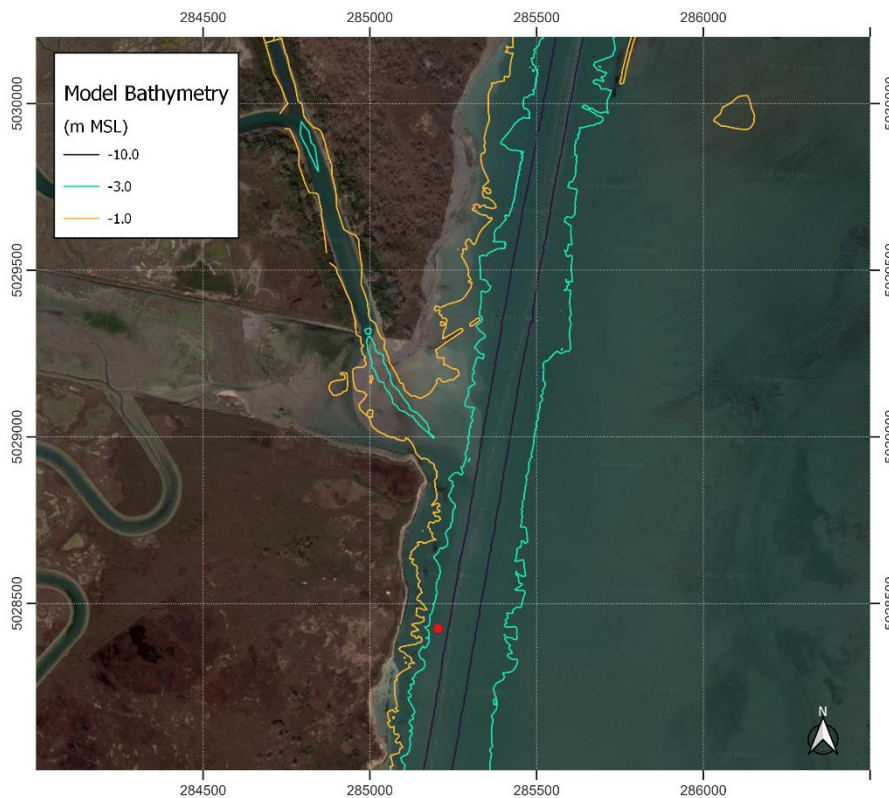


Figure 2.17. Position of measurement location used in the CNR database.

2.7.1.2 The HS Marine Dataset

The HS Marine dataset contains measurements of water level and depth averaged current speed measured on 16th May 2022 during 9 vessel passages. The measurement locations of the HS Marine dataset are shown in Figure 2.18 and detailed in Table 2-6. The detailed description of the field campaign is illustrated in Appendix B.



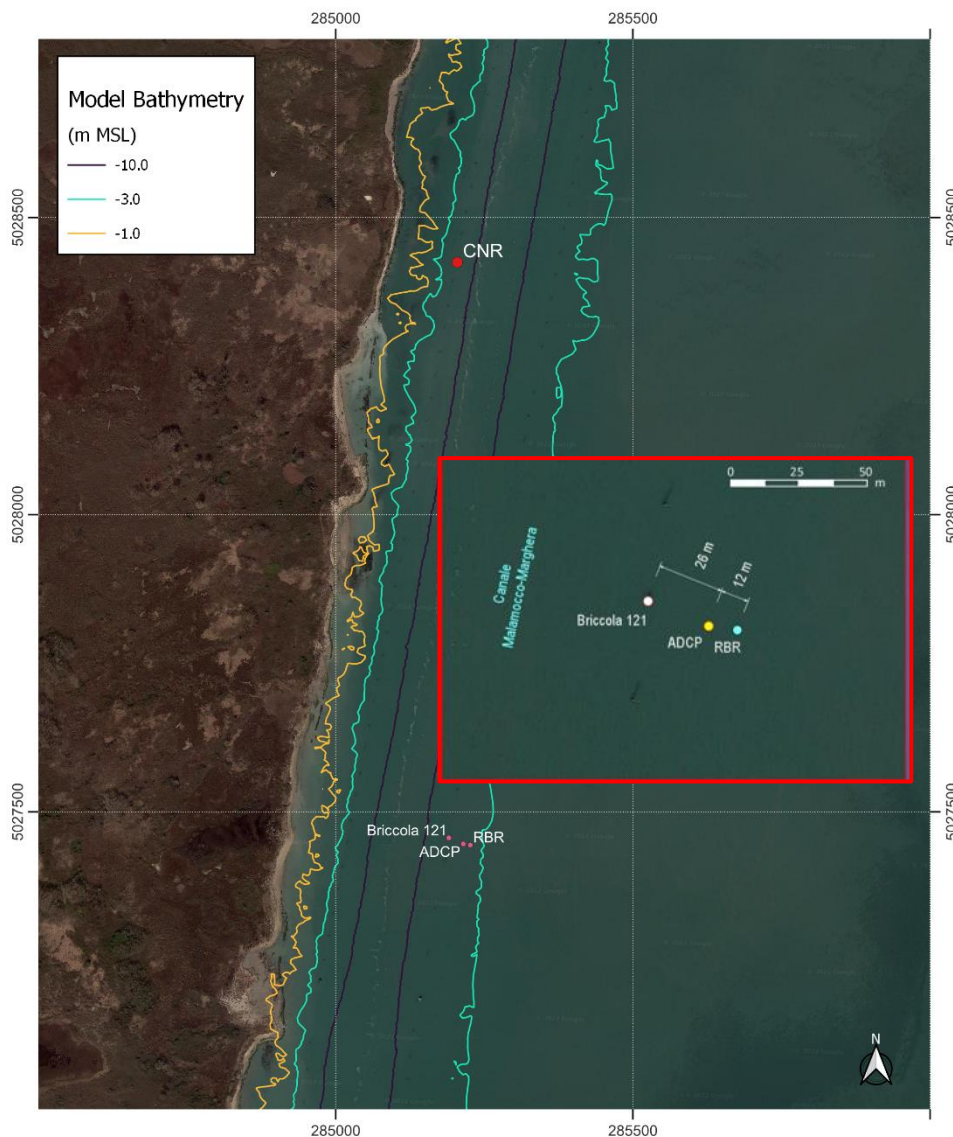


Figure 2.18. Position of measurement locations used for the HS Marine dataset. (Briccola 121) location of water level tide gauge. (ADCP) location of ADCP. (RBR) location of pressure sensor.

Water level has been measured at the rim of the channel using a tide gauge mounted on Briccola 121. The current speed (delivered as depth averaged values) has been measured by an ADCP positioned between Briccola 121 and the pressure gauge. More details on instruments and measurement methods can be found in [5].

Table 2-6. Locations of instruments used for HS Marine dataset.



HSM Dataset	Name	Instrument	Longitude (°E)	Latitude (°N)
Water level	Briccola 121	Terry Ferraris MU-C3	45.3676750	12.2569083
Current speed	ADCP	ADCP, Rio Grande 1200 kHz ZedHed	45.3675889	12.2572194
Pressure	RBR	Pressure cell, RBRonly	45.3675750	12.2573722

The measurements causing the largest draw downs (i.e., where the amplitude could be separated from background conditions) are listed below.

Table 2-7. Vessel passages in HS Marine dataset.

Time 16/05/2022	Name	Length (m)	Width (m)	Draft (m)	Speed (knt)	H _{Briccola} (m)	CS _{max} (m/s)
06:42	Spirit of Chennai	160.0	24.8	6.9	9.2	0.32	0.76
06:50	Luise Borchard	132.6	19.2	6.3	9.9	0.23	0.44
07:27	Eurocargo Alexandria	200.9	26.5	7.5	10.5	0.70	1.18
09:31	Nervion Valley	176.0	31.0	7.3	9.0	0.43	1.10

2.7.2 Model calibration

In the present section the calibration of the displacement wave model will be presented. Three main simplifications are considered:

- During the model calibration (and during the planned production modelling) a single vessel track is considered, see Figure 2.19. This track is positioned in the central part of the channel. In principle, the track is likely to vary from passage to passage depending on the vessel and meteomarine conditions. However, for numerical reasons a single track is considered because the quad-based computational mesh resolving the channel needs to follow the curvature of the track to avoid numerical instabilities.



- During the model calibration the vessel is accelerated slowly to the speed given at the monitoring location. Once the vessel has reached this speed, it proceeds at constant speed. In reality the vessel speed may have varied along the track.
- The model water level is set to zero m MSL, unless stated otherwise.

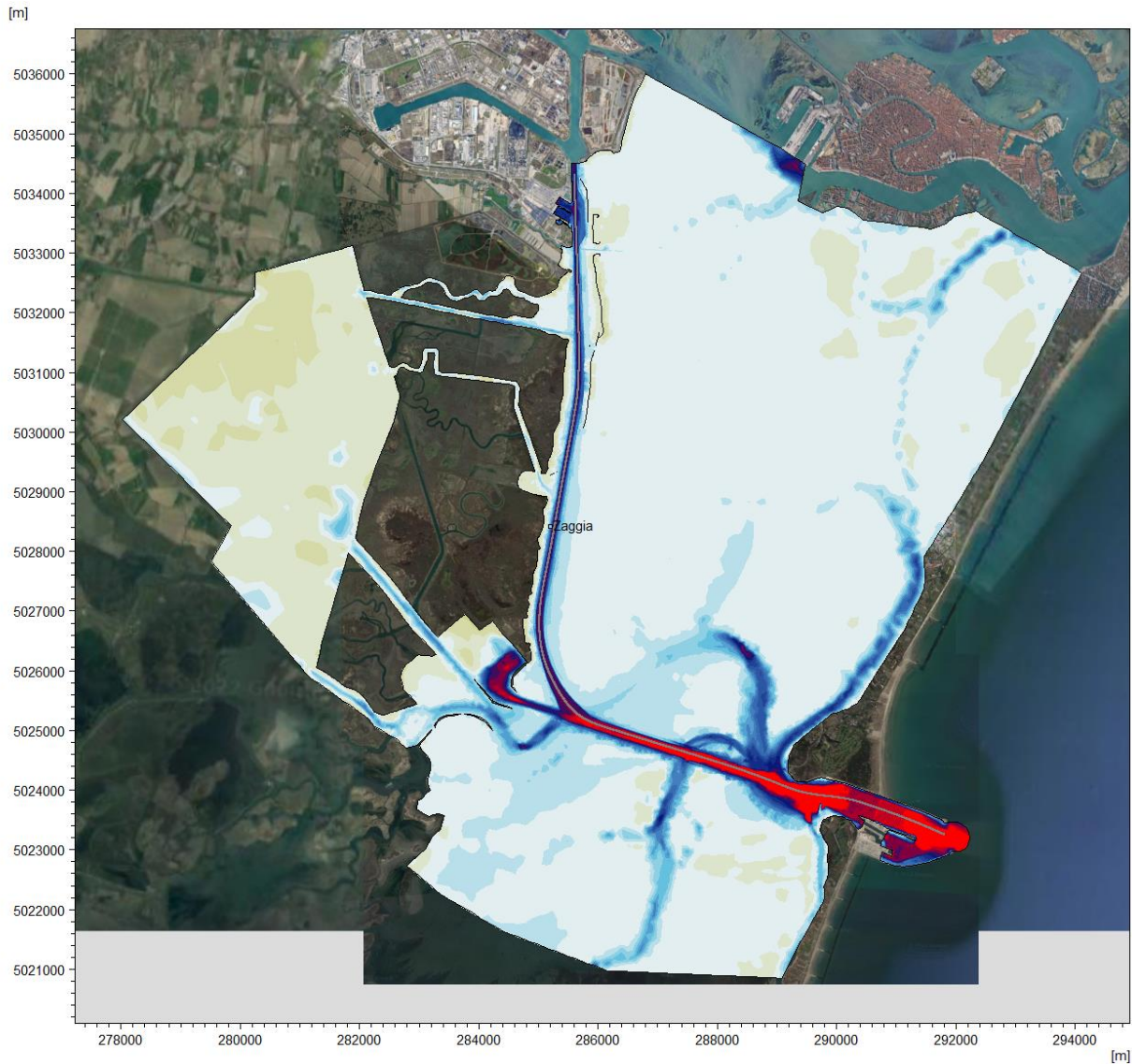


Figure 2.19. Visualization of the used vessel track.



2.7.2.1 Calibration against data from CNR Database

Three cases from the CNR database have been selected: a tanker vessel, a container vessel, and a Ro-Ro ferry, see Table 2-8.

Table 2-8. Calibration cases from CNR Database

Vessel	Type	Date	H (m)	Speed (knt)	Dir.	L (m)	B (m)	Draft (m)
Alicudi M	Oil/Chemical Tanker	21/10/2019 10:14	0.8	9.3	Going in	176	31	8.7
RDO Concord	Container Vessel	20/09/2019 10:28	1.4	8.2	Going out	304	40	9.9
Cruise Olympia	Ro-Ro Passenger	12/09/2019 06:18	0.95	9.7	Going out	225	34	6.8

The moving pressure field is created through use of a scaled grid-file representation of the vessel. The scaling of the hull is limited to +/- 15% so the model representation is limited by the grid file geometry and availability.

At the time of model calibration, the digital representation of the Ro-Ro vessel type was not available. Instead, a bulk carrier was used to represent 'Cruise Olympia'. Note also that the scaling of the z-axis for this vessel should have been 0.568 but has been set to 0.85 to avoid over-scaling of the grid. For the 'RDO Concord' a scaling of 0.83 on the y-axis has been used as it is only slightly more than 15% down scaling, see Table 2-9.

Table 2-9. Applied vessel hulls and scales for CNR calibration.

Vessel	Grid file	Scale X	Scale Y	Scale Z
Alicudi M	Tanker_3.grd	0.910	1.006	1.089
RDO Concord	Con-11.hull	0.967	0.83	1.008
Cruise Olympia	Bul-05_Bulker_49300t.hull	1.126	1.056	0.85

The measurements from the CNR database consist of measurements of depth. To make a more direct comparison between the modelled water level a translation has been made:



$$WL_{meas} = depth_i - depth_{i=1} \quad Eq. 2.6$$

Here i indicates the timestep index of the measurement. The measured and modelled depth of the first time step is given in Table 2-10. The model bathymetry was found to be considerably deeper than the depth indicated by the measurement. In the model, the measurement location is positioned on the slope from the channel to the western bank. In the model, about 50 m west of the measurement location, depths similar to those of the measurement location are found in the model.

Table 2-10. Overview of measured and modelled depth at timestep 1 during CNR modelling.

Depth _{i=1} (m)	Alicudi M	RDO Concord	Cruise Olympia
CNR Database	2.6	2.7	2.5
Model	6.2	6.2	6.2

This local depth discrepancy between the real channel bathymetry and the model bathymetry will introduce some uncertainty in the comparison between model results and the measured water level variations.

2.7.2.1.1 In-going passage of Alicudi M

Given that the vessel type of the grid file matches the real vessel and that the scaling of the grid file is well below 15% the model should be able to provide a good representation of the vessel passage. From Figure 2.20 this is also seen to be the case. The magnitude of the drawdown event is well captured by the model – even the sub-subsequent waves are visible and relatively well captured by the model. This is very encouraging since the largest bed shear stresses happen during the draw down, see Figure 2.24.

Some minor differences in the draw down magnitude and size of the subsequent smaller waves were observed. These differences are partly related to the difference in ambient depth between the measurement and model. The relative distance from the vessel to the measurement location (the chosen track) may also have had an importance.



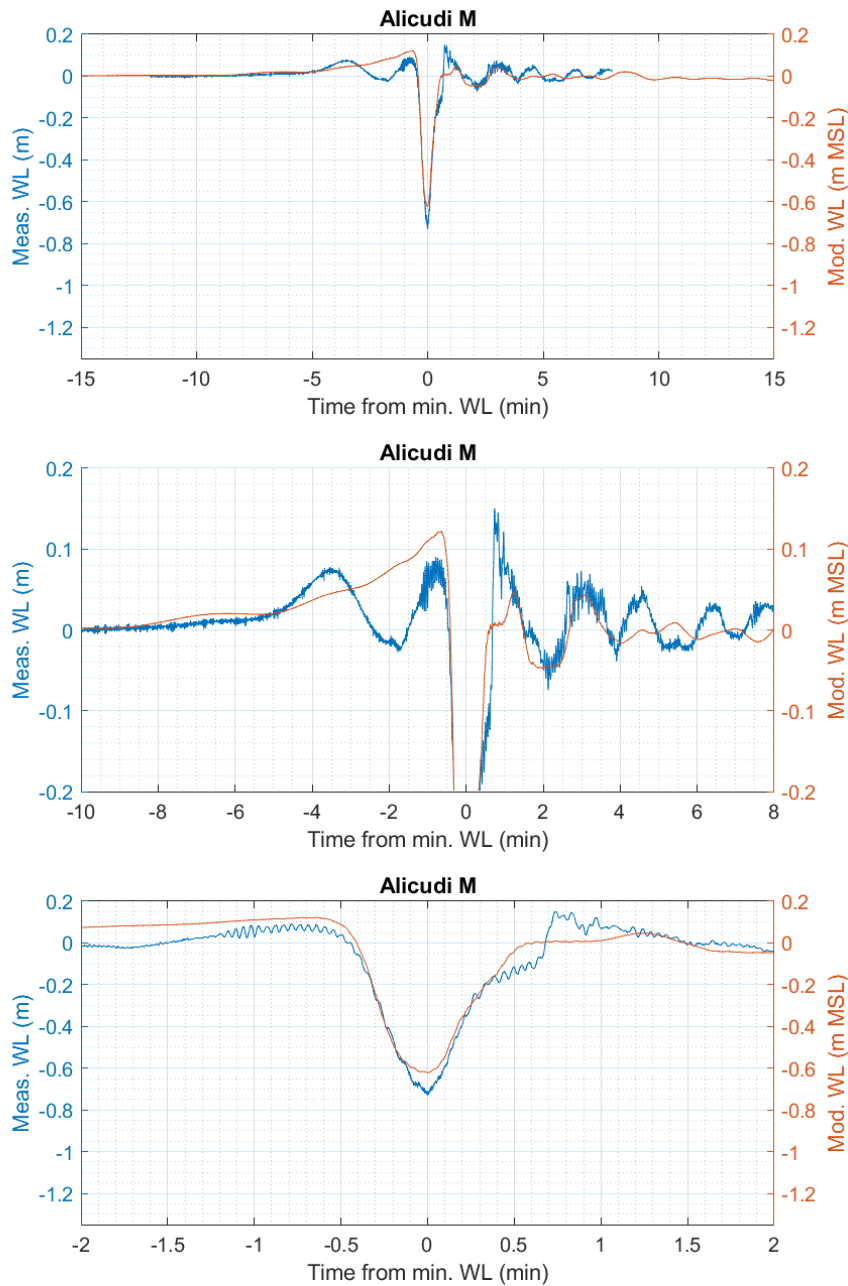


Figure 2.20. Time series comparison of water level at CNR measurement location during the in-going passage of Alicudi M.

2.7.2.1.2 Out-going passage of RDO Concord

The model captures the shape of the draw down and the subsequent waves fairly well, though the size of draw down is underestimated at the measurement location, see Figure 2.21.



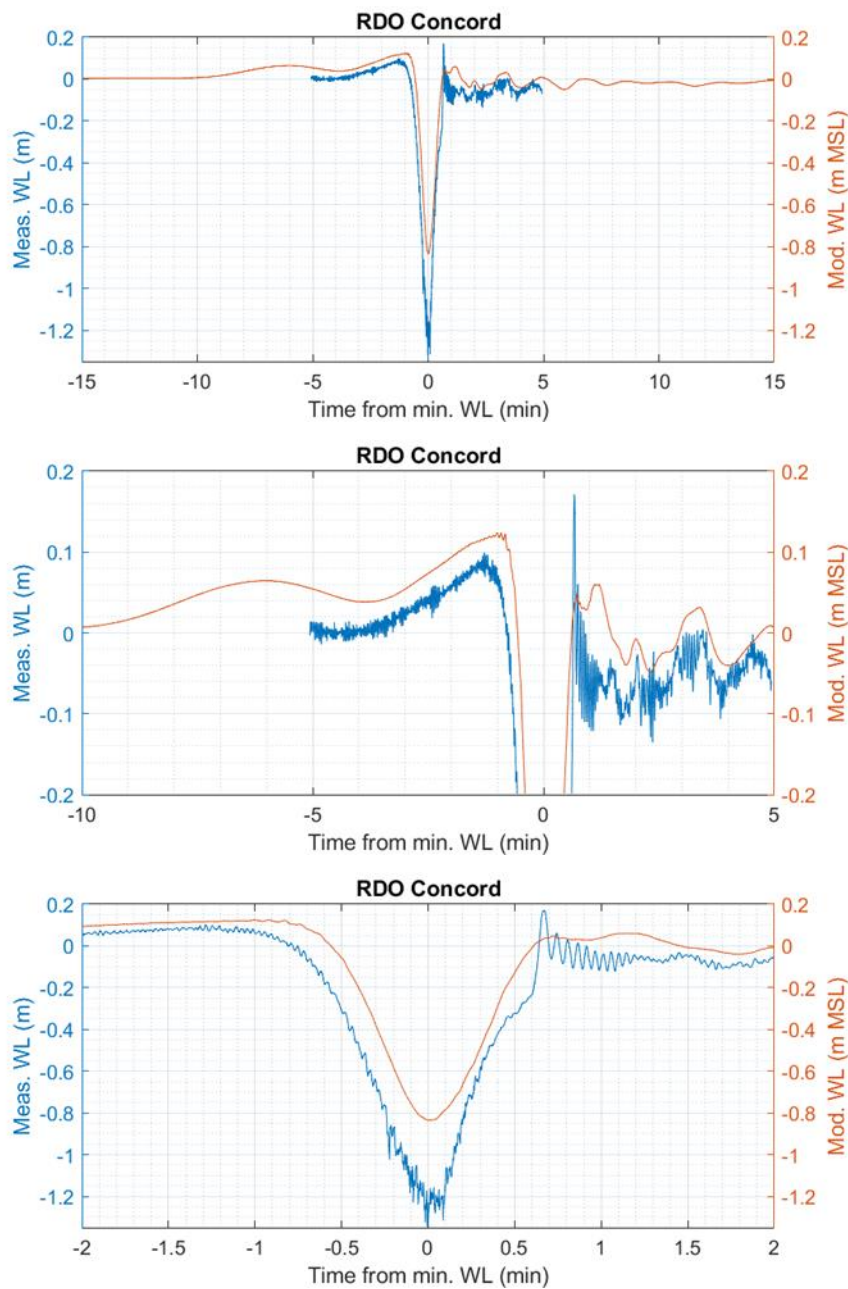


Figure 2.21. Time series comparison of water level at CNR measurement location during the outgoing passage of RDO Concord.

Closer to shore, where the water depth in the model matches the measured values better, the model displays a draw-down of similar magnitude as the measurement, see Figure 2.22. Hence despite the local depth discrepancy the model does produce a similar draw down magnitude and re-produces



the re-adjustment waves sufficiently accurate. The model was found to be able to evaluate the bed shear stresses and erosion of the flats surrounding the MMC satisfactorily.

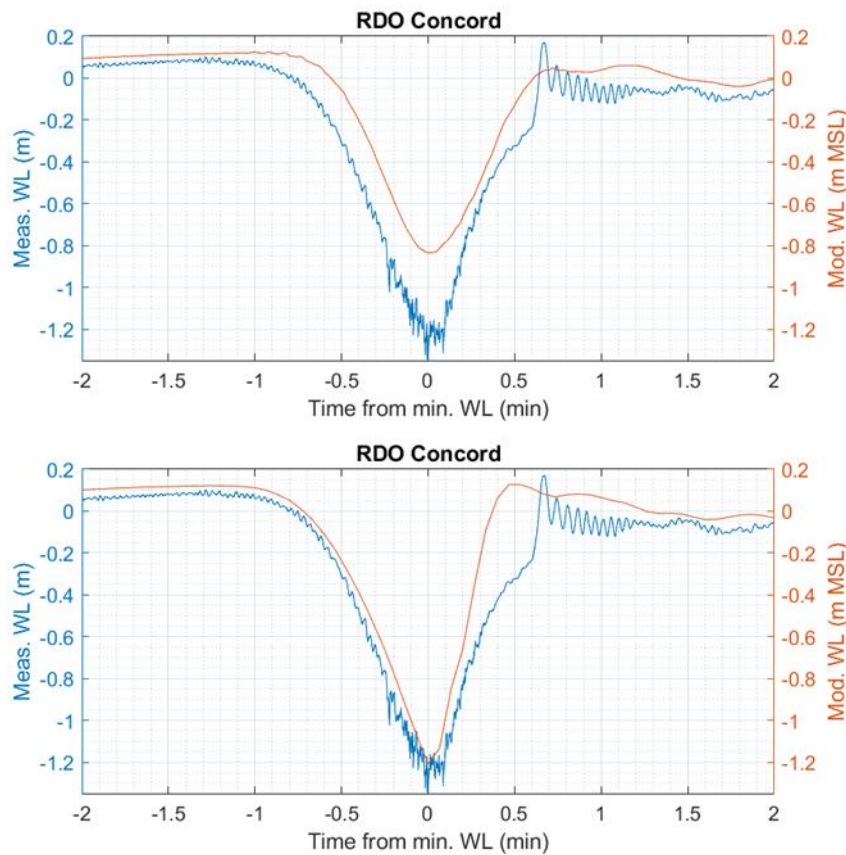


Figure 2.22. Time series comparison of water level at (Top) CNR measurement location and (Bottom) ~50 m closer to shore during the out-going passage of RDO Concord.

2.7.2.1.3 Out-going passage of Cruise Olympia

Comparisons for the out-going passage of the Ro-Ro passenger ship, Cruise Olympia, are presented in Figure 2.23. The measurements indicate an increase in ambient water level during the measurement of around 0.10 m. In the model a constant water level was assumed. The rising water level has an effect on the measured flow, both in the channel and on the flats. It is clear that these observed unsteady conditions will introduce some uncertainty in the comparison between model results and measurements. Considering the discrepancy between the local depth and the measured depth, and the fact that the grid file doesn't match the vessel type exactly (scaling of the z-axis had to be limited), the model was found to represent the event very well.



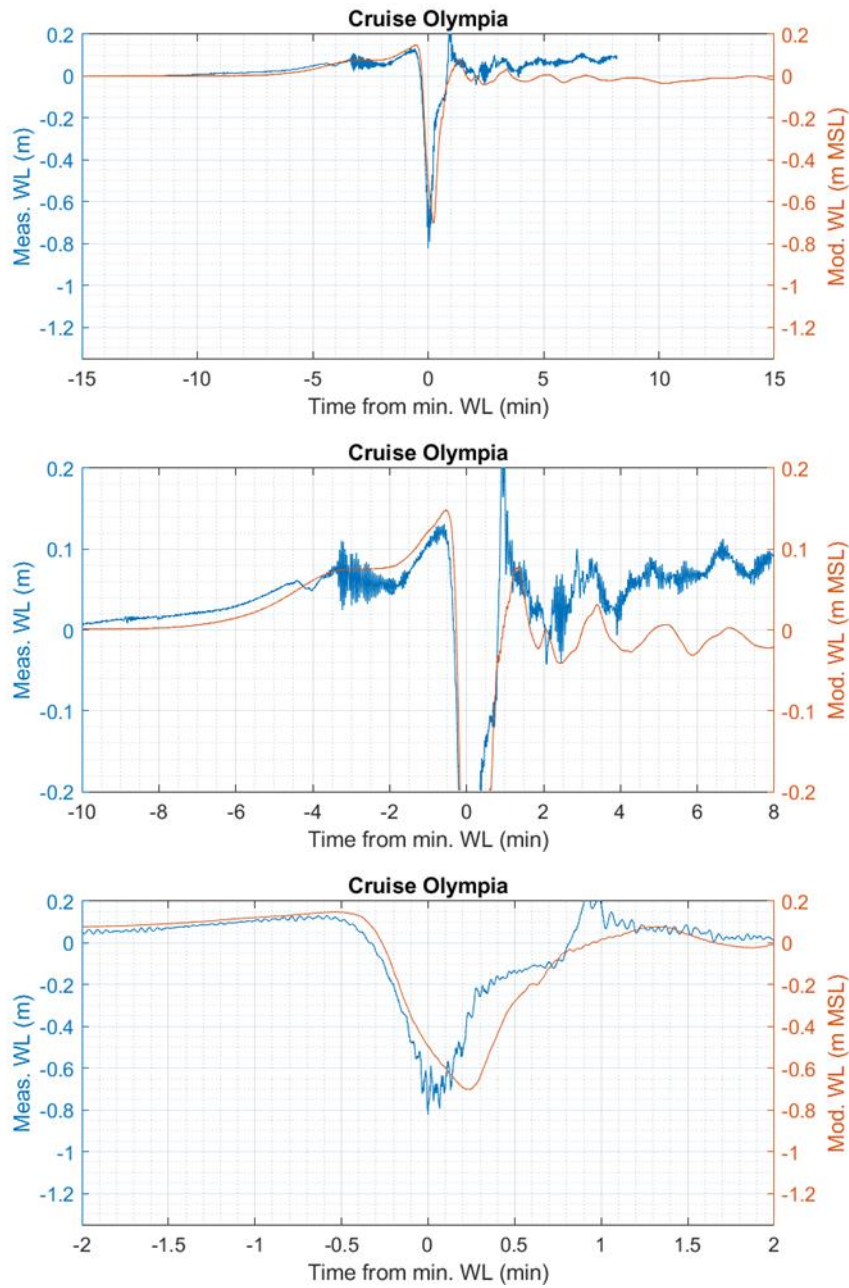


Figure 2.23. Time series comparison of water level at CNR measurement location during the outgoing passage of Cruise Olympia.



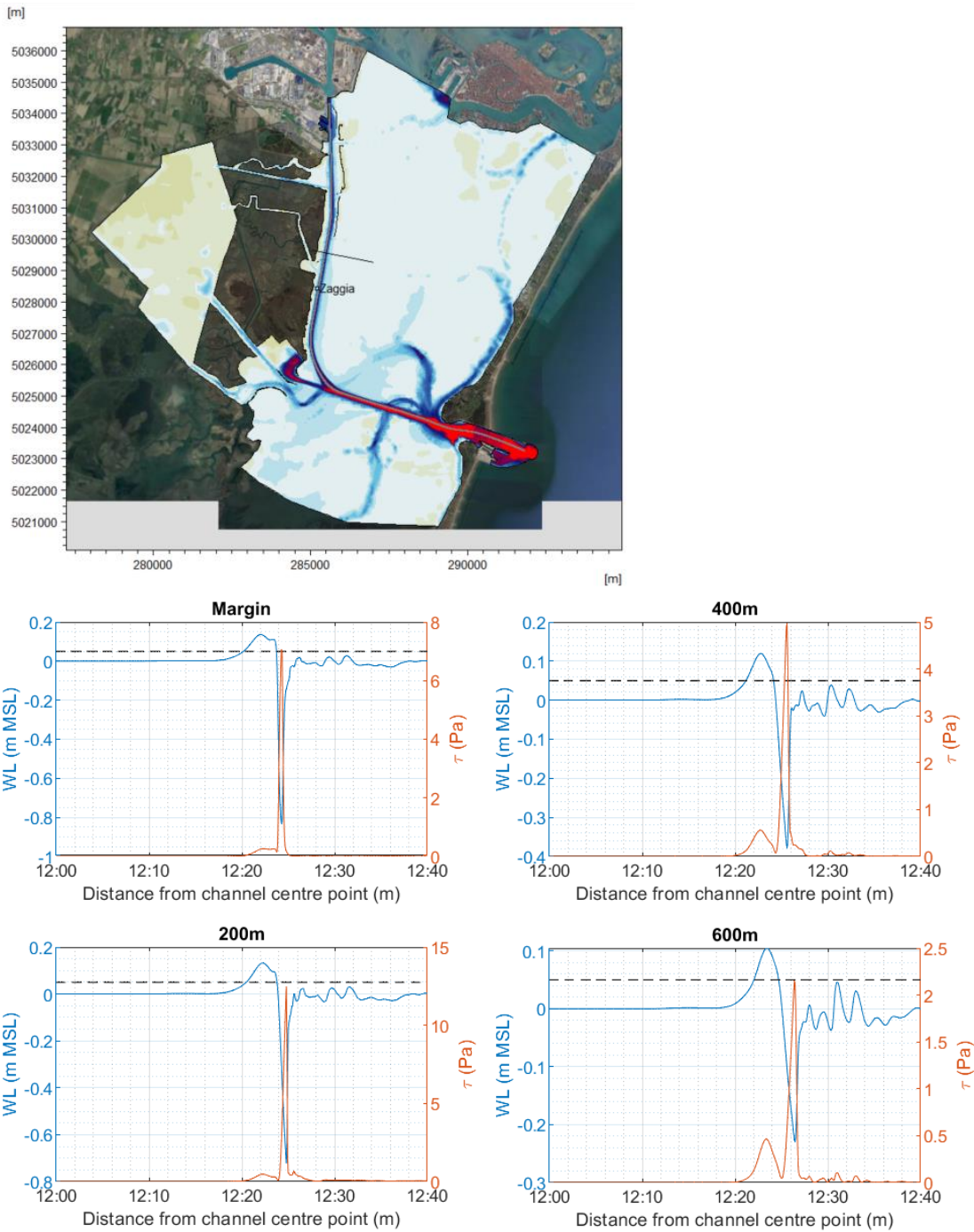


Figure 2.24. Water level and bed shear stress calculated by hydrodynamic model during passage of Cruise Olympia. Extraction line indicated in top panel.



2.7.2.1.4 Concluding remark

The modelling of displacement waves in a real navigation channel is associated with some simplifications. Some uncertainty is introduced by differences between the measured bathymetry and the model bathymetry that was derived from previous field surveys. Furthermore, some uncertainty is caused by the way the vessel is represented in the model. This includes both the track (position, speed and direction of the vessel) as well as the scaling of the vessel hulls.. Overall, the model was found able to reproduce the observed vessel generated water level variation well. As such, the model provides a good basis for evaluation of the effects of measures aimed at mitigating the negative impacts of the maritime traffic through the MMC.

2.7.2.2 Calibration against data from HS Marine Dataset

One of the cases measured by HS Marine has been simulated, see Table 2-11. Some sensitivity tests have additionally been performed as listed below:

- Case 1 (Mesh v00g): Original model bathymetry (also used during CNR calibration).
- Case 2 (Mesh v00g2): Re-interpolated model bathymetry using tightened prioritization polygon around bathymetric MMC scatter data.
- Case 3 (Mesh v00g2, east shifted track): Case 2 with an east shifted track reducing the distance to Briccola 121 from about 97 m to about 71 m.
- Case 4 ((Mesh v00g2, east shifted track, WL = -0.1 m MSL): Case 3 with an ambient water level of -0.1 m MSL.

Table 2-11. Calibration case from HS Marine Dataset

Vessel	Type	Date	Speed (knt)	Dir.	L (m)	B (m)	Draft (m)
Nervion Valley	Oil/Chemical Tanker	16/05/2022 09:31	9.0	Going out	176	31	7.3

To represent Nervion Valley the grid file specified in Table 2-12 has been used. All scales are well below 15% and the hull type matches the real vessel type. As such the uncertainties in this regard are fairly small.



Table 2-12. Applied vessel hull and scales for HS Marine calibration.

Vessel	Grid file	Scale X	Scale Y	Scale Z
Nervion Valley	Tanker_3.grd	0.910	1.006	1.089

In the present case the model also displays local depth discrepancies, see Table 2-13. To minimize these a re-interpolation of the model bathymetry has been made giving rise to a better match between measured and modelled ambient depth. Note that the re-interpolation has not had any effect on the ambient model depth at the CNR measurement location.

Table 2-13. Overview of approximate measured and modelled depth at HS Marine locations during timestep 1.

	HS Marine	Model-1	Model-2
Briccola 121 Depth _{i=1} (m)	-	5.7	5.6
ADCP Depth _{i=1} (m)	3.3	5.3	3.4
RBR Depth _{i=1} (m)	2.9	3.4	3.4

The results of the sensitivity tests are shown in Figure 2.25. Note that the pressure at RBR has been converted to water depth assuming a water density of 1025 kg/m³ and hydrostatic pressure. This calculated depth has then been converted to WL using Eq. 2.6. These tests indicate that the relative distance from the vessel to the measurement location (i.e. the banks) have a significant influence on the current speed and therefore also the bed shear stress.



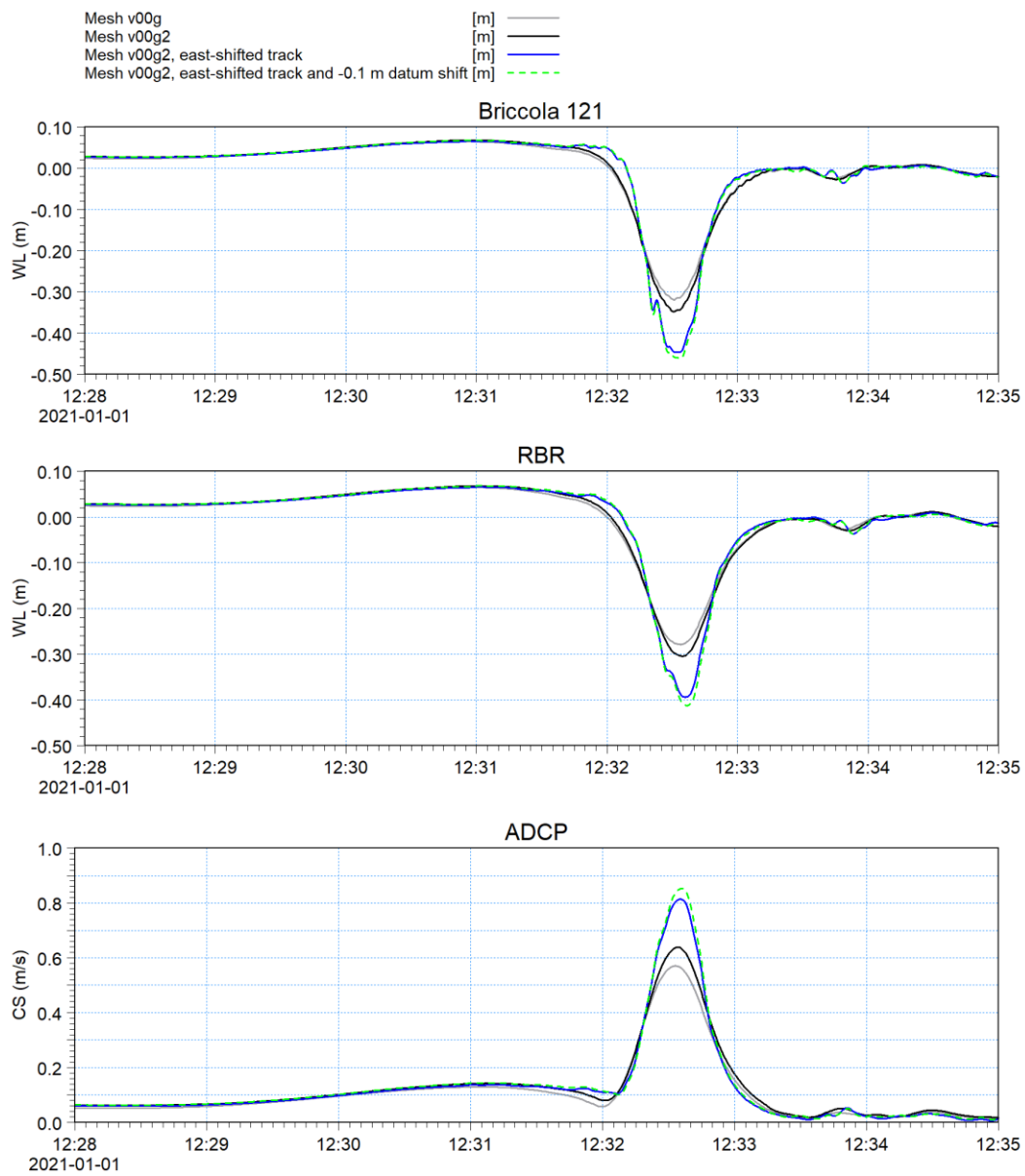


Figure 2.25. Model results of sensitivity tests during out-going passage of Nervion Valley.

Figure 2.26 presents the model results in terms of Case-4 water level relative to the measurements made by HS Marine.

- Top Panel: Water level at Briccola 121. In the figure title the water depth at the ADCP location is stated. Measured values are indicated as a solid blue line and modelled values as a dashed orange line.



- Bottom Panel: Water level at RBR. In the figure title the water depth at the RBR location is stated. Measured values are indicated as a solid blue line and modelled values as a dashed orange line.

The agreement between measured and modelled water level is seen to be good – despite the local differences in depth and uncertainty related to the relative vessel position.

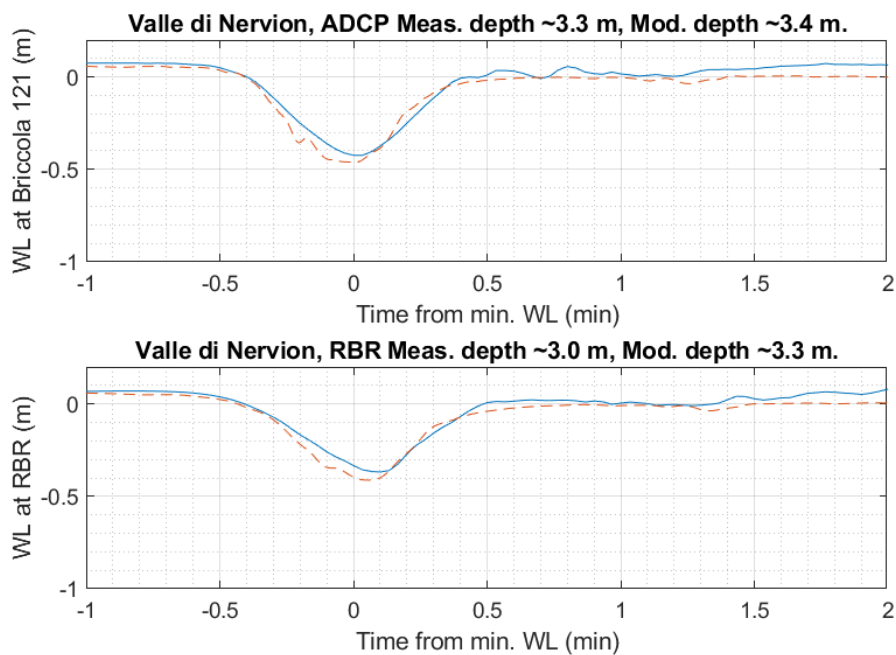


Figure 2.26. Time series comparison of water level at HS Marine measurement locations during the out-going passage of Nervion Valley.

Figure 2.27 presents the model results in terms of Case-4 current speed relative to the measurements made by HS Marine. In the figure title the water depth at the ADCP location is stated.

- Top Panel: Water level on the left axis and current speed on the right axis.
 - Measured water level at Briccola 121 and RBR is indicated as solid lines, blue and black respectively.
 - Modelled water level at ADCP is indicated as a dashed blue line.
 - Measured/modelled current speed at ADCP is indicated as a solid/dashed orange line.
- Middle Panel: Current speed on the left axis and current direction on the right axis.



- Measured/modelled current speed at ADCP is indicated as a solid/dashed blue line.
- Measured/modelled current direction at ADCP is indicated as orange rings/dots.
- Bottom Panel: Current speed multiplied by ambient depth on the left axis and current direction on the right axis.
 - Measured/modelled current speed times local measured/modelled ambient depth at ADCP is indicated as a solid/dashed blue line.
 - Measured/modelled current direction at ADCP is indicated as orange rings/dots.

The model is able to reproduce the measured current speed magnitude quite well. Especially considering that there are uncertainties in terms of the relative vessel position, the bathymetry and the fact that the model does not include any additional forcing from tides or wind. Furthermore, the model was found to reproduce the observed current directions quite well, considering the above mentioned uncertainties.

It was concluded that the hydrodynamic model is able to reproduce the governing hydrodynamics (water level variation, flow speeds and patterns) of vessel driven displacement waves to a satisfactory level for evaluation of their influence on the sediment transport and erosion along the MMC.

Further investigations prepared by Cetena, who implemented a simulation of the passage of a ship with a Computational Fluid Dynamics (CFD) naval model, allowed to conclude that the approach adopted with the moving pressure fields allows to obtain results in terms of draw down completely comparable to those obtained with a sophisticated and computationally unsustainable naval model (for the purposes of the study) such as a CFD model. The assumptions, setup and results of the CFD model exercise are reported in Appendix D.



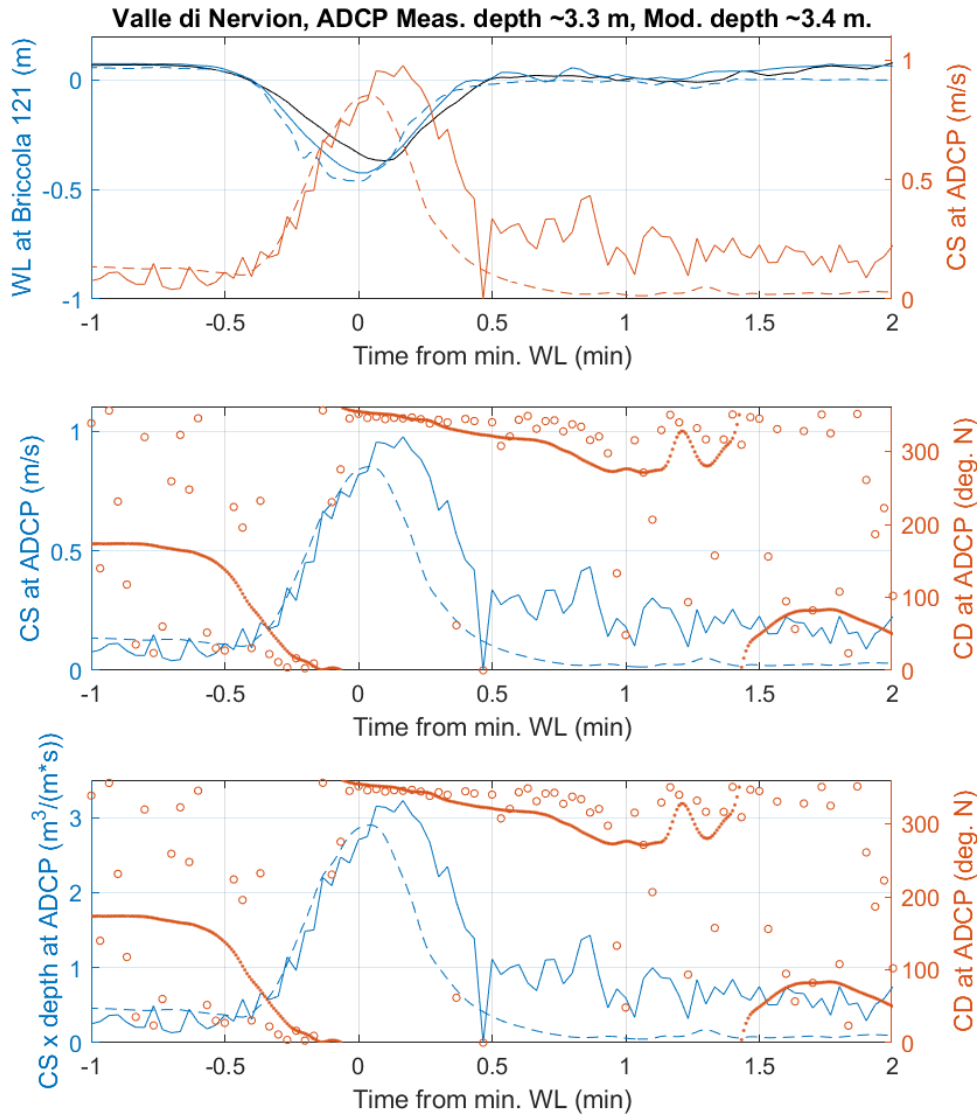


Figure 2.27. Time series comparison of current speed at HS Marine measurement locations during the out-going passage of Nervion Valley.



2.8 Establishment of representative vessel traffic

To calculate the impact of maritime traffic on the sediment balance for the channel and the surrounding areas, an overview was made of all vessel types that navigate through the MMC and their respective occurrence. This was done based on the CNR Database described in Section 2.7.1.1, and the Port of Venice (PoV) Database. This database of the channel traffic has been made available by Port of Venice and spans 2021 to 12th August 2022 (588 days). The PoV Database does not contain information on the vessel speed, but it does contain a much larger dataset of vessel types and sizes than the CNR Database. This makes it suitable for selecting representative vessel geometries. The PoV data base contains the following information:

- Vessel name and IMO code
- Vessel type
- Vessel length, width and draft
- Time

Based on the PoV Database 5 main vessel categories were selected. In addition to these five categories PoV have requested the inclusion of two cruise vessels (one 230 m long and one 300 m long). The following vessel categories were identified:

1. Container vessels, 27.1% of events
2. Tanker vessels, 20.5% of events
3. Bulk carriers, 15.5% of events
4. General cargo vessels, 15.3% of events
5. Ro-Ro vessels, 14.6% of events
6. Cruise vessels

The five main categories make up 93% of the events in the PoV Database and will therefore practically represent the entire traffic in the MMC.

As agreed with PoV, the cruise vessels should be included with one passage per week from 1st April to 1st November (30 weeks), hence 120 events (in-bound + out-bound). Relative to the total number of events in the PoV Database this is about ~2% of the time.



2.8.1 Vessel geometry

The vessel geometries of the 5 main categories were selected by finding the vessel corresponding to the 50th and 75th percentile vessel length in the PoV Database. NB. General cargo and Ro-Ro vessels are represented by the 50th percentile vessel – matching the most frequent length interval, see Figure 2.28.

Table 2-14. Vessel geometries from PoV Database.

Vessel Type	Name	Length Percentile	Abbr. Name	Length (m)	Breadth (m)
Container vessel	Atlantic Silver	50	Con. S	175.1	27.9
Container vessel	Lavaux	75	Con. L	199.6	29.8
Tanker vessel	Minstrel	50	Tan. S	161.1	23.0
Tanker vessel	AS Pamira	75	Tan. L	179.9	32.2
Bulk carrier	MSC Asli	50	Bul. S	175.6	23.1
Bulk carrier	Valsesia	75	Bul. L	190.0	28.5
General cargo	Syn Zaura	50	Gen.	109.7	17.8
Ro-Ro	Loyal	50	Ro-Ro	200.9	26.5
Cruise vessel	-	-	Cru. S	230	-
Cruise vessel	-	-	Cru. L	300	-

The drafts of all vessels were selected based on the scaled vessel grid files such that it matches min (10.5 m, draft of fully loaded hull). The widths of the cruise vessel were selected in a similar way such that they match the width of the scaled vessel grid file. The resulting geometries are given in Table 2-15 along with the original PoV geometry for convenience. Figure 2.29 provides bar charts of the vessel drafts contained in the PoV database. These bar charts confirm that the selected draft is reasonable.



Table 2-15. Vessel geometries. Original from PoV Database and from scaled vessel grid files to be used in the displacement wave model.

Abbr. Name	Org. Length (m)	Org. Breadth (m)	Hull Length (m)	Hull Breadth (m)	Hull Draft (m)
Con. S	175.1	27.9	175.1	27.9	9.0
Con. L	199.6	29.8	199.6	29.8	10.1
Tan. S	161.1	23.0	161.1	23.0	9.2
Tan. L	179.9	32.2	179.9	32.2	10.5
Bul. S	175.6	23.1	175.6	25.3	9.3
Bul. L	190.0	28.5	190.0	28.5	10.5
Gen.	109.7	17.8	109.7	17.8	7.5
Ro-Ro	200.9	26.5	200.9	26.5	6.2
Cru. S	230.0	-	251.6	27.4	7.0
Cru. L	300.0	-	300.0	32.6	8.3



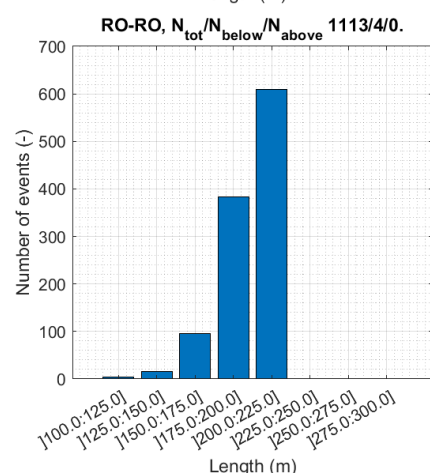
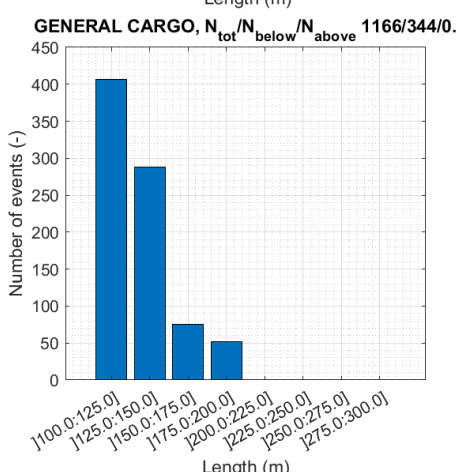
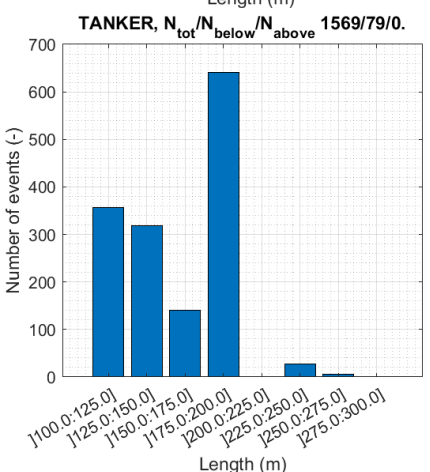
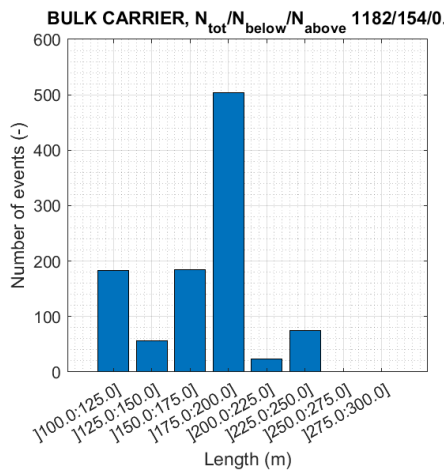
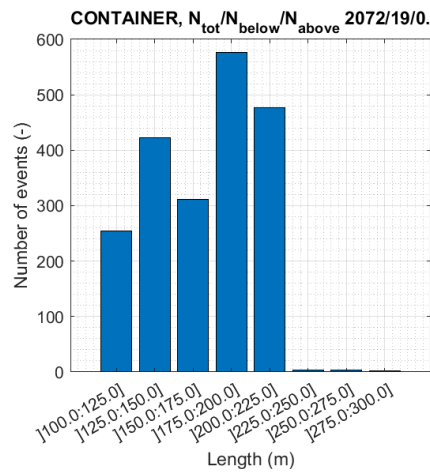


Figure 2.28. Length distribution of the five vessel categories. The numbers stated in the title indicate the total number of (e.g. container vessel) indices in the dataset and the number of indices that are below/above the minimum/maximum of the chosen range.



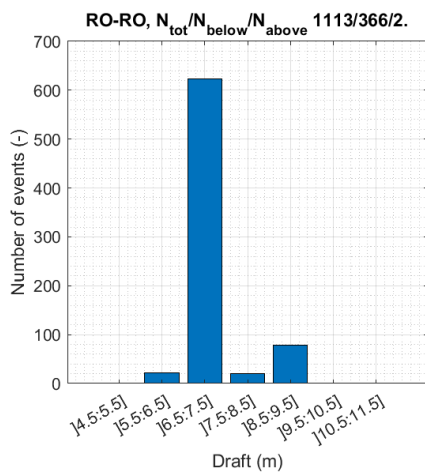
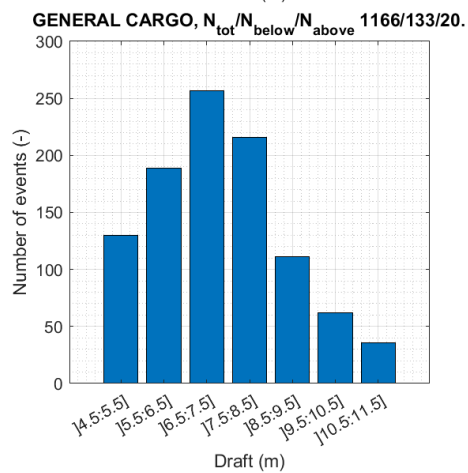
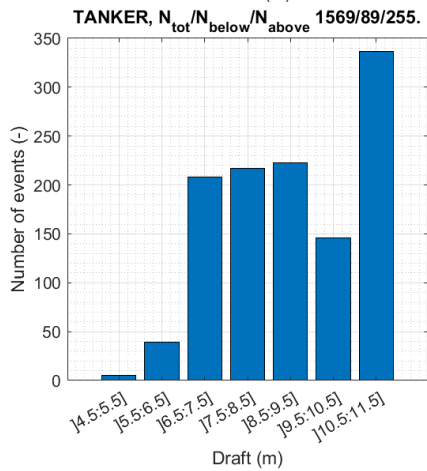
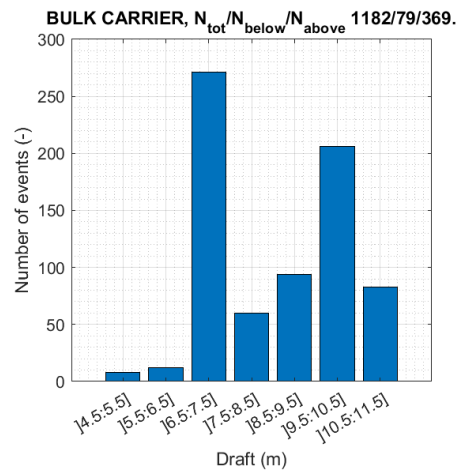
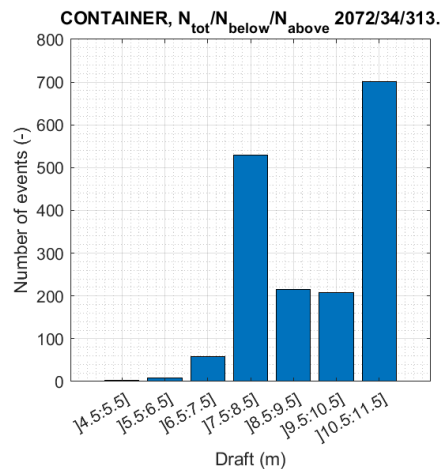


Figure 2.29. Draft distribution of the five vessel categories. The numbers stated in the title indicate the total number of (e.g. container vessel) indices in the dataset and the number of indices that are below/above the minimum/maximum of the chosen range.



2.8.2 Vessel speed

To get an impression of the velocity distribution within the five main vessel categories (container vessels, tankers, bulk carriers, general cargo vessels and ro-ro's) the bar charts in Figure 2.31 has been made based on the CNR Database. The columns in the bar chart represents data in the range:

$$V_{bin} - 1 \text{ knt} < data \leq V_{bin}$$

Additionally, a table of maximum and minimum vessel speed is provided in Table 2-16 to enable estimation of where the outliers from the velocity range in the bar charts are located in terms of speed.

Table 2-16. Maximum and minimum vessel speed per category based on the CNR Database.

	Container	Tanker	Bulk	General	Ro-Ro
Min. speed (knot)	6.1	5.3	6.4	5.5	7.2
Max. speed (knot)	12.5	11.9	10.8	11.7	11.2

The bar charts clearly indicate that the majority of the vessels pass the CNR measurement location at speeds of about 8-10 knots, particularly 9 and 10 knots occur frequently. Considering that the speed limit in the channel south of Fusina is 10 knots this is not surprising.

Based on the CNR data and the known speed limit it therefore seems reasonable to consider the representative vessel traffic as navigating at 10 knots throughout the MMC, see vessel speed principle in Figure 2.30. The influence from reducing the vessel speed (tentatively up to 8 knots) in the north-south oriented part of the channel will then be investigated during the investigation of mitigation measures.





Figure 2.30. Vessel speed profile of in-bound passage.



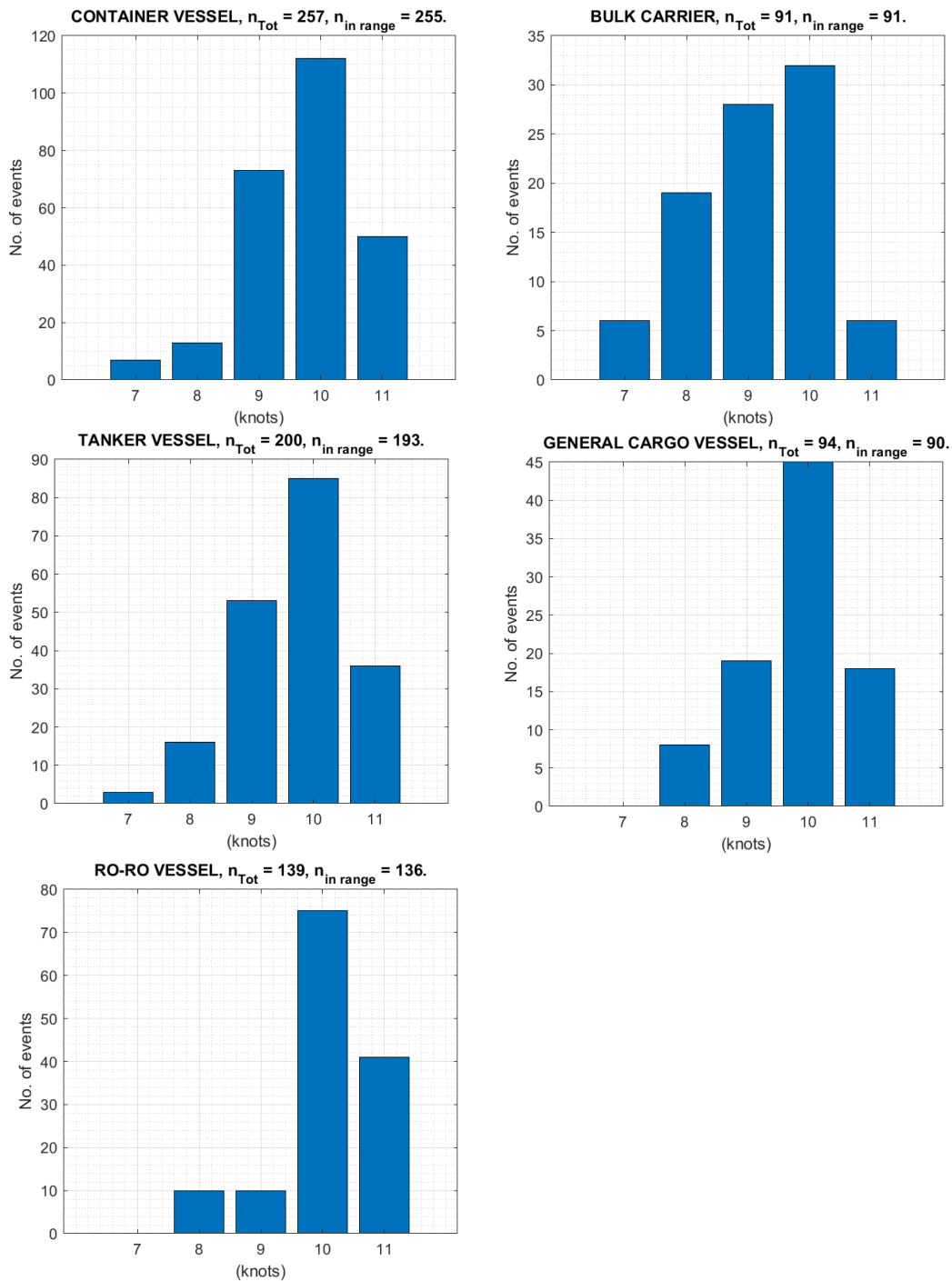


Figure 2.31. Velocity distribution of the five vessel categories considering 7-11 knot velocity range. The numbers stated in the title indicate the total number of (e.g. container vessel) indices in the dataset and the total number of (e.g. container vessel) incidents in the velocity range.



2.8.3 Production modelling of displacement waves

The production modelling work of displacement waves consists of the following tasks:

- Baseline modelling
- Mitigation modelling
 - Effect from reduction of speed
 - Effect of short-term channel layout (not settled upon time of writing)
 - Additional effects e.g., increased water level or long-term channel layout

During the baseline modelling, all selected vessels will be simulated in-bound and out-bound (towards Fusina/Malamocco respectively). The navigation speed in all simulations will be 10 knots and the ambient water level is set to zero m MSL. Each model run contains an acceleration/deceleration phase to/from 10 knots at the beginning and end of the track. The acceleration/deceleration of the vessel takes about 12/20 minutes respectively to avoid numerical shock waves from forming in the model.

The accumulated effect of the traffic for 1 year will be calculated by considering the weighted contribution of each selected vessel category as shown in Table 2-20. The baseline modelling will also investigate whether there is a difference between in-bound and out-bound traffic with respect to the erosion potential.

A series of additional model simulations will be carried out for to analyze the impact of possible mitigation measures. These additional simulations will include a few scenarios that are most important in terms of sediment transport and risk of erosion. The additional simulations will be selected based on the results of the simulations for the present situation. The mitigation measures to be considered will mainly be the reduction of speed, see Figure 2.32 and Figure 2.33. The possible effects of the new channel layout will be assessed later when the preliminary layout of the channel has been developed.



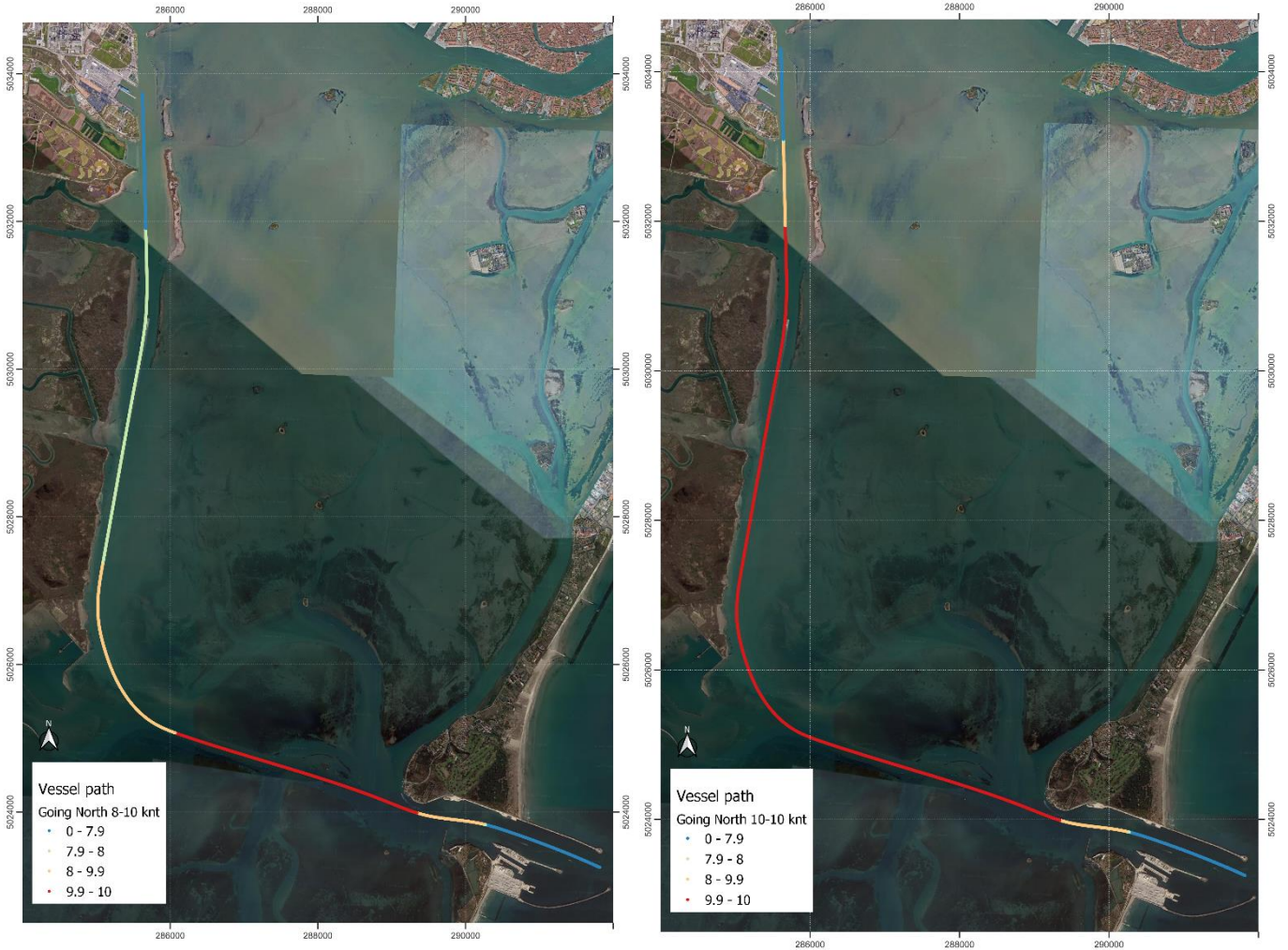


Figure 2.32. Production vessel track for in-bound passages with (left) 10 to 8 knots and (right) 10 knots.



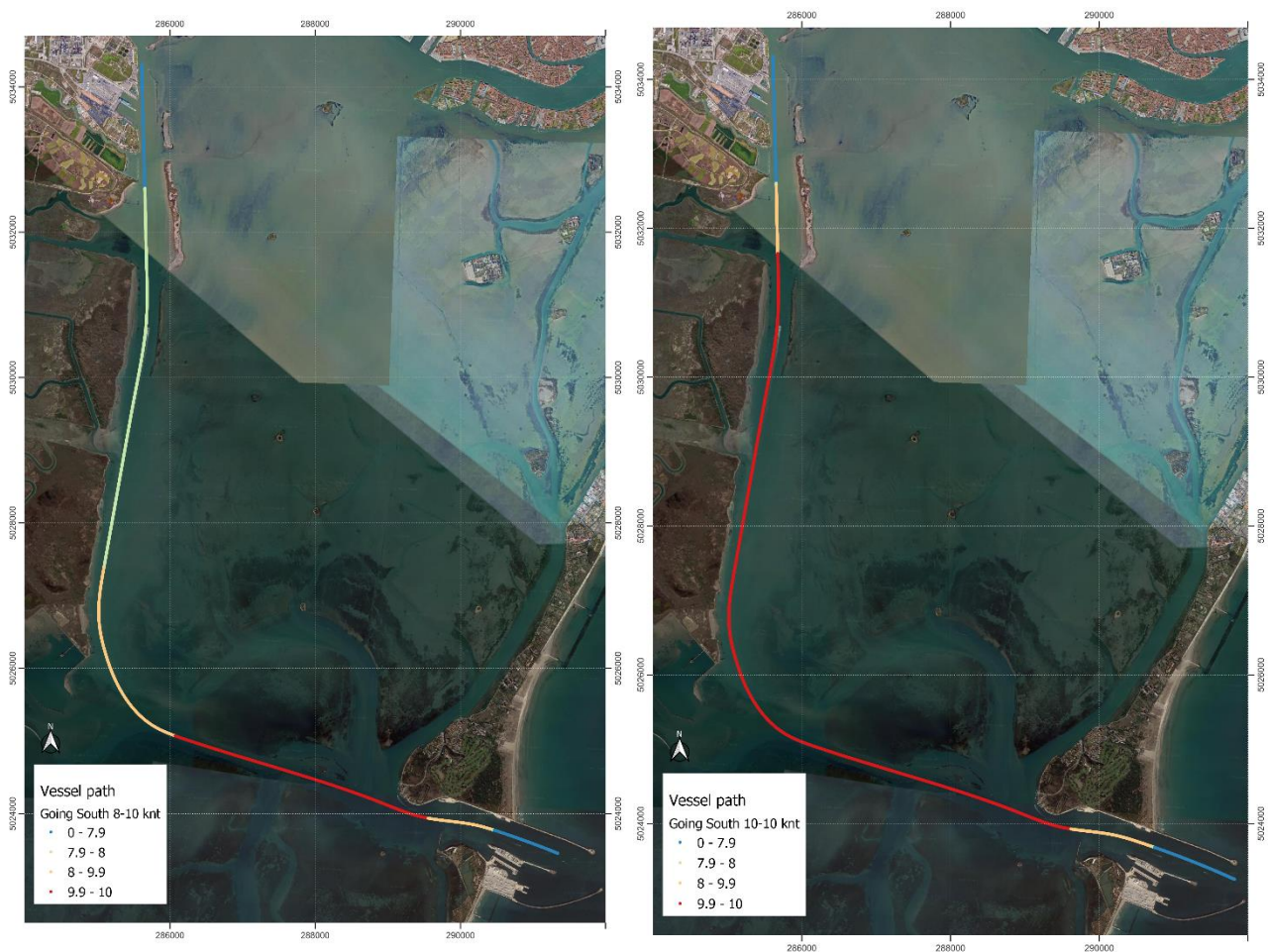


Figure 2.33. Production vessel track for out-bound passages with (left) 8 to 10 knots and (right) 10 knots.

2.9 Kelvin Waves

The movement of a ship through water is often characterized by a system of waves originating from the ship's bow and stern, see Figure 2.34 and Figure 2.35. This wave pattern is termed the Kelvin wake or the secondary waves. They arise as the result of pressure differences along the ship's hull. Since the hydrodynamic displacement wave model solves the shallow water equations, these waves cannot be directly included in the hydrodynamic model of the MMC as opposed to the primary waves. Therefore, the effect from Kelvin waves on the sediment budget needs to be investigated separately. The present section is concerned with the derivation of the hydrodynamic properties and their effect on the sediment transport.



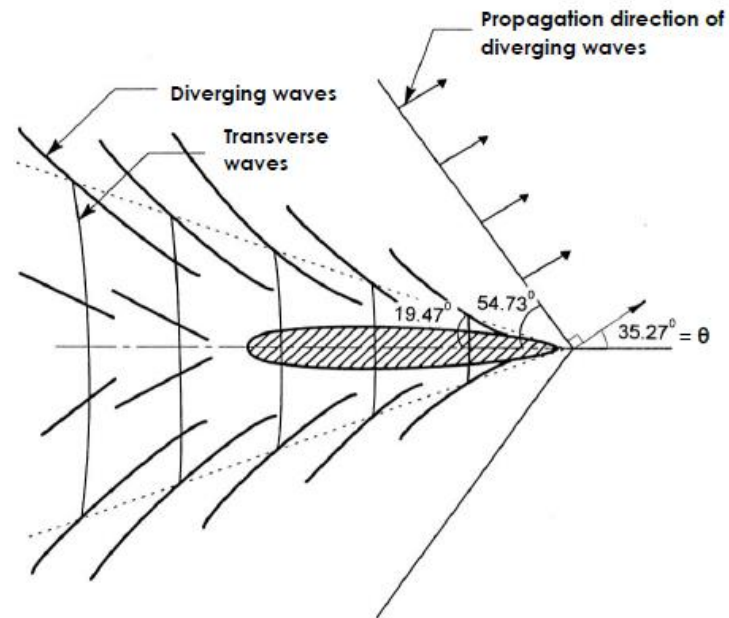


Figure 2.34. Theoretical illustration of Kelvin Wake.

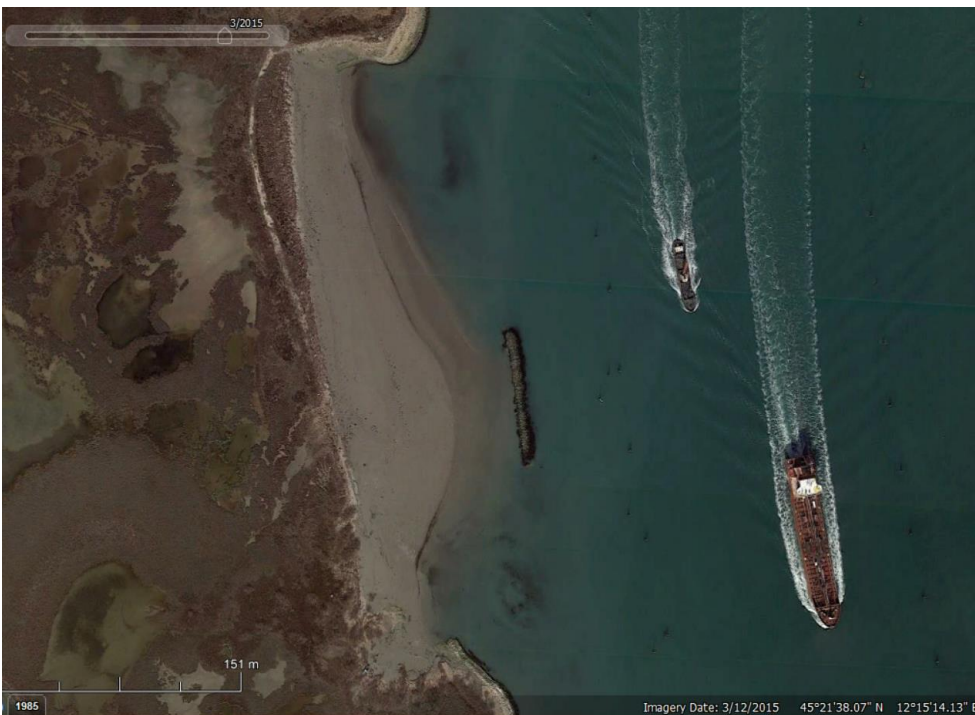


Figure 2.35. Google Earth satellite image from 3rd December 2015 illustrating Kelvin waves in MMC at northern part of the San Leonardo bend.



2.9.1 Estimation of Kelvin wave properties

The wave generation of a vessel is characterised by the Froude number, which in deep water is based on the length (L_s) of the ship and in shallow water on the still water depth (h), see Eq. 2.7 and Eq. 2.8.

$$Fr_{L_s} = \frac{V_s}{\sqrt{gL_s}} \quad \text{Eq. 2.7}$$

$$Fr_{h} = \frac{V_s}{\sqrt{gh}} \quad \text{Eq. 2.8}$$

Here V_s is the speed of the vessel (m/s) and g is the acceleration due to gravity (m/s^2).

When the ship operates at sub-critical speed, $Fr_{h} < 1$, the wave system consists of diverging and transverse waves. The combination of these two wave types is restricted in a wedge-shape (the so-called Kelvin wake) with a cusp angle of about 19.5° , see Figure 2.34. The diverging waves spread out on each side of the ship at an angle of $+35.3^\circ$ relative to the course of the ship. The transverse waves on the other hand move in the same direction as the ship. The diverging waves are important as they refract and shoal towards shore generating some sediment transport in this process. This is not the case for the transversal waves, why only the diverging waves are treated in the following.

2.9.1.1 Wave direction and period

Based on the data from the CNR Database (see Section 2.9.2.1), the vessels navigate at speeds in the range 8-10 knots (some even higher than 11 knots) but with an average speed of around 9.3 knots (~ 4.5 m/s). Since the MMC has a depth of ~ 12 m, this indicates that navigation takes place at sub-critical speeds.

The period (T) of the diverging waves can be estimated from the wave celerity, c .

$$c = \frac{gT}{2\pi} \quad \text{Eq. 2.9}$$

In deep water the wave celerity can be approximated by projecting the vessel speed onto the propagation direction of the diverging waves:

$$c_d = V_s \cos(\theta) \quad \text{Eq. 2.10}$$



Assuming θ equal to 35.3° the wave period can be approximated by Eq. 2.11 inserting the vessel speed in knots:

$$T \approx 0.27 V_s \quad \text{Eq. 2.11}$$

With vessel speeds in the range 8-10 knots the diverging waves thus have wave periods in the range 2.2-2.7 s.

The wave direction is assumed equal to 35.3° relative to the course of the ship.

2.9.1.2 Wave height

The maximum wave height of the diverging waves is estimated based on the empirical model of [6]. This model is based on:

- Vessel geometry
 - Length: L_s
 - Taken at the water line.
 - Bow entry length: L_e
 - Taken at the water line.
 - Draft: D
 - Blocking coefficient: C_b
- Water depth at sailing line: h
 - Assumed to be 12 m.
- Vessel speed: V
- Distance from sailing line: y
 - Assumed to be 15 m.

It is noted that the governing speed is the speed of the vessel through the water. Hence in an opposing/following current of 1 knot, the speed through the water is increased/decreased by 1 knot respectively. The ambient current in the channel reaches up to about 1 knot on both falling and rising tide so in this sense the speed range for calculation of the maximum Kelvin wave height is 7-11 knots rather than 8-10 knots.

The maximum wave height may be estimated based on Eq. 2.12.



$$\frac{gH}{V^2} = \beta(F_* - 0.1)^2 \left(\frac{y}{L_s}\right)^{-\frac{1}{3}} \quad \text{Eq. 2.12}$$

Here F_* is a modified Froude number calculated as a function of $f(V, L_s, C_b, D, h)$, see Eq. 2.13.

$$F_* = \frac{V}{\sqrt{gL_s}} \exp\left(\frac{\alpha D}{h}\right) \quad \text{Eq. 2.13}$$

$$\alpha = 2.35(1 - C_b) \quad \text{Eq. 2.14}$$

The blocking coefficient is calculated based on the vessel displacement volume (V) and geometrical properties: $C_b = \frac{V}{LBD}$.

$$\beta = 1 + 8 \tanh^3\left(0.45\left(\frac{L_s}{L_e} - 2\right)\right) \quad \text{Eq. 2.15}$$

An overview of the geometric parameters used in the calculation of the coefficients are shown in Table 2-17. Note that this table considers the vessels which will be used in the production modelling elaborated in Section 2.8. A constant water depth of 12 m (matching the maximum water depth of the north-south oriented part of the MMC) has been assumed in the calculation of the maximum Kelvin wave height. This calculation is made at a distance (y) of 15 m from the vessel, hence close to the rim of the channel.

Table 2-17. Overview of geometric vessel parameters for determination maximum Kelvin wave height. Here L_s and L_e have been estimated based on the vessel grid file in the MIKE Frequency response viewer.

Vessel	L_s (m)	LPP (m)	L_e (m)	D (m)	C_b (-)
Con. S	171	88.0	49	9.0	0.62
Con. L	190	111.0	45.0	10.1	0.66
Tan. S	157	94.5	26.4	9.1	0.81
Tan. L	174	100.7	35.0	10.5	0.79
Bul. S	172	91.0	44.0	9.3	0.82
Bul. L	186	99.0	45.0	10.5	0.81
Gen.	104	62.5	20.5	7.5	0.72
Ro-Ro	200	79.0	82.0	6.2	0.59
Cru. S	245	173.0	55.5	7.0	0.67
Cru. L	292	198.0	69.0	8.1	0.61



An overview of the variation in maximum Kelvin wave height and wave period for the 10 vessels is shown in Figure 2.36 for velocities in the range 7-11 knots. Generally speaking, the maximum Kelvin height is typically below 10 cm for vessel speeds below 8 knots. Only the large container vessel and the general cargo vessel (which generally provides the largest waves) cause wave heights above 10 cm at a speed of 8 knots.

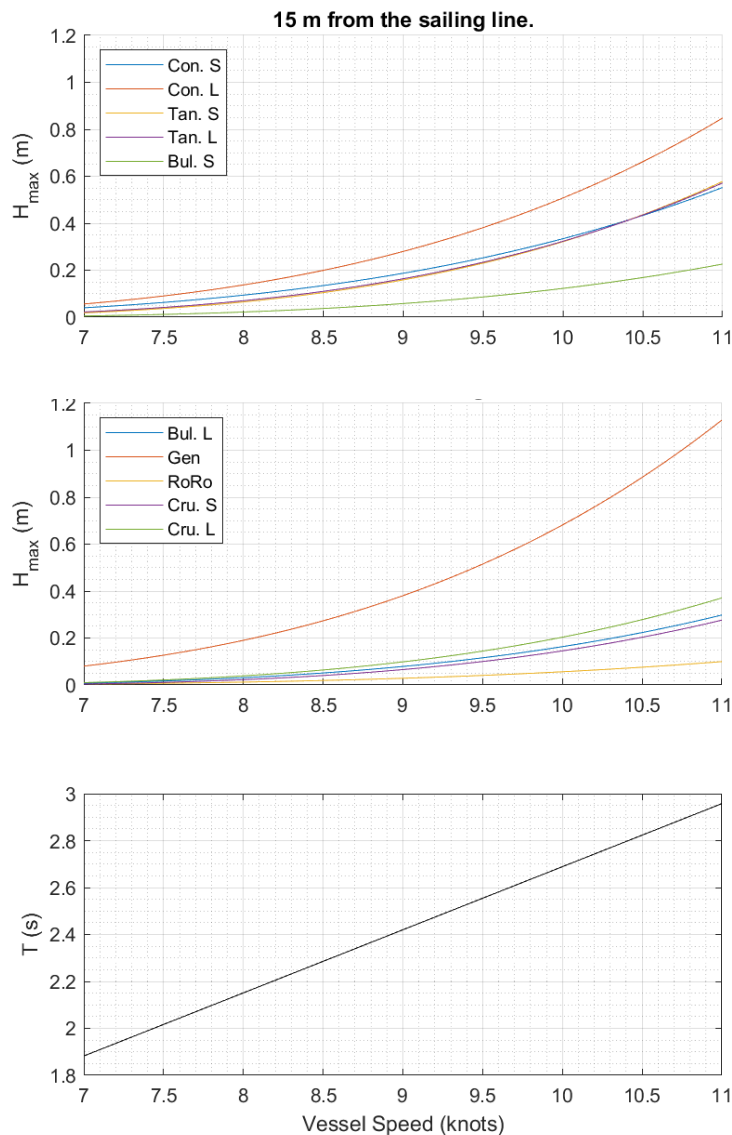


Figure 2.36. Maximum Kelvin wave height and wave period of the 10 selected vessels with varying vessel speed.



Table 2-18. Overview of maximum Kelvin wave height. Bottom row shows weighted average using the frequency of each vessel category (Container, Tanker, Bulk Carrier, General Cargo, Ro-Ro and Cruise Vessels) as weights, see Table 2-19.

H_{max} (m)	7 knots	8 knots	9 knots	10 knots	11 knots
Con. S	0.03	0.07	0.15	0.26	0.43
Con. L	0.05	0.11	0.23	0.42	0.71
Tan. S	0.02	0.05	0.13	0.27	0.48
Tan. L	0.02	0.06	0.14	0.28	0.49
Bul. S	0.00	0.02	0.05	0.10	0.18
Bul. L	0.01	0.02	0.06	0.13	0.23
Gen.	0.07	0.16	0.33	0.58	0.97
Ro-Ro	0.00	0.01	0.02	0.04	0.07
Cru. S	0.00	0.02	0.06	0.13	0.24
Cru. L	0.01	0.04	0.09	0.19	0.34
Average	0.03	0.07	0.14	0.27	0.46

2.9.2 Kelvin waves with time

Kelvin waves are highly transient – where wind generated waves typically persist for several hours, Kelvin waves are closely linked to the travelling vessel and therefore a group of Kelvin waves will only be active in a location for a short period of time (order of seconds). It is therefore necessary to get a sense of how large a percentage of time, these waves are active. This will be estimated based on the vessel speed and the calculated wave period.

The vessel speed was analyzed in Section 2.8.2 and Section 2.9.2.1 provides the chosen value for the Kelvin wave height analyses. The frequency of the vessel types is presented in Section 2.9.2.2. Finally, the annual duration with Kelvin waves is calculated per vessel type in Section 2.9.2.3.

2.9.2.1 Vessel speeds per category

The bar charts in Figure 2.31 clearly indicated that the majority of the vessels pass the CNR measurement location at speeds of about 8-10 knots. Hence based on the CNR data and the known speed



limit of 10 knots it therefore seems reasonable to consider diverging waves from vessels navigating at 10 knots to get a representative and conservative estimate of events.

2.9.2.2 Vessel frequency per category

Port of Venice (PoV) have made a database of the channel traffic spanning 2021 to 12th August 2022. Based on this database the distribution in Table 2-19 is found.

Note that cruise vessels are not present in the dataset, but PoV has specified 2 cruise vessel types to be included with 1 passage per week from 1st April to 1st November. Relative to the total number of events in the dataset this approximately equals 2% of the events.

Table 2-19. Percentage of events per category based on PoV database.

	Container	Tanker	Bulk	General	Ro-Ro	Cruise
(% of events)	27.1	20.5	15.5	15.3	14.6	~2

In total this distribution covers about 95% of the events, with container and tanker vessels representing about half of these events.

The average number of vessels per year has been calculated based on the PoV database as exemplified below for the container vessels:

$$N_{\text{container, per year}} = \frac{N_{\text{container}}}{N_{\text{days}}} \cdot 365 = \frac{2072}{588} \cdot 365 \approx 1286$$

Hence this number, summarized in Table 2-20, includes both in- and out-bound traffic.

Table 2-20. Number of vessels per year.

	Container	Tanker	Bulk	General	Ro-Ro	Cruise
Events per year (-)	1286	974	734	734	691	120

In Figure 2.37 an overview of the arrivals and departures for the five vessel categories included in the PoV database is shown per week day.



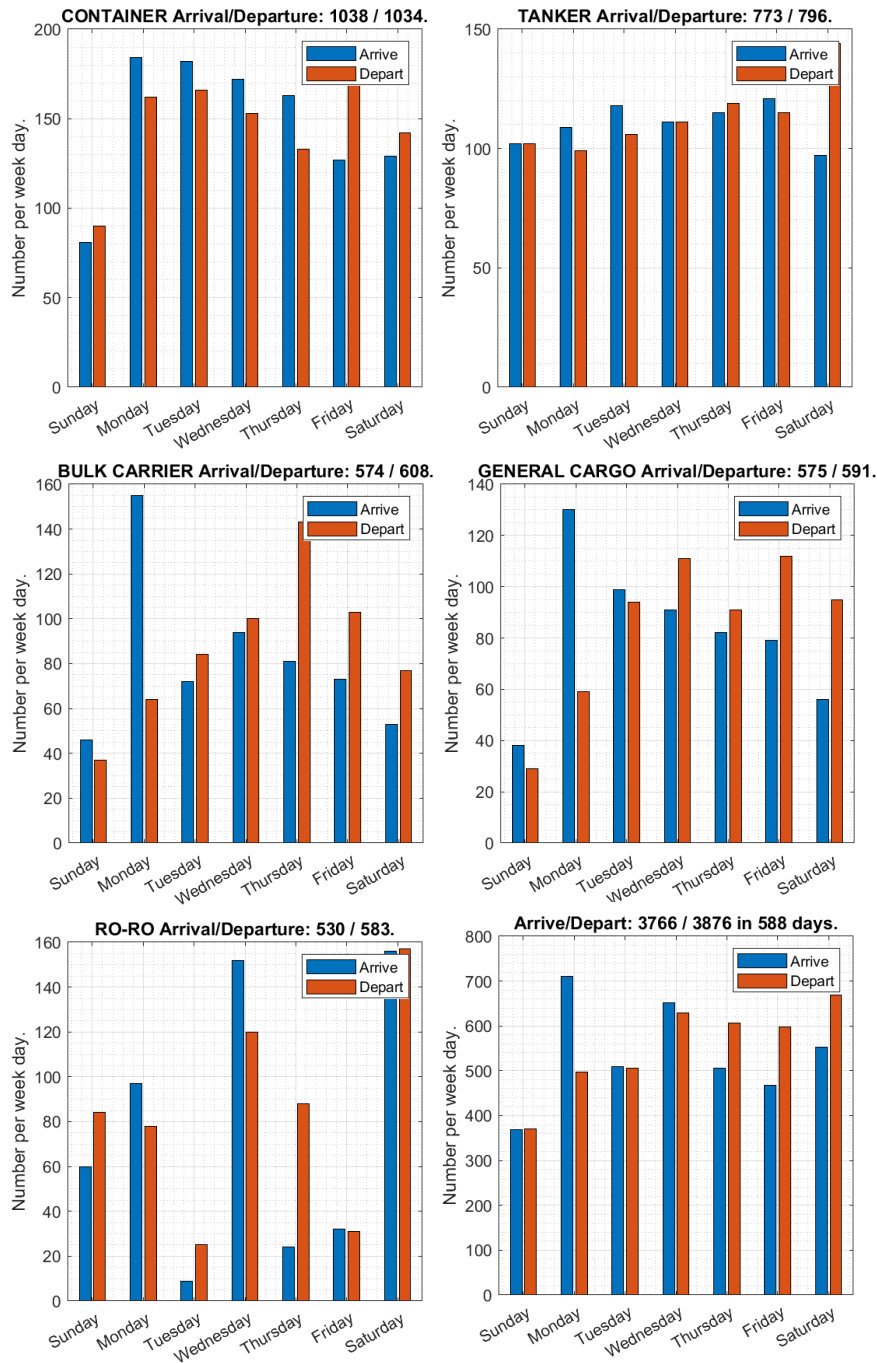


Figure 2.37. Overview of vessel arrivals and departures per week day. The bottom right corner shows arrivals and departures per week day for the entire PoV database i.e. also including other vessels than the five main categories.



2.9.2.3 Duration with diverging Kelvin waves per year

Since the Kelvin wave generation is associated with pressure differences along the hull of the ship, the number of waves in each Kelvin wave group is assumed related to the length of the vessel (taken as the length between perpendiculars at the water line LPP), the vessel speed and the wave period:

$$N_{waves} = \frac{\text{Passing time}}{T} = \frac{LPP/V}{T} \quad \text{Eq. 2.16}$$

Table 2-21. Number of Kelvin waves based on Eq. 2.16.

N_{waves} (-)	7 knots	8 knots	9 knots	10 knots	11 knots
Con. S	13	10	8	6	5
Con. L	16	13	10	8	7
Tan. S	14	11	8	7	6
Tan. L	15	11	9	7	6
Bul. S	13	10	8	7	5
Bul. L	15	11	9	7	6
Gen.	9	7	6	5	4
Ro-Ro	12	9	7	6	5
Cru. S	26	20	15	13	10
Cru. L	29	22	18	14	12

Using the number of vessels per year stated in Table 2-20 the total duration can be calculated using the wave period:

$$Duration = N_{events,per\ year} \cdot N_{waves,per\ event} \cdot T$$

Two types of container vessels, tankers and bulk carriers are specified. The small one represents a 50th percentile vessel and the large one a 75th percentile. In the calculation of the duration, the number of events per year (Table 2-20) will however be split equally between the two categories. With these assumptions the durations stated in Table 2-22 have been calculated. Here it is seen that for a vessel speed of 10 knots the duration varies from about 1.2 hrs/year to 3.9 hrs/year giving an accumulated duration of 24.2 hrs/year.



Table 2-22. Duration (hrs/year) with Kelvin waves. Includes in- and out-bound events.

	7 knots	8 knots	9 knots	10 knots	11 knots
Con. S	4.4	3.9	3.5	2.9	2.7
Con. L	5.4	5.0	4.3	3.9	3.7
Tan. S	3.6	3.2	2.6	2.6	2.4
Tan. L	3.8	3.2	3.0	2.6	2.4
Bul. S	2.5	2.2	2.0	1.9	1.5
Bul. L	2.9	2.4	2.2	1.9	1.8
Gen.	3.5	3.1	3.0	2.8	2.4
Ro-Ro	4.4	3.7	3.3	3.1	2.9
Cru. S	1.6	1.4	1.2	1.2	1.0
Cru. L	1.8	1.6	1.5	1.3	1.2

2.9.3 Bed shear stresses from diverging Kelvin waves

The diverging Kelvin waves propagate away from the vessel, out of the channel and onto the shallow flats. If the wave generated velocities are high enough, they can mobilize sediment at the bed and cause a net transport.

To get an impression of where the diverging Kelvin waves can cause a contribution to the vessel generated sediment transport, the bed shear stresses considering a wave period of 2.7 s and wave height of 0.27 m (corresponding to the weighted average wave height in Table 2-18 at 10 knots) have been calculated.

This has been done by supplying the Kelvin wave properties as boundary conditions to a MIKE Spectral Wave model, see [7] for details. The model considers the computational domain shown in Figure 2.38, which represents a sub-domain of the displacement wave model domain. The spectral wave model is run as directionally decoupled using the quasi-stationary time formulation. The model will not resolve the individual waves in the wave group, but it will provide a reasonable input for calculation of the bed shear stress magnitude – an estimate suitable for comparison to the maximum bed shear stresses from the displacement waves. The roughness used in the spectral wave model is identical to the one used in the hydrodynamic displacement wave model.



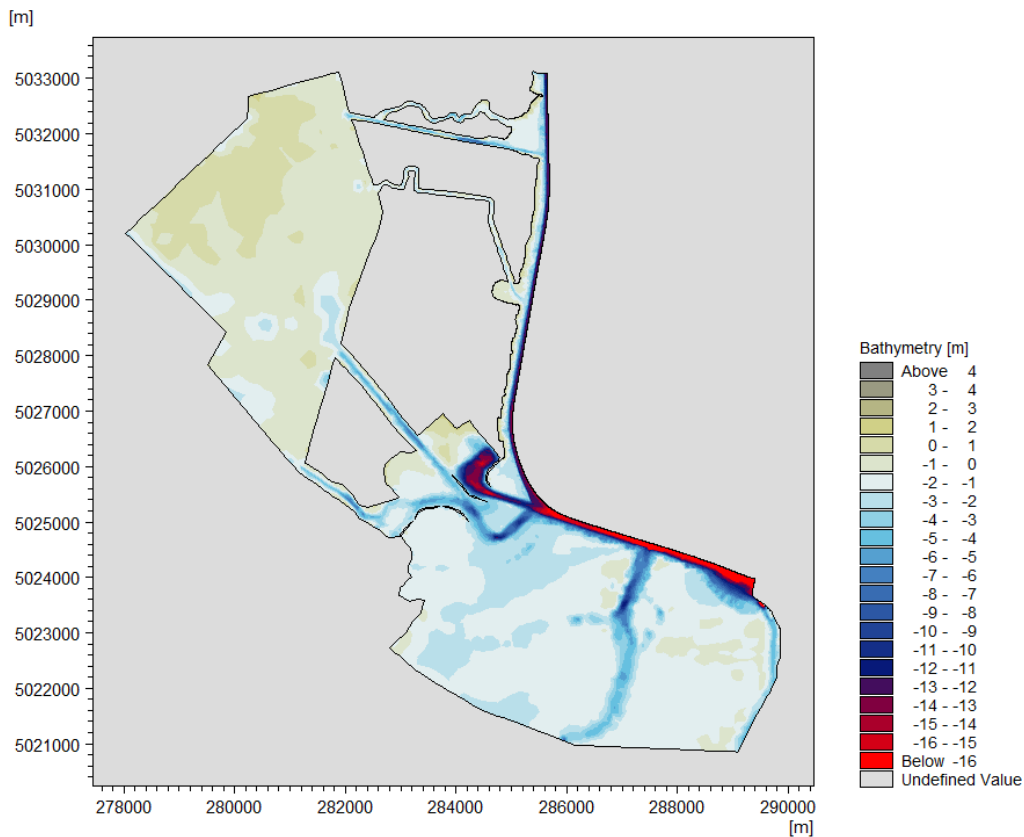


Figure 2.38. Model domain for modelling of shear stresses from Kelvin waves.

The waves calculated with the spectral wave model is supplied as forcing for calculation of the bed shear stresses. The bed shear stress calculation considers the same bed roughness as used in the sediment transport model i.e. it varies from 1 mm in the channel to 7.5 mm on the flats.

The resulting bed shear stresses are shown in Figure 2.39.

- The top map considers the maximum bed shear stress during an outbound passage of Nervion Valley (used for hydrodynamic model calibration) travelling at 9 knots.
- The bottom map considers the average Kelvin wave height corresponding to 10 knots outbound.

The critical bed shear stress for erosion on the flats is about 0.7 Pa (see chapter 3 and Appendix C) and as such the Kelvin waves should only be expected to contribute notably to the vessel generated sediment transport close to shore and not to any large extent on the flats along the MMC. None the



less, an analysis of the sediment transport from diverging Kelvin waves has been made in the following section.

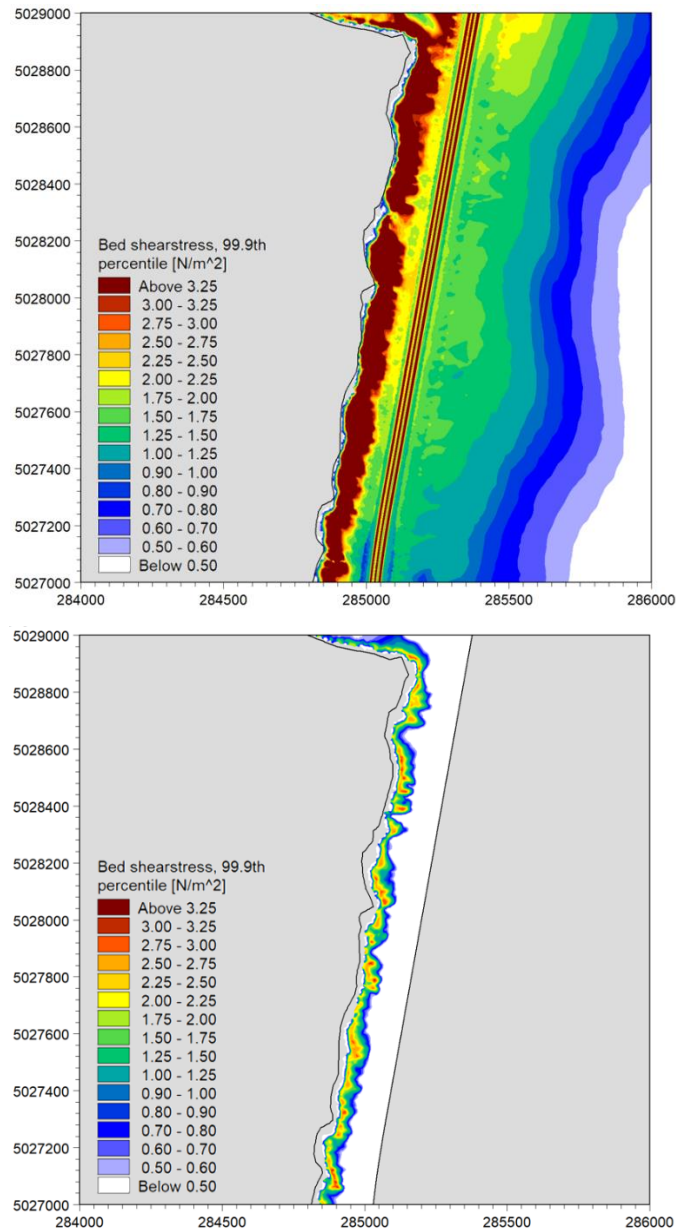


Figure 2.39. Map of bed shear stresses from primary waves (top) and Kelvin waves (bottom).



2.9.4 Sediment transport from diverging Kelvin waves

As mentioned, the hydrodynamic conditions under diverging Kelvin waves are different from the conditions under natural waves. Firstly, the diverging Kelvin waves occur in small, isolated groups, that consist typically of 5 to 10 individual waves, see Table 2-21. For natural waves, which persist for longer periods of time, an equilibrium situation will be established where the mass drift of the waves is compensated by a gradient in the mean water level that drives a near-bed return current (known as the undertow) to balance the mass drift. For the vessel-generated waves this equilibrium condition cannot be established as the duration of the diverging Kelvin wave trains is too short.

Secondly, as the waves enter shallow water, they become increasingly non-linear. The flow velocities under the wave crest become higher than under the wave trough, which depending on the sediment characteristics can result in a net bed load transport in the direction of the wave propagation.

Thirdly, the conditions for suspended sediment concentrations are different from natural wave conditions. Under natural waves the suspended sediment concentration at the beginning of the wave period is defined by the previous wave(s). For Kelvin waves it is more realistic to assume that initial concentrations are zero at the arrival of the wave train.

In order to limit the number of model simulations the vessels were assumed to navigate either with 8 knots or with 10 knots. A simplified test matrix was derived by merging the five columns of vessel speed listed in Table 2-22 into two, as shown in Table 2-23.

Table 2-23. Test matrix for sediment transport simulations related to diverging Kelvin waves.

Run	VESSEL	Speed = 8 knots				Speed = 10 knots			
		H (m)	T (s)	Duration (hour/yr)	N (-)	H (m)	T (s)	Duration (hour/yr)	N (-)
1	Con. S	0.07	2.2	10.05	10	0.26	2.7	7.35	6
2	Con. L	0.11	2.2	12.55	13	0.42	2.7	9.75	8
3	Tan. S	0.05	2.2	8.1	11	0.27	2.7	6.3	7
4	Tan. L	0.06	2.2	8.5	11	0.28	2.7	6.5	7
5	Bul. S	0.02	2.2	5.7	10	0.10	2.7	4.4	7
6	Bul. L	0.02	2.2	6.4	11	0.13	2.7	4.8	7
7	Gen.	0.16	2.2	8.1	7	0.58	2.7	6.7	5
8	Ro-Ro	0.01	2.2	9.75	9	0.04	2.7	7.65	6
9	Cru. S	0.02	2.2	3.6	20	0.13	2.7	2.8	13
10	Cru. L	0.04	2.2	4.15	22	0.19	2.7	3.25	14
		Total		76.9		Total		59.5	

In order to analyze the effect of Kelvin waves on sediment transport in- and around the channel a series of model simulations were made using a specially tailored version of DHI's sediment transport model STP. In this version, it was assumed that the mass drift is not balanced by a return current so the mean shear stress due to the sloping water surface was assumed to be zero. The wave distribution of the wave trains and the non-linear orbital motions were calculated using the empirical relations presented in [8].

The concentration of suspended sediments was assumed to be zero at the arrival of the first Kelvin wave in the wave train. During the passage of the wave train the concentration was assumed to develop continuously as function of the varying bed sediment concentrations generated by the bed shear stress and the turbulence generated inside the wave boundary layer.

Inside the channel the height and period of the Kelvin waves were calculated as function of the vessel characteristics listed in Table 2-17. Each wave train consists of a discrete number of waves as listed in Table 2-21. The mean wave period was calculated as $0.27 V_s$ (e.g., Eq. 2.11) and the direction of the waves was assumed to be 35 degrees relative to the channel axis. Propagation and breaking of the individual waves were simulated using the model of [9].

Figure 2.40 shows an example of a model simulation. Inside the channel, a train of Kelvin waves was specified with a root mean square (rms) wave height of 0.8 m. The mean wave period was 2 s and the wave train was assumed to consist of seven waves.

The model results show that the waves start to lose energy when they enter the shallow areas along the channel. Waves are typically known to break when the wave height to water depth ratio reaches 0.8 i.e., $H/h = 0.8$. In this case the waves are relatively small compared to the water depth ($H/h = 0.8/2.0 = 0.4$). This means that only a small amount of wave energy is lost due to breaking. The wave height is seen to reduce gradually with distance from the channel due to the effect of bed friction.



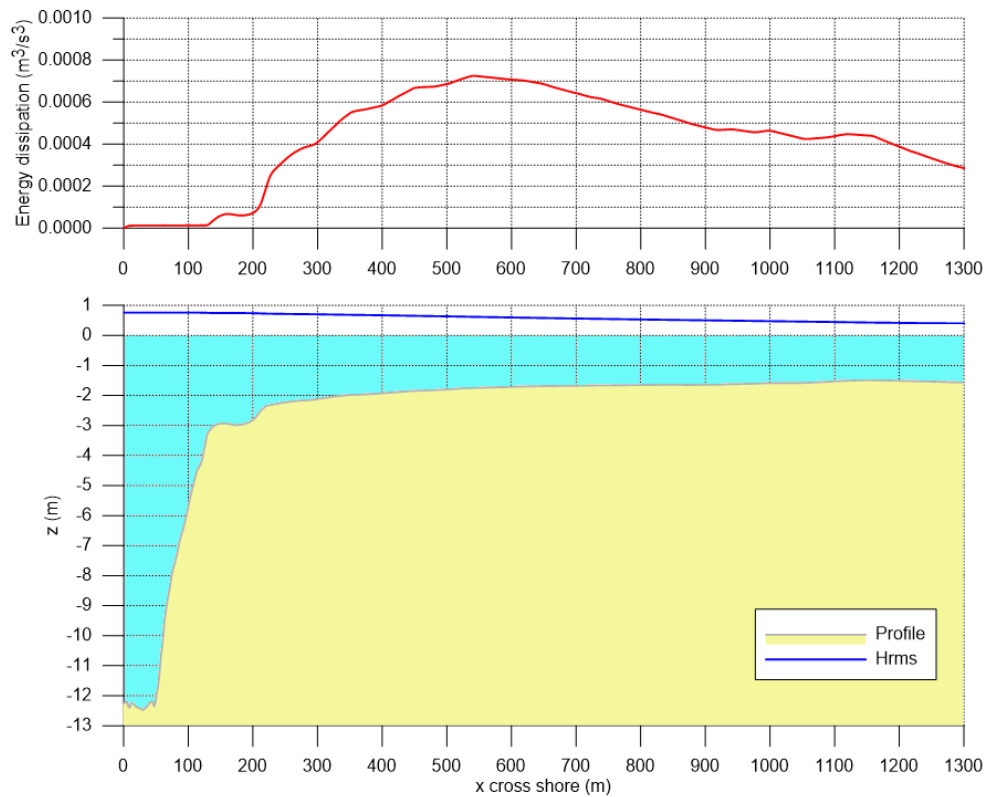


Figure 2.40. Example of simulation of diverging Kelvin waves across the channel. (Bottom) Cross shore profile and H_{rms} (blue line). (Top) Energy dissipation due to wave breaking and bed friction.

Figure 2.41 shows an example of simulated near bed orbital velocities under a group of diverging Kelvin waves at $x = 400$ m (see Figure 2.40). The Ursell number, defined as $(H L^2)/h^3$, is approximately 8, which corresponds to relatively short waves and low non-linearity. The figure indicates that flow velocities under the wave crest are only marginally higher than under the wave trough. The maximal flow velocity near the bed is around 0.6 m/s – approximately half the magnitude reached during the measured displacement wave of Nervion Valley, see Figure 2.27.

The time variation of the resulting sediment flux is shown in Figure 2.42. The model results indicate that most sediment is transported as bed load. The sediment flux under the wave crest is slightly higher than under the wave trough, which results in a small net transport in the direction of the wave propagation.



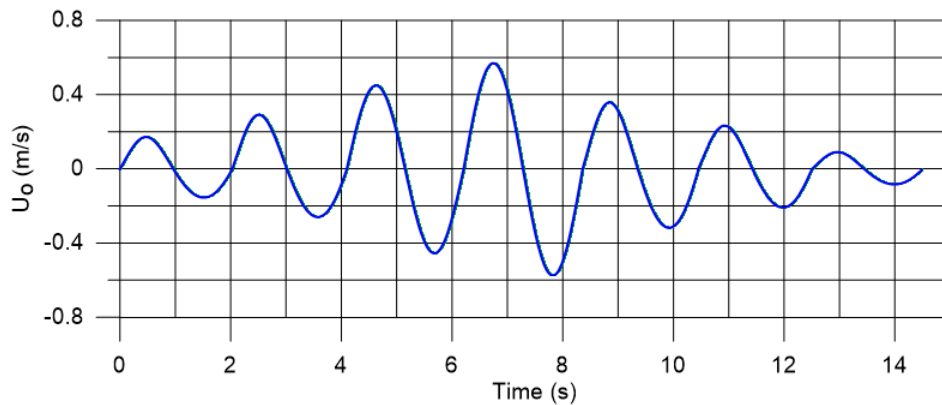


Figure 2.41. Simulated orbital velocities under a group of Kelvin waves.

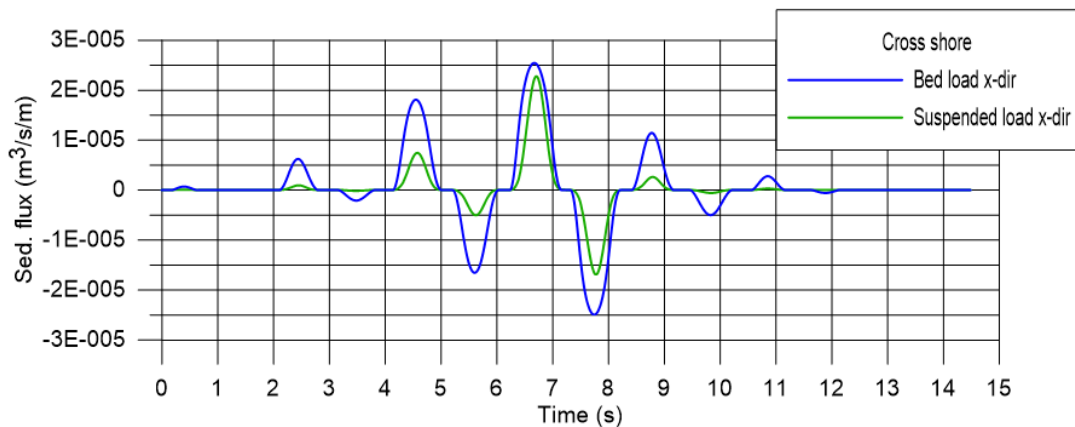


Figure 2.42. Simulated sediment flux under a group of Kelvin waves.

All wave events listed in Table 2-23 were simulated and the weighted contribution of each event to the total annual sediment transport was calculated. The results are shown in Figure 2.43. The net annual transport reaches a maximum of around 0.025 m³/m/year and is directed away from the channel (into the lagoon). Most of the sediment is transported as bed load. The net annual transport was found to increase with distance from the channel until a distance of around 600 m. At larger distances, the sediment transport was found to decrease with distance from the channel. The bed level changes caused by the variation in net annual sediment transport can be derived from the continuity equation:

$$\frac{\partial z}{\partial t} = - \frac{1}{1-n} \frac{\partial Q(x)}{\partial x} \quad \text{Eq. 2.17}$$



Where z is the bed level (m), t is time, n is the porosity of the bed material (-), $Q(x)$ is the net annual sediment transport $m^3/m/\text{time}$ and x is the cross shore coordinate (m).

The calculated bed level changes are indicated by the red line in the figure. Maximal bed level changes caused by the diverging Kelvin waves (in 1 year for all events) were found to be less than 0.5 mm/year and can thus be considered negligible.

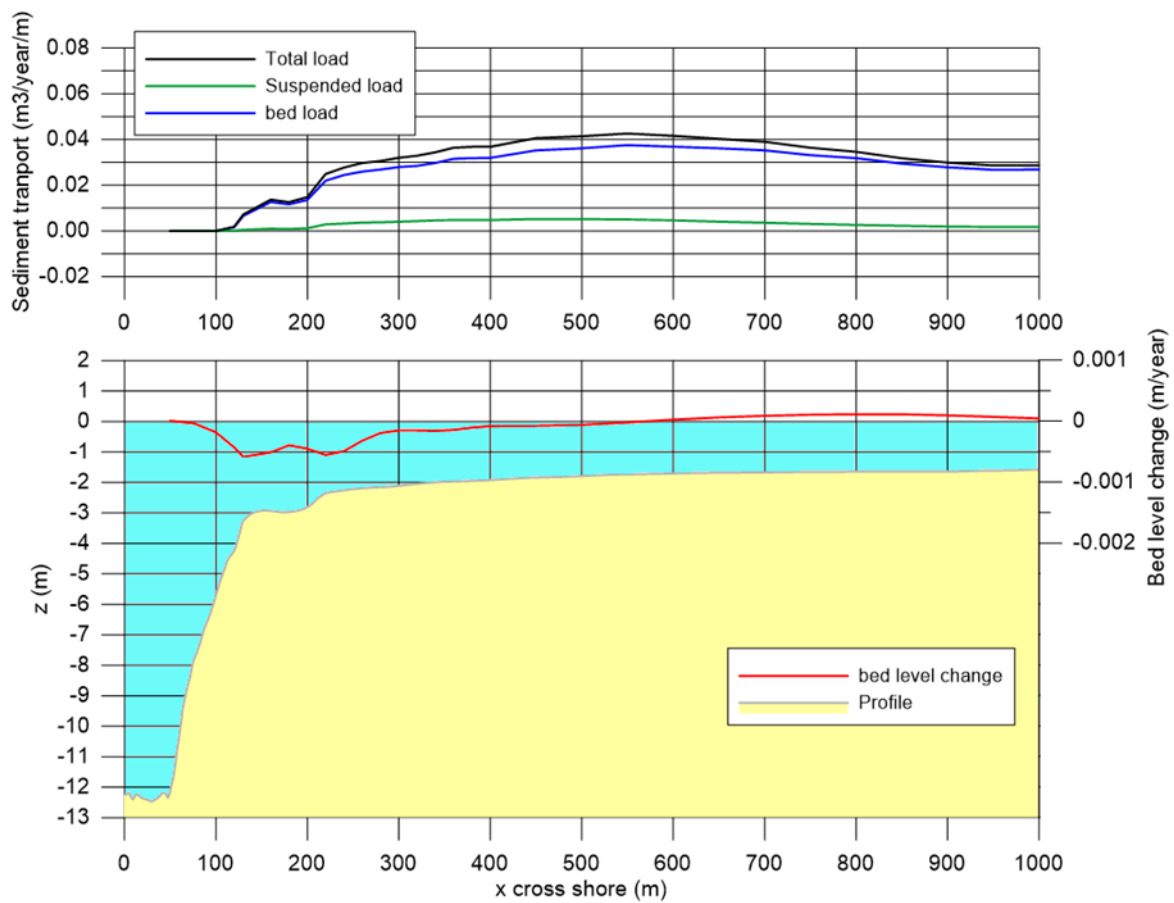


Figure 2.43. Simulated annual sediment transport due to diverging Kelvin waves.

2.9.5 Conclusion summary

An analysis was made of the magnitude and frequency of occurrence of Kelvin waves, generated by vessels navigating the MMC. The characteristic parameters of the diverging Kelvin waves were derived from empirical descriptions presented in [6]. The characteristics of the vessels and the frequencies of their appearances was derived based on data from the CNR and PoV databases.



The following main conclusions were drawn from the analyses:

1. The height of the Kelvin waves depends strongly on the vessel speed. An increase in vessel speed from 8 knots to 10 knots leads to an increase in the height of the Kelvin wave by a factor 3 to 5.
2. For a vessel speed of 8 knots, a maximal wave height of 0.16 m was found (General cargo vessel). For a vessel speed of 10 knots this value increases to 0.58 m
3. Model simulations show that Kelvin waves cause a net annual sediment transport of around $0.025 \text{ m}^3/\text{year}/\text{m}$. The annual bed level changes associated with the calculated transport patterns indicate a max bed level change of less than 0.5 mm/year.
4. Kelvin waves are small compared to natural waves and cause bed shear stresses that are significantly lower than the bed shear stresses caused by primary waves.
5. Kelvin waves, at least for vessel speeds below 10 knots, do not play a significant role in the sediment balance for the channel and the adjacent flats.



2.10 Propeller wash

The propellers of the vessels passing the Malamocco channel create jet flows that have an impact on the mobilization and transport of sediments on the channels bed. In this section the importance of the propeller-generated flow on the sediment balance in the channel is analyzed.

2.10.1 The basics of a water jet

The generation of the propeller generated jet is illustrated in Figure 2.44. As the ship propeller rotates, water is contracted and pushed backwards into a jet. Close to the ship, the width of the jet, indicated in Figure 2.44 as D_o , is slightly smaller than the radius of the ship propeller, D_p . The radius of the jet widens with distance from the ship. The strength of the flow decreases both with horizontal distance from the ship as well as the vertical distance from the centerline.

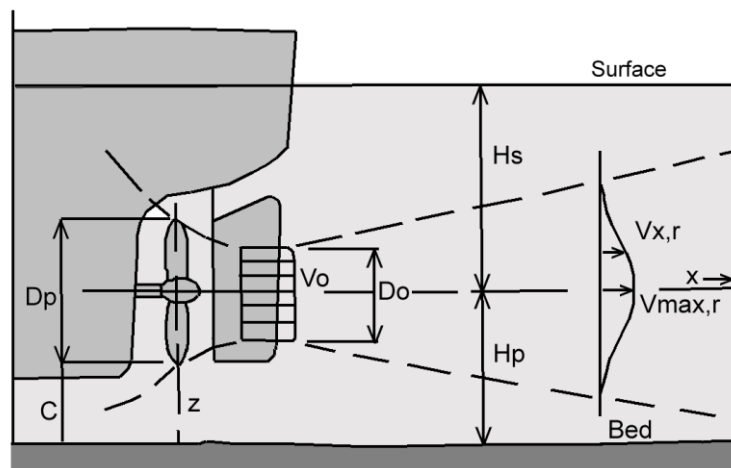


Figure 2.44. Illustration of propeller generated jet flow behind a ship.

At a certain distance behind the ship, the jet flow will reach the channel bed and may cause (re-)suspension and transport of sediment. According to (PIANC Report no. 180, [10]) the flow velocity V_0 in the immediate proximity of the ship propeller can be expressed as:

$$V_0 = 1.60 n_d f_n D_p \sqrt{K_T} \quad , \quad (\text{non - moving vessel}) \quad \text{Eq. 2.18}$$



$$V_{0j} = V_0 \frac{\sqrt{J^2 + 2.55K_{Tj}}}{\sqrt{1.4 \frac{P}{D}}} \quad , \quad (\text{moving vessel}) \quad \text{Eq. 2.19}$$

Here V_0 is the maximum flow velocity at the ship propeller (m/s), n_d is the number of propeller rotations (s^{-1}), f_p is the propeller rate factor (~ 1) and D_p is the propeller diameter (m). K_T and K_{Tj} are the thrust coefficients calculated as follows:

$$K_T = 0.55 \frac{P}{D_p} \quad , \quad (\text{non - moving vessel}) \quad \text{Eq. 2.20}$$

$$K_{Tj} = K_T - 0.46 J \quad , \quad (\text{moving vessel}) \quad \text{Eq. 2.21}$$

P is the design pitch. The pitch to diameter ratio P/D_p can be taken as constant at 0.7. The propeller ratio J depends on a wake factor w (which varies from 0.20 to 0.45) and on the vessel speed V_s .

$$J = \frac{V_s(1 - w)}{n_d D_p} \quad \text{Eq. 2.22}$$

(Verheij, (1983), [11]) presented an expression for the maximal flow velocity (U_{max}) in the centerline of the jet as a function of the horizontal distance to the ship propeller (x):

$$\frac{U_{max}(x)}{U_0} = \left(\frac{x}{x_0}\right)^{-b} \quad \text{Eq. 2.23}$$

Here x_0 is a reference distance taken as $2D_0$, where D_0 is the width of the jet in this reference location, given by $D_0 = aD_p$, where $a \sim 0.8$ and b is a constant taken as 1.0.

The variation of the maximal flow speed with distance to the propeller, as calculated from Eq. 2.23, is shown graphically in Figure 2.45. The figure shows that the maximal flow speed decreases rapidly with distance from the propeller. At a distance of 40 m, the flow has become less than 10% of the flow speed at the propeller.



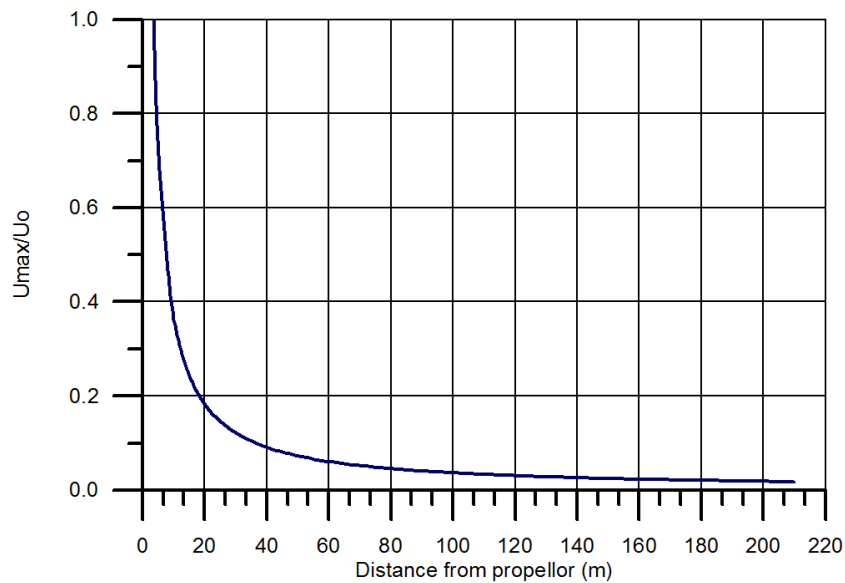


Figure 2.45. Maximal flow speed in the central axis of the jet as function of the distance to the propeller.

According to [11] the velocity distribution perpendicular to the jet's main axis can be expressed as:

$$\frac{U(x, r)}{U_{max}(x)} = \exp\left(-\frac{1}{2c^2} \frac{r^2}{x^2}\right) \quad \text{Eq. 2.24}$$

Here, r is the distance perpendicular to the main jet axis (m) and c is a constant taken as 0.18.

The variation of the flow velocity across the jet, according to Eq. 2.24 is shown in Figure 2.46. It is seen that for a ratio r/x larger than 0.4 the flow speed becomes less than 10% of the flow speed in the centerline of the jet.



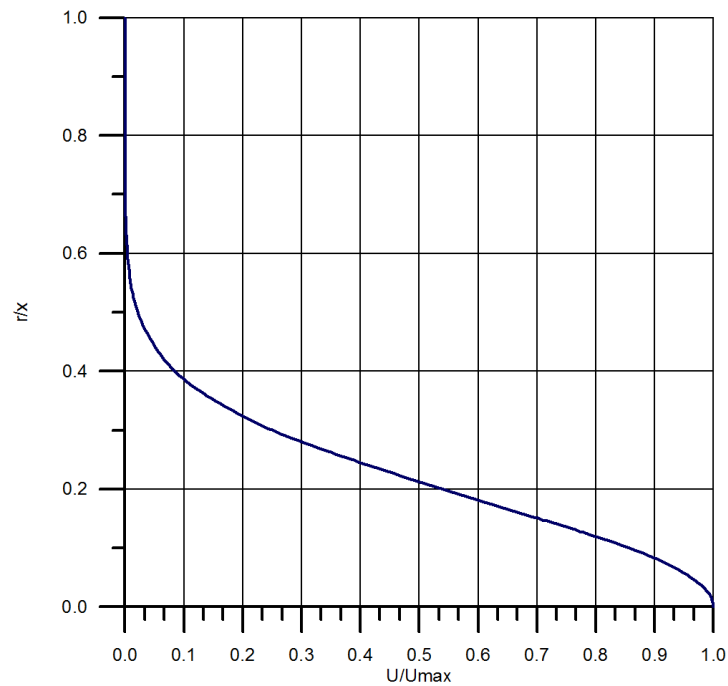


Figure 2.46. Variation of flow speed with distance from the central axis of the jet.

As can be seen from the equations the flow velocity near the bed depends on the distance from the propeller and the height of the propellers central axis above the channel bed. In an area close to the propeller, the jet flow occurs in the upper part of the water column only and has not reached the bottom. The larger the distance from the propeller, the more uniform the velocity distribution across the water column. This is shown in Figure 2.47, which shows the ratio between the flow velocity at the bed and the flow velocity in the central axis of the jet. In this figure, the vertical distance between the ship propeller and the seabed, was assumed 3 m.



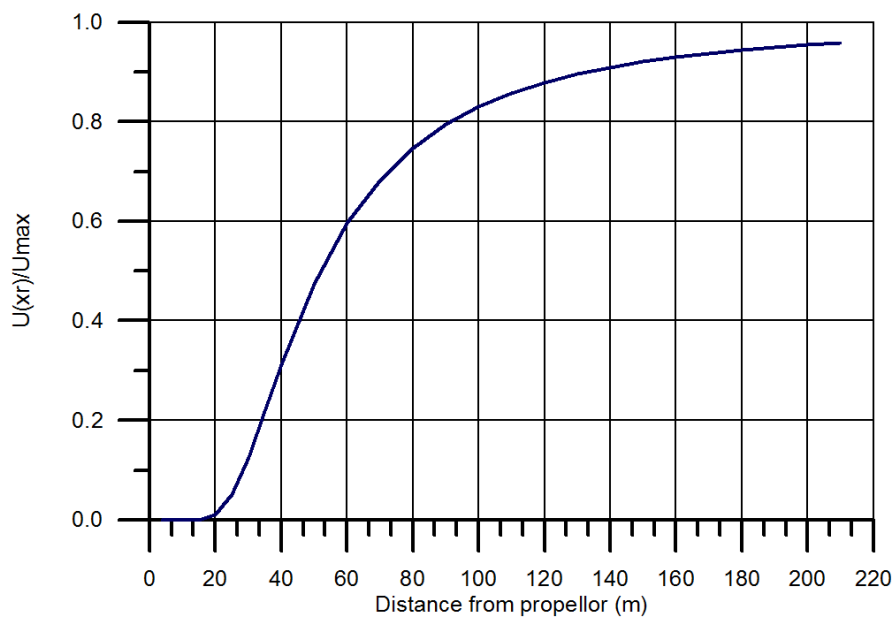


Figure 2.47. Ratio between flow velocity at the seabed and flow velocity in the central axis of the jet.

By combining Eq. 2.18 to Eq. 2.22, the flow speed near the bed is calculated. The calculated near bed flow velocities for a 200 m container vessel, navigating at a speed of 9.5 knots are shown in Figure 2.48. The draft of the vessel was assumed 10.5 m and the propeller was assumed to have a diameter of 6 m a rotation rate of 45 rpm, which is a normal value for this type of ship approaching the port. (Author’s private communication with professional helmsmen). The diameter of the propeller of this type of vessel typically lies between 5 and 7 m.



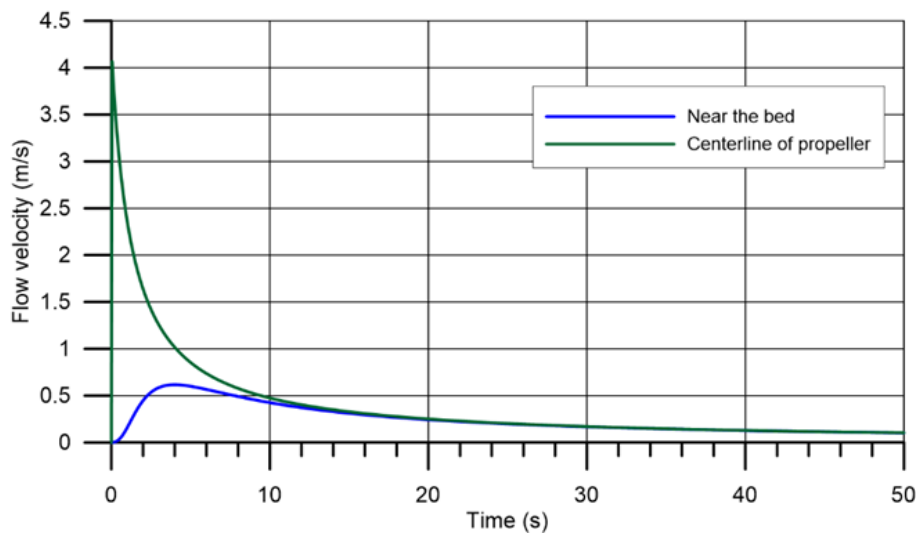


Figure 2.48. Maximal flow velocities near the bed as function of time.

The calculations show that the maximum flow speed in the centerline is approximately 4.2 m/s in this example and rapidly declines with time (and distance from the ship). A maximal near bed velocity of around 0.6 m/s was observed around 3.5 s after the passage of the vessel. After approximately 15 seconds (at a distance of around approximately 70 m behind the vessel) the flow becomes uniform across the water column e.g., the near bed flow velocity becomes equal to the velocity at the centerline of the propeller. After 30 seconds the maximal flow velocity near the bed has reduced to approximately 0.25 m/s.

2.10.2 Bed shear stress from ship propeller

The propeller generated flow initiates the formation of a turbulent boundary layer near the bed. The thickness of the boundary layer increases with time and eventually reaches the water surface. The development of the boundary layer is crucial for the transfer of momentum from the outer flow to the channel bed, where the bed shear stress is able to mobilize sediment from the channel bed and initiate its transports along the bottom (bed load) or higher up in the water column (suspended load).

The flow equation for the turbulent bottom boundary layer reads:

$$\rho \frac{\partial}{\partial t} (u_0 - u(z)) = - \frac{\partial \tau}{\partial z} \quad \text{Eq. 2.25}$$



Where u_0 is the free stream flow velocity, $u(z)$ is the velocity inside the boundary layer, τ is the shear stress and z is the distance from the bed.

According to the integrated momentum approach of (Fredsoe (1984), [12]), Eq. 2.25 is integrated across the boundary layer assuming a logarithmic velocity profile:

$$u(z) = \frac{U_f}{\kappa} \ln\left(\frac{z}{z_0}\right) \quad \text{Eq. 2.26}$$

Here z_0 is the bed level, taken as $k_n/30$, where k_n is the bed roughness. U_f is the friction (or shear) velocity defined as:

$$U_f = \sqrt{\frac{|\tau|}{\rho}} \quad \text{Eq. 2.27}$$

Where τ_b is the bed shear stress and ρ is the density of water.

Eq. 2.25 – Eq. 2.27 have been solved numerically in the time domain. A more detailed description of the model can be found in (Fredsoe (1984), [12]). Figure 2.49 shows the time development of the bed boundary layer after the passage of the vessel. The calculations show that the boundary layer grows initially from 0 to 1m during a period of 50 seconds after at the passage of the vessel.

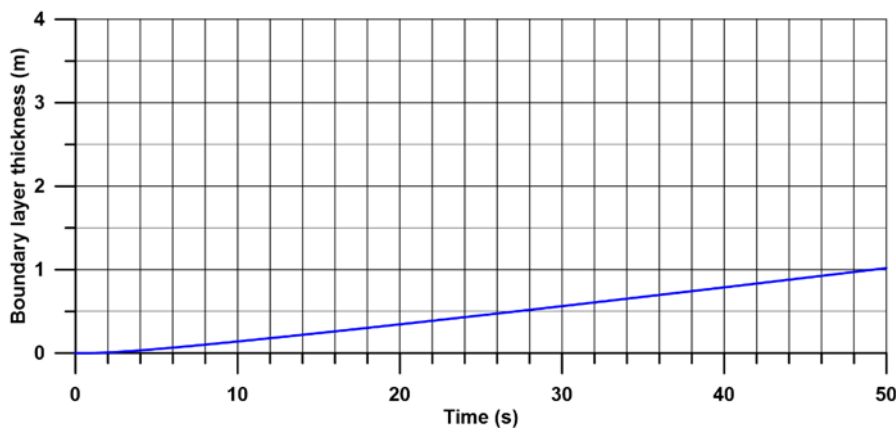


Figure 2.49. Time development of the turbulent bottom boundary layer after passage of a container vessel navigating at a speed of 9.5 knots, according to the model of (Fredsoe (1984), [12]).



The time variation of the bed shear stress is shown in Figure 2.50. The blue line represents the results calculated using the integrated momentum approach. The red dashed line represents the result calculated from the following expression:

$$\frac{\tau_b}{\rho} = \frac{1}{2} f_w U_0^2 \quad \text{Eq. 2.28}$$

Where the friction coefficient, f_w , is calculated as:

$$f_w = 0.04 \left(\frac{a}{k_n} \right)^{-0.25} \quad \text{Eq. 2.29}$$

Where a is defined as:

$$a = \frac{U_m T_r}{2\pi} \quad \text{Eq. 2.30}$$

Here, T_r is a representative period, calculated as $4T_{1m}$, where T_{1m} is the time between the passage of the vessel and the occurrence of the maximal flow velocity. For the present example, T_{1m} is around 4 s as can be derived from Figure 2.48.

The time variation of the bed shear stress (Figure 2.50) shows that the model based on the integrated momentum approach is able to predict the phase shift between the maximal bed shear stress and the maximal flow velocity. In the simple model (Eq. 2.28) the bed shear stress is directly related to the outer flow velocity so this phase shift cannot be resolved in this model. Besides this, the agreement between the two models is reasonable and for all practical purposes, the simple model can be used to derive a rough estimate of the maximal bed shear stress caused by the propeller.



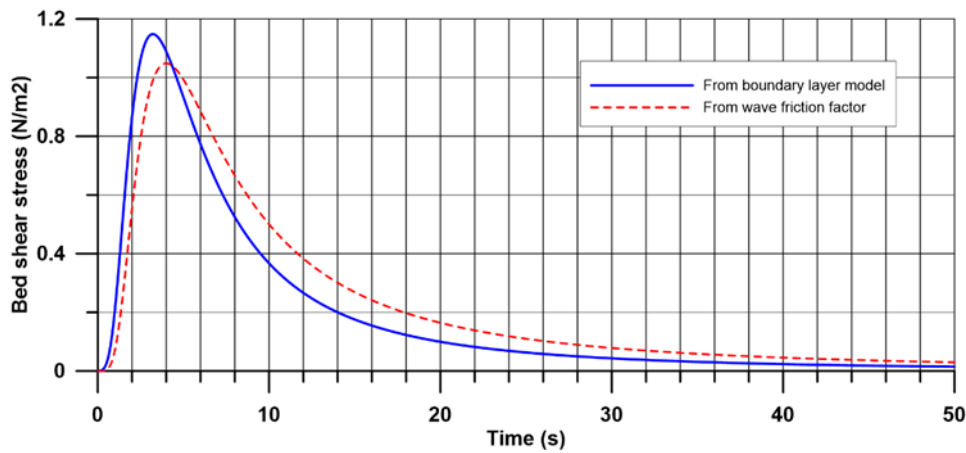


Figure 2.50. Time development of the propeller-generated bed shear stress caused by a container vessel with length of 200 m, navigating with a speed of 10 knots. Blue line: Calculated from integrated momentum method of [12]. Red dashed line: calculated using a constant friction factor.

The method presented above was used to calculate the maximal bed shear stress for a number of combinations of propeller characteristics and the elevation of the propeller above the channel bed. The results are shown in Table 2-24. The first column, Rpm, contains the number of rotations per minute. The column indicated as D represents the propeller diameter, r = elevation of the propellers' centerline above the channel bed. The column indicated as V_0 represents the maximal flow speed in the centerline of the propeller and the columns indicated as U_m and $T_{b\ max}$ represent the maximal flow speed near the bed and the maximal bed shear stress, respectively. From this table it is seen that the propellor generated bed shear stress for the considered cases is in the 0.3 to ~2 Pa.



Table 2-24. Calculated maximal flow at centerline of the propeller (V_o) and near the bed (U_m) as well as bed shear stress ($T_{b\ max}$).

Rpm (minute ⁻¹)	D (m)	r (m)	V_o (m/s)	U_m (m/s)	$T_{b\ max}$ (N/m ²)
250	2.5	10	6.3	0.29	0.25
250	2.5	9	6.3	0.32	0.31
250	2.5	8	6.3	0.36	0.39
100	4.5	8	4.2	0.42	0.50
100	4.5	7	4.2	0.47	0.65
100	4.5	6	4.2	0.55	0.89
45	6.0	6	2.7	0.46	0.65
45	6.0	5	2.7	0.56	0.93
45	6.0	4	2.7	0.69	1.45

2.10.3 Importance of propellor generated bed shear stress and turbulence on sediment transport

To evaluate the effect of the propellers on sediment transport it is important to consider the flow field near a passing vessel. Figure 2.51 shows the simulated bed shear stress for a 176 m long tanker vessel, navigating through the channel with a speed of 9.0 knots.



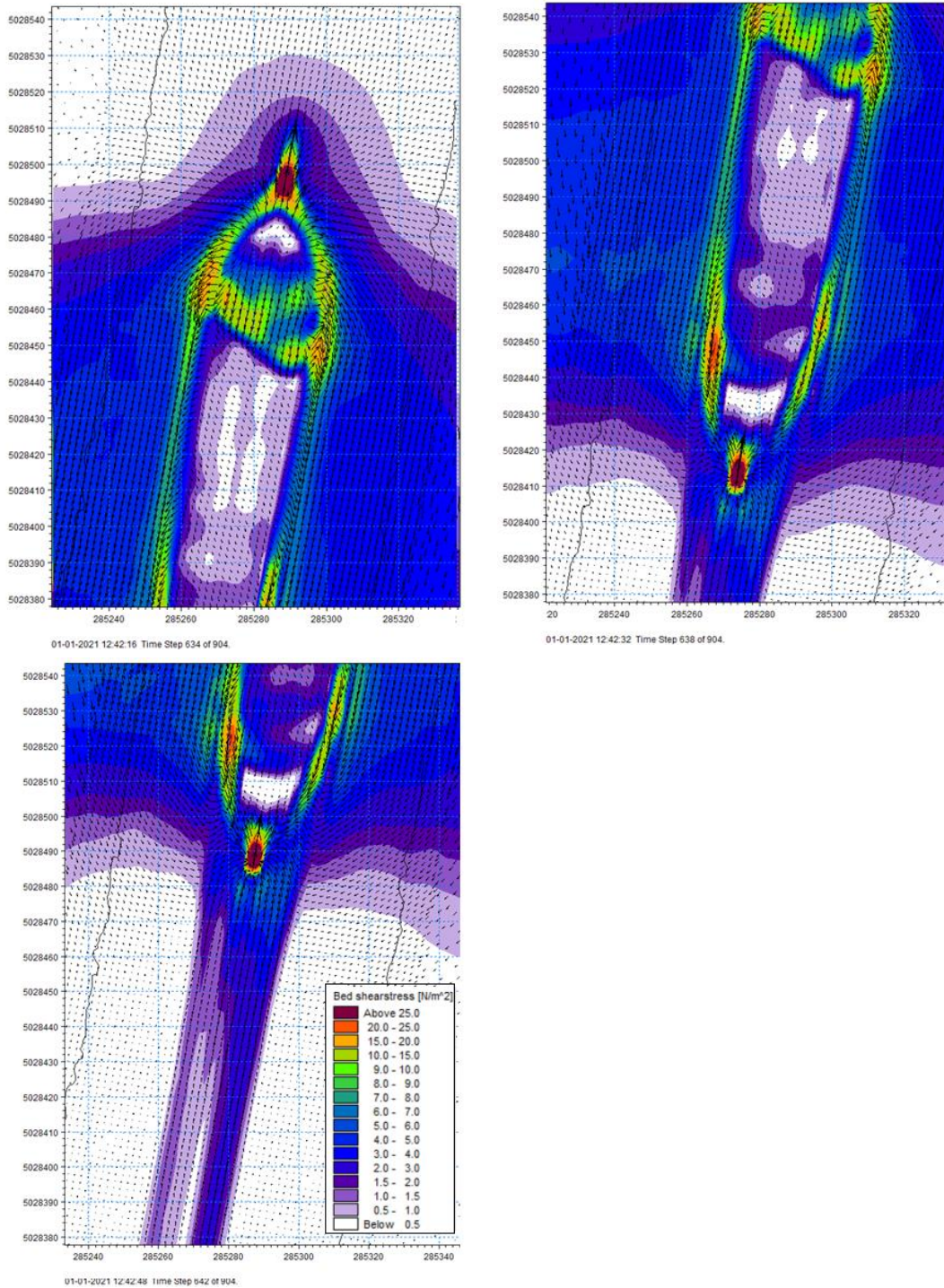


Figure 2.51. Simulated bed shear stress due to displacement wave under a passing vessel (Alicudi M, 176 m long, 9.0 knt, in-bound). Effect of propeller is not included.



The model simulations indicate that the bed shear stress generated by the displacement wave can reach values of up to 25 N/m^2 at the rear end of the ship (red colors in Figure 2.51). The calculations of maximal bed shear stress generated by the propeller wash, listed in Table 2-24, were found to be at least an order of magnitude smaller than the maximal bed shear stress generated by the displacement wave. Since the sediment transport rate in the displacement wave sediment transport model is governed by the bed shear stress magnitude, the additional small contribution from the propeller will not make a significant difference to the modelled erosion volume.

The flow patterns behind the vessel also indicate that the flow, or rather the bed shear stress, is directed towards the center line of the propeller. In the area further behind the vessel, a relatively weak flow is observed directed in the same direction as the propagating vessel. The flow was found to be limited mainly to the channel itself and did not show a component across the channel. Hence sediment brought into suspension in the channel (by the displacement wave and propeller) will tend to stay there.

It was found that the flow at the back of the vessel (which is also in the location where the bed shear stress caused by the ship propeller is highest) is directed into the channel. All in all, this means that even though the propellers may stir up large volumes of sediment from the channel bed, the sediment largely remains inside the channel and is only displaced along the channel itself. Therefore, the main effect of the ship propellers on the sediment is limited to additional stirring up of sediments from the channel bed, without causing a significant residual exchange of sediment between the channel and the surrounding flat areas.

Due to the continuous stirring up of bed sediments, both by the displacement waves and, to a lesser degree by the propellers, the density of the upper layer of the channel bed will remain relatively low. This effect is included in the model by assigning a sediment density in the channel of 180 kg/m^3 , which corresponds to very weakly consolidated sediment. Additionally, a diffusion factor of 5 has been applied constantly in the channel to mimic the added turbulence from the propeller. In reality, the turbulence of the propeller is transient and will decrease with time. This won't be the case in the model, but since only single passages are simulated without any background forcing this will not cause any significant problems for the interpretation of the results.





2.10.4 Conclusion summary

The model simulations clearly show that the maximal bed shear stress caused by the propellers is significantly smaller (at least an order of magnitude) than the maximal bed shear stress generated by the displacement waves.

The mean flow and the bed shear stress in the area behind the ship are both directed towards the center of the channel. Further away from the ship a weak residual current is generated in the propagation direction of the vessel, hence parallel to the channel.

The propellers will cause turbulent eddies in the area behind the vessel. The main effect of this additional turbulence is that suspended sediments will be mixed more intensively across the water column. Therefore, suspended sediment concentrations are high in the area at the rear of the vessels. However, there is no net flow that could cause significant exchange of sediment between the channel and the neighboring areas. Therefore, it is concluded that the propellers of the vessels will only have a marginal effect on the sediment balance of the channel which is strongly dominated by the dynamics of the displacement waves.



3 SEDIMENT TRANSPORT MODEL OF THE MALAMOCCO MARGHERA CHANNEL

As discussed in Section 2.9 and Section 2.10 Kelvin waves and propeller wash only have fairly small and localized influence on the vessel generated sediment transport along the MMC. Therefore, the sediment transport model described in the present section focuses on sediment transport from displacement waves.

3.1 Numerical model details for the modelling of the sediment transport

The sediment transport model is a MIKE MT model which receives its forcing from the MIKE 3 FM model described in Section 2.1 to Section 2.6. The MT model deals with the transport of fine sediment through dispersion and diffusion processes. Details on the model can be found in [13]; the coming sections will outline the applied model settings.

3.1.1 Sedimentary conditions

The sedimentary conditions of the model have been chosen based on data from Chapter 4 of [14] and Appendix C to the present document. Some of the figures from this report will be repeated here for completeness.

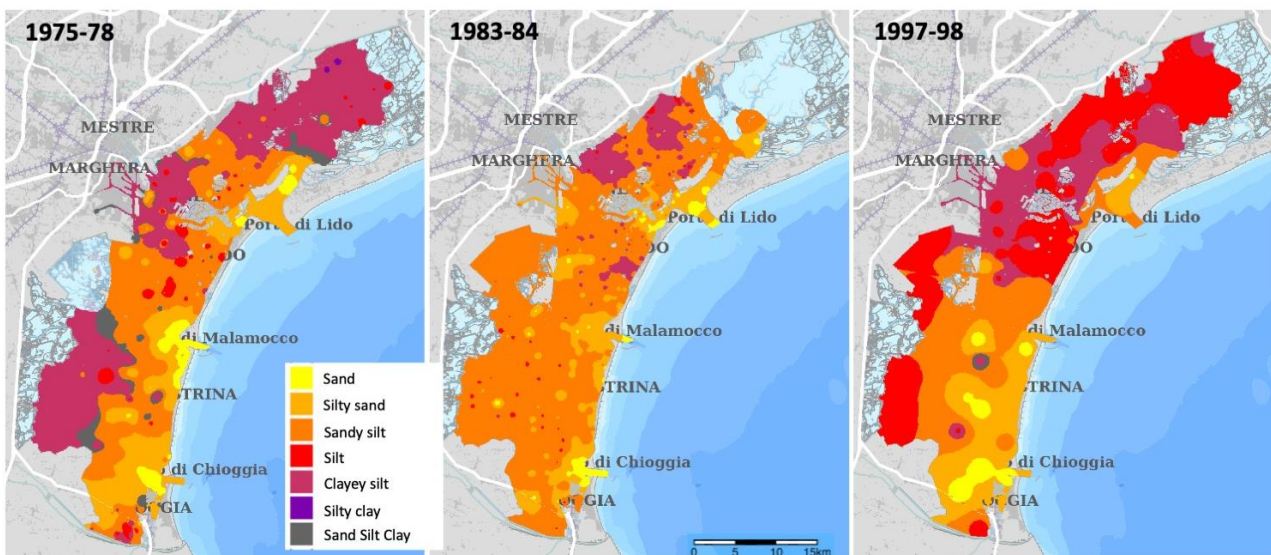


Figure 3.1. Sedimentological map of the Venice Lagoon. The classification is according to Shepard [15] (redrawn from <http://www.atlantedellalaguna.it>; Molinaroli et al., [16]).



The central part of the Venice lagoon (which is the focus of the current model) is characterized by silty to muddy sediments, see Figure 3.1. In the northern part of the area, the sedimentology is muddy whereas in the southern part conditions are silty going towards sandy approaching the entrance to the MMC in the south-east.

Detailed data on the sediment grain size has not been available i.e., details on the sediment located on the flats and along the sloping banks east and west of the MMC, the sediment located in the MMC itself and how the sediment vary along the trajectory of the channel has not been available. Some data from [17] (sample no. 70 and 80) are located on the flats in the central part of the lagoon and has provided an indication of the sediment gran sizes, see Table 3-1.

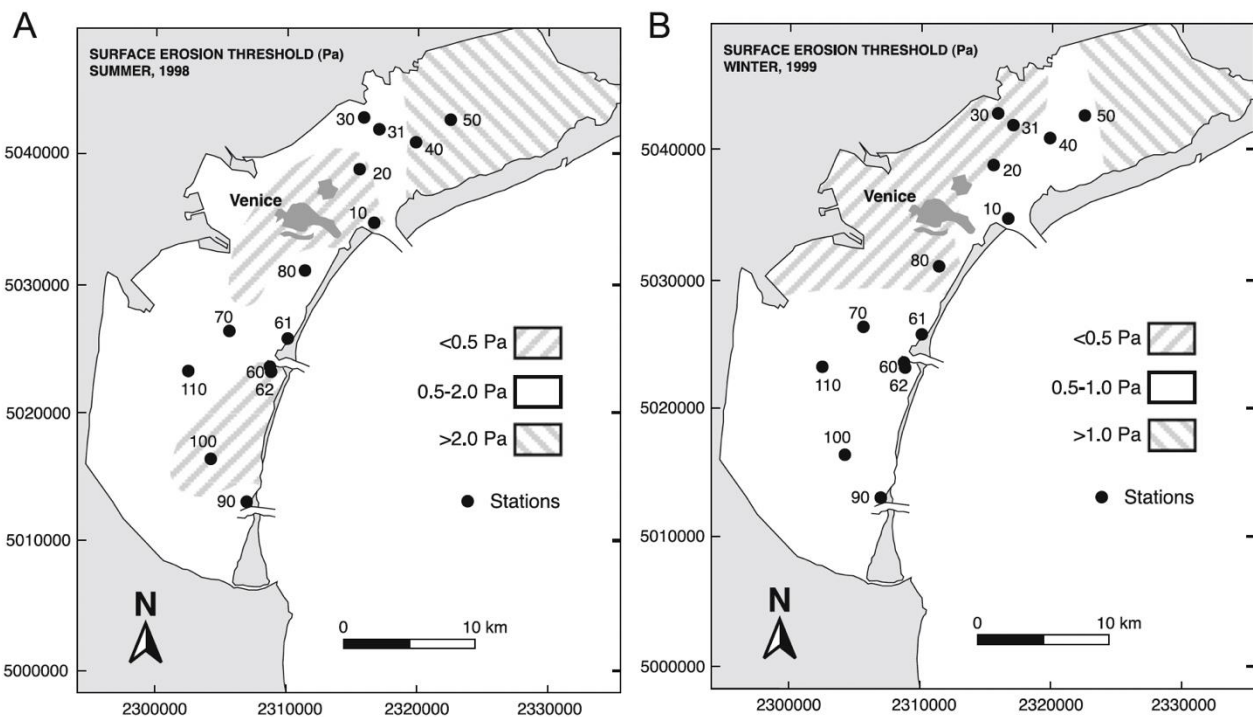


Figure 3.2. The sites occupied during the summer (A) and winter (B) surveys of Amos et al. [17]. Also shown are the regions of surface erosion threshold (τ_c) interpolated across the entire lagoon. Notice that in both periods, the highest threshold is found in the northern lagoon, and the lowest in a broad region around the city of Venice (after Amos et al., [18]).



Table 3-1. Summary of the sea-bottom characteristics for critical shear stress assessment (after Amos et al. [13] [14]. See Figure 3.2 for the reference sample points. (C.n. = *Cymodocea nodosa*; U.r. = *Ulva rigida*; d_{50} = median grain size in microns).

sample	characteristics	others	ρ_b (kg/m ³)		d_{50}		τ_c		τ_c average
			Summer	Winter	Summer	Winter	Summer	Winter	
20	bare mudflat		1763	1803	28	16	0.35	1.08	
21	bare mudflat		1843		33	20	0.22	1.13	
22	bare mudflat		1840		33		0.44		
70	bare mudflat	large ship effect	1720	1710	58	28	0.59	0.61	0.63
10	<i>Cymodocea nodosa</i> cover		1975						
60	<i>Cymodocea nodosa</i> cover	shelly sand with C.n.+U.r.	1865	1728	74	21	0.36	0.53	
62	<i>Cymodocea nodosa</i> cover	shelly sand with C.n.+U.r.			81	39			
90	<i>Cymodocea nodosa</i> dense mat		2100				0.86		0.58
33	high intertidal flat		1833		20		0.79		
40	high intertidal flat		1672	1672	22	26	3.06	0.84	
53	high intertidal flat		1630		16		2.23		
80	high intertidal flat	<i>Ulva rigida</i>	1865	1960	30	16	0.85	0.38	1.36
30	microphytobenthos		1705		23	46	0.80	0.3	
31	microphytobenthos		1909	1718		19	1.90	0.76	
32	microphytobenthos						0.83		
42	microphytobenthos				22		0.83		0.90
50	<i>Zoostera noltii</i> 20-60%		1630	1691	10	24	1.42	0.99	
51	<i>Zoostera noltii</i> 20-60%			1857		23	1.51	0.48	
52	<i>Zoostera noltii</i> 20-60%						2.12		
53	<i>Zoostera noltii</i> 20-60%		1630		16		2.23		
61	<i>Zoostera noltii</i> 20-60%		1992				1.13	0.62	
100	<i>Zoostera noltii</i> 20-60%		1495		21		0.39		
110	<i>Zoostera noltii</i> 20-60%		1352		23		0.88		1.18
41	not specified			1824	21	36	1.51	1.16	
43	not specified						1.37		
44	not specified		1820		32		0.86		
71	not specified					19		0.71	1.12

To describe the sandy to muddy sediment present in the lagoon, the model considers three sediment fractions, one consisting of fine sand, another consisting of medium silt and a third representing fine silt. Together the two silt fractions form the mud fraction. The model is started with an initial concentration of 15 mg/l consisting of Fraction 3 everywhere. This level matches reasonably with the measurements made by (Rapaglia et al. 2011, [19]) and (Scarpa et al. 2019, [20]).

Table 3-2. Sediment fractions used in the sediment transport model.

	Sand		Mud	
	Fraction 1	Fraction 2	Fraction 2	Fraction 3
d_{50} (μm)	100	40		15
W_s (mm/s)	8.09	1.29		0.18



It should be noted that the sediment along the western side of the channel is described by clayey and silty sediments from deeper layers. Clayey sediments are cohesive and tend to be sticky. Hence in reality, the erosion mechanism of such layers is different from the more sandy and silty sediments in the lagoon. In the model the clayey layers have a higher critical bed shear stress of erosion but the complexity of the erosion mechanism of the clayey layers cannot be included fully and therefore the model will likely overestimate the erosion in these areas.



Figure 3.3 Images of sediment bank west of the MMC from Luca Zaggia.

A Google Earth image of a vessel generated sediment plume in the channel is shown in Figure 3.4. This plume is 3,300 m long and is caused by an in-going vessel. At the bottom of the image another



vessel seemingly crossing the channel in the San Leonardo bend intercepts the plume. Based on the length of the plume and assuming a vessel speed of 10 knots, sediment is able to linger in the surface water of the channel for at least about 11 minutes – likely longer considering the intercepting vessel. Fraction 2 and 3 in the model take about 13 and 83 minutes to settle a single meter. Hence the fall velocity of Fraction 2 is reasonably well in line with the observations of the Google Earth image, whereas Fraction 3 may be too fine. The combination of Fraction 2 and 3 however captures the ranges of sample 70 and 80 in Table 3-1 quite well and so all fractions are included in the model bed material of the MMC since no grain size data from the actual channel has been available. However, based on the Google Earth image it should be kept in mind that the channel sediment may in fact be coarser than displayed by model fraction number 3.

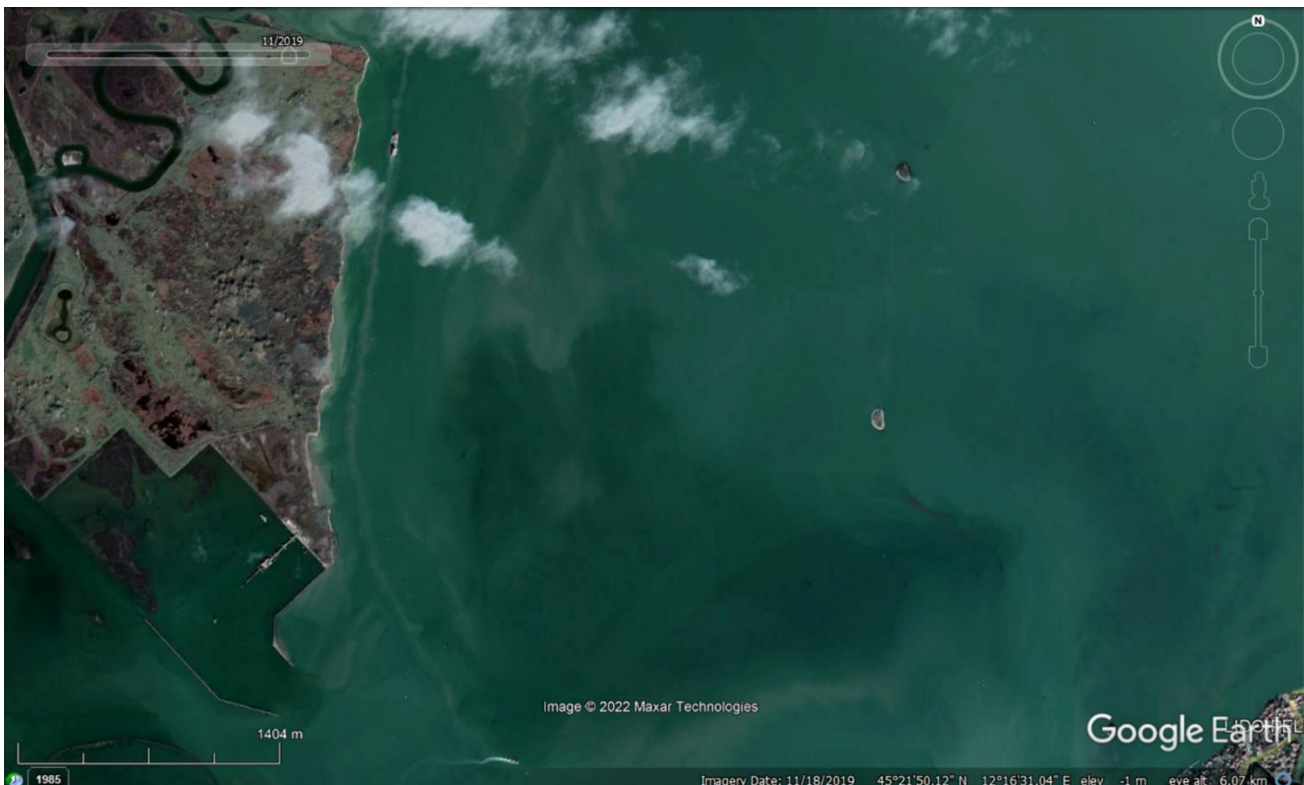


Figure 3.4. Vessel generated plume from Google Earth image of 18th November 2019.



3.1.2 Numerical model bed

The sediment bed of the model consists of three layers:

- A soft top layer
 - 5 cm thickness in the channel and zero everywhere else.
- A medium consolidated middle layer
 - 2 mm thickness everywhere.
- A consolidated layer
 - 5 mm thickness everywhere.

The content of the three sediment fractions varies across the area and through the bed layers:

Table 3-3. Fractional content of the model sediment bed.

Area	Bed layer	Fraction 1	Fraction 2	Fraction 3	Mud
North	1	0.25	0.45	0.30	0.75
	2	0.20	0.35	0.45	0.80
	3	0.20	0.20	0.60	0.80
Central	1	0.40	0.30	0.30	0.60
	2	0.35	0.30	0.35	0.65
	3	0.30	0.30	0.40	0.70
South-east	1	0.60	0.20	0.20	0.40
	2	0.60	0.15	0.25	0.40
	3	0.60	0.10	0.30	0.40

Similarly, the dry density of the material varies across the domain and through the bed layers, see Figure 3.5. Notice that inside the MMC the dry density varies from 180 kg/m³ in the top layer to 300 kg/m³ in the bottom layer. This very low dry density is used to reflect fluffy and unconsolidated mud caused by the continuous stirring up of the sediment from ship propellers and displacement waves.



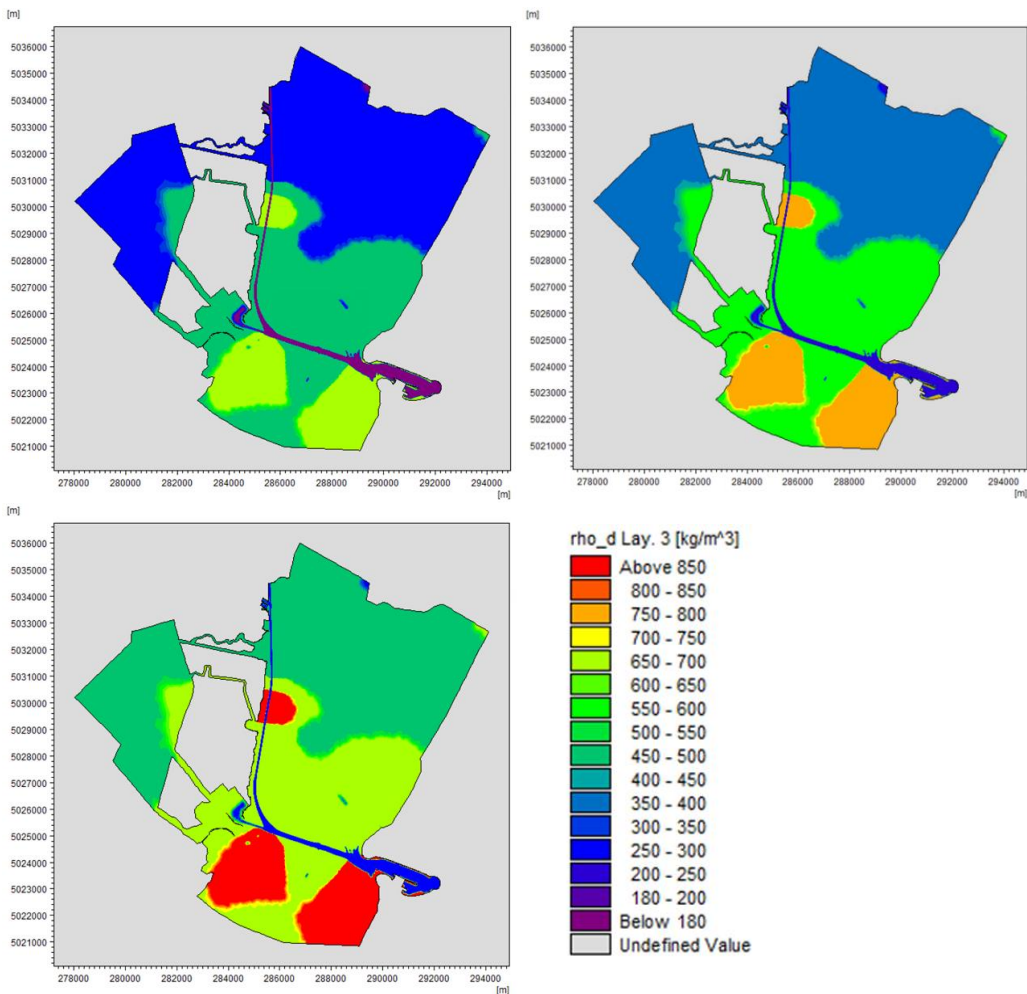


Figure 3.5. Dry density of model bed. (Top left) layer one from top, (Top right) layer 2 from top and (Bottom left) layer three from top.

The erosion from the bed is regulated by the bed shear stress magnitude. When the modelled bed shear stress exceeds a critical value, sediment is eroded from the bed and dispersed into the water column. The critical value of the bed shear stress for erosion varies across the domain and through the bed layers. Its values have been selected based on guidance from the detailed analysis illustrated in Appendix C to reflect:

- Tidal flats: 0.7 Pa
- Channel banks: 0.7 – 1.2 Pa
- Clam collection areas: 0.5 Pa
- Salt marsh: 1.8 Pa



The variation across the domain and through the bed layers is shown in Figure 3.6. Inside the MMC (and on the tidal flats) the critical bed shear stress for erosion is kept constant at 0.7 Pa whereas along the banks of the channel it varies from 0.7 Pa in the top layer to 0.9 Pa in the middle layer and 1.2 Pa in the bottom layer.

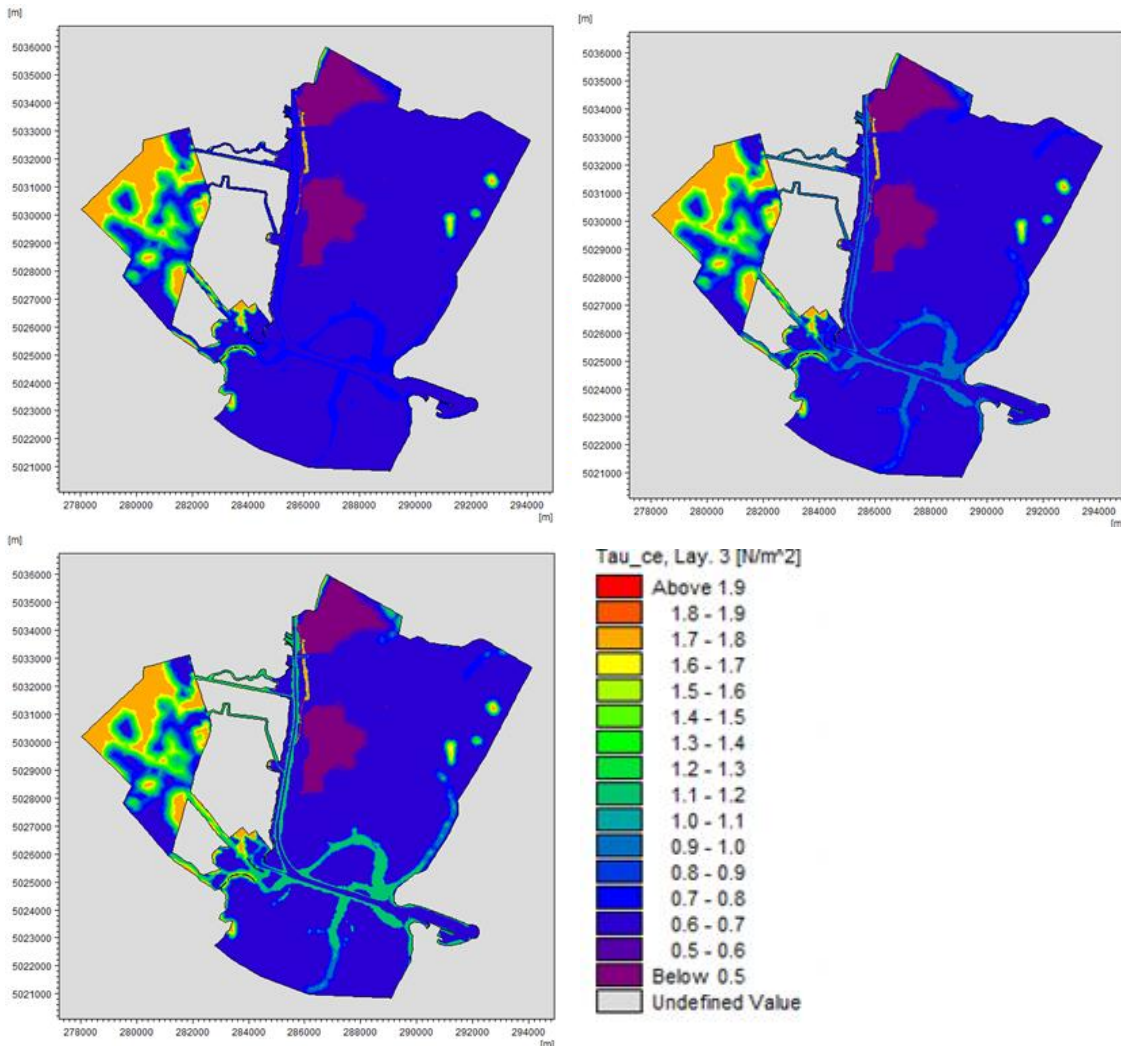


Figure 3.6. Critical model bed shear stress for erosion. (Top left) layer one from top, (Top right) layer 2 from top and (Bottom left) layer three from top.

The erosion rate E (kg/m²/s) depends on the bed layer description. The top layer is modelled as soft layer Eq. 3.1 whereas the two lower bed layers are modelled as hard layers Eq. 3.2.

$$E = E_0 \exp(\alpha \cdot (\tau_b - \tau_{ce})) \quad \text{Eq. 3.1}$$



$$E = E_0 \max\left(0, \frac{\tau_b}{\tau_{ce}} - 1\right)^\alpha \quad \text{Eq. 3.2}$$

Here E_0 is the erosion coefficient ($\text{kg/m}^2/\text{s}$) and α is the power of erosion. The variation is indicated in Figure 3.7 assuming a critical bed shear stress for erosion of 0.7 Pa. The settings of the erosion coefficient and power of erosion vary per layer as follows:

- Soft top layer: $E_0 = 5 \cdot 10^{-5} \text{ kg/m}^2/\text{s}$ and $\alpha = 8.3$
- Middle layer: $E_0 = 1 \cdot 10^{-3} \text{ kg/m}^2/\text{s}$ and $\alpha = 2$
- Bottom layer: $E_0 = 1 \cdot 10^{-4} \text{ kg/m}^2/\text{s}$ and $\alpha = 2$

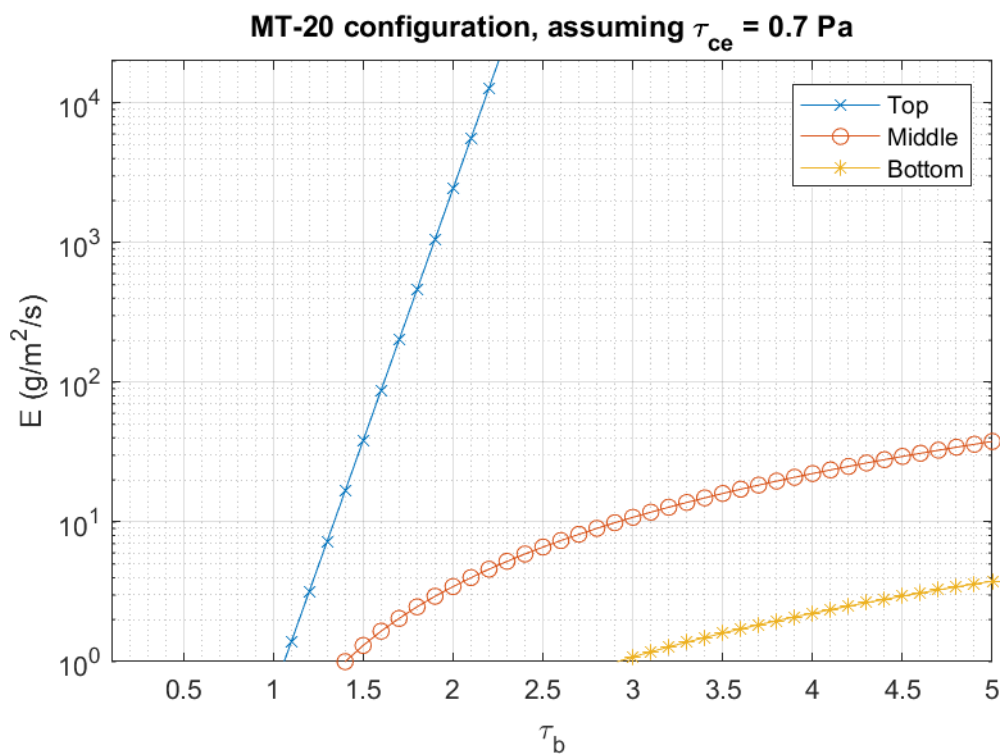


Figure 3.7. Model erosion rate.

The suspended material is allowed to settle and deposit onto the bed when the bed shear stress becomes smaller than 0.7 Pa (0.5 Pa in the clam collection areas).

The bed roughness used to calculate the bed shear stress in the model varies across the domain from 1 mm in the deep part of the channel to 7.5 mm on the flats and 20 mm in the clam collection



areas, see Figure 3.8. The presence of the clams and ruffling of the bed during the collection of the clams is assumed to increase the bed roughness in these areas.

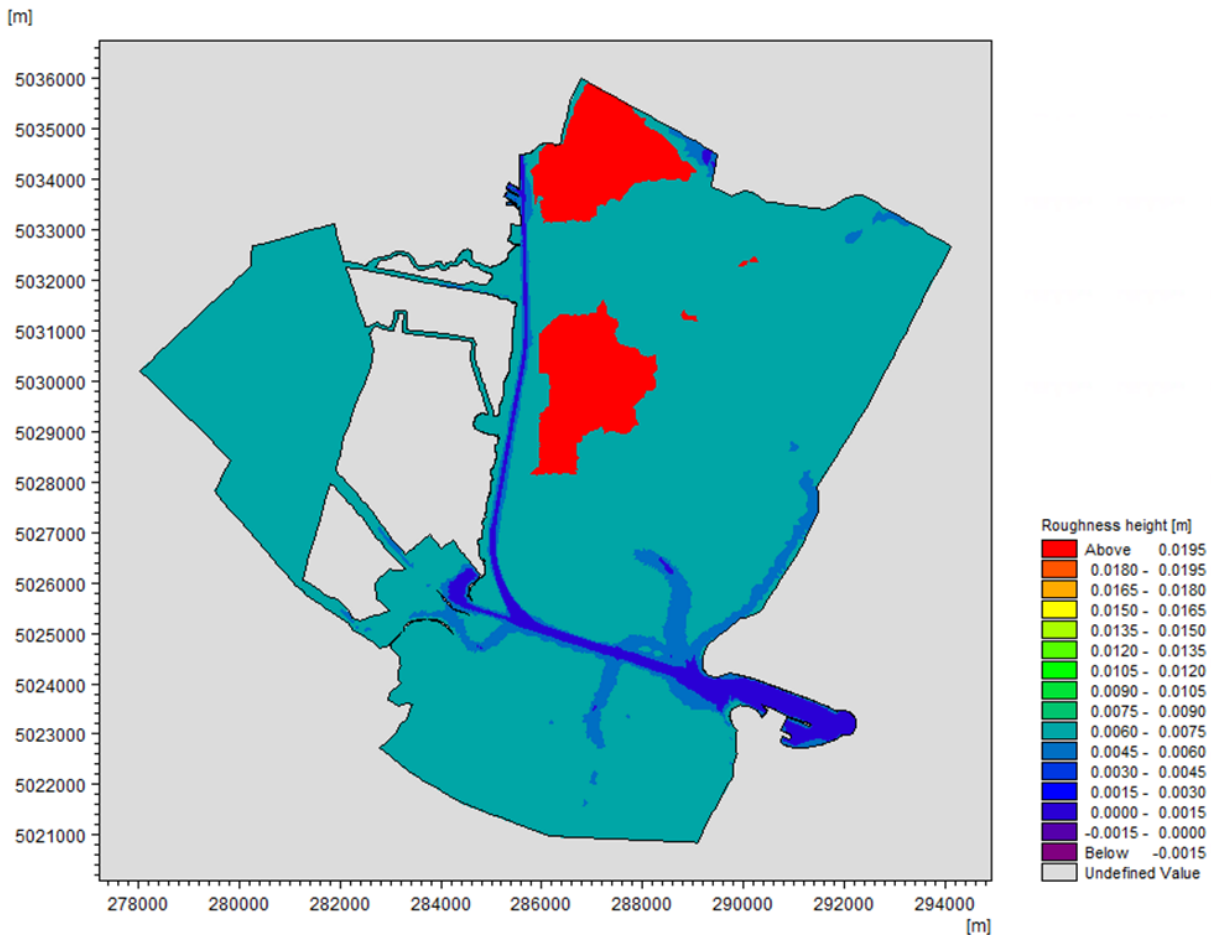


Figure 3.8. Model bed roughness varies from 1 mm in the deep part of the channel to 7.5 mm on the flats and 20 mm in the clam collection areas.

3.1.3 Dispersion

The diffusion processes of the sediment transport model are regulated as a scaled eddy variation. Hence the turbulence moving the sediment is calculated as the turbulence from the hydrodynamic model multiplied by a scaling coefficient. The scaling coefficient is set to 2.5 horizontally as a means to provide some additional horizontal spreading of the sediment since no other forcing than the moving vessel is present in the hydrodynamic model.



Vertically, a diffusion coefficient of 5 is used in the channel, see Figure 3.9, to address the stirring effect from the ship propellers. On the shallow tidal flats, the vertical diffusion coefficient is kept at 1.

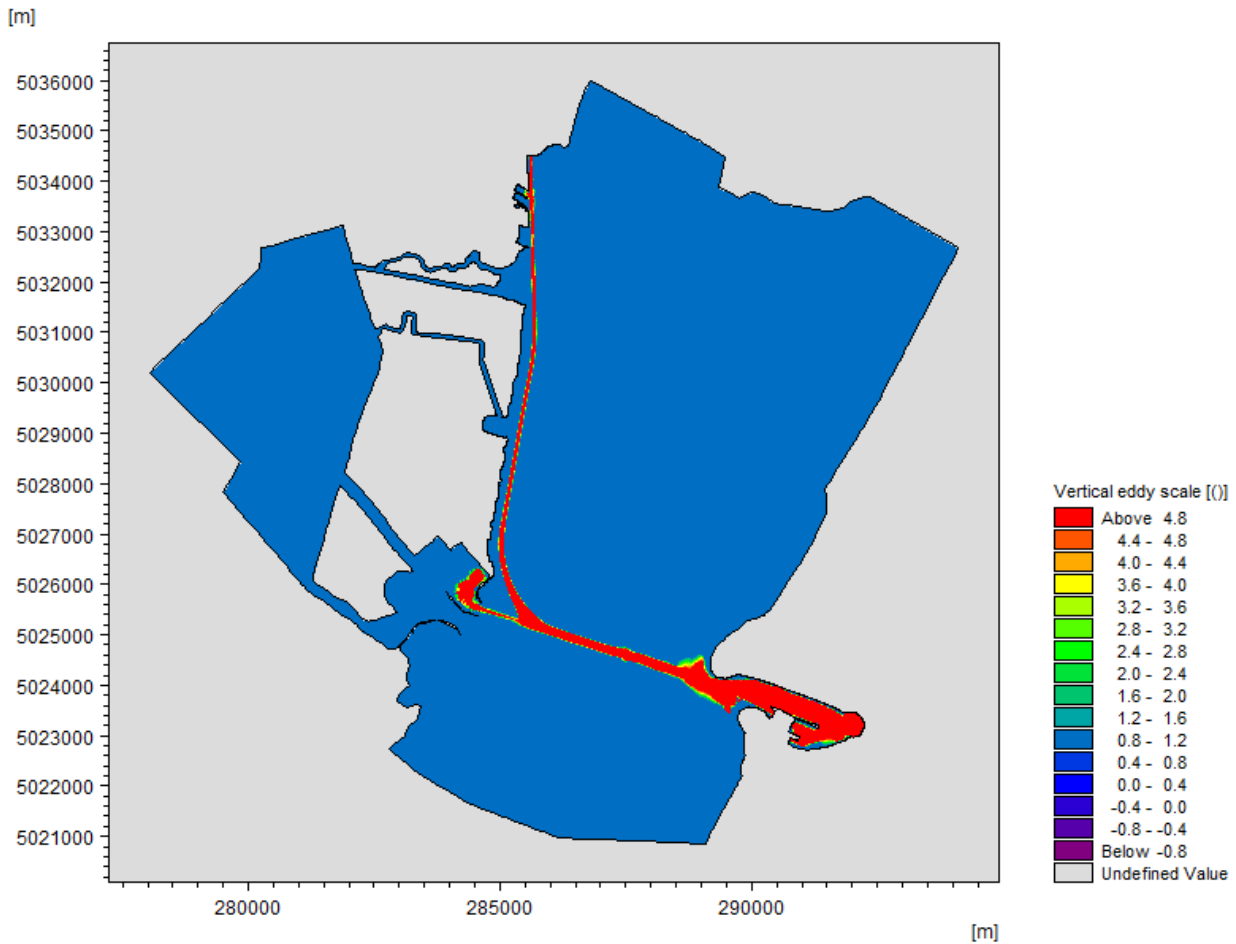


Figure 3.9. Vertical diffusion coefficient used in sediment transport model.

Figure 3.10 shows the effect of the increased vertical diffusion in the channel during a test case considering the out-going passage of Nervion Valley. The increased diffusion increases the suspended sediment concentration (SSC) in the surface layer of the water column momentarily after the vessel passage. This effect would otherwise take considerable time in the model due to the lack of the stirring effect from the propeller.



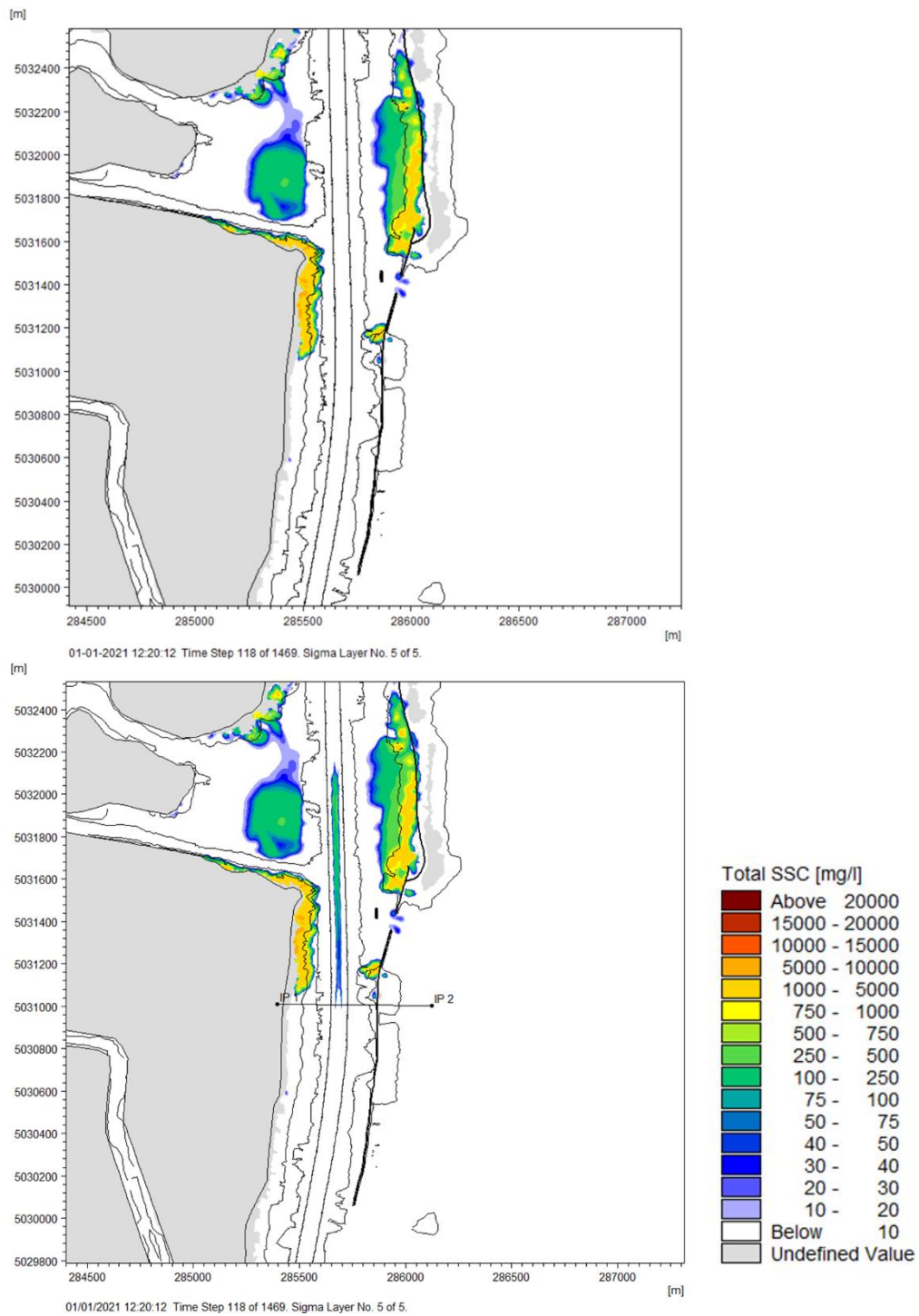


Figure 3.10. Total SSC in model surface during passage of Nervion Valley. (Top) factor 1.0 on vertical diffusion and (Bottom) factor 5.0 on vertical diffusion.



3.2 Calibration of the displacement wave sediment transport model

3.2.1 Calibration data

Four articles have been used to gain an overview of vessel generated SSC-levels and bed changes in the lagoon. The present section contains a summary of the findings in these articles.

(Rapaglia et al. 2011, [19]) have made a study of how ship wakes evolve as they propagate from the MMC onto the tidal flat at Fusina. In this connection the authors have measured turbidity levels (SSC levels) during some vessel passages in the summer of 2009, see Figure 3.11. The authors have measured SSC-levels reaching up to 100-400 mg/l about 300 m from the channel and reports increased SSC-levels to linger for 5-20 minutes in the channel – a settling time that seems to match reasonably with the one estimated from Figure 3.4 though it will take longer for the water column to become completely clear due to the presence of sediment with a relatively low fall velocity i.e., not all sediment settles within 5-20 minutes which is also seen in Figure 3.11.

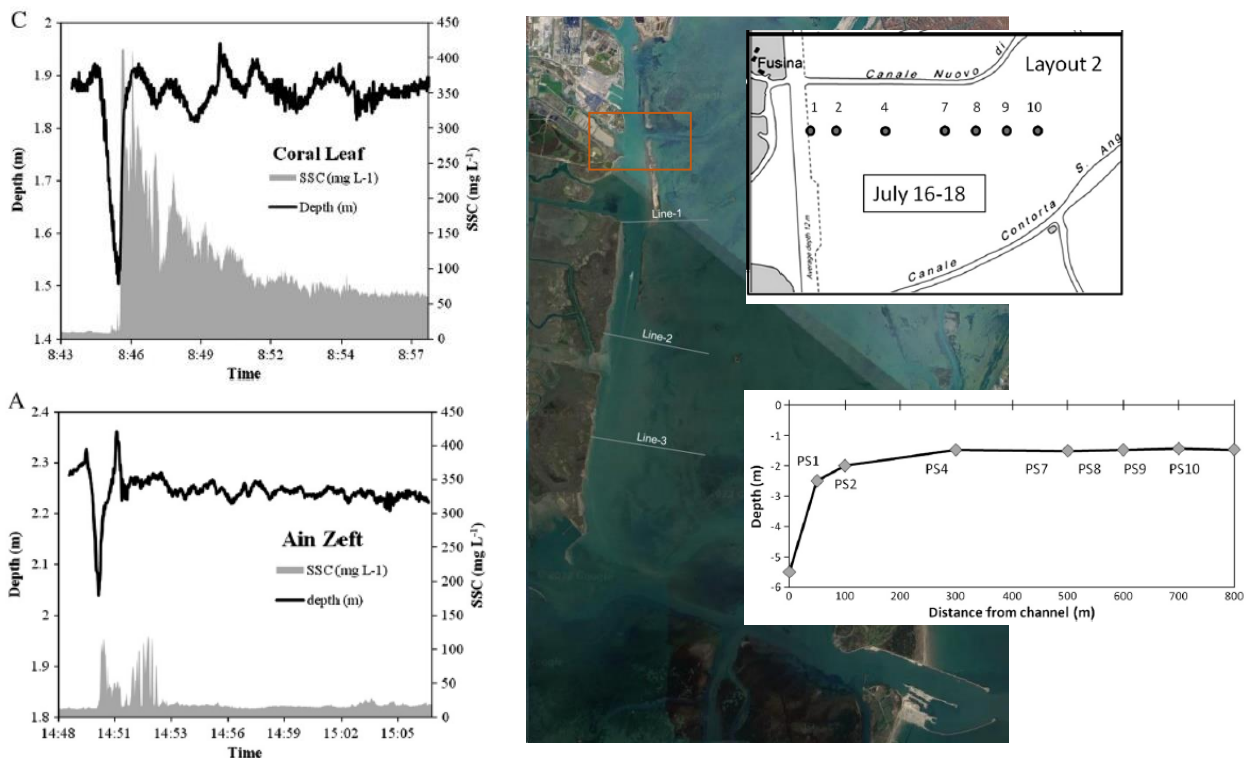


Figure 3.11. Measurement location and results from [19]. Orange frame mark the approximate measurement area on a recent Google Earth image.



(Scarpa et al. 2019, [20]), responsible for the CNR database, have reported turbidity levels during an out-bound passage of the RoRo vessel Hellenic Spirit taking place at 10.7 knots, see Figure 3.12. The measured SSC -levels have been collected 30 cm from the bed and thus represent near bed concentrations. The data has been supplied to DHI at the beginning of October 2022 and has served as the primary calibration dataset for the sediment transport model.

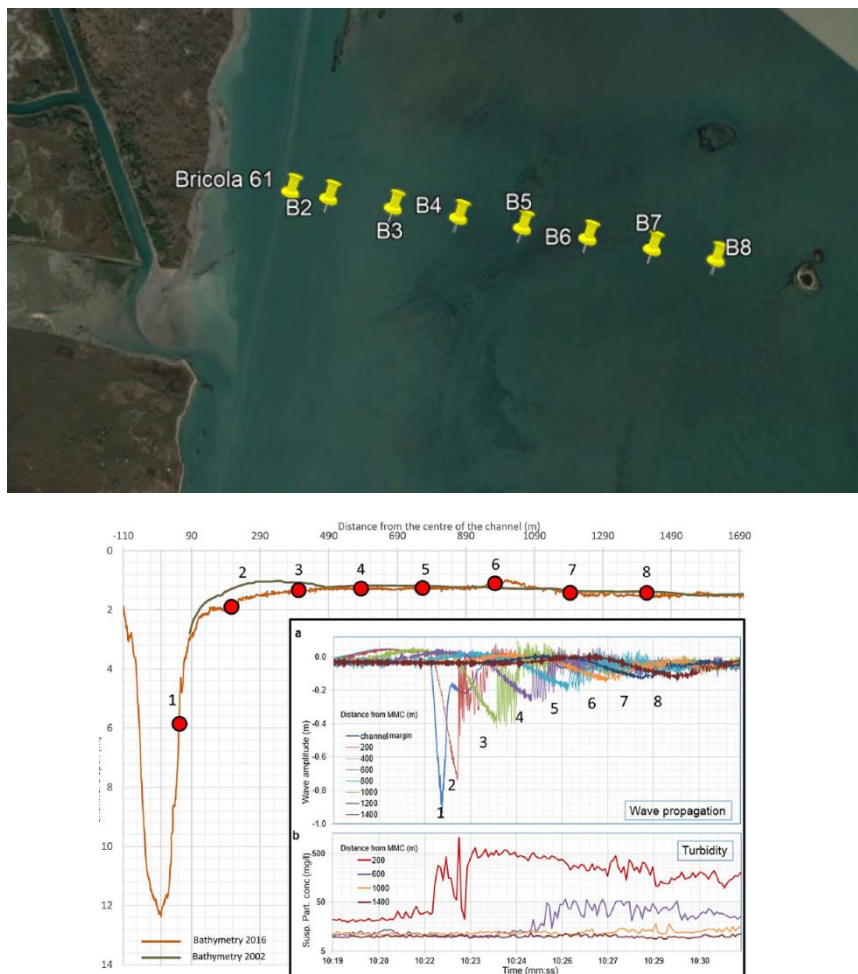


Figure 3.12. Measurement locations and data from [20] during an out-bound passage of Hellenic Spirit.

During the passage of Hellenic Spirit concentrations of 500-1,000 mg/l were observed at a distance of around 200 m from the channel and up to about 50 mg/l at 600 m from the channel. The authors report that the background SSC-levels of the lagoon, considered over a 10-year period with 15



minutes frequency, has varied as listed below per year with overall values highlighted in bold, see measurement location in Figure 3.13.

- 95th percentile: 17.7 to 38.2 mg/l, **22.2 mg/l**
- 99th percentile: 30.6 to 110.1 mg/l, **50.5 mg/l**

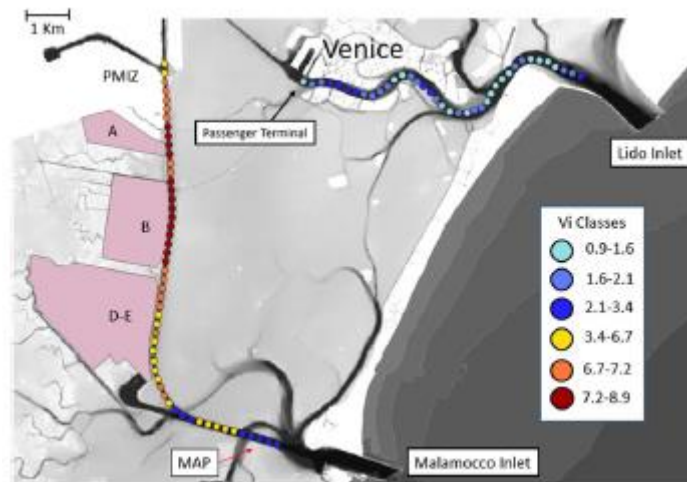


Figure 3.13. Measurement location of [20] used for background concentration marked by MAP.

This indicates that natural forcing is only able to exceed the vessel generated SSC-levels 1% of the time at a distance of ~500 m from the channel.

Figure 3.12 also shows the bathymetry at the cross-section in 2002 and 2016 making it possible to estimate an average erosion rate for the tidal flat east of the channel. Based on these data an erosion rate in the range 3 to 6 cm/year is found.

(Saretta et al. 2010, [21]) have made a historic study of the sediment budget for the Venice lagoon, which illustrates that the lagoon suffers from loss of sediment, see Figure 3.14, and that this sediment deficit causes erosion rates in the range 2.5 to 0.7 cm/year in the Malamocco basin. The upper value in this range seems to match with the range established from [20].



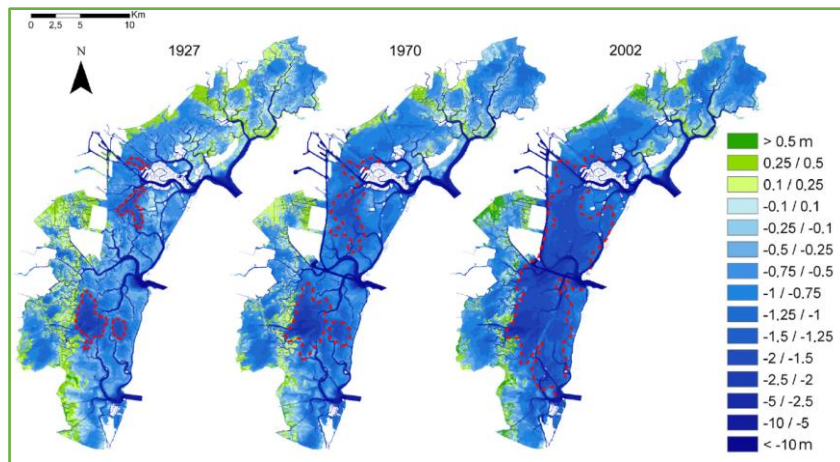


Figure 3.14. Bathymetry of the Venice lagoon from 1927 to 2002 as presented in [21].

(Zaggia et al 2017, [22]) have made an extensive study of available historic aerial images to establish the shoreline changes along the western side of the MMC. In combination with bathymetric measurements made in the period 2014-2015 bathymetric changes and types of vegetation present along the beach scarp has been established.

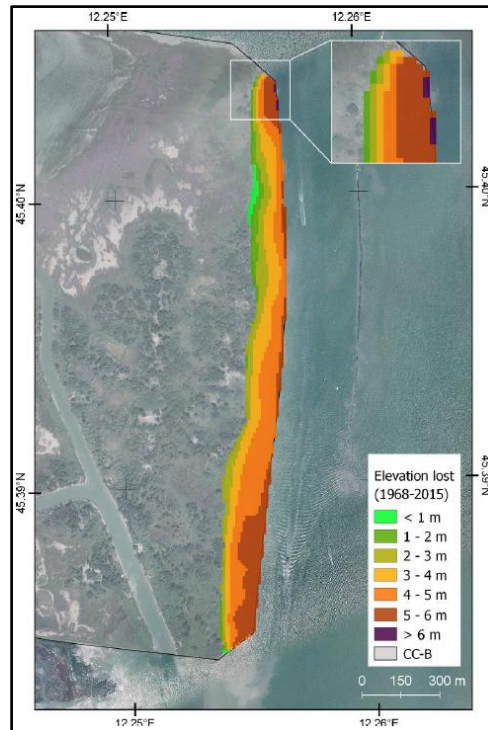


Figure 3.15. Bathymetric changes based on [22].



The study showed shoreline retreats of 3-4 m/year along the western shore. Considering that 5-6 m elevation has been lost on the western flats (see Figure 3.15) from 1968-2005, this corresponds to an erosion rate of 10-13 cm/year. It is thus clear the erosion takes place considerably faster along the western shore than the eastern flats.

Relating these erosion ranges to the number of vessels passing through the MMC it is possible to put them into a navigational context. Based on the PoV database approximately 4,700 events are recorded per year (in- and out-bound). Assuming that 75% are large vessels navigating at high speeds erosion levels should be in the range:

- East: 0.009 to 0.017 mm/event (3-6 cm/year)
- West: 0.03 to 0.04 mm/event (10-13 cm/year)

3.2.2 Model calibration

The present section will show the performance of the sediment transport model relative to the measured results of [20]. Initial calibration tests were made considering the out-going passage of the tanker vessel Nervion Valley (measured by HS Marine and used for calibration of the hydrodynamic displacement wave model). In October 2022, when the data for the out-going passage of Hellenic Spirit were made available (draft, speed and direction), the last tuning of the sediment transport model was made and the production modelling started.

The measurements of [20] (see Figure 3.12) were made 30 cm from the bed and thus represent near-bed concentrations. These results are compared to the model results extracted from the bottom layer resolving the model water column.

In Figure 3.16 and Figure 3.17 the results at station B2 (200 m from the channel) and B4 (600 m from the channel) are shown. The figures contain three panels:

- Top panel: Comparison of measured and modelled water level, (WL).
- Middle panel: Comparison of measured and modelled turbidity, (SSC).
- Bottom panel: Comparison of measured and modelled water level to ambient depth ratio, (WL/h_0).



The water level variation at 200 m from the channel is well captured by the model. The draw down level magnitude is slightly underestimated, but as discussed during the calibration of the hydrodynamic model, uncertainty in terms of the relative distance between the vessel and the measurement station, as well as the difference between measured and model bathymetric depth can explain this.

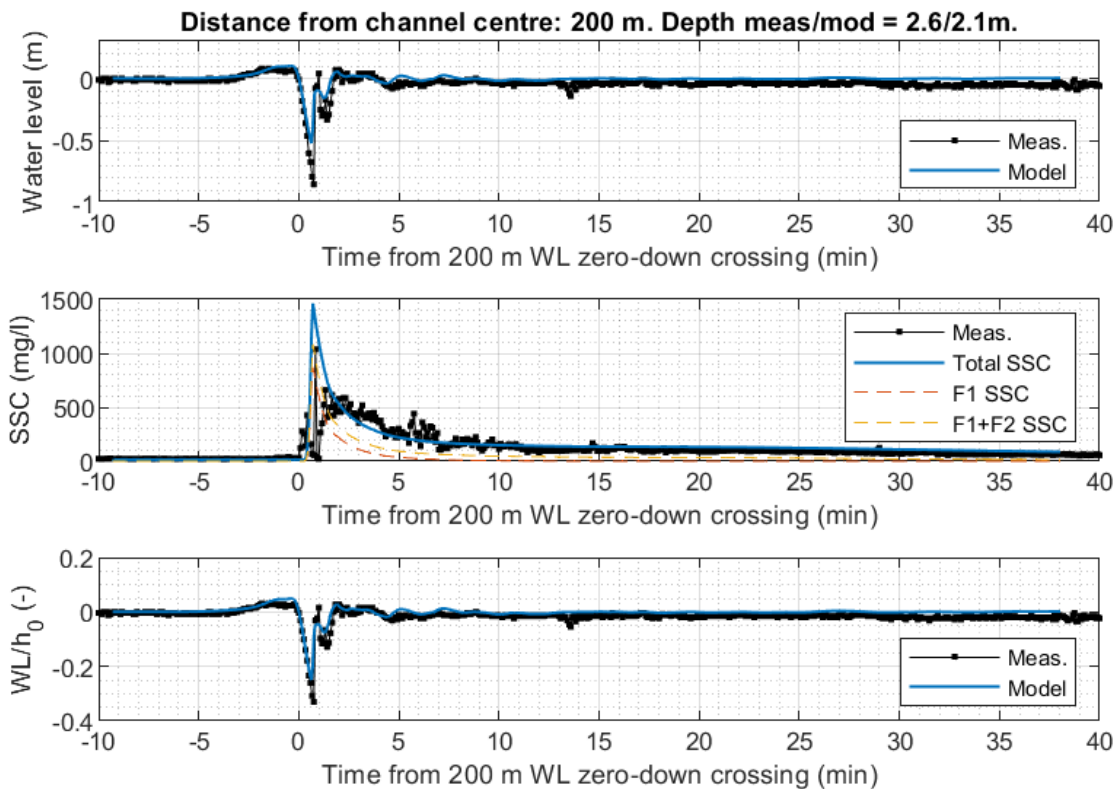


Figure 3.16. Water level and turbidity 200 m from channel during passage of Hellenic Spirit. Measurements from [20] marked in black.

The turbidity levels at 200 m from the channel are also captured well by the model, the settling time of Fraction 3 matches the measured conditions well though the peak value is slightly overestimated. The order of magnitude is however well within the uncertainties of the available sediment data.

The water level variation 600 m from the channel is also well captured by the model though again the draw down level magnitude is again slightly underestimated. This is partly related to the draw down level being initially a bit too small at 200 m and the fact that the model depth appears smaller than measured, why relatively more energy may be dissipated in the model than during measured



conditions. Another effect (also influencing the modelled draw down level) is that the measured saw-tooth like profile does not evolve to the same extent in the model i.e., the modelled signal is slightly less non-linear. Due to these effects, there is a phase-lag between measured and modelled minimum water level – the model reaches its minimum level sooner than the measured signal. This lag is also quite clear looking at the SSC-levels. The modelled peak in SSC-levels is directly linked to the minimum water level and reaches the measured magnitudes and settling profile quite nicely. However, the peak of the measured SSC-signal is less tightly linked to the minimum water level probably due to the slightly more non-linear water level signal. Additionally, as distance to the channel increases, natural forcing from tide and wind also become increasingly important.

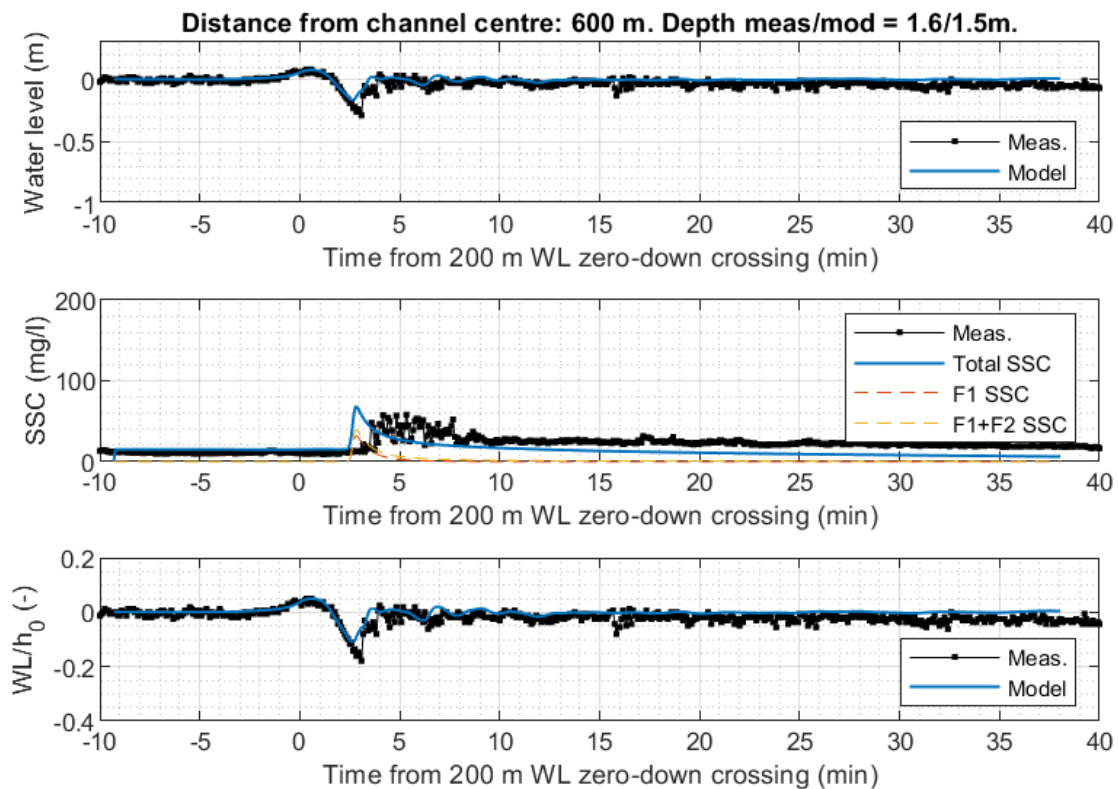


Figure 3.17. Water level and turbidity 600 m from channel during passage of Hellenic Spirit. Measurements from [20] marked in black.





As such the model has sufficient accuracy for modelling the effects of the displacement waves in the vicinity of the channel and provide good estimates and understanding of the changes caused by a reduction in vessel speed and modified channel layout.

In Figure 3.18 and Figure 3.19 maps of the modelled total SSC in the measurement area are provided considering bottom and surface layers. A single step represents 4 seconds; hence the maps represent a duration of about 4 minutes. In the maps the model contours representing -10, -3 and -1 m MSL are indicated as thin black lines and the structures as thick black lines.

The maps indicate high concentrations in the bottom of the channel (around 1000-5000 mg/l) and similar concentration levels are found in the shallow area along the western side of the channel. In this shallow area, concentrations are almost uniformly distributed over the water column. High levels of around 1000 mg/l are also seen near the bed at station B2 but on the eastern side of the channel, there is a bigger difference between the concentration levels near the bed and those at near the surface.



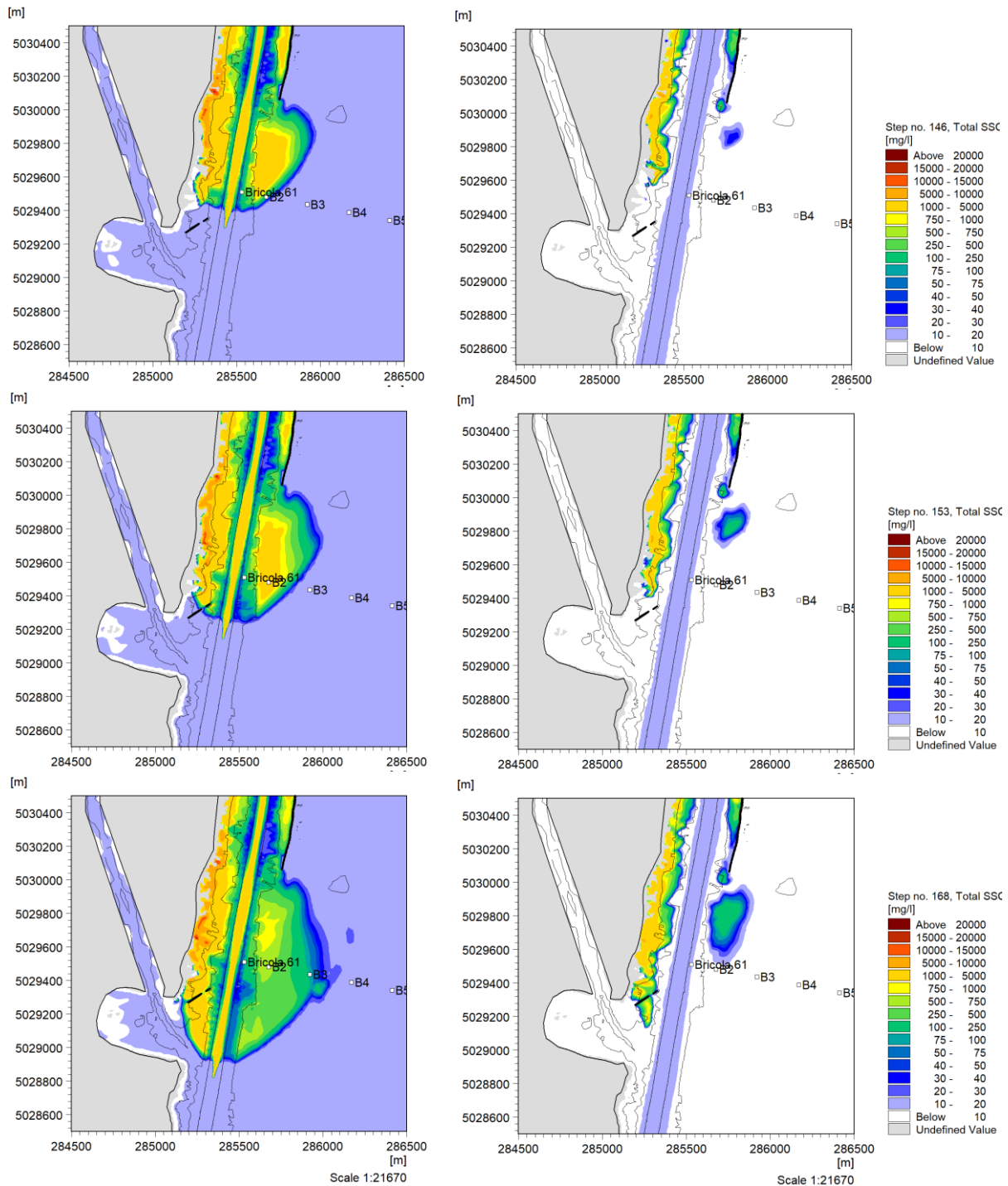


Figure 3.18. Maps of modelled total SSC during passage of Hellenic Spirit, Part I. (Left) Bottom layer. (Right) Surface layer.



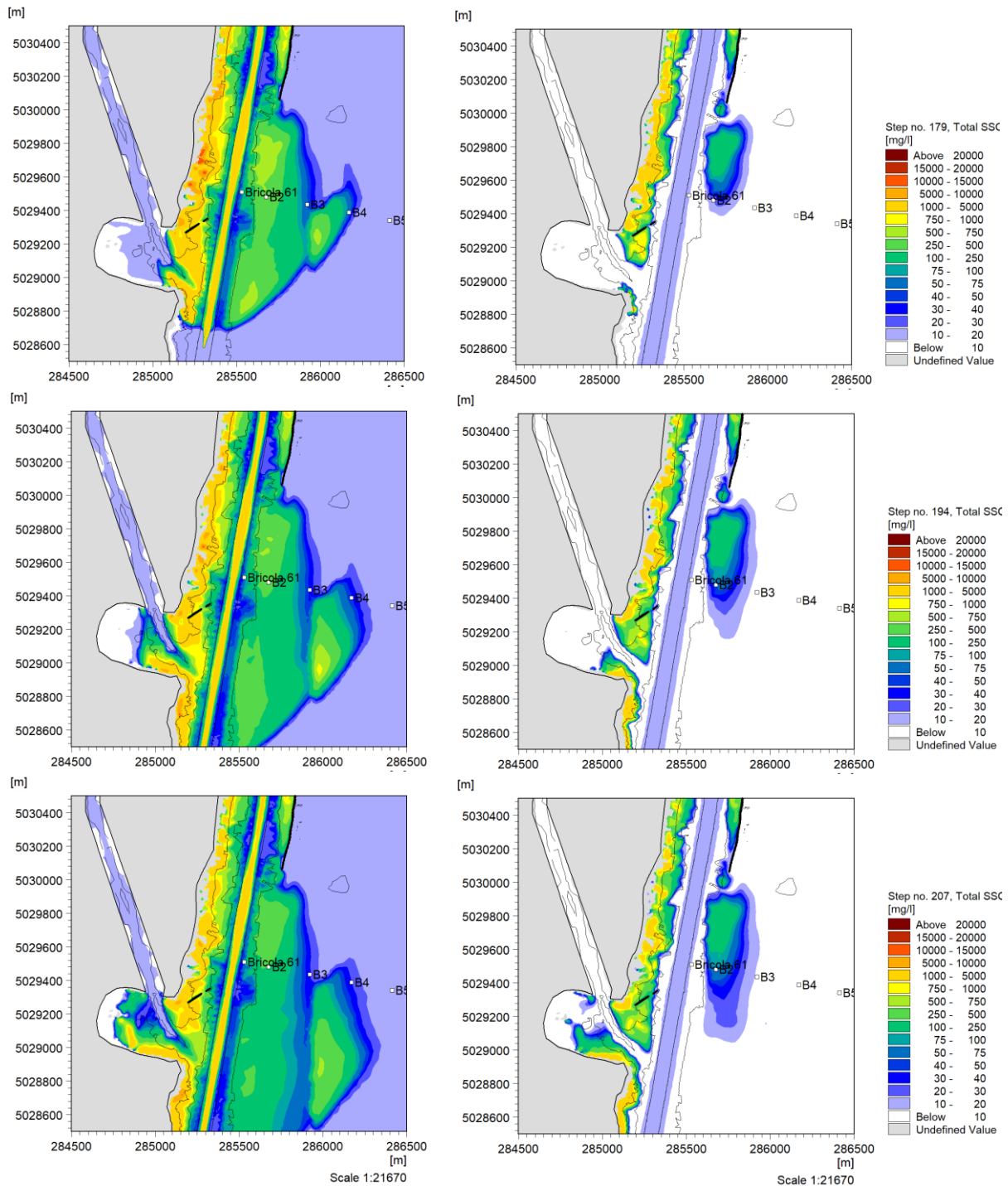


Figure 3.19. Maps of modelled total SSC during passage of Hellenic Spirit, Part II. (Left) Bottom layer. (Right) Surface layer.



In Figure 3.20 the modelled bed level changes after the passage of Hellenic Spirit are shown. These have been calculated from the deposited/eroded mass of sediment at the end of the simulation and transformed into a thickness assuming a bed dry density of 900 kg/m^3 . The sediment dry density is however uncertain and thus the selected value is an approximation used to convert between deposited dry mass and vertical bed level changes. [17] reports wet bed bulk densities of about $1700 - 1960 \text{ kg/m}^3$ on the flats in their Table 2. Hence the bed material on the flats may have a dry density of up to around 1500 kg/m^3 .

In the map the model contours representing -10, -3 and -1 m MSL are indicated as thin black lines and the structures as thick black lines. Additionally, three pink lines are shown. These lines, numbered 1 to 3 starting from north, will be used to evaluate the draw down levels modelled during the production simulations, so their location should be noted.

- Line-1 is located in an area where the displacement wave has a quite limited area to spread out on since the channel here is framed by the western shoreline and the eastern structures.
- Line-2 is located south of the area influenced by the eastern structures, close to the measurement section of [20] making it possible to relate the modelled results to those measured.
- Line-3 is located north of the San Leonardo bend in a fairly un-restricted part of the channel – far away from any structures framing the channel.

The modelled bed level changes in Figure 3.20 display a complicated pattern of erosion and deposition along the channel. There is a tendency for erosion to occur between -3 to -1 m MSL. On the western side erosion levels tend to be in the range $0.1 - 1 \text{ mm}$ whereas on the eastern side the levels tend to be in the range $<0.01 - 0.04 \text{ mm}$. Hence the model matches the expected behaviour with more erosion on the western side compared to the eastern side. The magnitudes are however somewhat overestimated compared to the expected event levels from Section 3.2.1. It is noted that the differences between simulated and measured levels are subject to uncertainties related to factors such as sediment density that were unknown and were therefore given estimated values. Also, on the western side the morphodynamics depend highly on the quality of the salt marshes and their stratigraphy. As mentioned previously, the erosion mechanism in this area is complex e.g., the number of cracks and varying levels of the silt/sand content will cause varying cohesive behaviour along the banks making them more erodible in some areas than others.



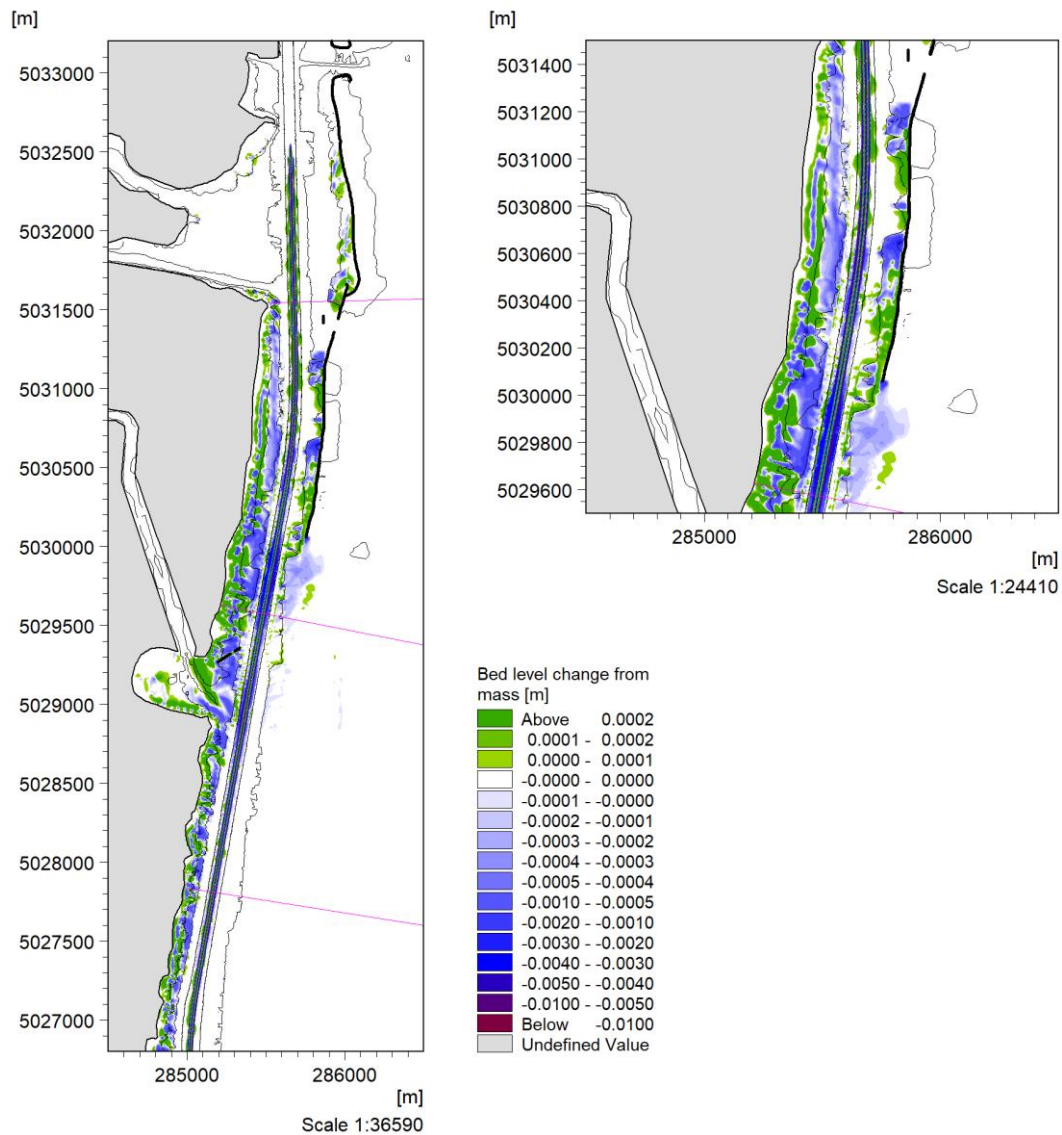


Figure 3.20. Modelled bed changes after passage of Hellenic Spirit. Extraction line 1, 2 and 3 are indicated by pink lines. Line numbering increases from north going south.



4 PRODUCTION MODELLING OF EXISTING CHANNEL LAYOUT

In Section 3.2.2 it was demonstrated that the sediment transport model reproduces the suspended sediment concentration levels (SSC) quite well. The modelled erosion pattern matches the expectation of relatively more erosion west of the channel than east of the channel. The main objective of the production modelling is to reproduce the observed erosion considering the combined effect of the representative traffic. Later on, the model will be used to evaluate the impact of various mitigation measures on the sediment balance and the erosion of the areas adjacent to the channel. The tendency for the model to overestimate the erosion magnitudes will be accounted for by scaling the weighted accumulated effect. Using the same scale during the evaluation of the mitigation measures a clear picture of their relative influence on the erosion along the channel will be obtained.

In the present section the results of the production modelling considering vessel speeds of 10 knots, and using the existing channel layout, will be presented. First, a detailed run through of the results of the small and most frequent container vessel (Con-S) will be given. Secondly, tabularized hydrodynamic results of the simulations will be presented and discussed. Thirdly, the weighted accumulated bed changes will be analysed.

The tabularized hydrodynamic results consider values extracted along the three lines indicated in Figure 3.20. The results are extracted at the points indicated in Table 4-1 and Table 4-2 below, see also Figure 4.1. Note that for Line-1 points 400 to 1400 m are located east of the structures. This means that during the out-bound passages these points will be practically uninfluenced by the displacement waves. For this reason, only the margin and 200 m point will be presented considering the east side of this line.

Table 4-1. Bathymetric depths of line extraction points east of the channel.

Depth (m MSL)	Margin	200 m	400 m	600 m	800 m	1000 m	1200 m	1400 m
Line-1	4.4	2.1	-	1.5	1.4	1.5	1.6	1.6
Line-2	5.9	2.0	1.6	1.5	1.5	1.4	1.6	1.7
Line-3	5.3	2.5	1.9	1.7	1.7	1.7	1.7	1.8



Table 4-2. Bathymetric depths of line extraction points west of the channel.

Depth (m MSL)	Margin	75 m	100 m	125 m	150 m
Line-1	5.8	3.5	1.3	0.6	-
Line-2	5.9	4.5	3.1	2.9	2.2
Line-3	5.8	5.8	2.6	1.3	0.7

Based on Figure 4.1 the channel cross section is wider at Line-3 than at Line-1 and Line-2. Hence smaller draw down magnitudes should be expected at Line-3 than at Line-1 and Line-2.

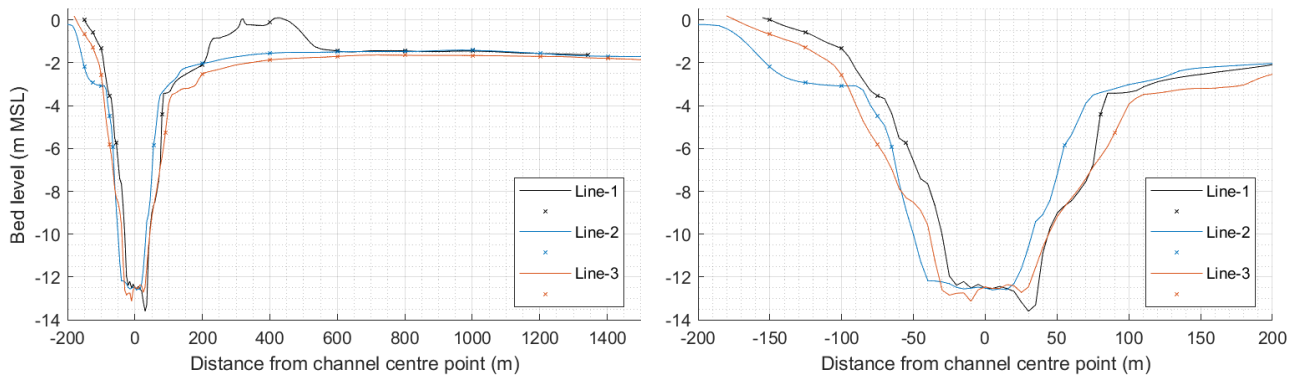


Figure 4.1. Visualization of bathymetry along extraction lines.



4.1 Detailed run though of Con-S passage

The modelled minimum water levels (the draw down levels) considering the in- and out-bound passage of Con-S are listed in Table 4-3 and Table 4-4, eastern and western extraction points respectively. The cells in the tables have been coloured according to the draw down magnitude.

Table 4-3. Overview of modelled minimum water levels at eastern line extraction points during in- and out-bound passage of Con-S.

WL (m MSL)	Margin	200 m	400 m	600 m	800 m	1000 m	1200 m	1400 m
Line-1, In	-1.05	-0.97	-	-	-	-	-	-
Line-1, Out	-0.61	-0.48	-	-	-	-	-	-
Line-2, In	-0.67	-0.49	-0.28	-0.22	-0.18	-0.14	-0.12	-0.10
Line-2, Out	-1.06	-0.69	-0.33	-0.22	-0.15	-0.12	-0.10	-0.08
Line-3, In	-0.53	-0.45	-0.34	-0.25	-0.13	-0.08	-0.05	-0.04
Line-3, Out	-0.64	-0.53	-0.36	-0.28	-0.21	-0.16	-0.13	-0.11

Table 4-4. Overview of modelled minimum water levels at western line extraction points during in- and out-bound passage of Con-S.

WL (m MSL)	Margin	75 m	100 m	125 m	150 m
Line-1, In	-1.14	-1.26	-	-	-
Line-1, Out	-0.73	-0.76	-	-	-
Line-2, In	-0.82	-0.79	-0.79	-0.79	-1.03
Line-2, Out	-1.11	-1.11	-1.09	-0.99	-1.13
Line-3, In	-0.72	-0.72	-0.77	-0.78	-0.49
Line-3, Out	-0.74	-0.74	-0.86	-0.9	-0.48

Based on the draw down tables the following observations are made:

- At Line-1 (located in the structure restricted northern part of the channel) the draw down levels are largest during the in-bound passage.
- At Line-2 and 3 (both located south of the structures) the draw down levels are largest during the out-bound passage.



- At Line 2 and 3 it is seen that the draw down magnitude decreases with increasing distance to the channel. This is especially clear east of the channel where distances are larger (and depths smaller at Line-2).
- Minimum water levels on the western side are slightly larger (more negative) but comparable to those found at the eastern margin and 200 m point.

The calculated relative reduction in draw down level, Eq. 4.1, has been plotted in Figure 4.2 considering the east side of Line-2 and 3. This figure indicates that about 60% of the draw down is dissipated at about 600 m from the channel center.

$$Red. = \frac{|WL_i| - |WL_1|}{|WL_1|} \quad Eq. 4.1$$

Further away into the lagoon the dissipation rate decreases (seen as a flattening of the curve) because the wave now propagates in an open area of similar depth and thus mainly dissipates as a result of bed friction.



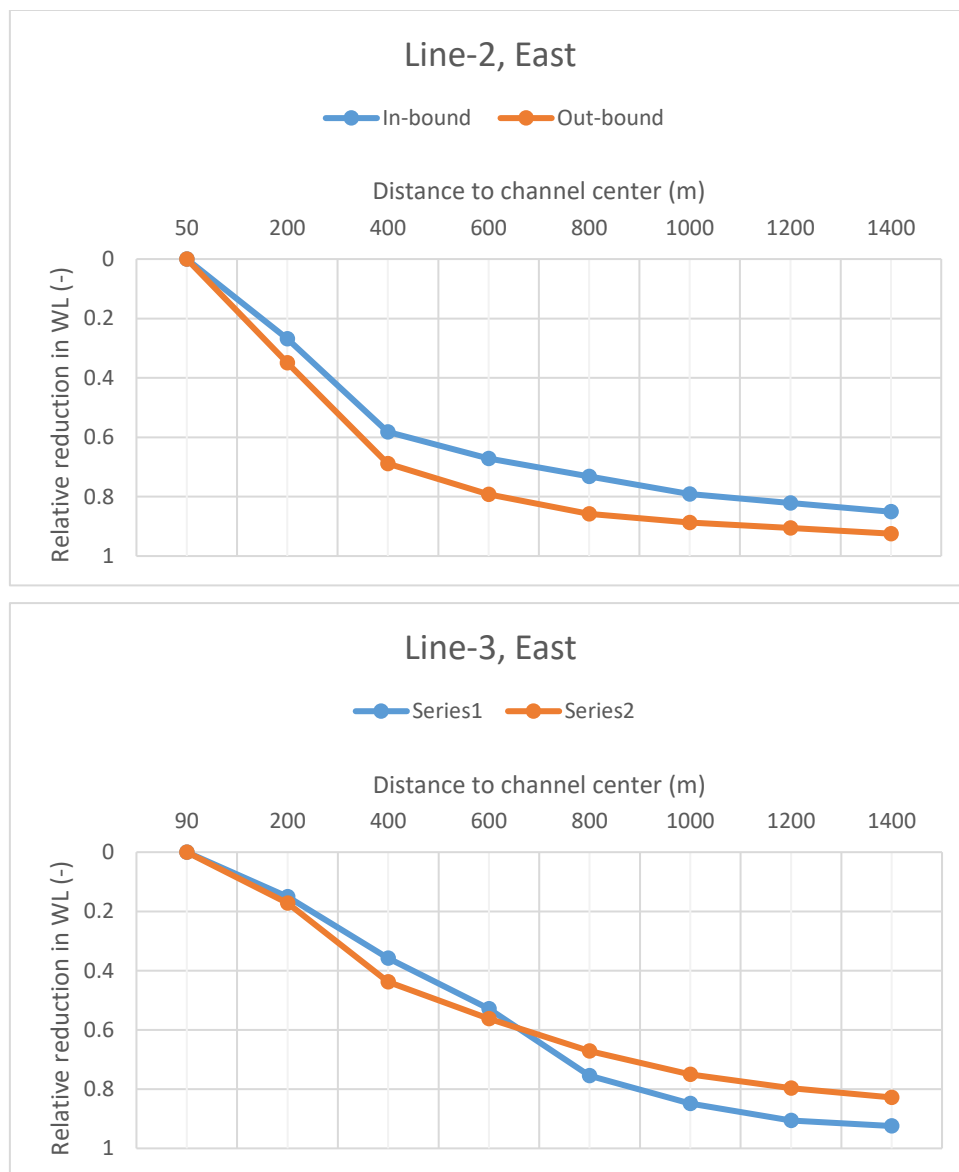


Figure 4.2. Relative reduction in draw down magnitude with distance from the channel during Con-S passage.

In Figure 4.3 a map of the maximum modelled bed shear stress is shown considering the in-bound passage of Con-S. The maximum bed shear stress is calculated as the 99.9th percentile value in each computational cell, thus forming a map. The difference between in-bound and out-bound passage is plotted as the right panel in the figure.



The figure illustrates that:

- In-bound passages cause larger bed shear stresses in the northern part of the domain, where the east-side structures are located.
- Outbound passages cause larger bed shear stresses in the southern part of the domain, south of the east-side structures.

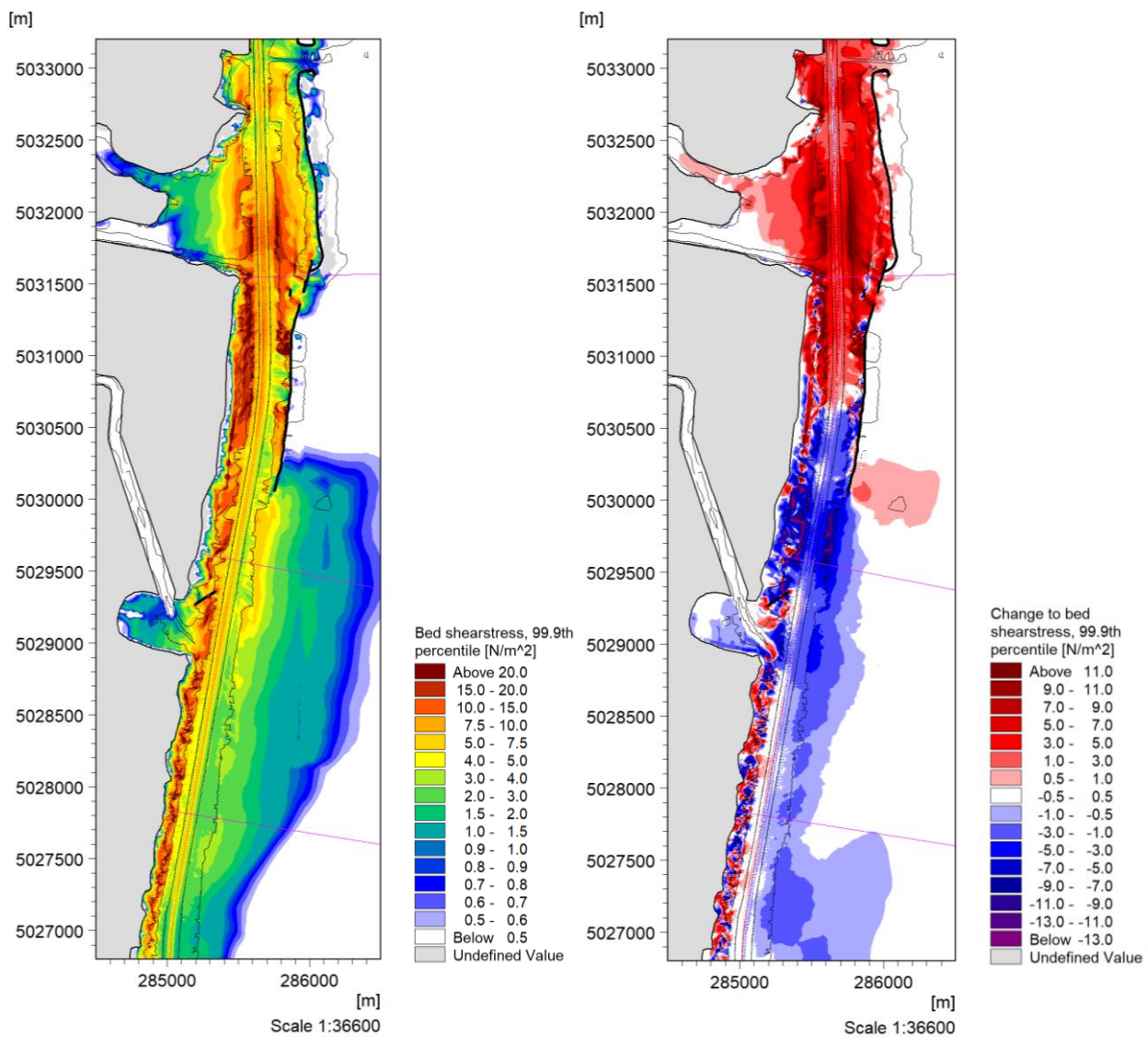


Figure 4.3. Map of maximum modelled bed shear stresses during in-bound passage of Con-S (Left). Map of difference between in-bound and out-bound maximum bed shear stress (in minus out) during Con-S passage (Right).



- Large bed shear stresses (>7.5 Pa) are found in the shallow area (above -3 m MSL) on the western side of the channel.
- Bed shear stresses are larger in the area with structures than on the east side of the channel south of the structures.
- In the area with structures large bed shear stresses (>7.5 Pa) are found on both sides of the channel where the bathymetry transitions from around -3 m MSL to smaller depths.

The fact that there is a difference between the bed shear stress magnitudes needs to be considered in relation with the evaluation of future mitigation measures. The maximum bed shear stress is directly linked to the maximum draw-down, see Figure 4.4. Here it is clearly seen that the draw down magnitude is larger during the in-bound/out-bound passage at Line-1/Line-2 respectively leading to the spatially mapped difference in maximum bed shear stress magnitude shown in Figure 4.3.

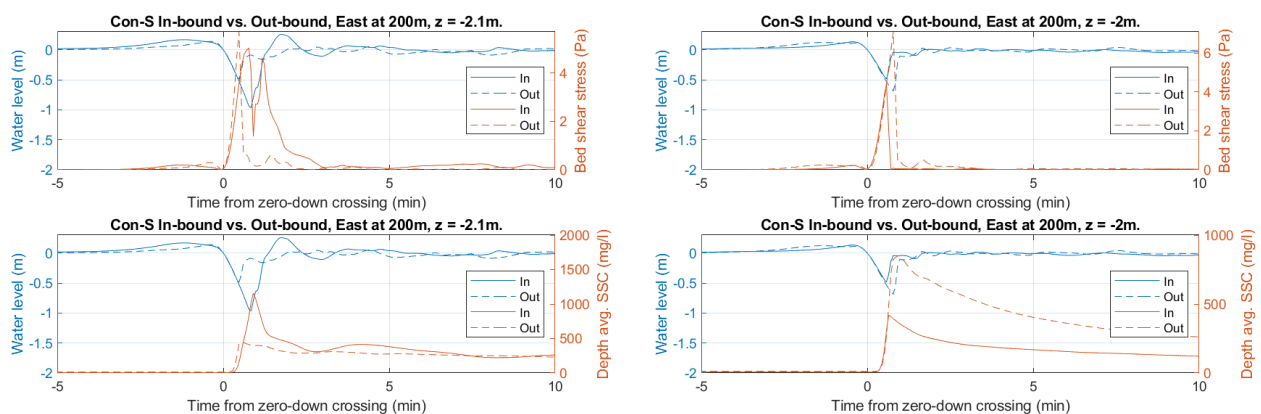


Figure 4.4. Timeseries of modelled water level, bed shear stress and SSC-level at (Left) Line-1 and (Right) Line-2.

As the vessel pass Line-1 during the out-bound passage it has travelled at 10 knots for about 116 m after a slow acceleration from zero velocity in the Fusina area. During the in-bound passage on the other hand, the vessel has travelled at 10 knots practically all the way from Malamocco as it passes Line-1. This difference has an influence on the evolution of the displacement wave at Line-1, an effect which is likely exaggerated to some extent in the model compared to real conditions, since in reality vessels are not accelerated from zero velocity starting in the Fusina area.

The implication of this is that the draw down level during the out-bound passage may be somewhat underestimated at Line-1 compared to real conditions. But for the sake of evaluating the relative



change between existing and mitigated conditions it will have no influence – since the difference will be present in both simulations.

4.2 Hydrodynamic results

In Appendix A tables of the minimum water levels and the associated bed shear stress magnitude and depth averaged SSC-level are presented for all vessel passages (in-bound and out-bound) at Line 1, 2 and 3. In the present section the minimum water level (i.e. maximum draw down level) will be shown graphically as bar charts for the sake of easy visual comparison. These bar charts are made only for the eastern side of the channel whereas the tables in Appendix A are also made for the western side of the channel. Note that at Line 1 only the margin and 200 m points are shown for the eastern channel side similar to Table 4-3.

Figure 4.5 to Figure 4.7 presents the bar charts for the channel east side of Line 1 to 3 respectively. The bar charts illustrate how the draw down level magnitude varies between the vessels, between in-/out-bound directions and how it decreases with distance from the channel at Line-2 and Line-3.

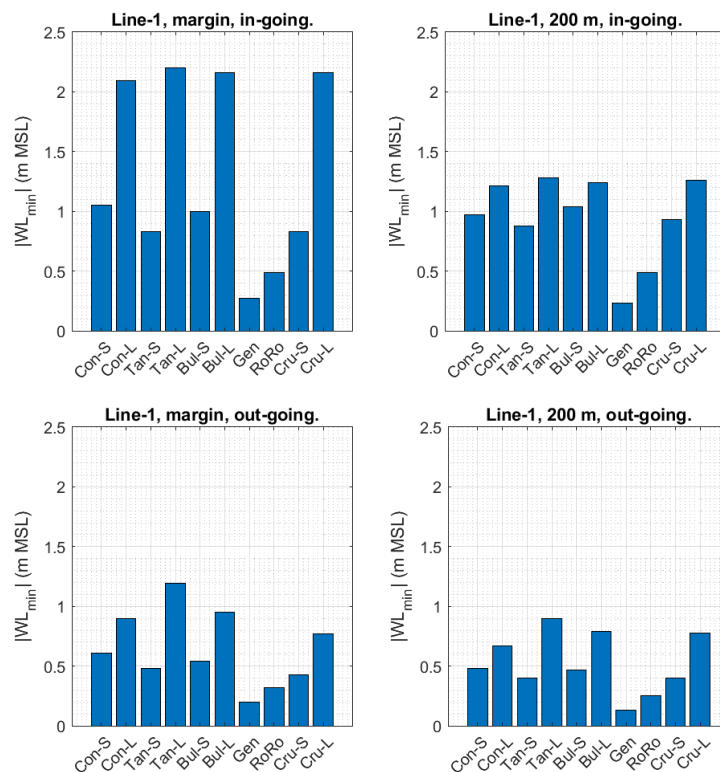


Figure 4.5. Line-1 minimum water level during in- and out-bound passages.



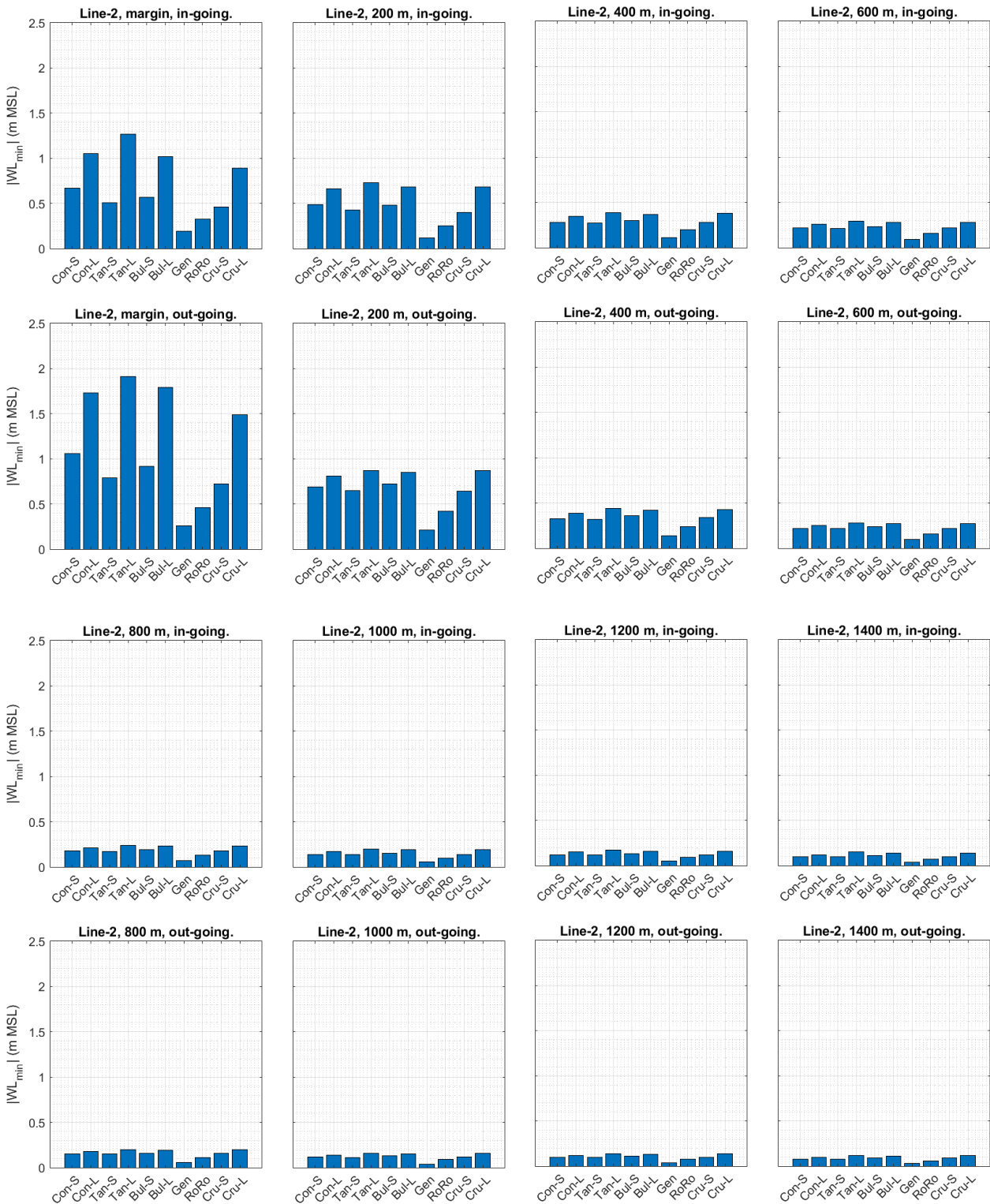


Figure 4.6. Line-2 minimum water level during in- and out-bound passages.



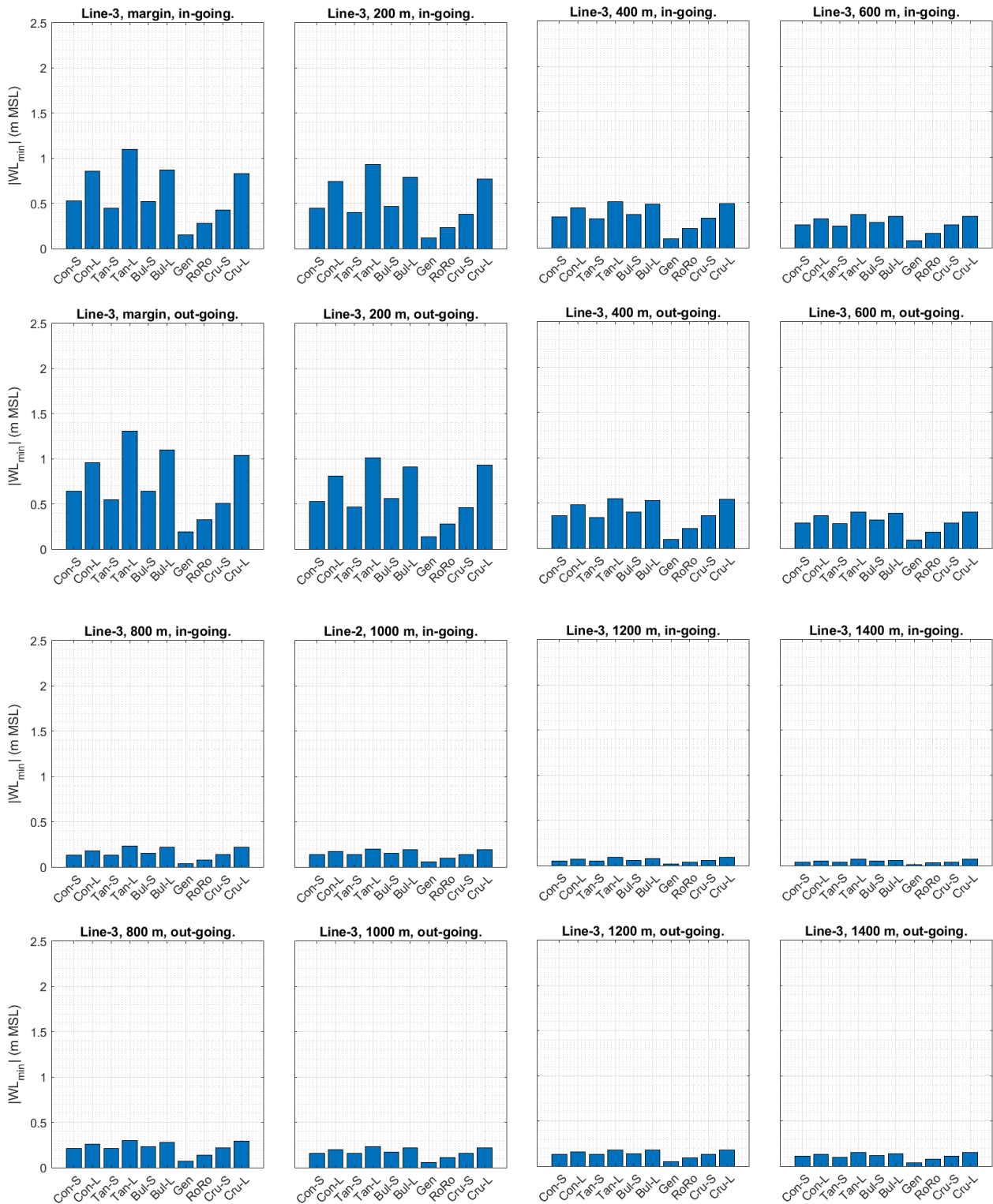
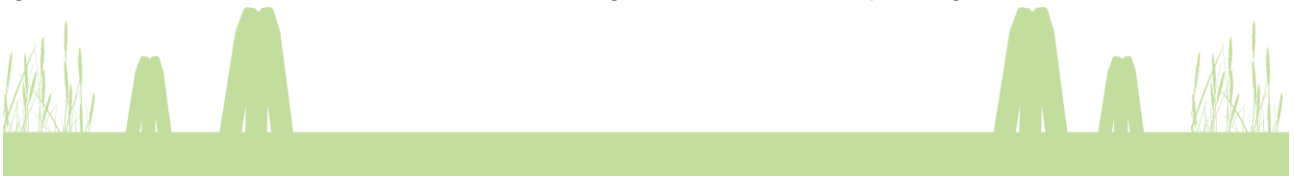


Figure 4.7. Line-3 minimum water level during in- and out-bound passages.



Comparing the size of the large cruise vessel (Cru-L) to the geometries of the large container vessel (Con-L), tanker vessel (Tan-L) and large bulk carrier (Bul-L) it is found that Cru-L mainly differs from the other large vessels in terms of its length, draft and blocking coefficient:

- Cru-L is about 50%/67%/57% **longer** considering Con-L/Tan-L/Bul-L respectively
- Cru-L is about 9%/1%/14% **wider** considering Con-L/Tan-L/Bul-L respectively
- Cru-L has about 18%/21%/21% **smaller** draft considering Con-L/Tan-L/Bul-L respectively
- Cru-L has about 41%/13%/17% **larger** displacement stencil considering Con-L/Tan-L/Bul-L respectively
- Cru-L has a **smaller** blocking coef. of 0.61 as opposed to 0.66/0.79/0.81 considering Con-L/Tan-L/Bul-L respectively

At the channel margins Cru-L causes draw down levels quite similar to Con-L and Bul-L whereas Tan-L causes the largest draw down levels – even though Cru-L has a larger displacement stencil. The reason for this is probably that Cru-L is quite similar to Tan-L in terms of width but differs considerably in terms of draft and blocking coefficient.

Similar to Figure 4.2 the bar charts in Figure 4.5-Figure 4.7 indicate that the size of the draw down wave decreases significantly within the first 600-800 m from the channel. Beyond this distance the draw down level magnitudes are in fact fairly similar across the vessels. Since the largest vessels clearly causes the largest draw down levels and most of the wave dissipation take place within the first ~600 m regardless of vessel type and size, this also means that the majority of the erosion of the channel banks is linked to these vessels. Based on Figure 2.28 a fairly large portion of the vessels navigating the channel are similar to the large modelled category. A such reducing the speed of these large vessels is expected to have a significant influence on the reduction of the channel bank erosion.

In Figure 4.8 - Figure 4.9 maps of a 0.7 Pa contour from the maximum bed shear stress map of each vessel (see Figure 4.3 as an example) has been extracted along part of the eastern side of the channel. The maps give an indication of the distance within which sediment transport related to displacement waves can be expected. Here it is clearly seen that the large vessels give rise to a wider morphologically active zone compared to the smaller vessels.



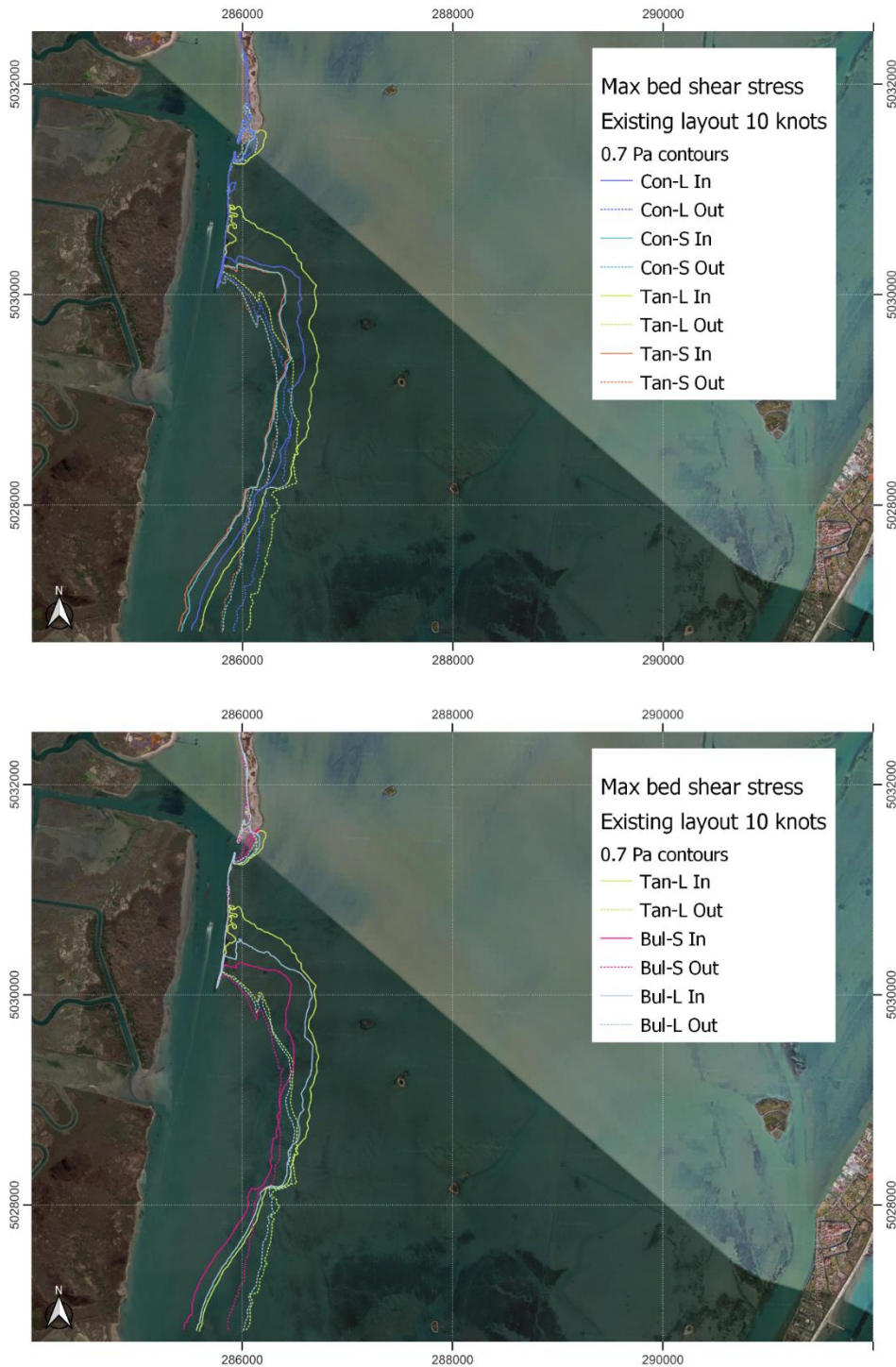


Figure 4.8. Map of maximum bed shear stress 0.7 Pa contour. (Top) Con-S, Con-L, Tan-S and Tan-L. (Bottom) Tan-L, Bul-S and Bul-L. The lines are coloured according to vessel and In-bound/Out-bound direction is marked by Solid/Dotted lines respectively.



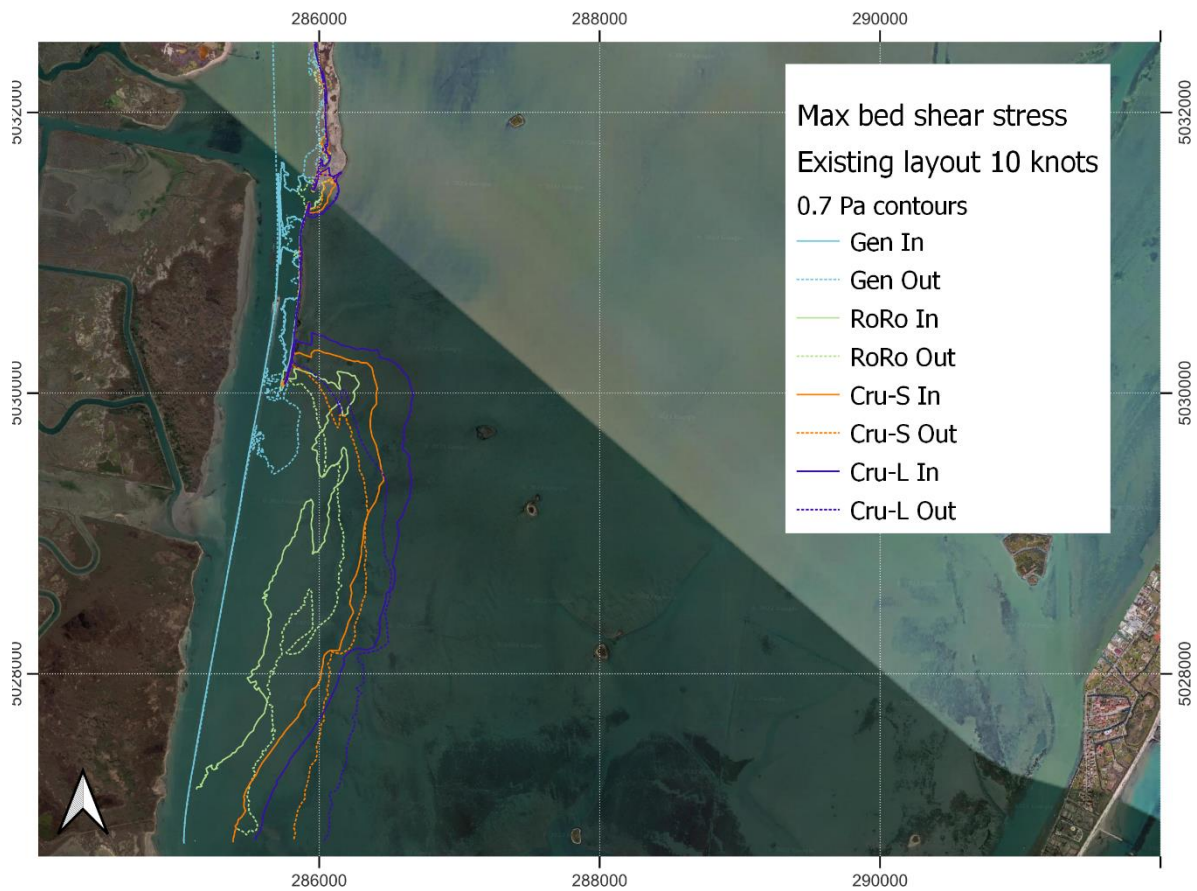


Figure 4.9. Map of maximum bed shear stress 0.7 Pa contour for Gen., RoRo, Cru-S and Cru-L. The lines are coloured according to vessel and In-bound/Out-bound direction is marked by Solid/Dotted lines respectively.

Based on these maps there is also a clear spatial difference between in- and out-bound passages:

- In-bound: The morphologically active zone has a wedge-like shape – the zone widens with increasing distance to the San Leonardo bend until reaching the structures east of the channel. The wedge continues some distance north along the east side of the structures.
- Out-bound: The morphologically active zone has almost constant width from the structures until the San Leonardo bend.

There is very little difference between the 0.7 Pa contours of Con-S and Tan-S whereas there is a clear difference between the contours of Con-L and Tan-L. This is linked to their displacement stencils (the submerged volume of the vessel), see Figure 4.10. Con-S and Tan-S have very similar displacement stencils, whereas Tan-L has a considerably larger displacement stencil than Con-L



thus impacting a larger area. The General Cargo vessel has the smallest displacement stencil of all the modelled vessels and is seen to have a very limited sediment transport related impact on the flats along the channel based on the 0.7 Pa contour.

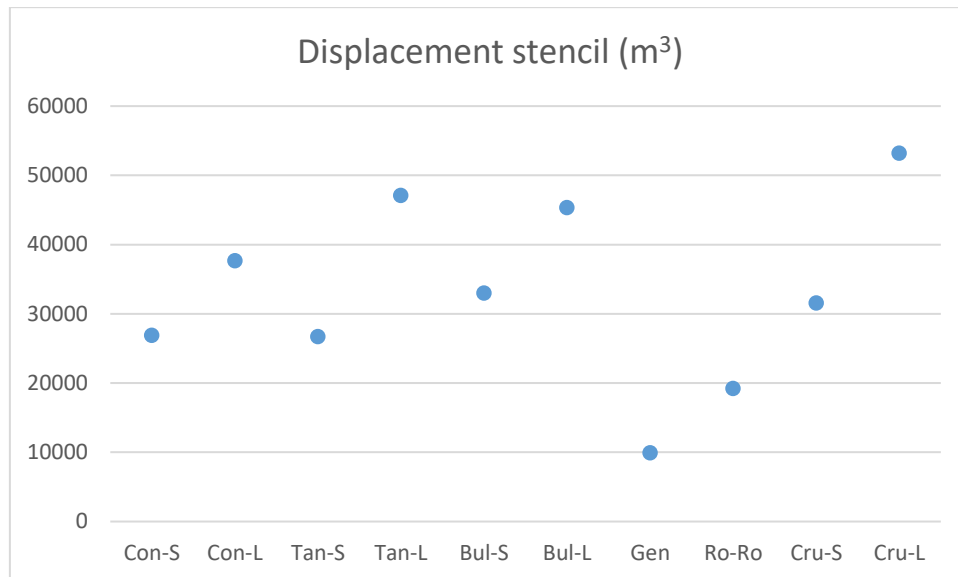


Figure 4.10. Vessel displacement stencils (m³).

Based on the bar charts and maps of 0.7 Pa bed shear stress contours, there appears to be a clear connection between the size of the vessel and the magnitude of the draw down level and hence the size of the morphodynamic zone. In Figure 4.11 a linear regression has been performed for the draw down level (at the 200 m point of Line-2) and 0.7 Pa bed shear stress distance (at Line-2). This regression is valid only for the existing channel layout and 10 knot vessel speed. During the study of the mitigation measures their impact on this regression can be investigated.

At 10 knots with existing channel layout:

- The draw down level 200 m from the channel during in-/out-bound passages increases (becomes more negative) by 0.01 to 0.02 mm per m³ (displacement stencil volume).
- The distance impacted by bed shear stresses above 0.7 Pa at Line-2 increases by about 0.015 – 0.017 m per m³ (displacement stencil volume) during in- and out-bound passages.



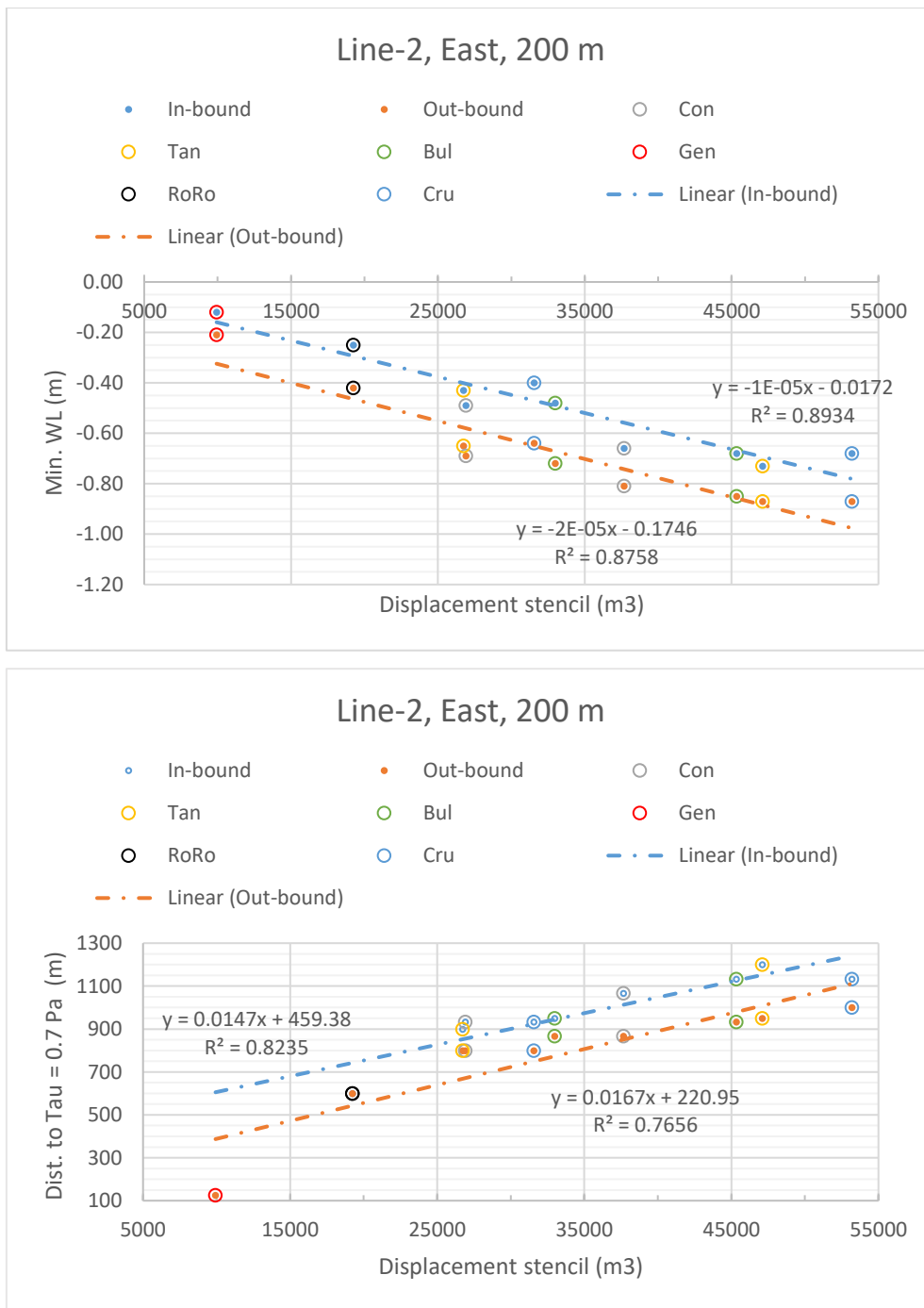


Figure 4.11. Hydrodynamics at Line-2 east 200 m point as function of vessel displacement stencil. Considering existing channel layout and a vessel speed of 10 knots. (Top) Draw down level. (Bottom) Distance from channel until $\tau_{max} = 0.7$ Pa as interpolated from the tables in Appendix A.



4.3 Accumulated bed changes

The accumulated effect of the representative vessel traffic on the erosion/deposition along the channel will be established based on the number of vessels per category following Table 2-20. The number of in- and out-bound passages per year per vessel type is given in Table 4-5. The calculation of the accumulated bed changes, Δz_{tot} , will be calculated as:

$$\Delta z_{tot} = \alpha \sum_{i=1}^{10} N_{in,i} \cdot \Delta z_{i,in} + N_{out,i} \cdot \Delta z_{out,i} \quad \text{Eq. 4.2}$$

Here α represents a scaling coefficient to account for overestimation of erosion levels as identified in Section 3.2.2. The bed level change, Δz_i , is calculated based on the deposited/eroded mass assuming a dry density of 900 kg/m^3 as described in connection with Figure 3.20.

Table 4-5. Number of in- and out-bound passages per year per vessel type of representative traffic.

Abbr. Name	Length percentile	Total no. per year	Weight	No. in-bound	No. out-bound
Con. S	50	1286	0.75	482	482
Con. L	75		0.25	161	161
Tan. S	50	974	0.75	365	365
Tan. L	75		0.25	122	122
Bul. S	50	734	0.75	275	275
Bul. L	75		0.25	92	92
Gen.	50	734	1	367	367
Ro-Ro	50	691	1	346	346
Cru. S	-	60	1	30	30
Cru. L	-	60	1	30	30

The result of the calculation is shown in Figure 4.12 which applies a scale of 1/10. The erosion levels established from literature are in the range 3-6 cm east of the channel and 10-13 cm west of the channel, see Section 3.2.1.



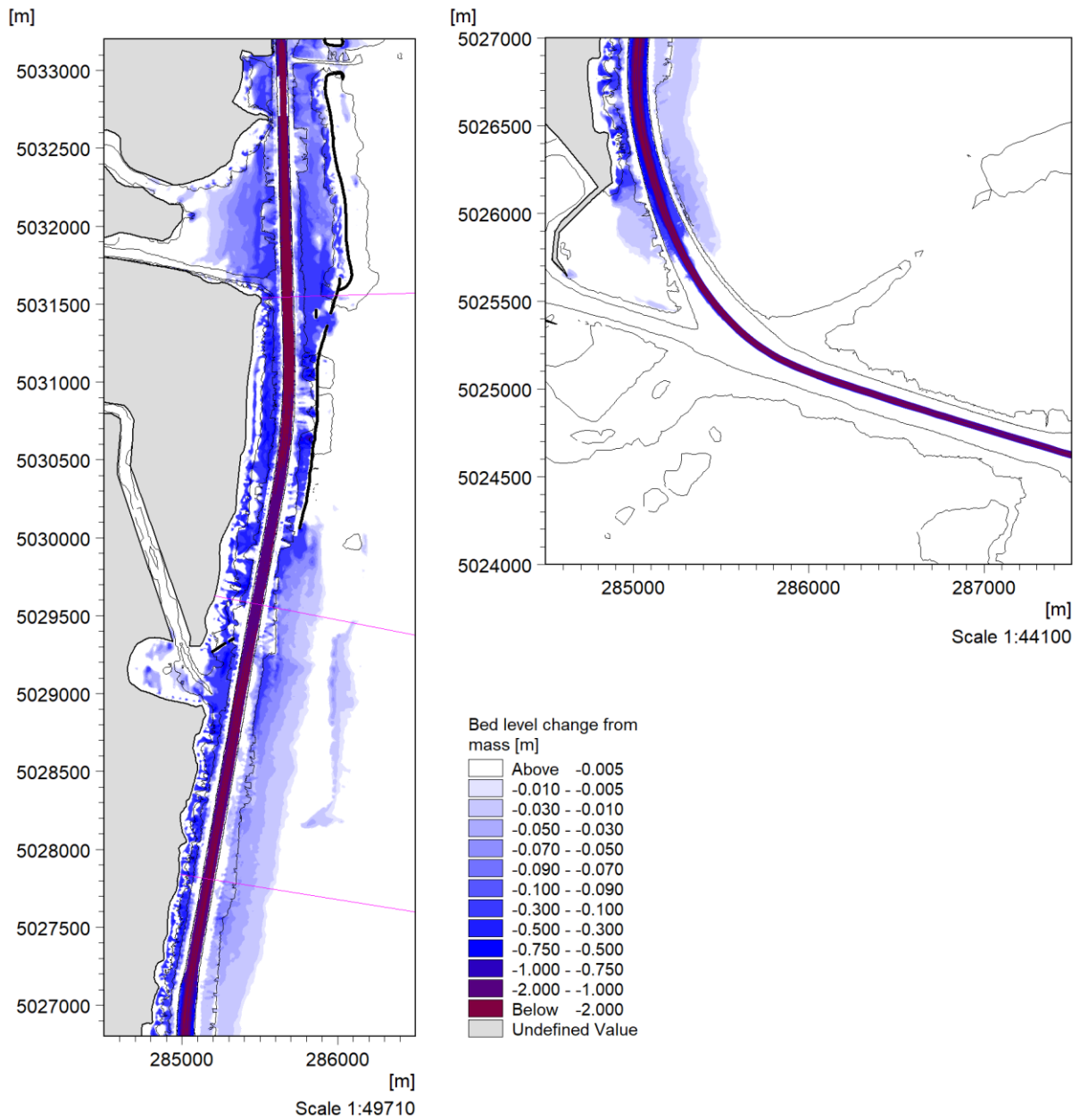


Figure 4.12. Accumulated erosion from modelled vessel traffic. For the sake of clarity, the color legend only shows the erosion.

The scaling of the model results accounts for the uncertainty in terms of bed density and material as well as the fact that the model applies an undisturbed sediment bed in each model run:

- **Bed dry density:** A bed dry density of 900 kg/m^3 has been assumed in the calculation of the bed changes. However, the dry density of the bed material is not known and is likely to vary



across the domain. As mentioned in connection with Figure 3.20 it may be up to about 1,500 kg/m³ on the flats but is likely to be considerably lower than that in areas where the bed gets remoulded e.g., by the vessel generated waves and propeller wash. Using a too small/large bed dry density will lead to over/under-estimation of the bed level changes. A value of ~900 kg/m³ represents material (containing sand and mud) with about 50% sand.

- **Bed material:** Details on the bed material are not known, hence the grain size and thus the amount of deposition is quite uncertain. Though the model matches measured near bed concentrations of suspended sediment about 200 m from the channel, the very fine fraction settles so slowly that it will only reach the bottom of the channel after several hours (~18 hrs) i.e., not within the simulated timeframe. Hence the modelled level of erosion in the channel is likely overestimated as a result hereof. In reality, it is possible that such fine material is not present in the channel but only in the bed material of the flats – no data has however been available to support this model observation.
- **Undisturbed bed:** In each model run, the model is started with an undisturbed bed. An alternative could be to update the bed between each model run. However, this would require more data in terms sediment parameters across the lagoon, along and inside the channel, to get the settling patterns more accurate. Additionally, it would require knowledge on for instance the order between vessels in convoy and the time between the vessels. This would leave a very large number of degrees of freedom that cannot be covered sufficiently by the limited number of simulations in the present scope. Instead, an undisturbed bed is used for simplicity, which means that the vessel generated hydrodynamics always meet a bed containing erodible material – never a starved bed, which may occur in reality. Therefore, the model will be prone to overestimate the erosion levels but will on the other hand give a good spatial picture of the erosive patterns.

The scaled modelled erosion levels on the flats east of the channel is mostly in the range 1 to 8 cm, which matches well with the range established from literature. In some areas the erosion levels on the flats reach above 10 cm east of the channel. This is especially seen in the area where the morphological structures are implemented. Hence these structures protect the flats of the lagoon from the effect of the displacement waves, but as consequence of the more restricted channel, the channel slopes are eroded more heavily in the model compared to the modelled changes on the eastern flats. This is also the reason why the modelled erosion levels are higher on the western side of the



channel compared to the eastern side – the salt marsh shore functions like a natural morphological structure restricting the channel and thus the draw down caused by the moving vessel cannot spread out. Instead, a larger more localized (thus more erosive) draw down is generated. The model does however overestimate the erosion levels west of the channel – reaching about 10-30 cm sometimes more than 50 cm. In the model, the salt marsh is modelled as dry 'solid' land. In reality, the salt marsh can be flooded and will likely also have a dissipative effect on the incoming waves. As such the modelled overestimation of the erosion levels west of the channel is likely linked to an overestimate of the restrictive nature of the west side land boundary.

It is noted that the modelled erosion levels do not account for consecutive vessel passages. When a consecutive vessel enters the channel, it will encounter relatively higher suspended sediment concentrations and the sediment bed will have already been disturbed. As such the draw down wave may be able to pull relatively more suspended matter into the channel and away from the tidal flats. However, on the other hand the leading wave (travelling ahead of the vessel) will generate a push towards the tidal flats – opposite the effect of the draw down. Based on the PoV database 75%/25% of the passages take place with more/less than 10 minutes separation and the average separation time is about 20 minutes. Most of the suspended sediment (sand and silt fraction) settles after ~5-10 minutes (based on calibration results provided by Scarpa et al 2019). Hence generally most passages occur with sufficient separation time for the sandy and silty sediment to have settled and as such the single vessel approach is not an unreasonable assumption when it comes to assessing the erosion though the initial sediment concentration encountered by a consecutive vessel will be higher than that encountered by a single passage.

To get an impression on the relative importance of the large vessels Figure 4.13 provides a map of the ratio between modelled erosion/deposition from large vessels (Con-L, Tan-L, Bul-L and Cru-L) and that of the total traffic. It should be noted that this ratio is made between positive and negative numbers representing deposition and erosion respectively. Hence the ratio is positive when taken between two negative and two positive numbers but becomes negative when only one of the numbers are positive i.e., when erosion and deposition areas do not match up in terms of location. A possibility which is expected to occur in some locations e.g., since the larger vessels will cause erosion further away from the channel compared to the smaller vessels.



The map shows that the large vessels explain in the range 20%-60% of the modelled erosion along the channel – even though the modelled large vessels represent only about 17% of the total number of modelled events. Further away from the channel, where deposition can take place considering the smaller vessels and the total erosion is therefore smaller relatively speaking, the ratio gets higher than 1.0.

Comparing the modelled draw down levels at the 200 m point of Line-2, see Table 4-6, the larger vessels cause draw down levels that are 20% to 34% larger than the corresponding smaller vessel. This matches reasonably well with the range depicted in Figure 4.13 in this area.

Table 4-6. Draw down level ratio (average of in- and outbound) at 200 m point east of channel at Line-2.

Con-S/Con-L	Tan-S/Tan-L	Bul-S/Bul-L	Cru-S/Cru-L
0.80	0.67	0.78	0.66



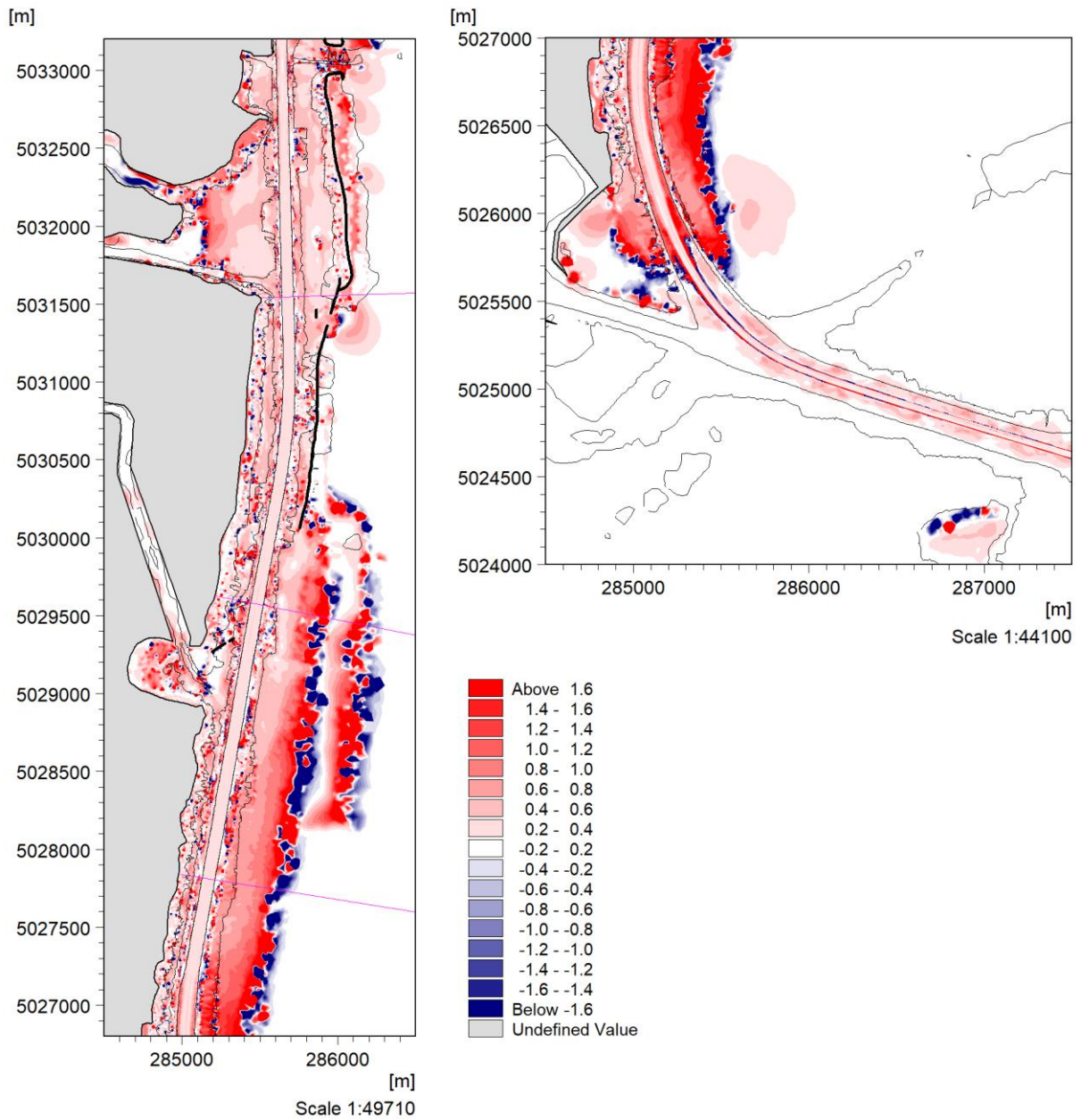


Figure 4.13. Ratio of deposition/erosion from large vessels relative to that of the total traffic.



5 DISPLACEMENT WAVES RELATIVE TO AMBIENT FORCING

The dynamics of the sediment plumes generated by passing vessels so far simulated do not account for the effects caused by natural forcings acting on the lagoon.

Natural forcings in such environment play, in fact, the twofold role of dispersing the sediment plume due to, primarily, tide generated currents and, on the other hand, are responsible for seabed erosion processes and sediment suspension generated by wind driven waves.

In this context it is relevant to gain an insight into the role each process may have in relation to the lagoon sediment budget. To achieve this, the 3D model so far described was forced by wave dynamics. To allow this, the passing vessel related dynamics were turned off from the model settings. A wave field database for the entire year 2020 was produced during phase 1 of the present study and it is described in the document “002-*Meteomarine and hydrogeological characterization of Venice Lagoon*” [14]. An intense (with low frequency of occurrence) and a frequently occurring sea state were simulated as representative events for describing sediment dynamics generated by waves. In doing so, a direct comparison between the anthropogenic and natural cause of seabed erosion (i.e., passing vessels vs wind driven waves respectively) can be carried out.

The influence of natural forcing on the sediment plumes dispersion computed by the two 3D models was assessed by making use of the 2D Hydrodynamics model developed during phase 1 and included in the same document [14] describing the wave database. The 2D model is capable of reproducing flow patterns in the lagoon environment generated by natural forcing such as incoming tides through the three lagoon inlets and wind driven currents. The key factor for the sediment plume dispersion is, in fact, the flow dynamics associated to the general circulation patterns in the lagoon.

To allow seamless coupling of the 3D produced output to the 2D model, the sediment concentrations generated by the two 3D models at different vertical layers have been integrated over the water column to obtain depth averaged concentrations. It must be noted that, in doing so, the mass budget along the water column is preserved although information on the single sediment concentration along the different layers is no longer accessible.

For the 3D model simulating the effect of passing vessels, different concentration plumes were generated for inbound and outbound journeys, making the analysis dependent on the choice thereof. To overcome this, the 75-th quantile of the depth averaged concentrations was provided as input to the 2D model. It must be noted that the application of this approach may lead to an overestimation of the total mass in suspension within the modelling domain, thus to an increase of sediment load leaving the lagoon during ebbing tides.



For both model configurations, the fate of the sediment plumes for the three fractions was assessed in terms of total mass of suspended sediment leaving the lagoon during a typical tidal cycle.

It must be noted, moreover, that the focus of this analysis is not to compute the exact sediment budget of the lagoon under the action exerted by natural forcings, but rather to provide a way of comparison between the effects on sediment dynamics generated by passing vessels in relation to the wave action.

In this regard, it is worth mentioning, that the 3D sediment model forced by wave field was not specifically calibrated for sediment erosion and dispersion, but it rather uses similar settings of the 3D model used to simulate the passing vessels.

5.1 Transport and fate of the vessel-induced sediment plume

Three types of vessels were considered in this analysis: a typical small container, a small and large tanker. The vessels were chosen as representative ends of the spectrum encompassing frequently passing ships causing moderate impact on the sediment resuspension and less frequent passing ships generating larger stir-up effects on the seabed sediments.

The concentrations of the three sediment fractions computed by the 3D model simulating the passing vessels had been averaged over the water column depth and consumed by the 2D model as initial conditions.

The sediment resuspension across the water column is bound in space and time to the vessel passage thus, depending on its position, the sediment plume of larger concentrations may be generated in an area distant from the Malamocco mouth leading to an underestimation of the sediment leaving the lagoon under natural forcings. In this regard, it must be noted that the maximum vessel travelling time considered in this analysis is about 1 hr, which represents approximately 16.7% of an ebbing tide emi-cycle which is the main mechanism responsible for the sediment flush-out effect.

To overcome this, the 75th quantile of the total suspended sediment for the three fractions computed by the 3D model along the entire vessel route is calculated and passed to the 2D depth-integrated model as water column sediment concentration initial conditions. It is worth mentioning that, using a 75th quantile may result in an overestimation of the total suspended sediment mass in the computational domain, to this end this approach is to be considered conservative in relation to the assessment of the total volume of sediment leaving the lagoon through the Malamocco mouth.

The seabed in the 2D model is treated as a non-erodible floor characterized by hard mud associated to large values of critical shear stress. The incoming sediment flux through the three inlets and from other sources



(such as rivers) are neglected, hence no additional supply of sediment is accounted for during the simulation time other than the three fraction concentrations provided as initial conditions.

The 75th quantile of sediment concentrations shows a moderate spatial variability between an inbound and outbound vessel trip, with a sediment mass budget, on average, in the range of 1-10% in excess for the inbound trips with respect to the outbound ones. In regard to this analysis, only inbound trips were considered.

In terms of mass budget, fraction n°3 represents the largest sediment load accounting for a 68 % of the total sediment in suspension, followed by fraction n°2 (22%) and fraction n°1 (10%).

The 2D model was run for a full tidal cycle starting from mid-ebb tide when the maximum outgoing currents are expected. In general, the same plume dynamics are observed irrespectively of the type of vessel simulated. Figure 5.1 to Figure 5.3 show that most of the suspended sediment (about 75%) settles within a full tidal cycle.

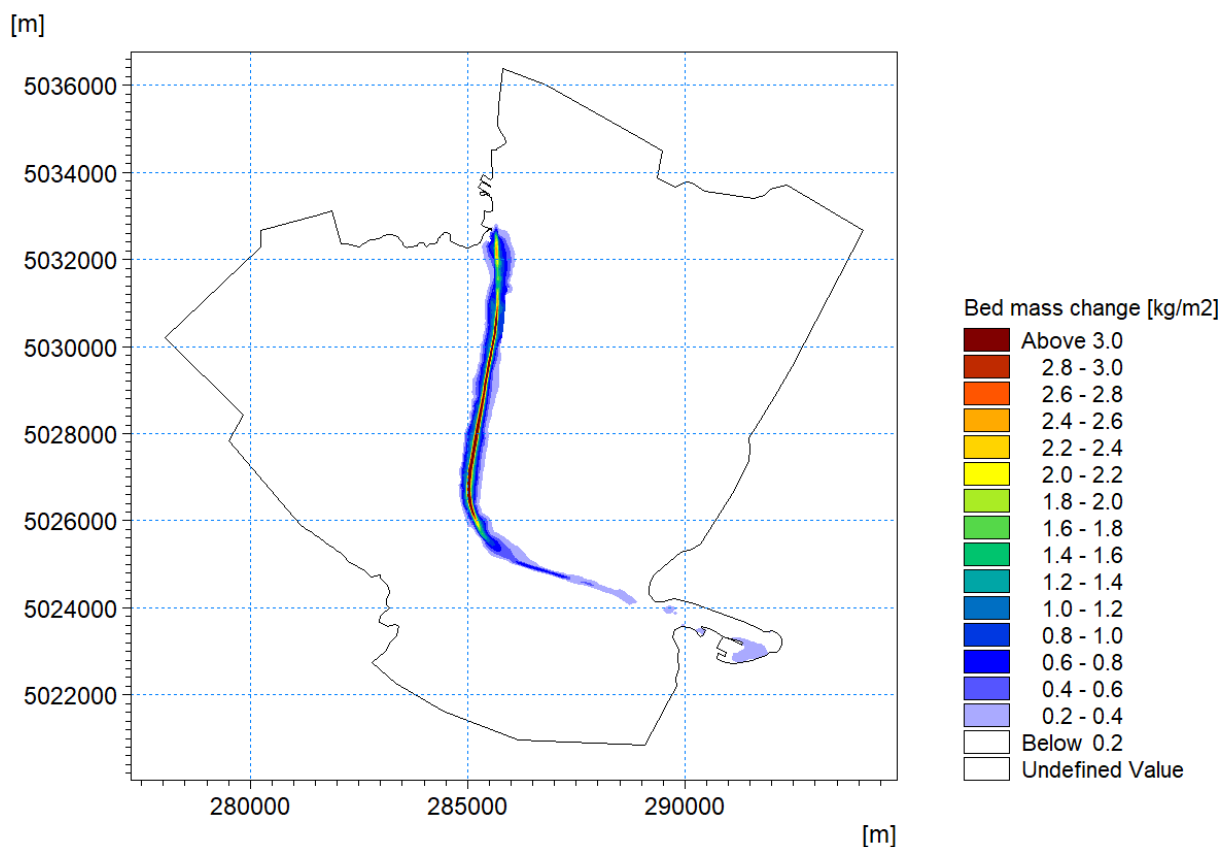


Figure 5.1. Total sediment mass settled to the seafloor after a full tidal cycle (12 hours). Passing vessel: small container (Con-S).



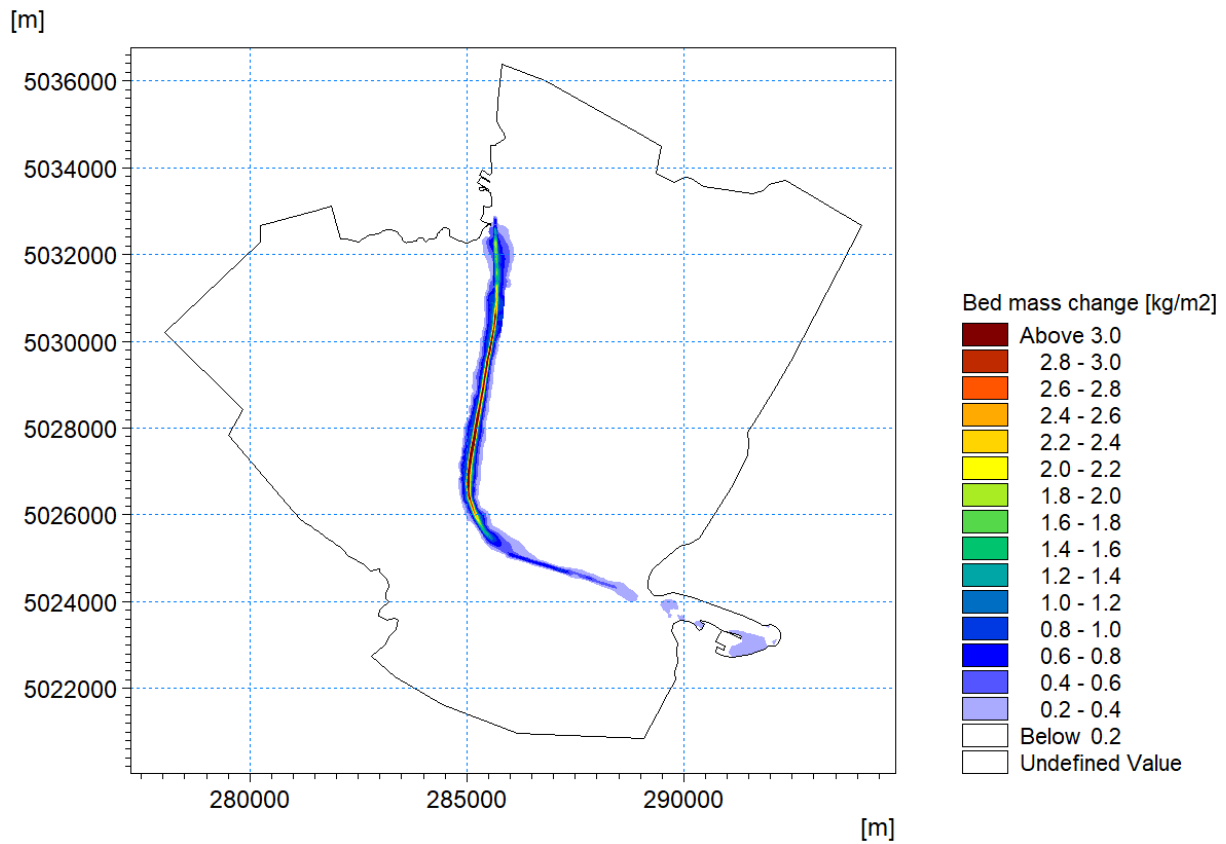


Figure 5.2. Total sediment mass settled to the seafloor after a full tidal cycle (12 hours). Passing vessel: small tanker (Tan-S).



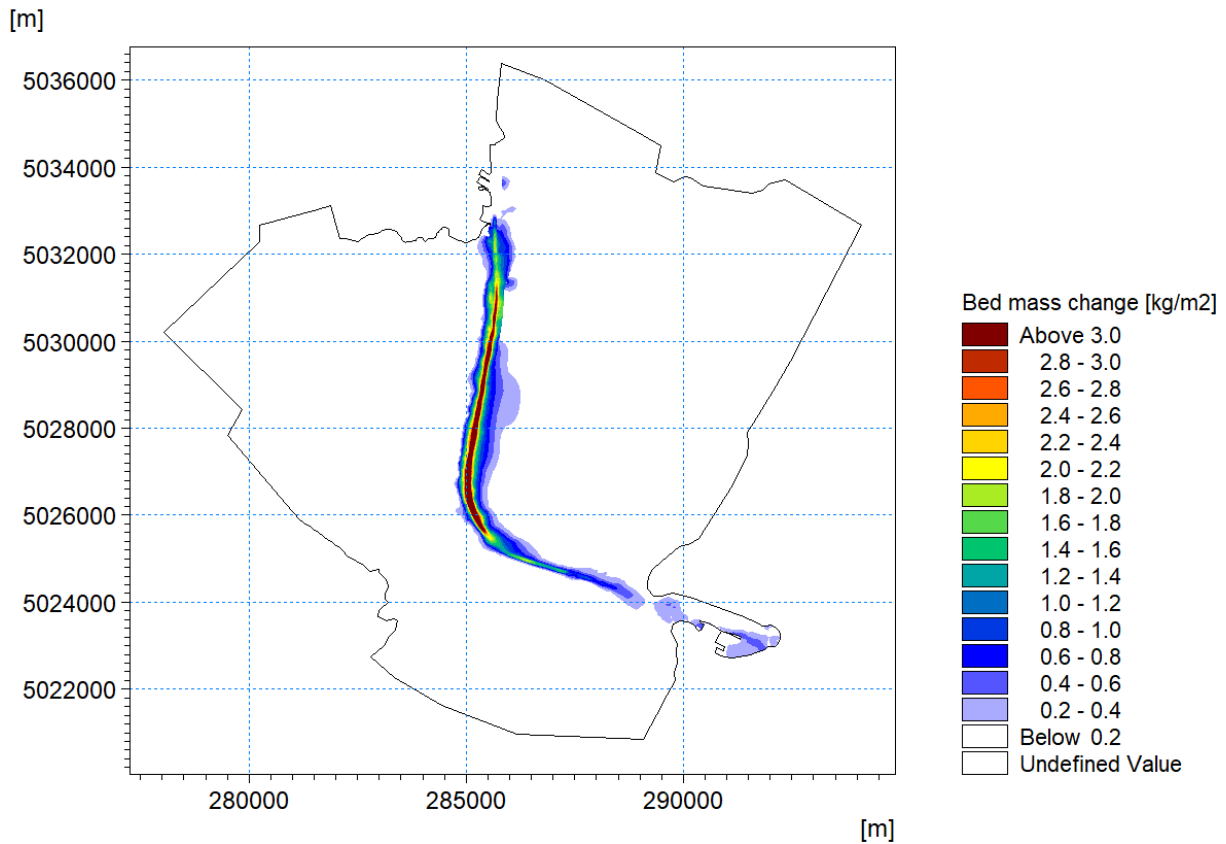


Figure 5.3. Total sediment mass settled to the seafloor after a full tidal cycle (12 hours). Passing vessel: small tanker (Tan-L).



The sediment mass leaving the computational domain (through the Malamocco mouth) during the tidal cycle is shown in Figure 5.4 to Figure 5.6.

The sediment fraction n°3 is characterized by the finest grain size (i.e. $d_{50} = 15 \mu\text{m}$) corresponding to smaller settling velocity followed by increasing falling velocities for fraction n°2 and fraction n°3. Decreasing settling velocity are associated with increasing plume dispersion and travelling time in suspension. Figure 5.4 to Figure 5.6 show that a complete termination of the sediment transport dynamics through the Malamocco mouth is expected after about 1 hour and 20 minutes for the coarser grain size (i.e. fraction 1 corresponding to $d_{50} = 100 \mu\text{m}$) followed by approximately 4 hours for the fraction n°2 (i.e. grain size $d_{50} = 40 \mu\text{m}$) and approximately 9 hours for the finer fraction n°3.

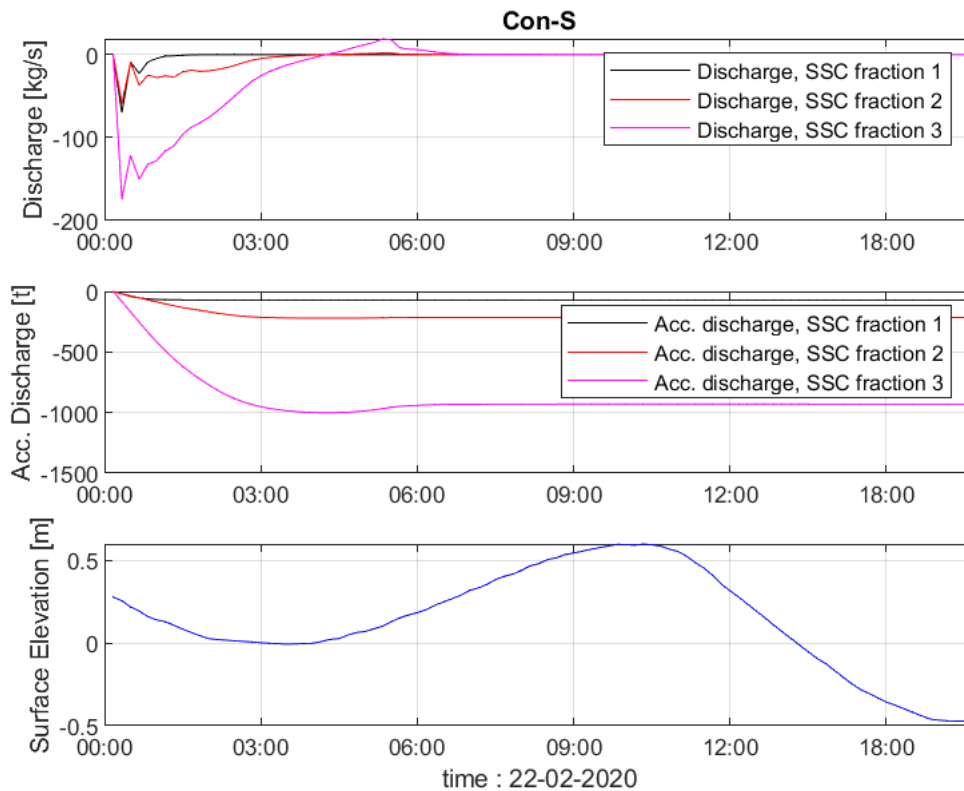


Figure 5.4. Suspended Sediment discharge (top plot) and accumulated discharge (mid plot) through the Malamocco mouth. Passing vessel: small container (Con-S). Negative discharge and accumulated discharge values are associated to sediment leaving the lagoon.



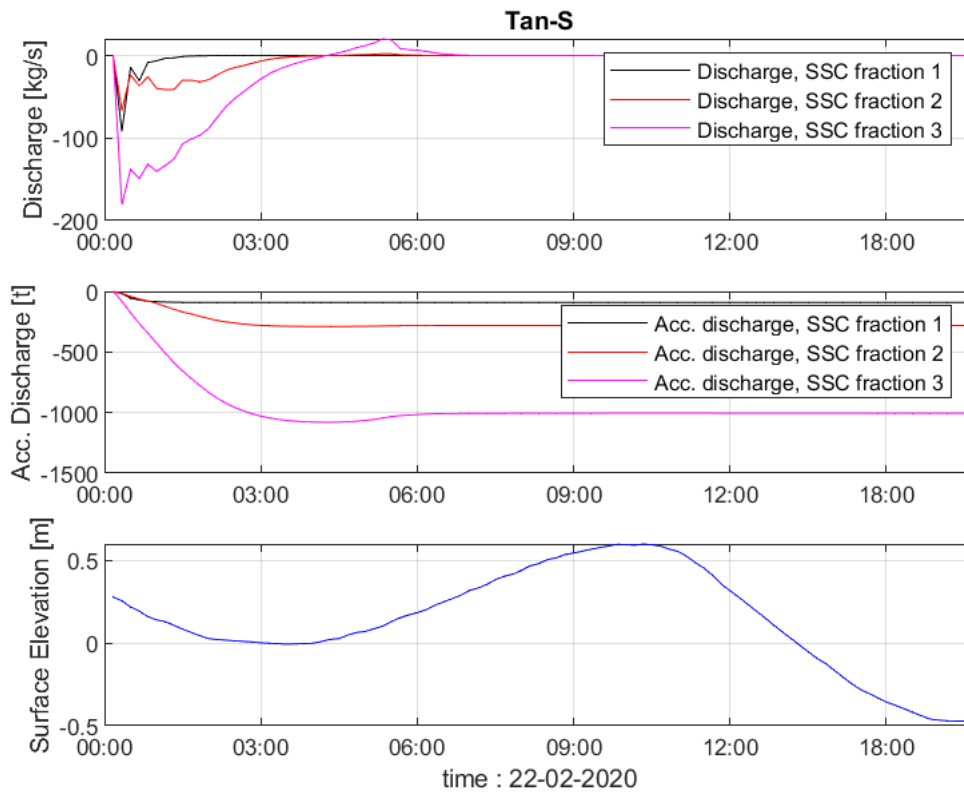


Figure 5.5. Suspended Sediment discharge (top plot) and accumulated discharge (mid plot) through the Malamocco mouth. Passing vessel: small tanker (Tan-S). Negative discharge and accumulated discharge values are associated to sediment leaving the lagoon.



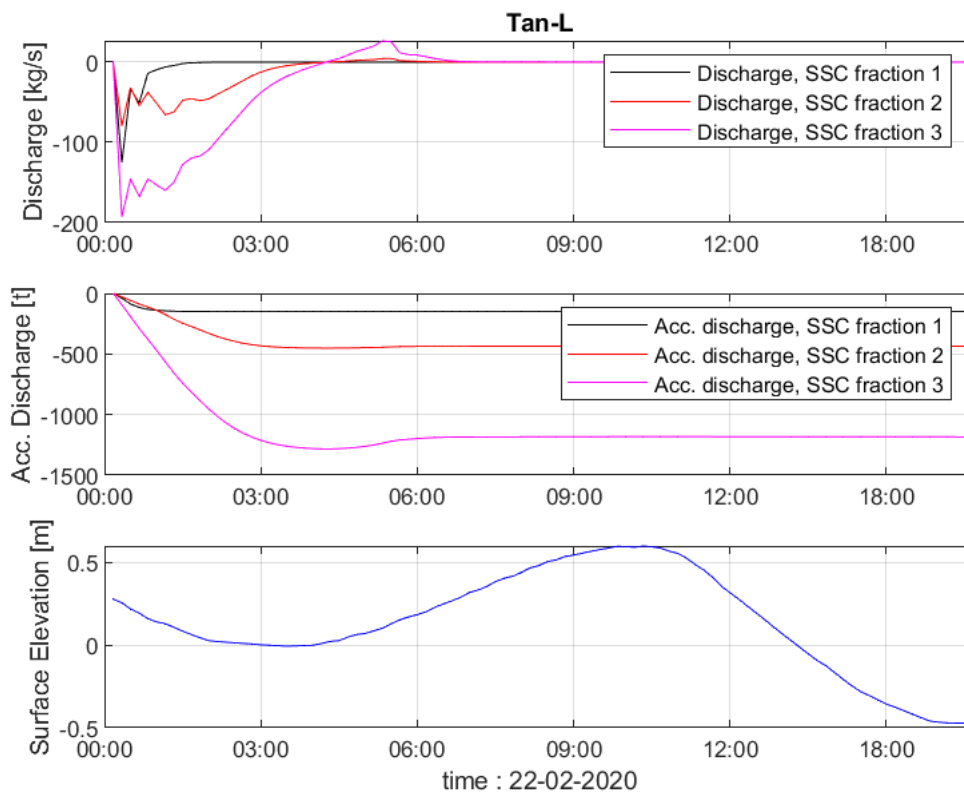


Figure 5.6. Suspended Sediment discharge (top plot) and accumulated discharge (mid plot) through the Malamocco mouth. Passing vessel: large tanker (Tan-L). Negative discharge and accumulated discharge values are associated to sediment leaving the lagoon.

5.2 Transport and fate of the “natural forcing generated” sediment plume

The influence of waves on the lagoon seabed erosion mechanisms and resulting sediment resuspension is investigated by means of a 3D model. The wave forcing was derived from a comprehensive database of sea states inside the lagoon produced during project phase 1 and derived by wave hindcast modelling (see [14]).

The bed shear stress acting upon the sea-bottom is directly correlated to the current speed generated by the wave action, in this regard the choice of the sea state simulated largely affect the level of turbidity expected in the lagoon.



Two representative sea states generated by north-easterly wind system (i.e. Bora) were simulated, one energetic and rather rarely occurring sea state and a more frequent one. Figure 5.7 to Figure 5.8 show the significant wave height values reached in the lagoon at the peak of the two sea states.

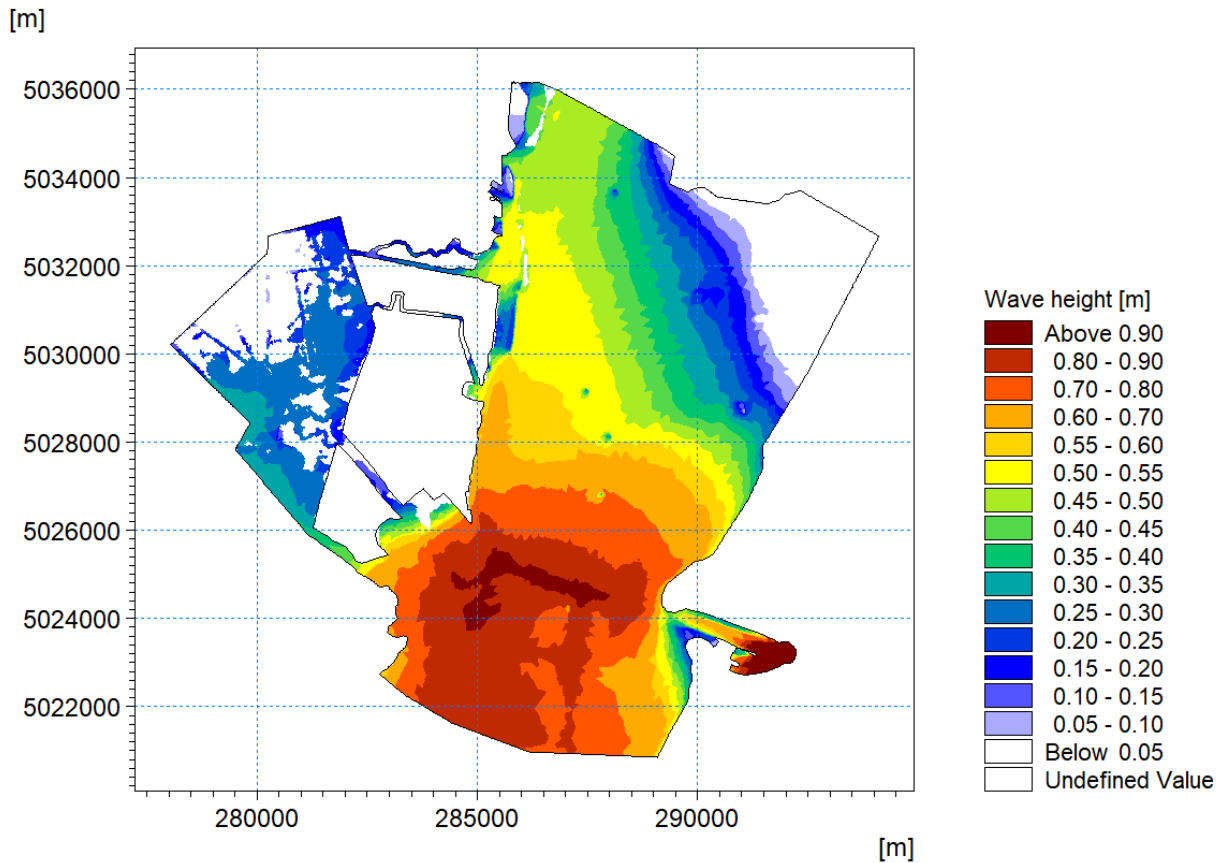


Figure 5.7. Map of significant wave height (H_{m0}) for a representative infrequent energetic sea state.



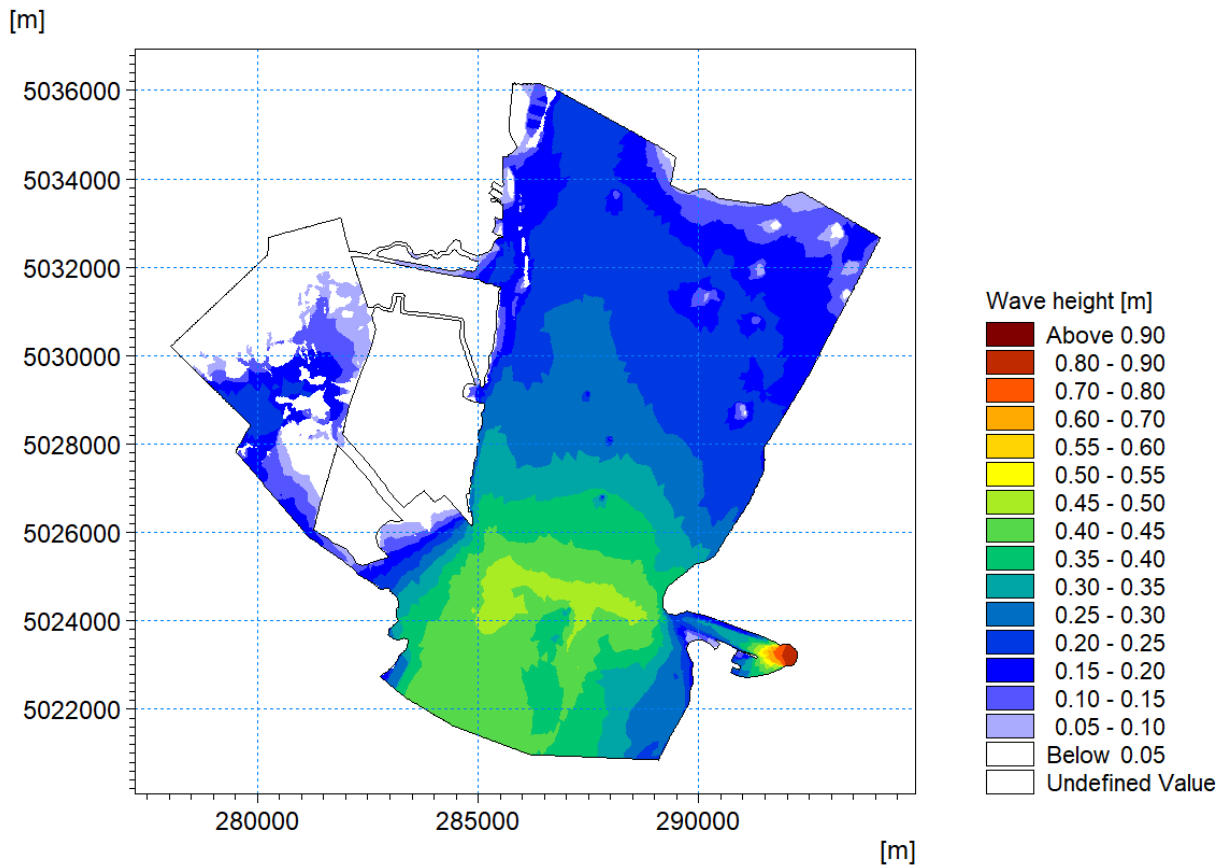


Figure 5.8. Map of significant wave height (H_{m0}) for a representative frequent sea state.

Maps of maximum (99.9-th quantile) bed shear stress reached at each computational domain node at any time for the simulated sea states are illustrated in Figure 5.9 and Figure 5.10. The levels of shear stress associated to the more energetic wave field are of comparable magnitude to the bottom stress produced by Kelvin waves generated by passing vessels and of lower relevance when compared to vessel displacement waves, although potentially covering a much wider area of the lagoon. Expectedly, lower values of bed shear stresses are observed in deeper navigation and natural lagoon channels.

More frequent and less energetic sea states show a little impact to sea bottom in terms of total stress leading in turn to reduced seabed erosion and water turbidity.



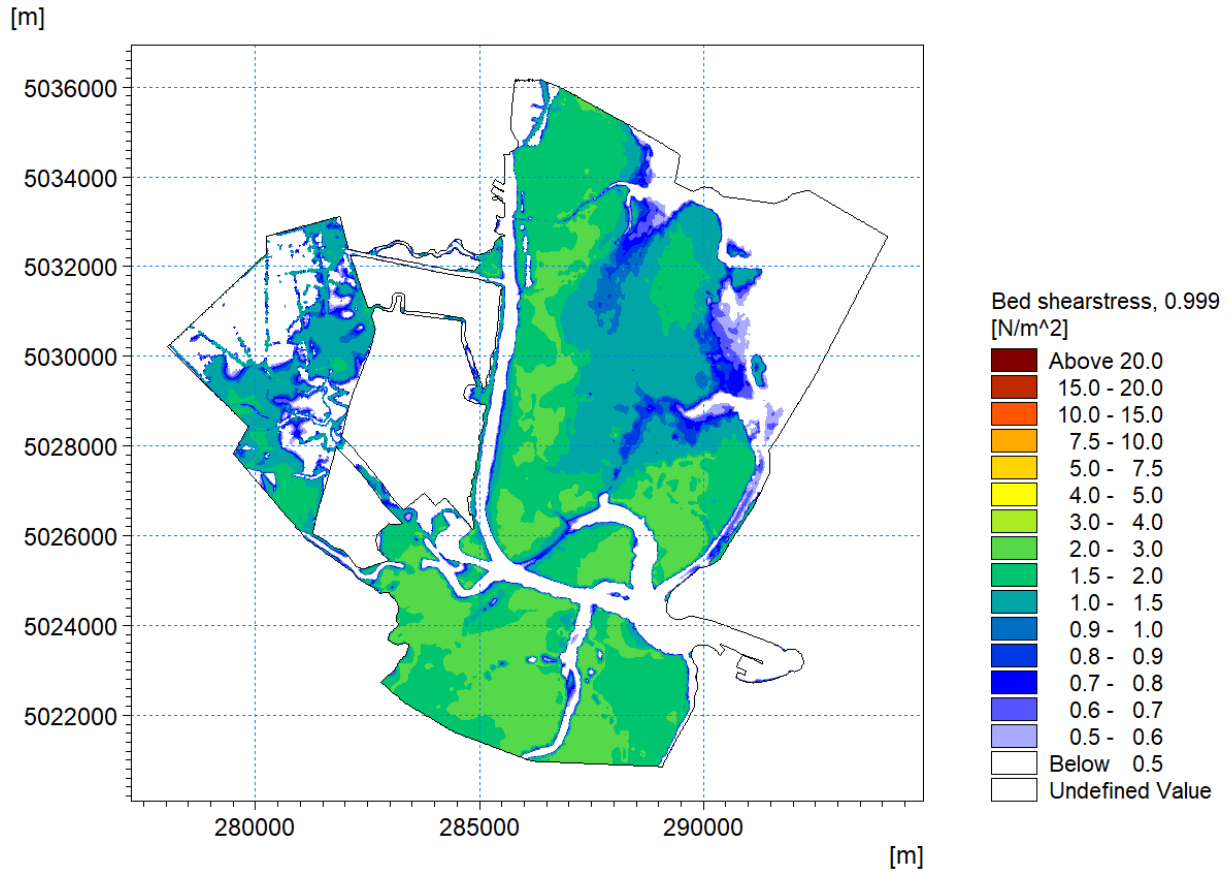


Figure 5.9. Map of maximum (99.9-th quantile) bed shear stress (BSS) associated to the infrequent energetic sea state.



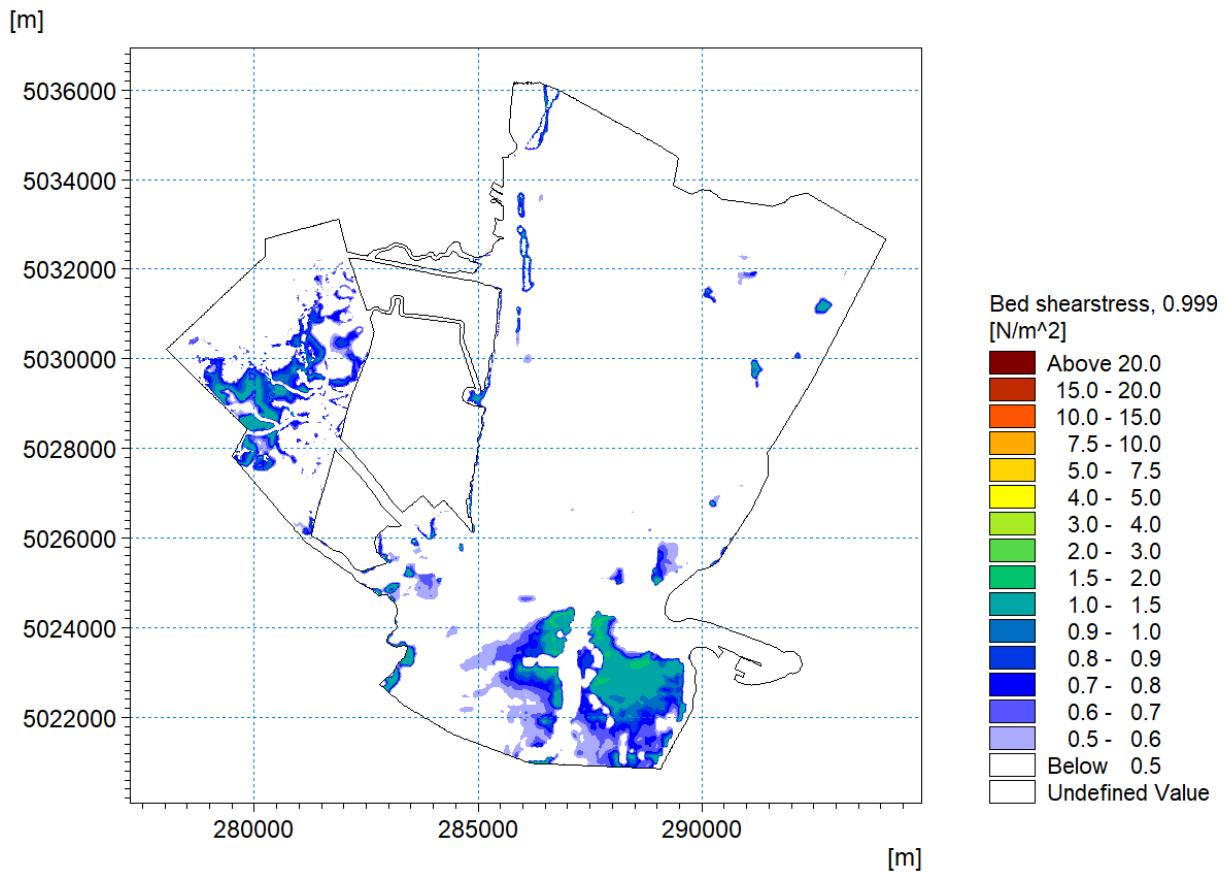


Figure 5.10. Map of maximum (99.9-th quantile) bed shear stress (BSS) associated to the representative frequent sea state.

In agreement with the analysis described in section 4, the concentrations of the three sediment fractions computed by the 3D model had been averaged over the water column depth and provided for the 2D model as initial conditions. The process is repeated for both simulated sea states.

Figure 5.11 and Figure 5.12 show the results of the depth-averaging operation for the suspended sediment concentration (SSC) obtained as the summation of the three sediment fractions.

The distribution of the three sediment fractions varies slightly between the two wave scenarios simulated. For the more energetic sea state case study fraction n°1 accounts for circa 38% of the total mass of sediment in suspension provided as initial condition for the 2D model, followed by fraction n°3 with circa 36% and fraction n°2 with circa 26%; whereas for the less energetic sea state scenario



fraction n°3 accounts for a larger value of the sediment mass in suspension (ca. 41%) followed by similar mass values for fraction n°1 and n°2 with a 30% and 31% respectively.

The maximum values of depth averaged SSC reached in the lagoon during at the peak of the more energetic sea state are in the range of 100-500 mg/l on shallow tidal flats with lower levels of concentration below 5-10 mg/l observed in the Malamocco-Marghera, deeper natural channels and area less exposed to waves. For more frequent and less energetic sea states the turbidity level drops drastically to values below 10mg/l for almost the entirety of the lagoon.

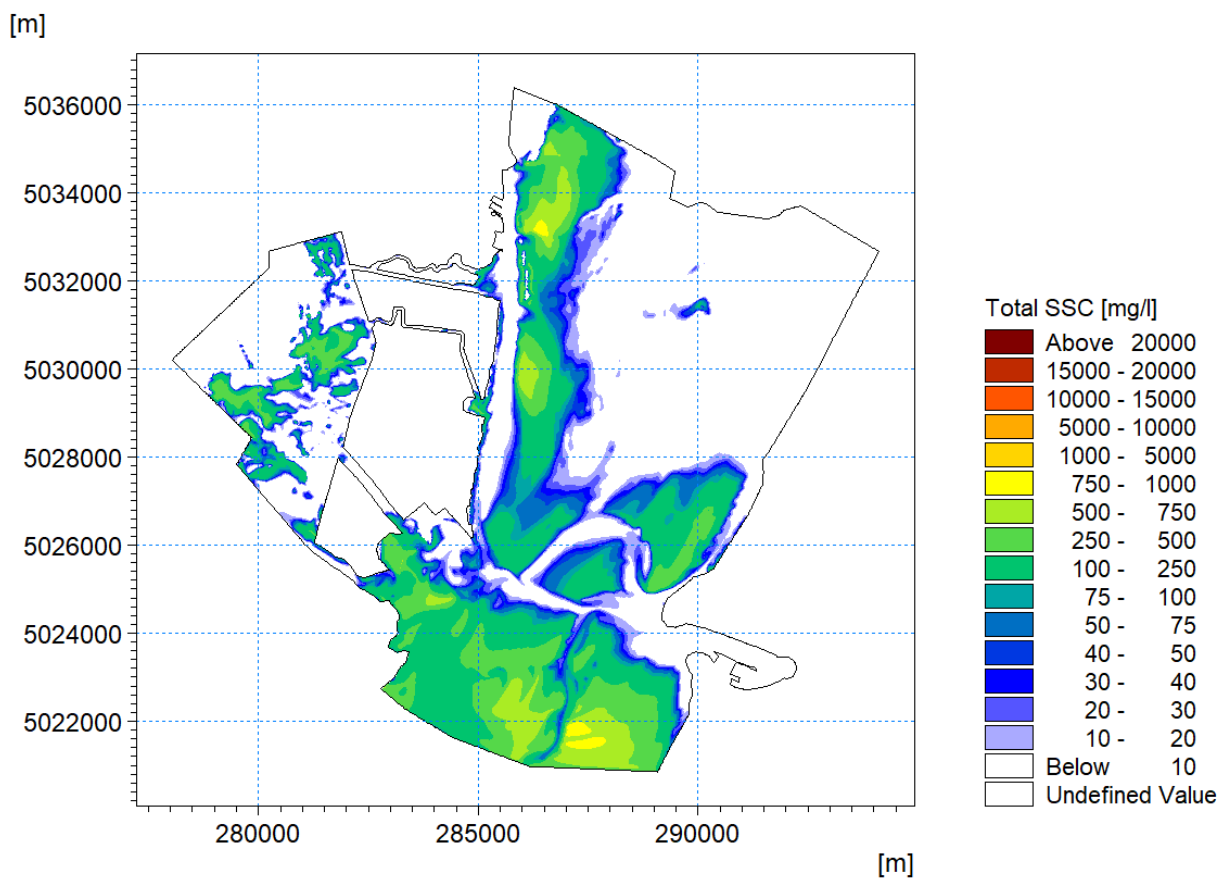


Figure 5.11. Map of the depth averaged suspended sediment concentration (SSC) generated at the peak of the representative and infrequent energetic sea state.



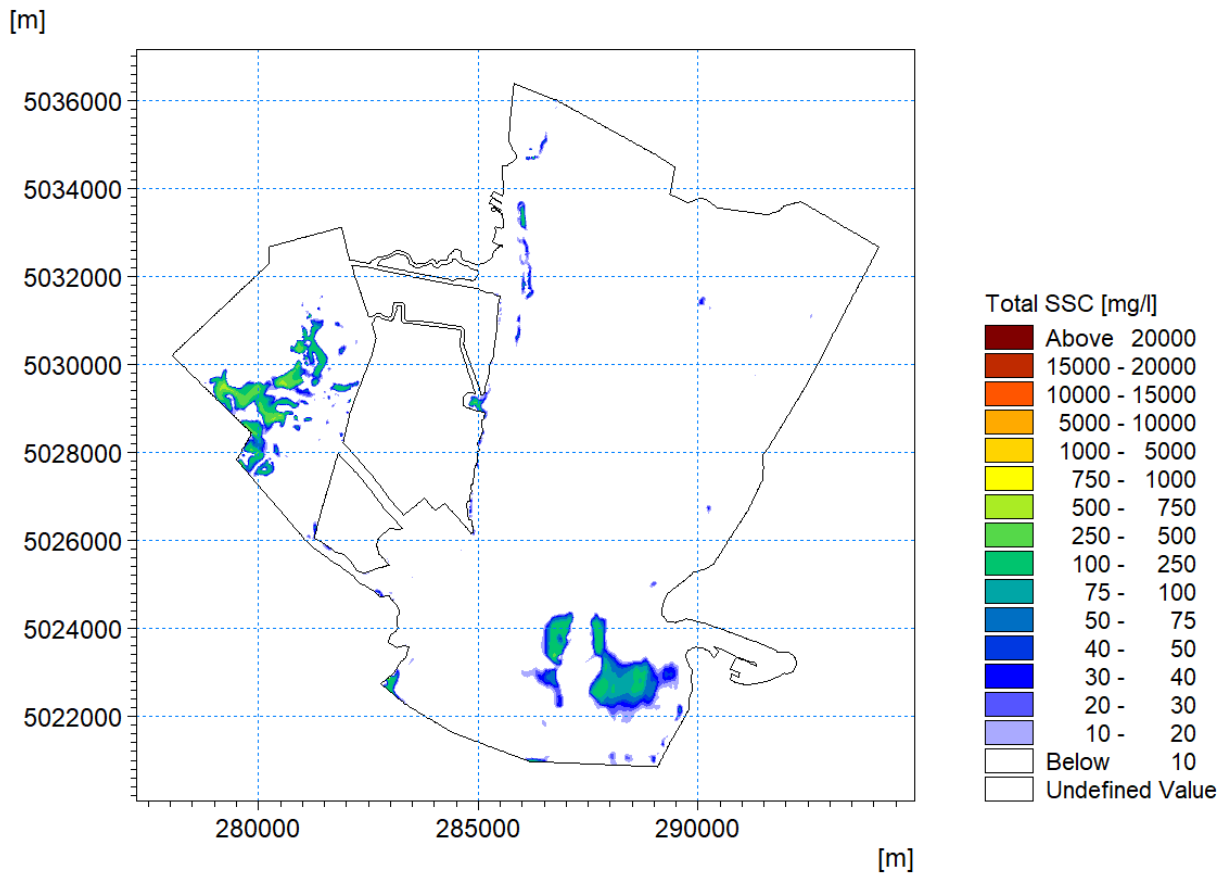


Figure 5.12. Map of the depth averaged suspended sediment concentration (SSC) generated at the peak of the more frequent and less energetic sea state.

In analogy with the dynamics described for the sediment suspension generated by passing vessels, the entirety of the sediment mass provided as initial condition to the 2D model (nearly 100 %) settles to the sea floor within a full tidal cycle. Figure 5.13 and Figure 5.14 show the total amount of sediment deposited at the end of tide cycle (12 hours) for the two wave scenarios simulated. The notable difference in settled mass values derived from the two simulated scenario is correlated to the large difference in SSC initial conditions between the two study cases.



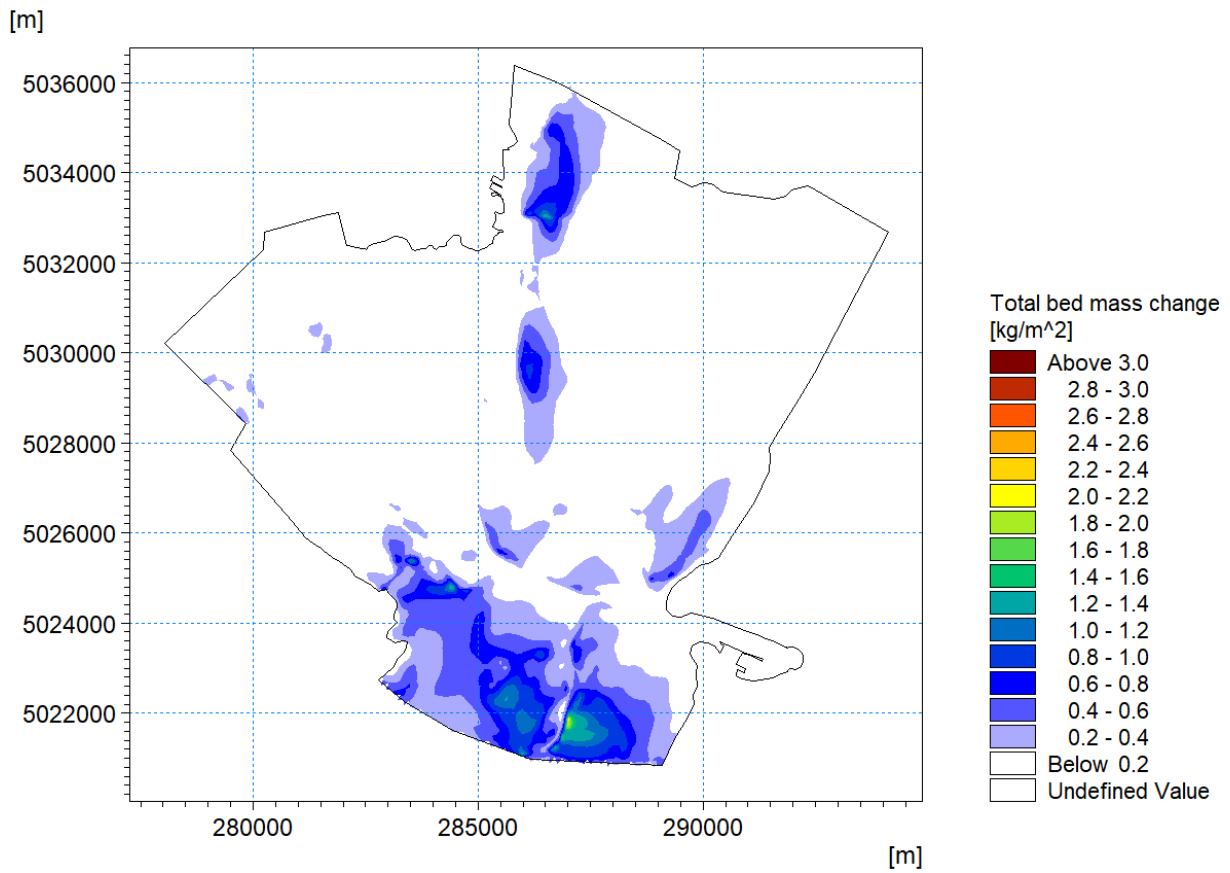


Figure 5.13. More energetic sea state: total sediment mass settled to the seafloor after a full tidal cycle (12 hours).



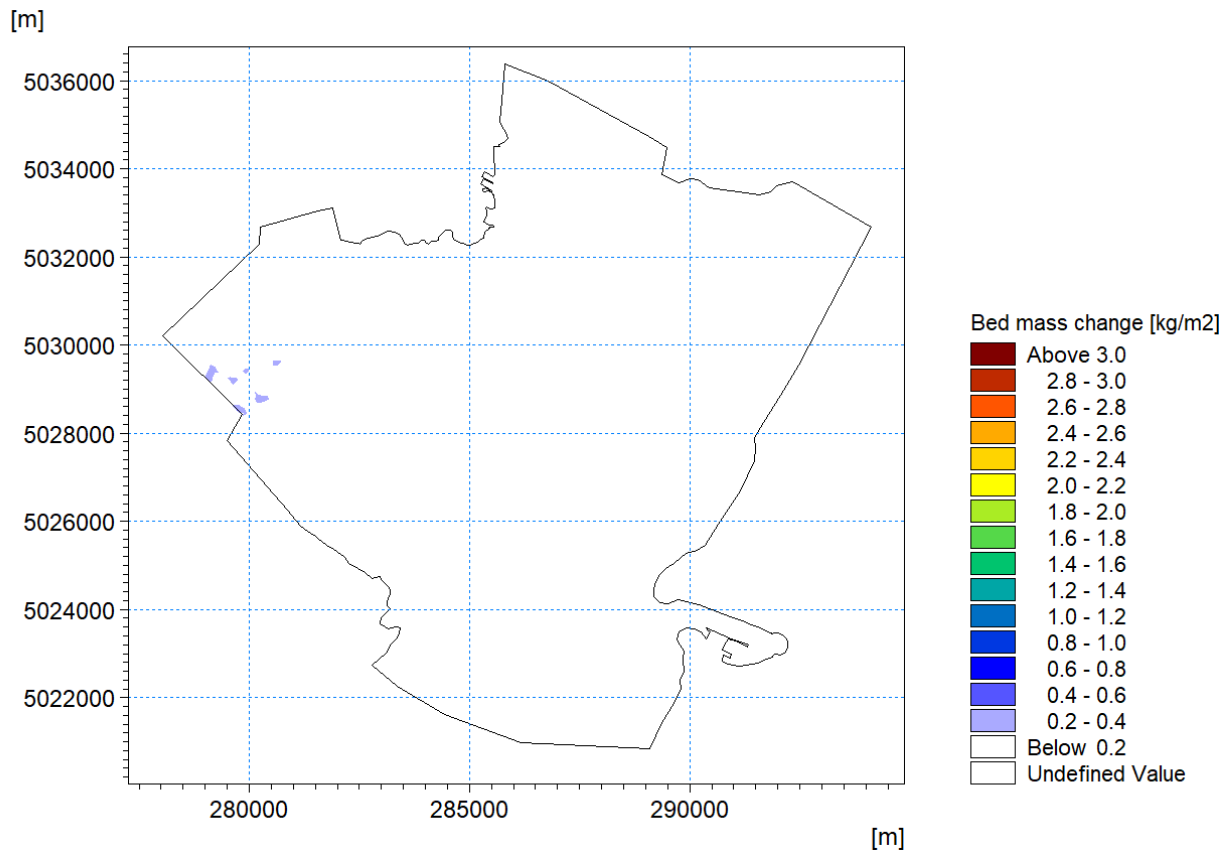


Figure 5.14. *Less energetic sea state: total sediment mass settled to the seafloor after a full tidal cycle (12 hours).*

The portion of sediment mass that does not settle on the seabed within a full tidal cycle travels outside the lagoon (i.e., the computational domain). Figure 5.15 and Figure 5.16 show a complete termination of sediment dynamics through the Malamocco mouth after about 7 hours for the two finer fractions n°2 and n°3. Most of the mobilized fraction n°1 sediment re-settles rather quickly on the sea floor resulting in a negligible sediment flux through the Malamocco mouth.

Regardless the type of passing vessel and wave scenario simulated, a few common differences can be observed between the sediment flux curves describing the rate of mass discharge through the Malamocco mouth. Typically, the mass flux carrying the sediment plume generated by the passing vessel is initiated at an earlier stage (nearly instantly) with respect to the sediment plume caused by the wave action which reaches the lagoon mouth after about 1 hour from the mid-ebbing tide. The



difference in behaviour must be attributed to the larger flow velocity reached in the Malamocco-Marghera acting as a “sediment pump”.

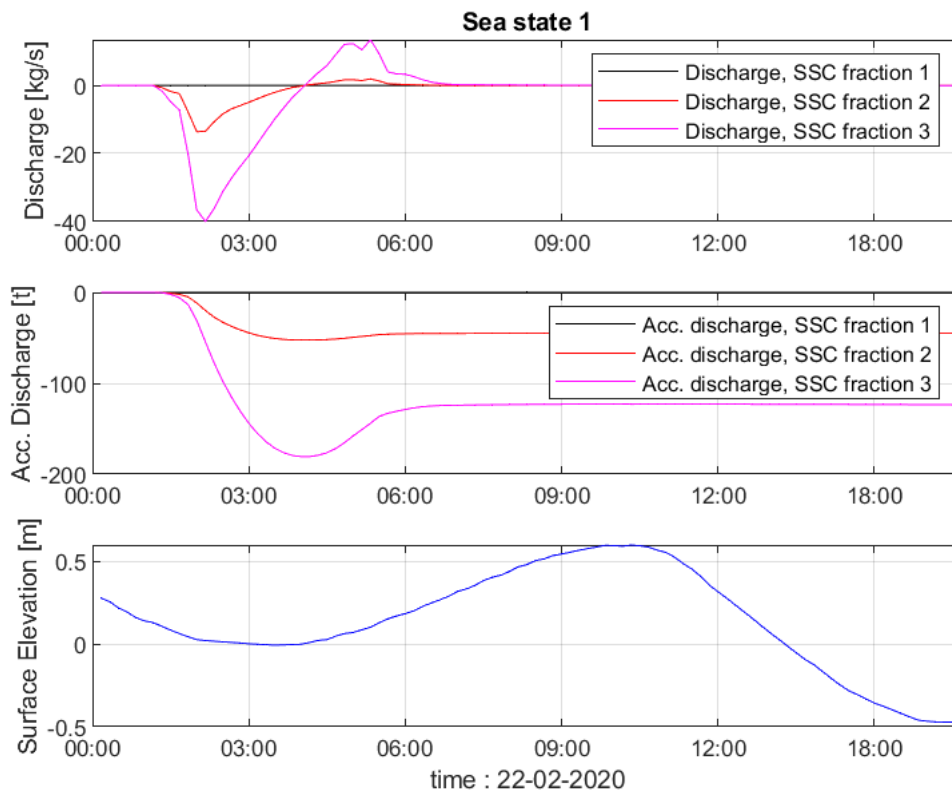


Figure 5.15. Suspended Sediment discharge (top plot) and accumulated discharge (mid plot) through the Malamocco mouth for the infrequent, energetic sea state. Negative discharge values are associated to sediment leaving the lagoon.



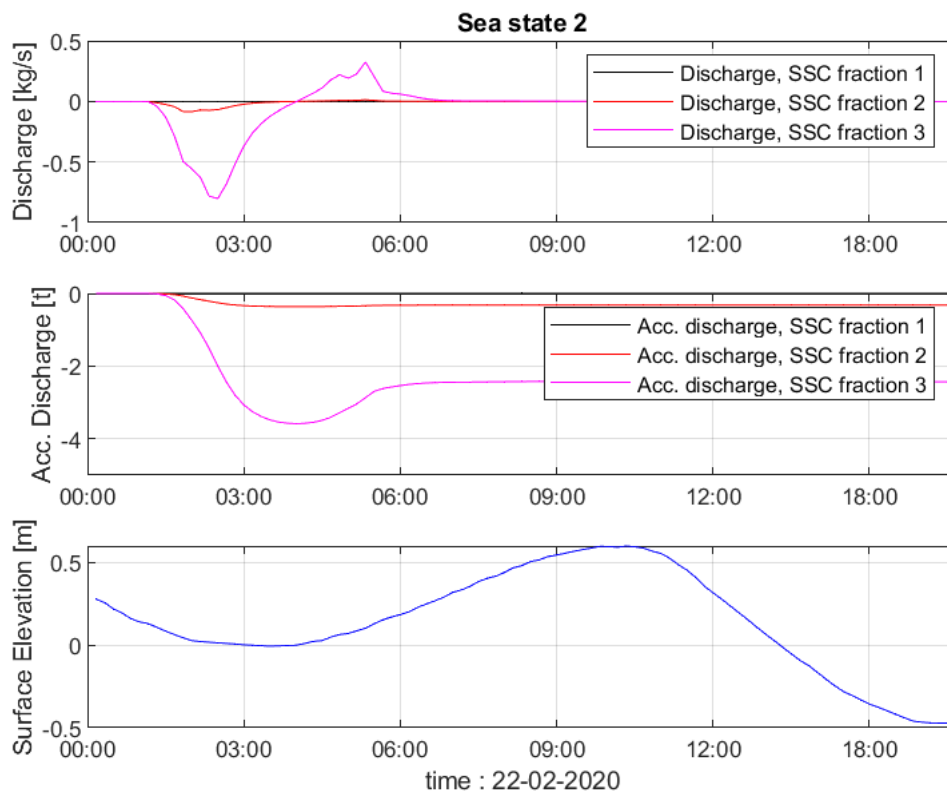


Figure 5.16. Suspended Sediment discharge (top plot) and accumulated discharge (mid plot) through the Malamocco mouth for the frequent, less energetic sea state. Negative discharge values are associated to sediment leaving the lagoon. (The y-axis of the mid plot is changed with respect to the plot representing the “Sea State 1” results to provide a better graphical representation).

5.3 Conclusion summary

The level of the shear stress exerted by the passing vessels and wave action associated flows determines the degree of seabed erosion and sediment suspension in the water column.

Displacement waves generated by passing vessels are associated to larger stresses affecting the area along the navigation track and immediately surrounding areas. On the other hand, wave action is responsible for lower magnitude of bottom shear stress which is, however, exerted on larger portion of the lagoons corresponding mainly to shallow tidal flats.

The combined effect of bed shear stress magnitude and the extent of its area of influence gives raise to different level of water turbidity.





In general, the contribution of very rare sea state may occasionally generate larger turbidity level in the lagoon than a more frequently occurring instance of passing vessel. The more frequent wave fields in lagoon, carrying a reduced energy content, are found to have a moderate to negligible effect on tidal flats with resulting sediment concentration in the water column below 2 mg/l in most of the area simulated.

The “shape” of the sediment plume is found to have an influence on the total sediment discharge through the lagoon mouth. A plume footprint lying along the Malamocco-Marghera finds its way out of the lagoon quicker than a more spatially distributed plume across the lagoon due to the funneling effect of the navigation channel on the tidal induced currents. From a quantitative perspective, the sediment discharge caused by an energetic and rarely occurring sea state through the Malamocco mouth is found to be about 25% of sediment flux caused by a passing vessel.

In general, regardless the forcing, most of the sediment in suspension re-settle to lagoon seabed within a tidal emi-cycle.



6 CONCLUSIONS

The present report details the setup of a hydrodynamic model for vessel generated displacement waves along the Malamocco Marghera Channel (MMC) in the lagoon of Venice along with analyses of the modelled results.

The hydrodynamic model, a MIKE3 FM model with 5 vertical layers, has been calibrated and shows good agreement with measurements of both water level and current speed provided by CNR, see the description of the CNR Database in Section 2.7.1.1, and HS Marine, see the description of the HS Marine Dataset in Section 2.7.1.2.

The hydrodynamic model has been coupled with a sediment transport model, a MIKE MT model, concerned with the advection and diffusion of fine sediment. The sediment transport model contains three sediment fractions: fine sand, medium silt and fine silt with d_{50} of 100, 40 and 15 μm respectively. The sediment transport model considers critical shear stresses for erosion in the range 0.5 Pa to 1.8 Pa and has been calibrated against data from available literature, (Scarpa et al. 2019, [20]), (Saretta et al. 2010, [21]) and (Zaggia et al 2017, [22]). The model shows good agreement with measured data in terms of suspended sediment concentrations indicating that the physics of the dispersion and advection processes are well captured by the model.

The model framework, hydrodynamic and sediment transport model, has in the present study been run considering the existing conditions i.e., existing channel layout and representative vessel traffic navigating at 10 knots. This investigation has shown:

- The draw down level depends highly on the bathymetry of the channel: the larger and more unrestricted the channel (width and depth) the smaller the draw down wave. Therefore, the draw down levels also increase moving north from the San Leonardo bend and become especially large in the area where the channel is framed by structures along the eastern side.
 - Whilst the structures prevent the draw down from spreading out and impacting the lagoon, the draw down level becomes larger locally in the area west of the structures.
- The draw down level of the vessel generated displacement wave depends on the channel geometry but generally increases with the displacement volume of the vessel.



- 200 m east of the channel centre line near the measurement locations of (Scarpa et al. 2019, [20]) the following linear relation between the vessel displacement volume in m^3 (x) and the draw down level has been found:
 - In-bound: $WL_{min} = -1 \cdot 10^{-5} \cdot x - 0.0172$
 - Out-bound: $WL_{min} = -2 \cdot 10^{-5} \cdot x - 0.0175$
- The draw down level decreases with distance to the channel centre line.
 - About 600 m from the channel, the draw down level has been reduced by approximately 60%. This indicates that the majority of the energy is dissipated relatively close to the channel (<800 m from the channel).
 - The draw down levels become relatively similar (in the order of 10 cm) across the modelled vessels after about 1,000 m from the channel.
 - Larger vessels have considerably larger draw down magnitudes near the channel, about 20%-34% larger at Line-2, see Table 4-6.
- The width of the zone with active sediment transport from vessel generated displacement waves depends on the channel geometry but increases relatively linearly with the displacement stencil volume:
 - 200 m east of the channel centre line near the measurement locations of (Scarpa et al. 2019, [20]) the following linear relation between the vessel displacement volume in m^3 (x) and the distance between the channel and the location where the modelled bed shear stress reaches a value of 0.7 Pa has been found:
 - In-bound: $Dist = 0.015 \cdot x + 459$
 - Out-bound: $Dist = 0.017 \cdot x + 221$
- The modelled large vessels represent about 17% of the total modelled events but can cause up to 60% of the total modelled erosion. This indicates that if the mitigation measures can be targeted at the larger vessels, it will have a significant influence in terms of reducing the vessel generated erosion along the channel.

Pre-liminary model tests investigating the reduction of vessel speed from 10 to 8 knots between the San Leonardo turn and Fusina were made from mid-August to start September 2022. These tests showed that the vessel speed has a significant influence on the draw-down magnitudes and thus also the bed shear stress magnitudes on the flats. The tests were made before the sediment transport model was fully calibrated and therefore the direct influence on the erosion





could not be quantified. It is planned to provide this investigation along with the influence of the updated channel layout later as one complete mitigation report.



7 BIBLIOGRAPHY

- [1] MIKE by DHI A/S, “MIKE 3 Flow Model FM - Hydrodynamic and Transport Module Scientific Documentation,” DHI A/S, Copenhagen, 2022a.
- [2] “Autorità di Sistema Portuale del Mare Adriatico Settentrionale,” [Online]. Available: <https://www.port.venice.it/it/autorita-portuale-di-venezia.html>. [Accessed 2022].
- [3] “Provveditorato Interregionale per le Opere Pubbliche per il Veneto, Trentino Alto Adige e Friuli Venezia Giulia - Ex Magistrato alle Acque - Venezia,” [Online]. Available: <http://provveditoratovenetia.mit.gov.it/index.html>. [Accessed 2022].
- [4] “Consiglio Nazionale delle Ricerche,” [Online]. Available: <https://www.cnr.it/>. [Accessed 2022].
- [5] M. Tondello and B. Mattichio, “Campaign of measurements of speed, current and wave motion generated by the transit of merchant vessels in the Malamocco Marghera Channel,” HS Marine srl, Venice, 2022.
- [6] D. L. Kriebel and W. N. Seelig, “An empirical model for ship-generated waves,” in *In proceedings of fifth international symposium on ocean wave measurement and analysis - Waves 2005*, Madrid, 2005.
- [7] MIKE by DHI A/S, “MIKE 21 Spectral Wave Module Scientific Documentation,” 2022b.
- [8] B. Elfrink, D. M. Hanes and B. G. Ruessink, “Parametrization of near bed orbital velocities under irregular breaking waves on a sloping bed.,” *Coastal Engineering*, vol. 53, pp. 915-927, 2006.
- [9] W. R. D. Dally and R. Dalrymple, “Wave height variation across beaches of arbitrary profile,” *Journal of Geophysical Research*, vol. 90, no. 10, pp. 11917-11927, 1985.
- [10] PIANC, “Guidelines for protecting berthing structures from scour caused by ships,” PIANC Maritime Navigation Commission, Bruxelles, 2015.



- [11] J. H. Verheij, "The stability of bottom and banks subjected to the velocities in the propeller," in *8th Int. Harbour Congress*, Antwerp, 1983.
- [12] J. Fredsøe, "Turbulent boundary layers in wave-current motion," *Journal of Hydrologic Engineering (ASCE)*, vol. 110, no. 8, pp. 1103-1120, 1984.
- [13] MIKE by DHI A/S, "MIKE 21 & MIKE 3 Flow Model FM - Mud Transport Module Scientific Documentation," 2022c.
- [14] M. Guerrini, G. Fontolan and A. Pedroncini, "Meteomarine and hydrogeological characterization of Venice lagoon," DHI, 2022.
- [15] F. Shepard, "Nomenclature based on sand-silt-clay ratios.," *Journal of Sedimentary Research*, vol. 24, pp. 151-158, 1954.
- [16] E. Molinaroli, S. Guerzoni, A. Sarretta, M. Masiol and P. M., "Thirty-year changes (1970 to 2000) in bathymetry and sediment texture recorded in the Lagoon of Venice sub-basins, Italy," *Marine Geology*, vol. 258, pp. 115-125, 2009.
- [17] C. Amos, A. Bergamasco, G. Umgiesser, S. Cappucci, D. Cloutier, L. DeNat, M. Flindt, M. Bonardi and S. Cristante, "The stability of tidal flats in Venice lagoon – the results of in-situ measurements using two benthic, annular flumes," *Journal Marine Systems*, 2004.
- [18] C. Amos, G. Umgiesser, C. Ferrarin, C. Thompson, R. Whitehouse, T. Sutherland and A. Bergamasco, "The erosion rates of cohesive sediments in Venice lagoon, Italy.," *Continental Shelf Research*, 2010.
- [19] J. Rapaglia, L. R. K. Zaggia, M. Gelinas and H. Bokuniewicz, "Characteristics of ships' depression waves and associated sediment resuspension in the Venice lagoon Italy," *Journal of Marine Systems*, vol. 85, pp. 45-56, 2011.
- [20] G. M. Scarpa, L. Zaggia, G. Manfè, G. Lorenzetti, K. Parnell, T. Soomere, J. Rapaglia and E. Molinaroli, "The effects of ship wakes in the Venice lagoon and implications for the sustainability of shipping in coastal waters," *Scientific Reports - Nature Research*, vol. 9, 2019.





- [21] A. Sarretta, S. Pillon, E. Molinaroli, S. Guerzoni and G. Fontolan, "Sediment budget in the Lagoon of Venice.," *Continental Shelf Research*, vol. 30, pp. 934-949, 2010.
- [22] L. Zaggia, G. Lorenzetti, G. Manfè, G. M. Scarpa, E. Molinaroli, K. Parnell, J. Rapaglia, M. Gionta and T. Soomere, "Fast shoreline erosion induced by ship wakes in a coastal lagoon: Field evidence and remote sensing analysis," *PLOS One*, 2017.
- [23] "Città di Venezia," [Online]. Available: <https://www.comune.venezia.it/it/content/dati-dalle-stazioni-rilevamento>.





APPENDICES



AROUND WATER
di Andrea Zamariolo, Ph.D. Geol.





AROUND WATER
di Andrea Zamariolo, Ph.D. Geol.





APPENDIX A

TABULARIZED HYDRODYNAMIC AND SEDIMENT TRANSPORT RESULTS



AROUND WATER
di Andrea Zamariolo, Ph.D. Geol.





AROUND WATER
di Andrea Zamariolo, Ph.D. Geol.



This appendix provides tables of minimum water level, associated bed shear stress and depth averaged SSC-level in the extraction points of the three extraction lines. In the first/second sub-section tables for the east/west side of the channel are presented respectively.

A 1. East side of channel

Table A 1. Modelled Line-1 east-side parameters of Con-S and Con-L during existing conditions.

Line-1, East		Margin	200 m	400 m	600 m	800 m	1000 m	1200 m	1400 m
Con-S, In	WL _{min} (m)	-1.05	-0.97	-	-	-	-	-	-
	τ (Pa)	11.3	4.1	-	-	-	-	-	-
	SSC (mg/l)	214.1	1019.9	-	-	-	-	-	-
Con-S, Out	WL _{min} (m)	-0.61	-0.48	-	-	-	-	-	-
	τ (Pa)	4.4	5.7	-	-	-	-	-	-
	SSC (mg/l)	91.4	421.2	-	-	-	-	-	-
Con-L, In	WL _{min} (m)	-2.09	-1.21	-	-	-	-	-	-
	τ (Pa)	52.4	4.1	-	-	-	-	-	-
	SSC (mg/l)	538.7	1615	-	-	-	-	-	-
Con-L, Out	WL _{min} (m)	-0.9	-0.67	-	-	-	-	-	-
	τ (Pa)	8.9	9.6	-	-	-	-	-	-
	SSC (mg/l)	217	503.1	-	-	-	-	-	-

Table A 2. Modelled Line-2 east-side parameters of Con-S and Con-L during existing conditions.

Line-2, East		Margin	200 m	400 m	600 m	800 m	1000 m	1200 m	1400 m
Con-S, In	WL _{min} (m)	-0.67	-0.49	-0.28	-0.22	-0.18	-0.14	-0.12	-0.1
	τ (Pa)	3.9	4.4	1.6	1.2	0.9	0.6	0.4	0.2
	SSC (mg/l)	62.6	306	43.4	55.4	31.9	6.5	3.8	4.3
Con-S, Out	WL _{min} (m)	-1.06	-0.69	-0.33	-0.22	-0.15	-0.12	-0.1	-0.08
	τ (Pa)	8.3	7.1	1.9	1.2	0.7	0.4	0.3	0.2
	SSC (mg/l)	248.2	823.6	99.6	74.2	14.9	8.9	8.9	9
Con-L, In	WL _{min} (m)	-1.05	-0.66	-0.35	-0.26	-0.21	-0.17	-0.15	-0.12
	τ (Pa)	8.9	7.3	2.2	1.6	1.2	0.8	0.5	0.4
	SSC (mg/l)	272.5	764.6	161.3	198.7	86.5	25.5	5.3	4.3
Con-L, Out	WL _{min} (m)	-1.73	-0.81	-0.39	-0.25	-0.18	-0.14	-0.12	-0.1
	τ (Pa)	20.1	8.8	2.4	1.5	0.8	0.5	0.3	0.2
	SSC (mg/l)	370.6	842.9	283.5	144.3	28.1	10.5	9	9.1

Table A 3. Modelled Line-3 east-side parameters of Con-S and Con-L during existing conditions.

Line-3, East		Margin	200 m	400 m	600 m	800 m	1000 m	1200 m	1400 m
Con-S, In	WL _{min} (m)	-0.53	-0.45	-0.34	-0.25	-0.13	-0.08	-0.05	-0.04
	τ (Pa)	2.6	3	1.8	1	0.3	0.1	0.1	0
	SSC (mg/l)	35.3	68	55.9	9.6	5.9	5.7	5.6	5.9
Con-S, Out	WL _{min} (m)	-0.64	-0.53	-0.36	-0.28	-0.21	-0.16	-0.13	-0.11
	τ (Pa)	3.5	4	2	1.3	0.8	0.5	0.3	0.2
	SSC (mg/l)	62.5	197.9	98.9	24.9	9.2	8	7.9	8
Con-L, In	WL _{min} (m)	-0.86	-0.74	-0.44	-0.32	-0.18	-0.1	-0.07	-0.05
	τ (Pa)	6.5	8	2.8	1.5	0.6	0.2	0.1	0.1
	SSC (mg/l)	193.1	498.7	188.9	45.2	6	5.8	5.7	5.8
Con-L, Out	WL _{min} (m)	-0.96	-0.81	-0.48	-0.36	-0.26	-0.2	-0.16	-0.13
	τ (Pa)	7.3	8.9	3.2	1.9	1.1	0.6	0.5	0.3
	SSC (mg/l)	245.9	525.1	396	89.9	20.2	8.2	8	8

Table A 4. Modelled Line-1 east-side parameters of Tan-S and Tan-L during existing conditions.

Line-1, East		Margin	200 m	400 m	600 m	800 m	1000 m	1200 m	1400 m
Tan-S, In	WL _{min} (m)	-0.83	-0.88	-	-	-	-	-	-
	τ (Pa)	7.10	3.10	-	-	-	-	-	-
	SSC (mg/l)	162.90	906.50	-	-	-	-	-	-
Tan-S, Out	WL _{min} (m)	-0.48	-0.40	-	-	-	-	-	-
	τ (Pa)	2.70	4.10	-	-	-	-	-	-
	SSC (mg/l)	58.90	268.30	-	-	-	-	-	-
Tan-L, In	WL _{min} (m)	-2.20	-1.28	-	-	-	-	-	-
	τ (Pa)	57.80	1.90	-	-	-	-	-	-
	SSC (mg/l)	612.90	2051.20	-	-	-	-	-	-
Tan-L, Out	WL _{min} (m)	-1.19	-0.90	-	-	-	-	-	-
	τ (Pa)	16.00	14.30	-	-	-	-	-	-
	SSC (mg/l)	295.20	772.90	-	-	-	-	-	-

Table A 5. Modelled Line-2 east-side parameters of Tan-S and Tan-L during existing conditions.

Line-2, East		Margin	200 m	400 m	600 m	800 m	1000 m	1200 m	1400 m
Tan-S, In	WL _{min} (m)	-0.51	-0.43	-0.27	-0.21	-0.17	-0.14	-0.12	-0.10
	τ (Pa)	2.40	3.30	1.50	1.20	0.80	0.60	0.40	0.20
	SSC (mg/l)	41.10	179.90	34.30	49.70	28.60	5.80	3.80	4.30
Tan-S, Out	WL _{min} (m)	-0.79	-0.65	-0.32	-0.22	-0.15	-0.11	-0.10	-0.08
	τ (Pa)	4.50	6.20	1.80	1.20	0.70	0.40	0.30	0.20
	SSC (mg/l)	94.90	806.40	95.20	72.60	14.50	8.90	8.90	9.00
Tan-L, In	WL _{min} (m)	-1.27	-0.73	-0.39	-0.29	-0.24	-0.20	-0.17	-0.15
	τ (Pa)	12.60	8.70	2.70	1.80	1.40	1.00	0.70	0.50
	SSC (mg/l)	311.80	846.30	308.60	393.70	206.10	66.80	15.10	4.90
Tan-L, Out	WL _{min} (m)	-1.91	-0.87	-0.44	-0.28	-0.20	-0.16	-0.14	-0.12
	τ (Pa)	21.70	9.40	2.80	1.60	1.00	0.60	0.40	0.30
	SSC (mg/l)	568.20	979.30	438.40	345.10	77.40	22.20	9.40	9.40

Table A 6. Modelled Line-3 east-side parameters of Tan-S and Tan-L during existing conditions.

Line-3, East		Margin	200 m	400 m	600 m	800 m	1000 m	1200 m	1400 m
Tan-S, In	WL _{min} (m)	-0.45	-0.40	-0.32	-0.24	-0.13	-0.08	-0.05	-0.04
	τ (Pa)	1.90	2.20	1.60	0.90	0.30	0.10	0.10	0.00
	SSC (mg/l)	20.80	58.70	40.80	8.20	5.90	5.70	5.70	5.90
Tan-S, Out	WL _{min} (m)	-0.55	-0.47	-0.34	-0.27	-0.21	-0.16	-0.13	-0.10
	τ (Pa)	2.60	3.10	1.80	1.20	0.70	0.40	0.30	0.20
	SSC (mg/l)	50.60	105.30	73.10	20.30	8.70	8.00	7.90	8.00
Tan-L, In	WL _{min} (m)	-1.10	-0.93	-0.51	-0.37	-0.23	-0.13	-0.09	-0.07
	τ (Pa)	10.30	12.40	3.30	1.90	0.90	0.40	0.20	0.10
	SSC (mg/l)	236.20	589.40	496.50	110.80	10.30	5.90	5.80	5.90
Tan-L, Out	WL _{min} (m)	-1.31	-1.01	-0.55	-0.40	-0.30	-0.23	-0.18	-0.15
	τ (Pa)	13.20	13.10	4.00	2.20	1.30	0.80	0.60	0.40
	SSC (mg/l)	258.50	615.10	562.10	164.40	35.30	9.70	8.30	8.20

Table A 7. Modelled Line-1 east-side parameters of Bul-S and Bul-L during existing conditions.

Line-1, East		Margin	200 m	400 m	600 m	800 m	1000 m	1200 m	1400 m
Bul-S, In	WL _{min} (m)	-1.00	-1.04	-	-	-	-	-	-
	τ (Pa)	9.90	4.10	-	-	-	-	-	-
	SSC (mg/l)	181.60	1158.50	-	-	-	-	-	-
Bul-S, Out	WL _{min} (m)	-0.54	-0.47	-	-	-	-	-	-
	τ (Pa)	3.40	5.50	-	-	-	-	-	-
	SSC (mg/l)	84.60	440.90	-	-	-	-	-	-
Bul-L, In	WL _{min} (m)	-2.16	-1.24	-	-	-	-	-	-
	τ (Pa)	53.30	2.80	-	-	-	-	-	-
	SSC (mg/l)	597.70	1866.20	-	-	-	-	-	-
Bul-L, Out	WL _{min} (m)	-0.95	-0.79	-	-	-	-	-	-
	τ (Pa)	10.00	11.90	-	-	-	-	-	-
	SSC (mg/l)	233.20	568.00	-	-	-	-	-	-

Table A 8. Modelled Line-2 east-side parameters of Bul-S and Bul-L during existing conditions.

Line-2, East		Margin	200 m	400 m	600 m	800 m	1000 m	1200 m	1400 m
Bul-S, In	WL _{min} (m)	-0.57	-0.48	-0.30	-0.23	-0.19	-0.15	-0.13	-0.11
	τ (Pa)	2.90	4.00	1.80	1.40	1.00	0.60	0.50	0.30
	SSC (mg/l)	52.10	352.90	60.40	76.50	45.90	11.90	3.90	4.30
Bul-S, Out	WL _{min} (m)	-0.92	-0.72	-0.36	-0.24	-0.16	-0.13	-0.11	-0.09
	τ (Pa)	6.00	7.20	2.10	1.30	0.80	0.50	0.30	0.20
	SSC (mg/l)	223.10	822.60	175.30	121.00	20.50	9.40	8.90	9.10
Bul-L, In	WL _{min} (m)	-1.02	-0.68	-0.37	-0.28	-0.23	-0.19	-0.16	-0.14
	τ (Pa)	8.30	7.50	2.50	1.80	1.30	0.90	0.60	0.40
	SSC (mg/l)	270.90	791.60	228.50	263.50	139.80	44.40	9.70	4.50
Bul-L, Out	WL _{min} (m)	-1.79	-0.85	-0.42	-0.27	-0.19	-0.15	-0.13	-0.11
	τ (Pa)	21.80	9.00	2.70	1.60	0.90	0.60	0.40	0.30
	SSC (mg/l)	508.40	906.90	366.50	223.00	41.30	14.10	9.20	9.20

Table A 9. Modelled Line-3 east-side parameters of Bul-S and Bul-L during existing conditions.

Line-3, East		Margin	200 m	400 m	600 m	800 m	1000 m	1200 m	1400 m
Bul-S, In	WL _{min} (m)	-0.52	-0.47	-0.37	-0.28	-0.15	-0.09	-0.06	-0.05
	τ (Pa)	2.40	3.10	2.10	1.20	0.40	0.20	0.10	0.10
	SSC (mg/l)	43.40	101.30	82.50	18.60	6.00	5.80	5.70	5.90
Bul-S, Out	WL _{min} (m)	-0.64	-0.56	-0.40	-0.31	-0.23	-0.17	-0.14	-0.12
	τ (Pa)	3.40	4.20	2.40	1.50	0.90	0.50	0.40	0.30
	SSC (mg/l)	83.40	268.90	142.30	42.30	11.30	8.10	8.00	8.00
Bul-L, In	WL _{min} (m)	-0.87	-0.79	-0.48	-0.35	-0.22	-0.13	-0.08	-0.06
	τ (Pa)	6.40	8.80	2.90	1.70	0.80	0.30	0.20	0.10
	SSC (mg/l)	217.60	521.70	365.40	83.20	7.80	5.90	5.80	5.90
Bul-L, Out	WL _{min} (m)	-1.10	-0.91	-0.53	-0.39	-0.28	-0.22	-0.18	-0.14
	τ (Pa)	9.40	11.10	3.60	2.10	1.20	0.70	0.50	0.40
	SSC (mg/l)	239.50	586.70	558.30	134.80	29.20	8.80	8.20	8.10

Table A 10. Modelled Line-1 east-side parameters of Gen. and RoRo during existing conditions.

Line-1, East		Margin	200 m	400 m	600 m	800 m	1000 m	1200 m	1400 m
Gen, In	WL _{min} (m)	-0.27	-0.23	-	-	-	-	-	-
	τ (Pa)	0.70	0.70	-	-	-	-	-	-
	SSC (mg/l)	5.50	0.00	-	-	-	-	-	-
Gen, Out	WL _{min} (m)	-0.20	-0.13	-	-	-	-	-	-
	τ (Pa)	0.50	0.50	-	-	-	-	-	-
	SSC (mg/l)	14.40	13.30	-	-	-	-	-	-
RoRo, In	WL _{min} (m)	-0.49	-0.49	-	-	-	-	-	-
	τ (Pa)	2.50	1.90	-	-	-	-	-	-
	SSC (mg/l)	34.60	128.60	-	-	-	-	-	-
RoRo, Out	WL _{min} (m)	-0.32	-0.25	-	-	-	-	-	-
	τ (Pa)	1.20	1.60	-	-	-	-	-	-
	SSC (mg/l)	15.60	22.90	-	-	-	-	-	-

Table A 11. Modelled Line-2 east-side parameters of Gen. and RoRo during existing conditions.

Line-2, East		Margin	200 m	400 m	600 m	800 m	1000 m	1200 m	1400 m
Gen, In	WL _{min} (m)	-0.19	-0.12	-0.11	-0.09	-0.07	-0.06	-0.05	-0.04
	τ (Pa)	0.40	0.30	0.30	0.20	0.20	0.10	0.10	0.00
	SSC (mg/l)	12.10	6.30	4.20	3.80	3.50	3.10	3.70	4.20
Gen, Out	WL _{min} (m)	-0.26	-0.21	-0.14	-0.10	-0.06	-0.04	-0.04	-0.03
	τ (Pa)	0.60	0.80	0.40	0.30	0.10	0.10	0.00	0.00
	SSC (mg/l)	13.90	11.70	10.10	9.60	9.20	8.70	8.80	9.00
RoRo, In	WL _{min} (m)	-0.33	-0.25	-0.20	-0.16	-0.13	-0.10	-0.09	-0.07
	τ (Pa)	1.00	1.20	0.80	0.70	0.50	0.30	0.20	0.10
	SSC (mg/l)	12.70	11.00	5.50	8.60	4.30	3.20	3.70	4.20
RoRo, Out	WL _{min} (m)	-0.46	-0.42	-0.24	-0.16	-0.11	-0.09	-0.08	-0.06
	τ (Pa)	1.80	2.80	1.10	0.70	0.40	0.30	0.20	0.10
	SSC (mg/l)	20.40	103.20	18.40	15.50	9.30	8.60	8.80	9.00

Table A 12. Modelled Line-3 east-side parameters of Gen. and RoRo during existing conditions.

Line-3, East		Margin	200 m	400 m	600 m	800 m	1000 m	1200 m	1400 m
Gen, In	WL _{min} (m)	-0.15	-0.12	-0.10	-0.08	-0.04	-0.03	-0.02	-0.01
	τ (Pa)	0.20	0.20	0.20	0.10	0.00	0.00	0.00	0.00
	SSC (mg/l)	12.30	9.30	7.00	6.20	5.80	5.60	5.60	5.90
Gen, Out	WL _{min} (m)	-0.19	-0.14	-0.10	-0.09	-0.07	-0.06	-0.05	-0.04
	τ (Pa)	0.30	0.30	0.20	0.20	0.10	0.10	0.10	0.00
	SSC (mg/l)	13.20	10.90	9.20	8.50	8.10	8.00	7.90	8.10
RoRo, In	WL _{min} (m)	-0.28	-0.23	-0.21	-0.16	-0.08	-0.05	-0.04	-0.03
	τ (Pa)	0.80	0.80	0.70	0.40	0.10	0.10	0.00	0.00
	SSC (mg/l)	12.40	9.40	7.20	6.30	5.80	5.70	5.70	5.90
RoRo,Out	WL _{min} (m)	-0.33	-0.28	-0.22	-0.18	-0.14	-0.11	-0.09	-0.08
	τ (Pa)	1.00	1.10	0.80	0.60	0.40	0.20	0.20	0.10
	SSC (mg/l)	13.60	13.20	9.80	8.50	8.10	7.90	7.90	8.00

Table A 13. Modelled Line-1 east-side parameters of Cru-S and Cru-L during existing conditions.

Line-1, East		Margin	200 m	400 m	600 m	800 m	1000 m	1200 m	1400 m
Cru-S, In	WL _{min} (m)	-0.83	-0.93	-	-	-	-	-	-
	τ (Pa)	6.50	3.40	-	-	-	-	-	-
	SSC (mg/l)	171.40	974.80	-	-	-	-	-	-
Cru-S, Out	WL _{min} (m)	-0.43	-0.40	-	-	-	-	-	-
	τ (Pa)	2.10	3.70	-	-	-	-	-	-
	SSC (mg/l)	41.90	274.20	-	-	-	-	-	-
Cru-L, In	WL _{min} (m)	-2.16	-1.26	-	-	-	-	-	-
	τ (Pa)	51.20	1.70	-	-	-	-	-	-
	SSC (mg/l)	549.60	2022.00	-	-	-	-	-	-
Cru-L,Out	WL _{min} (m)	-0.77	-0.78	-	-	-	-	-	-
	τ (Pa)	6.80	10.80	-	-	-	-	-	-
	SSC (mg/l)	216.60	535.30	-	-	-	-	-	-

Table A 14. Modelled Line-2 east-side parameters of Cru-S and Cru-L during existing conditions.

Line-2, East		Margin	200 m	400 m	600 m	800 m	1000 m	1200 m	1400 m
Cru-S, In	WL _{min} (m)	-0.46	-0.40	-0.28	-0.22	-0.18	-0.14	-0.12	-0.10
	τ (Pa)	1.90	2.70	1.50	1.20	0.90	0.60	0.40	0.30
	SSC (mg/l)	21.90	153.60	39.70	60.00	27.80	6.70	3.80	4.20
Cru-S, Out	WL _{min} (m)	-0.72	-0.64	-0.34	-0.22	-0.16	-0.12	-0.10	-0.09
	τ (Pa)	3.80	5.90	1.90	1.20	0.70	0.50	0.30	0.20
	SSC (mg/l)	77.50	795.20	113.80	87.00	16.40	8.90	8.80	9.00
Cru-L, In	WL _{min} (m)	-0.89	-0.68	-0.38	-0.28	-0.23	-0.19	-0.16	-0.14
	τ (Pa)	6.20	7.10	2.50	1.80	1.30	0.90	0.60	0.40
	SSC (mg/l)	274.90	789.90	244.20	288.90	147.50	40.10	8.70	4.40
Cru-L,Out	WL _{min} (m)	-1.49	-0.87	-0.43	-0.27	-0.20	-0.16	-0.14	-0.12
	τ (Pa)	14.70	9.40	2.80	1.70	1.00	0.70	0.40	0.30
	SSC (mg/l)	414.60	948.10	460.30	285.00	53.60	16.20	9.10	9.10

Table A 15. Modelled Line-3 east-side parameters of Cru-S and Cru-L during existing conditions.

Line-3, East		Margin	200 m	400 m	600 m	800 m	1000 m	1200 m	1400 m
Cru-S, In	WL _{min} (m)	-0.43	-0.38	-0.33	-0.25	-0.14	-0.08	-0.06	-0.04
	τ (Pa)	1.70	2.00	1.60	1.00	0.40	0.20	0.10	0.00
	SSC (mg/l)	19.90	56.60	45.00	9.50	5.90	5.70	5.70	5.80
Cru-S, Out	WL _{min} (m)	-0.51	-0.46	-0.36	-0.28	-0.22	-0.16	-0.13	-0.11
	τ (Pa)	2.20	2.80	1.90	1.30	0.80	0.50	0.30	0.20
	SSC (mg/l)	43.90	108.90	82.40	22.90	9.10	8.00	7.90	8.00
Cru-L, In	WL _{min} (m)	-0.83	-0.77	-0.49	-0.35	-0.22	-0.13	-0.09	-0.07
	τ (Pa)	5.80	8.00	3.10	1.70	0.80	0.40	0.20	0.10
	SSC (mg/l)	216.50	543.60	378.60	69.10	7.30	5.80	5.70	5.80
Cru-L, Out	WL _{min} (m)	-1.04	-0.93	-0.54	-0.40	-0.29	-0.22	-0.18	-0.15
	τ (Pa)	8.20	10.90	3.80	2.10	1.20	0.80	0.50	0.40
	SSC (mg/l)	236.50	589.10	588.40	147.50	32.10	9.00	8.10	8.10

A 2. West side of channel

Table A 16. Modelled Line-1 west-side parameters of Con-S and Con-L during existing conditions.

Line-1, East		Margin	75 m	100 m	125 m	150 m
Con-S, In	WL _{min} (m)	-1.14	-1.26	-1.13	-0.59	-
	τ (Pa)	9.7	16.1	2.3	0.5	-
	SSC (mg/l)	149.8	416.8	1415.1	345.3	-
Con-S, Out	WL _{min} (m)	-0.73	-0.76	-0.7	-0.39	-
	τ (Pa)	5.3	10	11.7	5.2	-
	SSC (mg/l)	85.1	246	1234	1370.4	-
Con-L, In	WL _{min} (m)	-1.64	-2.06	-1.19	-0.59	-
	τ (Pa)	19.7	39.9	2.2	0.6	-
	SSC (mg/l)	180.1	1388.3	1118	298	-
Con-L, Out	WL _{min} (m)	-1.09	-1.29	-0.91	-0.42	-
	τ (Pa)	11.6	26	30.4	9.9	-
	SSC (mg/l)	155.2	461.3	1361.1	1235.6	-

Table A 17. Modelled Line-2 west-side parameters of Con-S and Con-L during existing conditions.

Line-2, East		Margin	75 m	100 m	125 m	150 m
Con-S, In	WL _{min} (m)	-0.82	-0.79	-0.79	-0.79	-1.03
	τ (Pa)	5.5	6.6	7.7	5.6	4.2
	SSC (mg/l)	142.6	174	485.6	440.9	2819.4
Con-S, Out	WL _{min} (m)	-1.11	-1.11	-1.09	-0.99	-1.13
	τ (Pa)	7.9	10.5	18.7	14.7	8.2
	SSC (mg/l)	266.6	570	590.8	604.8	2603.2
Con-L, In	WL _{min} (m)	-1.14	-1.15	-1.12	-1.13	-1.46
	τ (Pa)	10	13	15.3	9.6	3.8
	SSC (mg/l)	305	426.9	575.4	628.9	5258.4
Con-L, Out	WL _{min} (m)	-1.61	-1.74	-1.31	-1.2	-1.33
	τ (Pa)	16.1	25	26.7	17.8	9.1
	SSC (mg/l)	447.2	964.6	727.1	703.8	3619.1

Table A 18. Modelled Line-3 west-side parameters of Con-S and Con-L during existing conditions.

Line-3, East		Margin	75 m	100 m	125 m	150 m
Con-S, In	WL _{min} (m)	-0.72	-0.72	-0.77	-0.78	-0.49
	τ (Pa)	4.6	4.6	8.7	13.5	1.7
	SSC (mg/l)	83.7	83.7	745.9	1768.7	1356
Con-S, Out	WL _{min} (m)	-0.74	-0.74	-0.86	-0.9	-0.48
	τ (Pa)	4.1	4.1	8.5	20.8	4.3
	SSC (mg/l)	118.4	118.4	686.2	2537.3	1966.8
Con-L, In	WL _{min} (m)	-1.12	-1.12	-1.42	-0.84	-0.56
	τ (Pa)	10.2	10.2	30	17.6	1.1
	SSC (mg/l)	254.2	254.2	1782.1	2186.9	1311.1
Con-L, Out	WL _{min} (m)	-1.28	-1.28	-1.7	-0.97	-0.51
	τ (Pa)	11.5	11.5	33.5	20.6	3.6
	SSC (mg/l)	236.2	236.2	2666.9	2573.2	1636.4

Table A 19. Modelled Line-1 west-side parameters of Tan-S and Tan-L during existing conditions.

Line-1, East		Margin	75 m	100 m	125 m	150 m
Tan-S, In	WL _{min} (m)	-0.92	-1.03	-1.10	-0.59	-
	τ (Pa)	3.60	6.40	11.70	8.10	-
	SSC (mg/l)	61.30	241.70	1028.50	1202.20	-
Tan-S, Out	WL _{min} (m)	-0.58	-0.60	-0.66	-0.42	-
	τ (Pa)	5.30	10.00	11.70	5.20	-
	SSC (mg/l)	85.10	246.00	1234.00	1370.40	-
Tan-L, In	WL _{min} (m)	-2.01	-2.29	-1.13	-0.60	-
	τ (Pa)	35.50	39.70	3.40	0.40	-
	SSC (mg/l)	270.70	1399.70	1327.80	249.30	-
Tan-L, Out	WL _{min} (m)	-1.30	-1.66	-1.01	-0.45	-
	τ (Pa)	17.20	42.30	32.60	2.50	-
	SSC (mg/l)	200.10	806.10	2213.10	1066.30	-

Table A 20. Modelled Line-2 west-side parameters of Tan-S and Tan-L during existing conditions.

Line-2, East		Margin	75 m	100 m	125 m	150 m
Tan-S, In	WL _{min} (m)	-0.60	-0.61	-0.62	-0.65	-0.84
	τ (Pa)	3.10	3.90	4.50	3.40	2.40
	SSC (mg/l)	86.60	118.10	230.90	166.50	1519.40
Tan-S, Out	WL _{min} (m)	-0.80	-0.81	-0.80	-0.81	-0.99
	τ (Pa)	4.40	5.50	9.70	9.10	6.20
	SSC (mg/l)	175.50	355.70	530.60	548.30	2115.70
Tan-L, In	WL _{min} (m)	-1.33	-1.31	-1.26	-1.31	-1.64
	τ (Pa)	13.30	16.50	17.50	8.70	2.20
	SSC (mg/l)	362.10	511.10	610.00	885.00	6751.90
Tan-L, Out	WL _{min} (m)	-1.59	-1.78	-1.45	-1.41	-1.54
	τ (Pa)	13.30	23.40	30.40	20.30	5.20
	SSC (mg/l)	649.80	1002.70	940.10	996.20	4187.40

Table A 21. Modelled Line-3 west-side parameters of Tan-S and Tan-L during existing conditions.

Line-3, East		Margin	75 m	100 m	125 m	150 m
Tan-S, In	WL _{min} (m)	-0.61	-0.61	-0.65	-0.80	-0.54
	τ (Pa)	3.30	3.30	5.10	10.40	1.90
	SSC (mg/l)	64.30	64.30	755.10	2338.60	1611.50
Tan-S, Out	WL _{min} (m)	-0.63	-0.63	-0.72	-0.88	-0.47
	τ (Pa)	3.10	3.10	5.90	9.40	4.50
	SSC (mg/l)	50.40	50.40	593.10	2824.60	1846.40
Tan-L, In	WL _{min} (m)	-1.45	-1.45	-1.84	-0.94	-0.54
	τ (Pa)	16.40	16.40	53.00	21.80	3.87
	SSC (mg/l)	344.50	344.50	2569.00	3539.00	651.60
Tan-L, Out	WL _{min} (m)	-1.42	-1.42	-1.95	-0.99	-0.47
	τ (Pa)	12.00	12.00	49.70	21.20	5.30
	SSC (mg/l)	349.80	349.80	3743.40	3145.60	1904.60

Table A 22. Modelled Line-1 west-side parameters of Bul-S and Bul-L during existing conditions.

Line-1, East		Margin	75 m	100 m	125 m	150 m
Bul-S, In	WL _{min} (m)	-1.15	-1.34	-1.19	-0.61	-
	τ (Pa)	10.10	19.70	1.10	0.30	-
	SSC (mg/l)	146.70	414.20	1688.00	289.70	-
Bul-S, Out	WL _{min} (m)	-0.62	-0.70	-0.74	-0.43	-
	τ (Pa)	4.30	8.60	8.60	8.10	-
	SSC (mg/l)	114.10	239.50	1322.40	1302.50	-
Bul-L, In	WL _{min} (m)	-2.37	-2.27	-1.10	-0.61	-
	τ (Pa)	42.10	43.00	5.80	0.30	-
	SSC (mg/l)	310.70	1570.80	1068.10	257.60	-
Bul-L, Out	WL _{min} (m)	-1.15	-1.43	-1.01	-0.46	-
	τ (Pa)	13.00	30.80	27.70	1.90	-
	SSC (mg/l)	167.20	522.20	1853.50	934.90	-

Table A 23. Modelled Line-2 west-side parameters of Bul-S and Bul-L during existing conditions.

Line-2, East		Margin	75 m	100 m	125 m	150 m
Bul-S, In	WL _{min} (m)	-0.68	-0.70	-0.72	-0.79	-1.06
	τ (Pa)	3.50	4.60	5.40	3.80	1.70
	SSC (mg/l)	177.60	270.00	411.00	321.60	3125.20
Bul-S, Out	WL _{min} (m)	-0.89	-0.93	-0.96	-1.00	-1.15
	τ (Pa)	5.60	7.30	13.50	11.90	6.70
	SSC (mg/l)	441.70	624.70	571.50	617.00	2936.90
Bul-L, In	WL _{min} (m)	-1.30	-1.39	-1.24	-1.31	-1.56
	τ (Pa)	12.60	18.00	15.50	4.00	0.80
	SSC (mg/l)	332.70	549.80	569.70	1138.90	6068.90
Bul-L,Out	WL _{min} (m)	-1.75	-1.88	-1.39	-1.28	-1.40
	τ (Pa)	21.00	28.30	28.60	17.30	6.70
	SSC (mg/l)	655.30	864.30	892.10	769.50	3614.60

Table A 24. Modelled Line-3 west-side parameters of Bul-S and Bul-L during existing conditions.

Line-3, East		Margin	75 m	100 m	125 m	150 m
Bul-S, In	WL _{min} (m)	-0.70	-0.70	-0.80	-0.90	-0.50
	τ (Pa)	4.40	4.40	5.30	10.90	5.70
	SSC (mg/l)	109.00	109.00	919.50	2688.70	1727.20
Bul-S, Out	WL _{min} (m)	-0.74	-0.74	-0.88	-0.99	-0.45
	τ (Pa)	3.90	3.90	6.70	8.90	0.80
	SSC (mg/l)	113.30	113.30	781.20	3286.20	3898.90
Bul-L, In	WL _{min} (m)	-1.36	-1.36	-1.75	-0.98	-0.53
	τ (Pa)	14.40	14.40	39.70	12.60	10.47
	SSC (mg/l)	327.00	327.00	2819.20	3511.00	1140.80
Bul-L,Out	WL _{min} (m)	-1.62	-1.62	-1.98	-1.02	-0.50
	τ (Pa)	16.70	16.70	49.90	11.20	4.80
	SSC (mg/l)	354.10	354.10	4401.50	3348.30	1617.40

Table A 25. Modelled Line-1 west-side parameters of Gen. and RoRo during existing conditions.

Line-1, East		Margin	75 m	100 m	125 m	150 m
Gen, In	WL _{min} (m)	-0.30	-0.29	-0.32	-0.41	-
	τ (Pa)	0.80	0.90	2.40	2.00	-
	SSC (mg/l)	11.60	9.60	196.80	1256.90	-
Gen, Out	WL _{min} (m)	-0.22	-0.20	-0.20	-0.23	-
	τ (Pa)	0.60	0.90	2.40	2.10	-
	SSC (mg/l)	14.40	14.20	63.30	490.70	-
RoRo, In	WL _{min} (m)	-0.54	-0.56	-0.73	-0.57	-
	τ (Pa)	2.40	3.50	6.30	0.50	-
	SSC (mg/l)	31.50	105.90	1036.70	475.10	-
RoRo,Out	WL _{min} (m)	-0.37	-0.36	-0.40	-0.38	-
	τ (Pa)	1.50	2.40	5.60	3.50	-
	SSC (mg/l)	16.40	52.60	528.00	1325.00	-

Table A 26. Modelled Line-2 west-side parameters of Gen. and RoRo during existing conditions.

Line-2, East		Margin	75 m	100 m	125 m	150 m
Gen, In	WL _{min} (m)	-0.26	-0.23	-0.21	-0.20	-0.21
	τ (Pa)	0.60	0.70	0.70	0.40	0.60
	SSC (mg/l)	11.90	10.70	8.80	8.70	6.60
Gen, Out	WL _{min} (m)	-0.29	-0.27	-0.24	-0.23	-0.24
	τ (Pa)	0.60	0.70	0.90	0.90	1.00
	SSC (mg/l)	13.60	13.40	12.90	12.80	11.60
RoRo, In	WL _{min} (m)	-0.38	-0.37	-0.36	-0.35	-0.41
	τ (Pa)	1.30	1.50	1.60	1.10	0.90
	SSC (mg/l)	13.60	13.80	18.10	13.70	42.80
RoRo,Out	WL _{min} (m)	-0.48	-0.49	-0.47	-0.46	-0.53
	τ (Pa)	1.80	2.20	3.30	3.20	2.60
	SSC (mg/l)	20.80	31.50	94.90	91.40	183.30

Table A 27. Modelled Line-3 west-side parameters of Gen. and RoRo during existing conditions.

Line-3, East		Margin	75 m	100 m	125 m	150 m
Gen, In	WL _{min} (m)	-0.22	-0.22	-0.22	-0.22	-0.33
	τ (Pa)	0.50	0.50	0.80	1.20	1.30
	SSC (mg/l)	12.40	12.40	9.70	48.00	718.80
Gen, Out	WL _{min} (m)	-0.21	-0.21	-0.22	-0.25	-0.38
	τ (Pa)	0.40	0.40	0.80	1.90	0.70
	SSC (mg/l)	13.20	13.20	10.30	130.00	661.30
RoRo, In	WL _{min} (m)	-0.35	-0.35	-0.35	-0.40	-0.51
	τ (Pa)	1.20	1.20	2.00	2.40	3.60
	SSC (mg/l)	13.20	13.20	65.10	560.80	1481.90
RoRo,Out	WL _{min} (m)	-0.40	-0.40	-0.42	-0.54	-0.47
	τ (Pa)	1.30	1.30	2.30	3.70	3.30
	SSC (mg/l)	14.20	14.20	79.40	1147.00	1429.50

Table A 28. Modelled Line-1 west-side parameters of Cru-S and Cru-L during existing conditions.

Line-1, East		Margin	75 m	100 m	125 m	150 m
Cru-S, In	WL _{min} (m)	-0.94	-1.09	-1.13	-0.62	-
	τ (Pa)	6.90	13.30	14.80	0.20	-
	SSC (mg/l)	140.50	362.30	1626.50	324.90	-
Cru-S, Out	WL _{min} (m)	-0.49	-0.52	-0.64	-0.47	-
	τ (Pa)	2.60	4.70	6.90	1.90	-
	SSC (mg/l)	38.50	222.50	938.90	1027.30	-
Cru-L, In	WL _{min} (m)	-2.21	-2.43	-1.21	-0.64	-
	τ (Pa)	42.00	52.60	1.70	0.10	-
	SSC (mg/l)	469.70	1543.20	878.50	278.50	-
Cru-L,Out	WL _{min} (m)	-0.94	-1.15	-1.06	-0.53	-
	τ (Pa)	8.40	17.30	12.70	1.20	-
	SSC (mg/l)	159.20	356.10	1643.10	513.60	-

Table A 29. Modelled Line-2 west-side parameters of Cru-S and Cru-L during existing conditions.

Line-2, East		Margin	75 m	100 m	125 m	150 m
Cru-S, In	WL _{min} (m)	-0.50	-0.51	-0.53	-0.57	-0.73
	τ (Pa)	2.00	2.50	2.70	2.00	1.00
	SSC (mg/l)	41.70	55.80	101.00	68.80	683.60
Cru-S, Out	WL _{min} (m)	-0.74	-0.75	-0.78	-0.85	-0.96
	τ (Pa)	3.80	4.70	8.50	7.70	4.50
	SSC (mg/l)	178.00	386.90	540.40	563.80	2141.40
Cru-L, In	WL _{min} (m)	-1.02	-1.02	-1.14	-1.31	-1.45
	τ (Pa)	7.10	8.90	10.30	5.20	0.50
	SSC (mg/l)	307.80	464.10	527.90	682.30	4725.10
Cru-L, Out	WL _{min} (m)	-1.62	-1.75	-1.51	-1.41	-1.45
	τ (Pa)	15.10	18.00	28.10	18.10	4.90
	SSC (mg/l)	587.80	1475.00	932.40	964.70	3257.30

Table A 30. Modelled Line-3 west-side parameters of Cru-S and Cru-L during existing conditions.

Line-3, East		Margin	75 m	100 m	125 m	150 m
Cru-S, In	WL _{min} (m)	-0.53	-0.53	-0.57	-0.77	-0.49
	τ (Pa)	2.50	2.50	3.30	3.90	3.60
	SSC (mg/l)	43.30	43.30	693.80	2216.70	2758.10
Cru-S, Out	WL _{min} (m)	-0.63	-0.63	-0.72	-0.82	-0.42
	τ (Pa)	2.80	2.80	4.60	11.80	3.90
	SSC (mg/l)	49.50	49.50	546.90	1759.60	1255.90
Cru-L, In	WL _{min} (m)	-1.14	-1.14	-1.57	-0.90	-0.49
	τ (Pa)	9.50	9.50	18.70	14.80	5.60
	SSC (mg/l)	311.10	311.10	2630.80	2593.10	1744.20
Cru-L, Out	WL _{min} (m)	-1.37	-1.37	-1.76	-0.89	-0.55
	τ (Pa)	10.60	10.60	21.40	18.00	4.30
	SSC (mg/l)	297.80	297.80	3748.80	2199.00	1164.10





AROUND WATER
di Andrea Zamariolo, Ph.D. Geol.





APPENDIX B

SHIP GENERATED WAVES AND CURRENT SPEED MEASUREMENTS CAMPAIGN AT MALAMOCCO-MARGHERA CHANNEL



AROUND WATER
di Andrea Zamariolo, Ph.D. Geol.





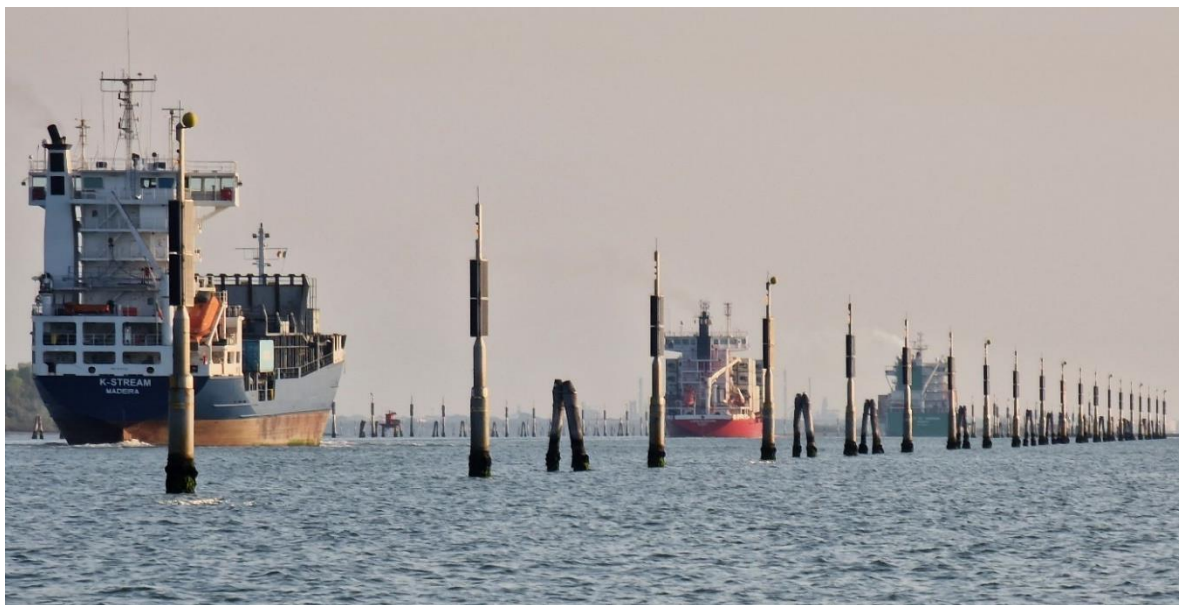
AROUND WATER
di Andrea Zamariolo, Ph.D. Geol.





AUTORITÀ DI SISTEMA PORTUALE
DEL MARE ADRIATICO SETTENTRIONALE
PORTI DI VENEZIA E CHIOGGIA

SHIP GENERATED WAVES AND CURRENT SPEED MEASUREMENTS CAMPAIGN AT MALAMOCCO - MARGHERA CHANNEL



Document

TECHNICAL REPORT

Execution:



HS marine Srl

via Panà 56 / a 35027

Noventa Padovana (PD)

e.mail: mail@hsmarinesrl.com

Dr. Massimo Tondello and Bruno Matticchio



Order: HSM864-20

REV: 00

Date: June 2022

INDEX

1	<u>SCOPE OF WORK</u>	4
2	<u>MEASUREMENT APPROACH AND INSTRUMENTS</u>	5
3	<u>MAY 12ND MEASUREMENT CAMPAIGN</u>	9
1.1.1	Characteristics of monitored vessel traffic	10
1.1.2	Depression wave measurement	10
1.1.3	Measurement of current speed	11
1.1.4	Syn Acrab	12
1.1.5	Ocean Brave	13
4	<u>MAY 16TH MEASUREMENT CAMPAIGN</u>	14
4.1	VESSEL TRAFFIC AND SHIP CHARACTERISTICS	14
4.2	DEPRESSION WAVE MEASUREMENT	15
4.3	CURRENT SPEED MEASUREMENT	17
4.3.1	Spirit of Chennai	18
4.3.2	Louise Borchard	21
4.3.3	Eurocargo Alexandria	24
4.3.4	Nervion Valley	27
4.4	CURRENT TRANSECTS ACROSS THE CHANNEL	30

	TITLE:	SHIP GENERATED WAVES AND CURRENT SPEED MEASUREMENTS CAMPAIGN AT MALAMOCCO -MARGHERA CHANNEL	
	ELAB ..	TECHNICAL REPORT	

INDEX OF FIGURES

Fig. 2.1 - Survey area and instruments array (May 16 th campaign)	5
Fig. 2.2 - Ultrasonic tide gauge installed on briccola 121 next to the channel (left) and Louise Borchard ship passage (right).....	6
Fig. 2.3 - Rio Grande ADCP profiler (left) and drone boat with ADCP housed in the central hull (right)	7
Fig. 2.4 - ADCP profiling (left) and drone boat operating next to the ultrasonic tide gauge (right).....	7
Fig. 2.5 - Leica Viva GS16 GPS antenna (left). Ohmex Sonarmite echosounder housed in the stern of the trimaran (right).....	7
Fig. 2.6 - RBR "solo" pressure gauge (diameter = 2.54 cm, length = 22 cm) positioned on the seabed about 38 m away from briccola 121.....	8
Fig. 3.1 - Drone boat movements during the May 12nd campaign, as compared with the position maintained in the following May 16 th campaign, when the drone boat was anchored.	9
Fig. 3.2 - GPS antenna height during Syn Acrab passage	10
Fig. 3.3 - GPS antenna height during Ocean Brave passage	11
Fig. 3.4 -Syn Acrab passing through the measuring range	
Fig. 3.5 - Vertical distribution of speed over time measured by ADCP	12
Fig. 3.6 - Average current speed and direction over time, as measured by ADCP	12
Fig. 3.7 - Current velocity vectors measured by ADCP	12
Fig. 3.8 -Ocean Brave passing through the measuring range.....	
Fig. 3.9 - Vertical distribution of current speed as a function of time (ADCP)	13
Fig. 3.10 - Average current speed and direction as a function of time (ADCP)	13
Fig. 3.11 - Current velocity vectors measured by ADCP	13
Fig. 4.1 - Level measured by the ultrasonic tide gauge at briccola 121 on May 16 th	15
Fig. 4.2 - Detail of water levels measured at briccola 121 during the passage of the first convoy.....	16
Fig. 4.3 - Detail of the water levels measured at briccola 121 during the passage of the second convoy ..	16
Fig. 4.4 - Pressure measured by the pressure gauge on May 16 th	16
Fig. 4.5 - Spirit of Chennai ship passing through the measuring range	18
Fig. 4.6 - Vertical distribution of current speed as a function of time (ADCP)	19
Fig. 4.7 - Average current speed and direction as a function of time (ADCP)	19
Fig. 4.8 - Current speed vectors measured by ADCP	19
Fig. 4.9 - Depression wave measured at different instruments (ultrasonic gauge at Briccola 121, GPS on drone boat and seabed pressure gauge)	20
Fig. 4.10 - Louise Borchard ship passing through the measuring range.....	21
Fig. 4.11 - Vertical distribution of current speed as a function of time (ADCP)	22
Fig. 4.12 - Average current speed and direction as a function of time (ADCP)	22
Fig. 4.13 - Current speed vectors measured by ADCP	22
Fig. 4.14 - Depression wave measured at different instruments (ultrasonic gauge at Briccola 121, GPS on drone boat and seabed pressure gauge)	23
Fig. 4.15 - Eurocargo Alexandria ship passing through the measuring range	24
Fig. 4.16 - Vertical distribution of current speed as a function of time (ADCP)	25
Fig. 4.17 - Average current speed and direction as a function of time (ADCP)	25
Fig. 4.18 - Current speed vectors measured by ADCP	25
Fig. 4.19 - Depression wave measured at different instruments (ultrasonic gauge at Briccola 121, GPS on drone boat and seabed pressure gauge)	26
Fig. 4.20 - Nervion Valley ship passing through the measurement range	27
Fig. 4.21 - Vertical distribution of current speed as a function of time (ADCP)	28
Fig. 4.22 - Average current speed and direction as a function of time (ADCP)	28
Fig. 4.23 - Current speed vectors measured by ADCP	28
Fig. 4.24 - Depression wave measured at different instruments (ultrasonic gauge at Briccola 121, GPS on drone boat and seabed pressure gauge)	29
Fig. 4.25 - Position of the survey area and of the ADCP transept near the Briccola 121	30
Fig. 4.26 - Tide measurement at Fusina quay (may 16 th campaign) and points of transept measurements	30

DRAFTED: BM	COMM HSM864-21 ..	REV.: 00	Page 2of 32
VERIFIED: MT, NS	FILE: 008-Appendix B.docx	DATE: June 2022	





	TITLE:	SHIP GENERATED WAVES AND CURRENT SPEED MEASUREMENTS CAMPAIGN AT MALAMOCCO -MARGHERA CHANNEL	
	ELAB .:	TECHNICAL REPORT	

Fig. 4.27 - Speed distribution along the transect at 7:40 in the channel	31
Fig. 4.28 - Speed distribution along the transect at 8:44 in the channel	32

DRAFTED: BM	COMM HSM864-21 ..	REV.: 00	Page 3of 32
VERIFIED: MT, NS	FILE: 008-Appendix B.docx	DATE: June 2022	

	TITLE:	SHIP GENERATED WAVES AND CURRENT SPEED MEASUREMENTS CAMPAIGN AT MALAMOCCO -MARGHERA CHANNEL	
	ELAB .:	TECHNICAL REPORT	

1 SCOPE OF WORK

The measurement campaign aimed at collecting a dataset for evaluating the effects of the ship generated depression wave in the Malamocco-Marghera canal on the nearby tidal flats. This activity is part of the project promoted by the Port Authority " *CHANNELING: the Green deal for Venice* ". The data collected will be used for calibrating the hydrodynamic and navigation simulations, which will be used for the assessment of maritime traffic hydrodynamic impact on the Malamocco-Marghera canal and on the nearby tidal flats.

Two separate campaigns were performed in two different days: on May 12nd a preliminary testing of the experimental setup was carried out. Based on test results, the final measurement campaign was carried out on May 16th.

In the May 12nd campaign measurements were carried out using a floating ADCP instrument equipped with an additional DGPS receiver.

The data collected in the following May 16th campaign of 16 May are:

- **Water level measurements:** an ultrasonic gauge was installed on a pile bordering the channel. The instrument was activated before starting the daily campaign and switched off at the end of the day.
- **Pressure measurements:** outside of the channel, about 40 m away from the pile (see above), a high frequency pressure gauge was placed on the seabed. The instrument was activated before starting the daily campaign and switched off at the end of the day.
- **Current measurements:** the measurements were carried out using an **ADCP** (Acoustic Doppler Current Profiler, model Rio Grande 1200 kHz ZedHed, produced by Teledyne –RDI). The instrument was installed on a trimaran drone boat. The drone was anchored between the pile (see above) and the pressure gauge (see above), about 26 m away from the channel and was activated at each ship transit (or convoy transit). The drone was also equipped with a DGPS receiver (Leica GS-16 operating in RTK mode) and a single- beam sonar (Ohmex Sonarmite) in order to measure both the current and the depression wave height.

DRAFTED: BM	COMM HSM864-21 ..	REV.: 00	Page 4 of 32
VERIFIED: MT, NS	FILE: 008-Appendix B.docx	DATE: June 2022	

2 MEASUREMENT APPROACH AND INSTRUMENTS

The survey area is located next to “briccola 121” (pile n. 121), located about 7 km from the Malamocco lagoon entrance, NE of Porto San Leonardo (Fig. 2.1).

The instrumental setup consists of 3 instruments: a water level gauge, an ADCP current meter (equipped with DGPS and SBES echosounder) and a pressure gauge. Tab. 2.1 -reports coordinates and characteristics of the instruments used in the campaign.

The water level gauge is of the ultrasonic one, model MU-C3, produced by Terry Ferraris. It was installed on “briccola 121” (Fig. 2.2). The sampling frequency has been set to 1 Hz.

The instrument was set and checked at the beginning and at the end of the daily campaign in order to assess drifts, if any, but none occurred. In the post-processing phase, data were averaged over a moving window of 2 s in order to smooth high frequency fluctuations and then extracted every 2 s.





Fig. 2.1 - Survey area and instruments array (May 16th campaign)

Instrument	Model	Waypoint	Latitude (° N)	Longitude (° E)	Sampling rate
Level meter	Terry Ferraris MU-C3	Briccola 121	45.3676750	12.2569083	1 Hz
ADCP current meter	Teledyne Workhorse Rio Grande 1200 kHz	ADCP	45.3675889	12.2572194	2 Hz
Pressure cell	RBRonly	RBR	45.3675750	12.2573722	8 Hz

Tab. 2.1 - Coordinates and instruments used in the May 16th campaign

DRAFTED: BM	COMM HSM864-21 ..	REV.: 00	Page 5 of 32
VERIFIED: MT, NS	FILE: 008-Appendix B.docx	DATE: June 2022	

	TITLE:	SHIP GENERATED WAVES AND CURRENT SPEED MEASUREMENTS CAMPAIGN AT MALAMOCCO -MARGHERA CHANNEL	
	ELAB ..:	TECHNICAL REPORT	

Current measurements were carried out using the Rio Grande ADCP current profiler. The instrument is about 20 cm in diameter and 20 cm in height. On its lower face there are 4 acoustic signal transceivers used to detect current patterns (direction and speed) at different depths, by processing the acoustic signal reflected by moving water particles, based on the Doppler effect.

The instrument has been installed on a floating support (drone boat). The profiler measures, at regular intervals, the current velocity profile along the vertical, from the surface to the bottom at regular intervals of depth. The water column is divided into "cells" of constant height; for each one current speed and direction is measured, thus obtaining the vertical profile. There are also a water temperature gauge, a compass and a "pitch and roll" for vertical deviations correction.

ADCP signals allow also for bottom tracking (depth measurement and drone speed). All data collected allow for processing of individual measured vertical profiles that, observed over time, provide the trend of the actual flow at the point considered. Data are processed and stored on a portal PC directly during the acquisition phase using a specific software (Teledyne RDI WinRiver II).

The ADCP profiler was anchored outside of the Malamocco-Marghera channel, about 26 m away from bricola 121 (Fig. 2.4). The instrument was used in WM12 mode, with a cell height of 20 cm and a sampling frequency of 2 Hz.

A DGPS receiver (Leica GS16) and a SBES echosounder were also installed on board the drone boat (Fig. 2.5). The DGPS was positioned in the center of the trimaran, in axis with the ADCP probe, while the echosounder was positioned on the stern of the central hull. The DGPS operated in RTK mode relying on the HxGN network SmartNet, thus achieving centimeter positioning accuracy. DGPS allowed for measuring the depression wave at the ADCP. The sonar was used as redundant data for bottom tracking and depth assessment, in addition to the bottom tracking provided by the ADCP.

The data of these instruments were acquired using the same software used for processing of current profiles (Teledyne RDI WinRiver II) using a frequency of 2 Hz.



Fig. 2.2 - Ultrasonic tide gauge installed on bricola 121 next to the channel (left) and Louise Borchard ship passage (right).

DRAFTED: BM	COMM HSM864-21 ..:	REV.: 00	Page 6of 32
VERIFIED: MT, NS	FILE: 008-Appendix B.docx	DATE: June 2022	



	TITLE:	SHIP GENERATED WAVES AND CURRENT SPEED MEASUREMENTS CAMPAIGN AT MALAMOCCO -MARGHERA CHANNEL	
	ELAB .:	TECHNICAL REPORT	



Fig. 2.3 - Rio Grande ADCP profiler (left) and drone boat with ADCP housed in the central hull (right)





Fig. 2.4 - ADCP profiling (left) and drone boat operating next to the ultrasonic tide gauge (right).



Fig. 2.5 - Leica Viva GS16 GPS antenna (left).
Ohmex Sonarmite echosounder housed in the stern of the trimaran (right).

DRAFTED: BM	COMM HSM864-21	REV.: 00	Page 7 of 32
VERIFIED: MT, NS	FILE: 008-Appendix B.docx	DATE: June 2022	

	TITLE:	SHIP GENERATED WAVES AND CURRENT SPEED MEASUREMENTS CAMPAIGN AT MALAMOCCO -MARGHERA CHANNEL	
	ELAB .:	TECHNICAL REPORT	

The pressure gauge was positioned 12 m away from the ADCP profiler, hence 38 m away from briccola 121. It was anchored on the seabed outside of the channel, on a gently sloping seabed in a depth of about -3 m m.s.l..

The instrument used is an RBR “solo” with a sampling frequency of 8 Hz (Fig. 2.6). It was kindly supplied for the campaign by CNR – Ismar. Instrument setup was performed by CNR in order to start acquisition at 11 pm on the day before the campaign and end acquisition at 11 pm of the daily campaign. During the campaign the probe does not provide real time data but records them in the internal data logger.

The data are made available at the end of the campaign after having been downloaded from the instrument. Just like the water level gauge, post-processed data were averaged over a 2 s moving window to smooth high frequency fluctuations and then extracted with a time interval of 2 s.



**Fig. 2.6 - RBR “solo” pressure gauge (diameter = 2.54 cm, length = 22 cm)
positioned on the seabed about 38 m away from briccola 121**

DRAFTED: BM	COMM HSM864-21 ..	REV.: 00	Page 8 of 32
VERIFIED: MT, NS	FILE: 008-Appendix B.docx	DATE: June 2022	

3 MAY 12ND MEASUREMENT CAMPAIGN

On May 12nd, 2022, a test campaign was performed in the survey area, aimed at optimizing and testing the instrumental setup for the following campaign of May 16th.

This paragraph reports test results, which are however significant with respect to the intended purposes and add useful data to the available dataset.

The instrumental equipment used for the test campaign consists of the ADCP profiler only (equipped with GPS and echosounder). The water level and pressure gauges were not used. The survey area is located beside the channel near bricola 121, as shown in Fig. 3.1.

During the test, the drone boat was not anchored on the seabed but towed by a manned boat, trying to remain in position by maneuvering during the transit of the ships to be monitored. As shown by GPS tracks in Fig. 3.1, it was almost impossible to keep the position due to strong current at ship passage; the instrument moved about 20÷25 m during the passage of the ships.

The GPS antenna, positioned on the drone boat, allowed for an additional accurate measurement of depression waves.

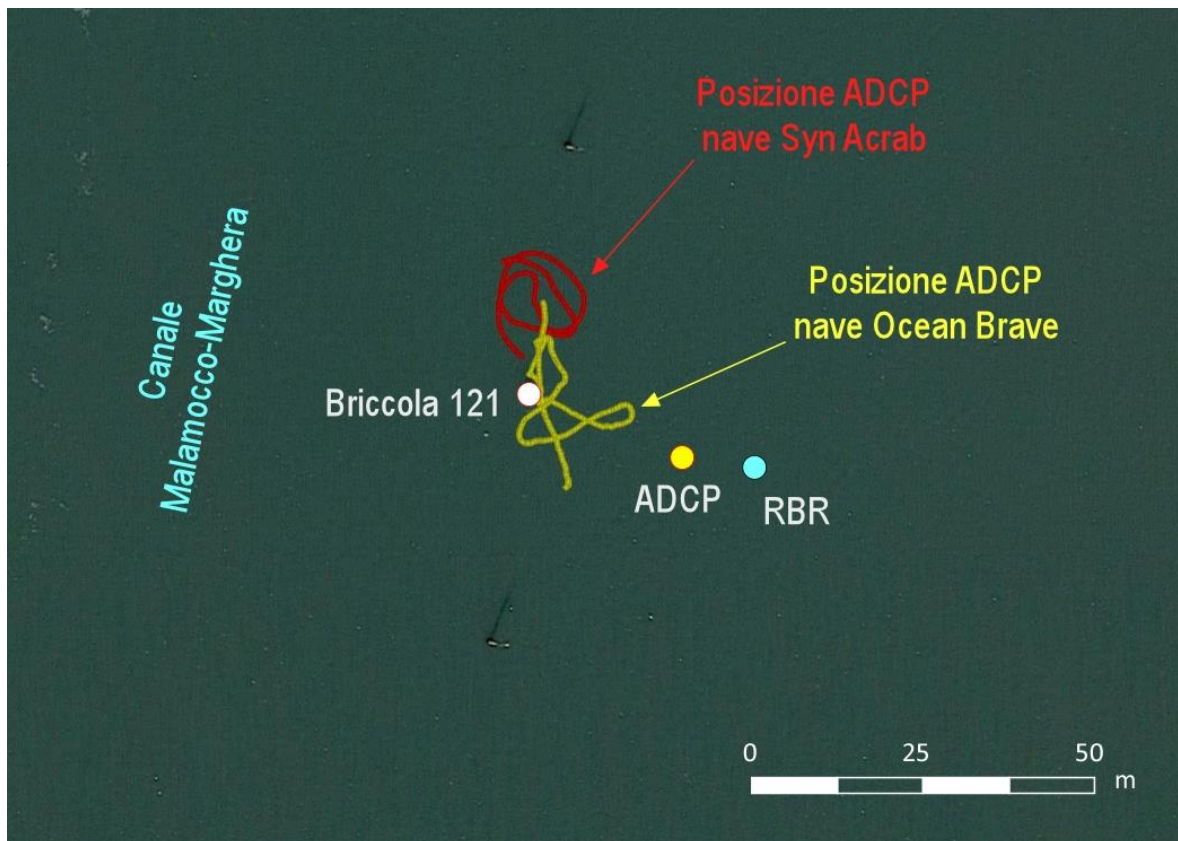


Fig. 3.1 - Drone boat movements during the May 12nd campaign, as compared with the position maintained in the following May 16th campaign, when the drone boat was anchored.

DRAFTED: BM	COMM HSM864-21 ..	REV.: 00	Page 9 of 32
VERIFIED: MT, NS	FILE: 008-Appendix B.docx	DATE: June 2022	

1.1.1 Characteristics of monitored vessel traffic

During the campaign, 2 commercial ships were monitored, the “Syn Acrab” and the “Ocean Brave”, both entering the lagoon, sailing from Malamocco to Marghera.

The characteristics of the ships are shown in Fig. 3.1 and were obtained from the naval traffic websites (www.marinetraffic.com and www.vesselfinder.com) and from the Coast Guard Approach Plan (<https://www.guardiacostiera.gov.it/venezia/Pages/Piano-Accosti.aspx>).

For the first ship, the speed at the time of transit in the survey area (“NR”) was not recorded.

Date	Now	Ship	Direction	Length (m)	Length (m)	Draft (m)	Speed (Kn)
12/05/2022	14:51	Syn Acrab	entrance	122.84	19.0	6.0	NO
12/05/2022	15:05	Ocean Brave	entrance	199.0	32.0	7.5	10.3

Tab. 3.1 - Characteristics of the vessels monitored during the test measurement of 12 May 2022; “NR” indicates that the speed of the ship was not detected.

1.1.2 Depression wave measurement

Processing the data measured by the GPS, it was possible to obtain the amplitude of the ship generated depression wave. Fig. 3.2 and Fig. 3.3 show the position of the GPS antenna at the passage of “Syn Acrab” and “Ocean Brave” ships. In the first case, the wave amplitude, measured from the still water level to the trough was 22 cm while in the second it was 53 cm.

The figures show both the original signal (blue curve) and the smoothed one (orange curve).

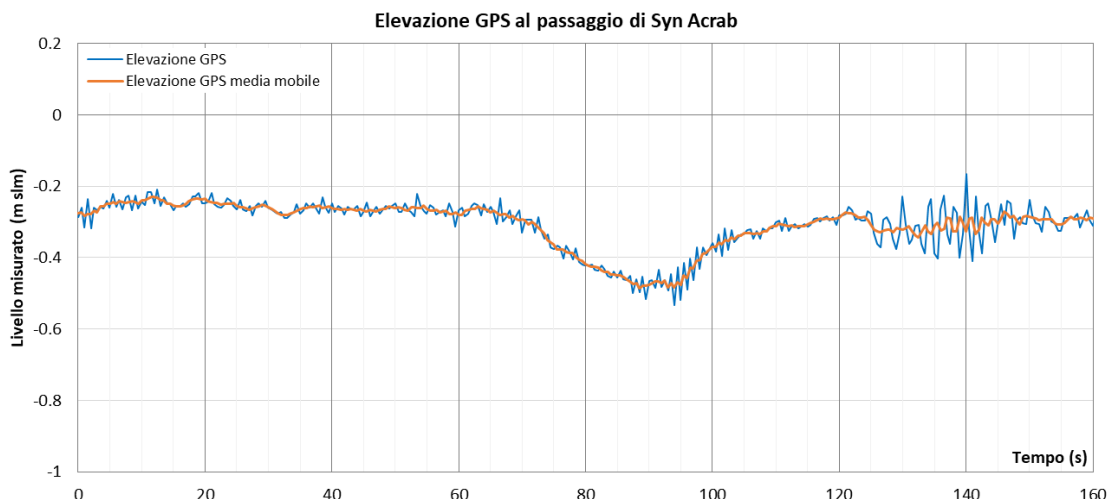


Fig. 3.2 - GPS antenna height during Syn Acrab passage

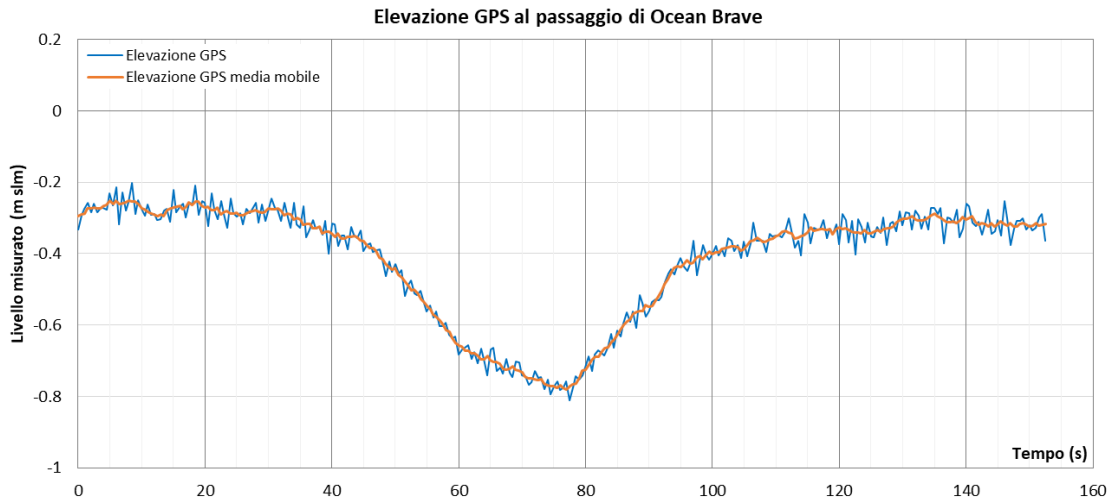


Fig. 3.3 - GPS antenna height during Ocean Brave passage

1.1.3 Measurement of current speed

From the processing of the data measured by the ADCP profiler, the speed and direction of the current during ships passage were obtained.

For each of them, the velocity contour plot is provided, i.e. the vertical distribution of velocities over time (Fig. 3.5), the trend over time of the average velocities and directions on the vertical (Fig. 3.6) and the stick velocity plot, i.e. the trend over time of velocity vectors (Fig. 3.7).

The maximum speed measured was 0.59 m / s for the ship “Syn Acrab” and 1.08 m / s for the ship “Ocean Brave”. From the velocity vectors it is possible to observe the strong lure effect of the waters triggered by the wave generated by the ships in transit, which for the ships entering the port produce vectors directed in the opposite direction (South-West) with respect to the direction of advance of the ship (North – North East).

Tab. 3.2 summarizes the characteristics of the monitored vessels and the results of the measurements in terms of wave amplitude and maximum speed of the current. The following paragraphs show the detailed speed graphs of the individual ships.

Time	Ship	Length (m)	Beam (m)	Draft (m)	Speed (kn)	Depression wave (m)	Max current speed (m/s)
14:51	Syn Acrab	122.84	19.0	6.0	NO	0.22	0.59
15:05	Ocean Brave	199.0	32.0	7.5	10.3	0.53	1.08

Tab. 3.2 - Amplitude of the depression wave generated by the passage of ships and maximum speed of the current measured by the ADCP; "NR" indicates that the speed of the ship was not detected

DRAFTED: BM	COMM HSM864-21	REV.: 00	Page 11 of 32
VERIFIED: MT, NS	FILE: 008-Appendix B.docx	DATE: June 2022	

1.1.4 Syn Acrab

“Syn Acrab” is a LNG ship heading to Porto Marghera. Draft is 6 m and ship speed was not monitored. Depression wave generated at ship passage was 0.22 m and strongest ship induced current 0.59 m/s.



Fig. 3.4 –Syn Acrab passing through the measuring range

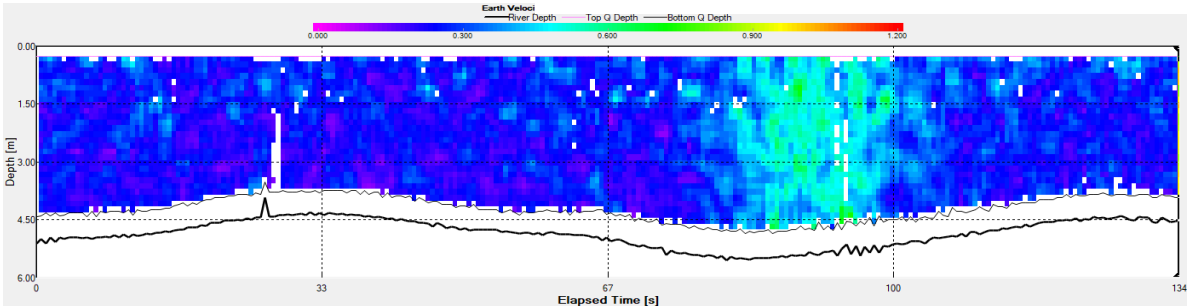


Fig. 3.5 - Vertical distribution of speed over time measured by ADCP

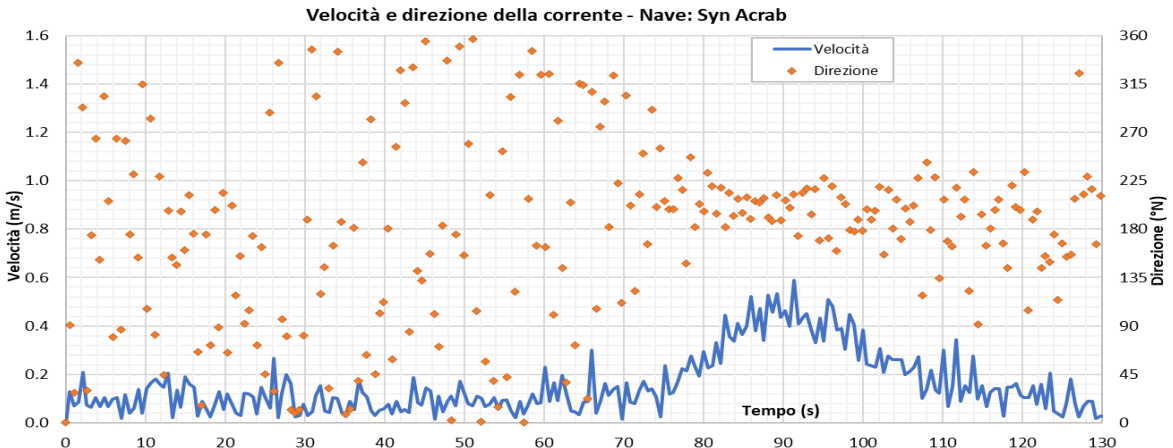


Fig. 3.6 - Average current speed and direction over time, as measured by ADCP

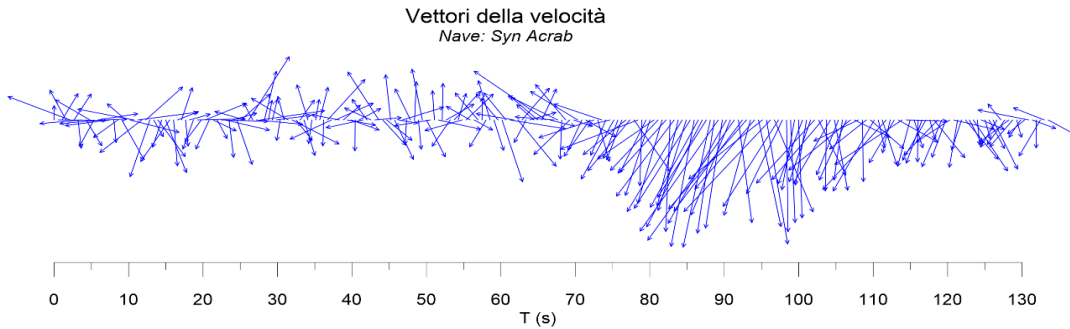


Fig. 3.7 - Current velocity vectors measured by ADCP

1.1.5 Ocean Brave

“Ocean Brave” is a bulk carrier heading to Marghera. Draft is 7.5 m and ship speed is 10.3 knots. Depression wave generated at ship passage was 0.53 m and strongest ship induced current 1.08 m/s.



Fig. 3.8 –Ocean Brave passing through the measuring range

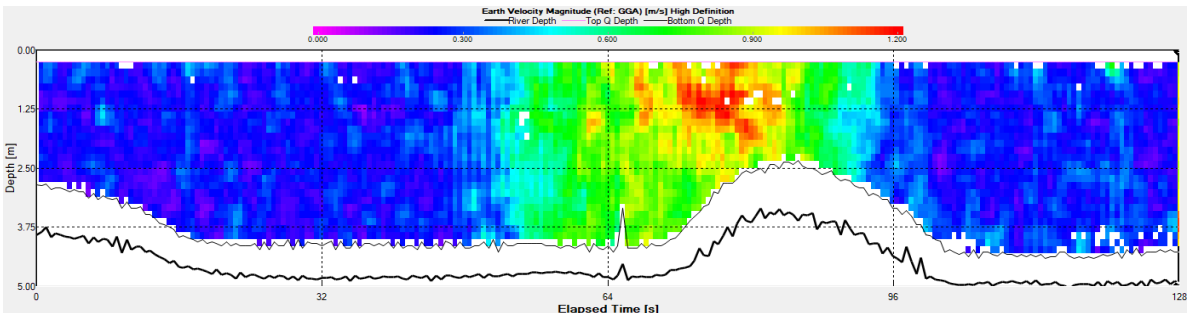


Fig. 3.9 - Vertical distribution of current speed as a function of time (ADCP)

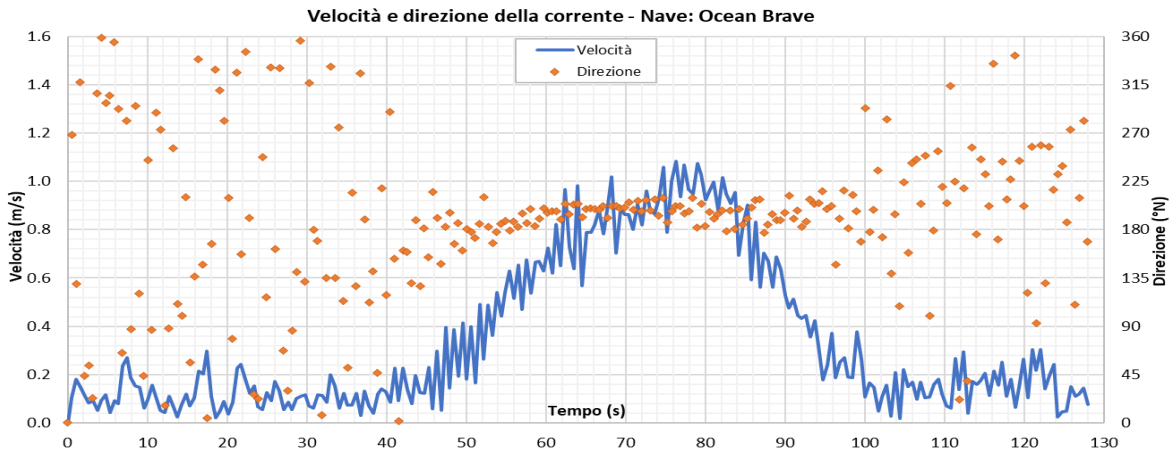


Fig. 3.10 - Average current speed and direction as a function of time (ADCP)

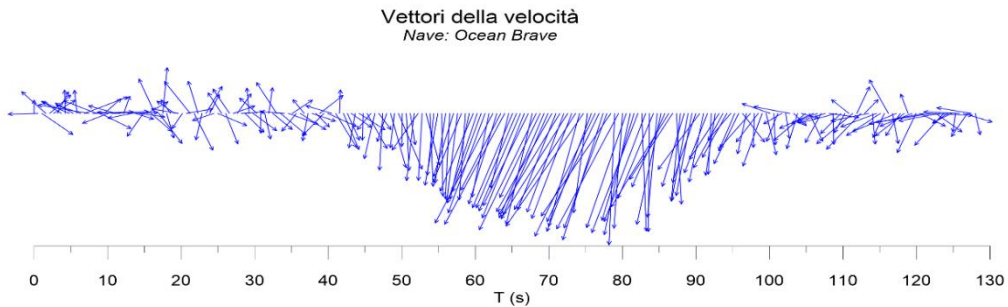




Fig. 3.11 - Current velocity vectors measured by ADCP

	TITLE:	SHIP GENERATED WAVES AND CURRENT SPEED MEASUREMENTS CAMPAIGN AT MALAMOCCO -MARGHERA CHANNEL	
	ELAB .:	TECHNICAL REPORT	

4 MAY 16TH MEASUREMENT CAMPAIGN

In light of the results of the test campaign, the measurement campaign on the ship transits of the day was carried out on May 16th.

The full instrument array is shown in Fig. 2.1, consisting of the ultrasonic water level gauge at bricola 121, the ADCP current profiler 26 m away from bricola 121 (outside of the channel) and the pressure gauge further 12 m away on the tidal flat side. All instruments were anchored in a fixed position.

4.1 Vessel traffic and ship characteristics

During the measurements campaign, 9 ships were monitored, seven of which 7 entering and 2 exiting Porto Marghera. There were medium-large ships ("Spirit of Chennai", "Eurocargo Alexandria" and "Valle di Nervion") exceeding 150 m length, with a draft in the order of 7 m and smaller vessels.

The "Levante" it is the smaller one, with a draft of 2 m and a length of about 50 m.

The characteristics of all the ships are shown in Tab. 4.1; they were obtained from the naval traffic websites (www.marinetraffic.com and www.vesselfinder.com) and from the Coast Guard Approach Plan (<https://www.guardiacostiera.gov.it/venezia/Pages/Piano-Accosti.aspx>).

Date	Time	Ship	Direction	Length (m)	Length (m)	Draft (m)	Speed (kn)
16/05/2022	6:31	Nordanvik	in	97.0	17.3	6.8	9.1
16/05/2022	6:42	Spirit of Chennai	in	159.98	24.81	6.9	9.2
16/05/2022	6:50	Louise Borchard	in	132.6	19.2	6.3	9.9
16/05/2022	6:54	K- Stream	in	121.93	18.45	4.5	10.3
16/05/2022	7:08	Ramzay	in	88.74	16.70	5.0	7.9
16/05/2022	7:27	Eurocargo Alexandria	in	200.85	26.50	7.5	10.5
16/05/2022	9:31	Valle di Nervion	out	176.0	31.0	7.3	9.0
16/05/2022	9:43	Levante	out	58.04	9.5	2.0	10.2
16/05/2022	10:51	Bomar Sedna	in	101.39	19.05	7.6	8.6

Tab. 4.1 - Monitored vessels characteristics during measurement campaign of May 16th

DRAFTED: BM	COMM HSM864-21 ..	REV.: 00	Page 14 of 32
VERIFIED: MT, NS	FILE: 008-Appendix B.docx	DATE: June 2022	

4.2 Depression wave measurement

The graphs obtained by processing the data recorded by water level gauge at bricola 121 and the pressure gauge on the adjacent seabed are shown below.

Fig. 4.1 shows data measured in the morning, since 6:20 and until 12:00. Ship transits occurred with rising tide, between about -0.6 and +0.2 m MPS; ship generated waves are clearly visible.

Fig. 4.2 and Fig. 4.3 shows two details at first and second convoy transits. The largest waves were generated by the “Eurocargo Alexandria”, with a depression wave height of 70 cm, and by the “Nervion Valley” with a height of 49 cm.

The data measured by the pressure gauge are shown in Fig. 4.3. Considering the probe location, about 40 m from the channel, the pressure gauge recorded a smaller wave height with respect to the water level gauge at bricola 121; wave height reduction is in the order of $5 \div 10\%$.

As far as instrument synchronization is concerned, a phase lag of some seconds has been noticed between the pressure gauge and the other instruments, perhaps due to different setup or DAQ delay. In the following paragraphs, time has been synchronized in post processing (see for example Fig. 4.9). The time of the GPS antenna has been taken as base reference.

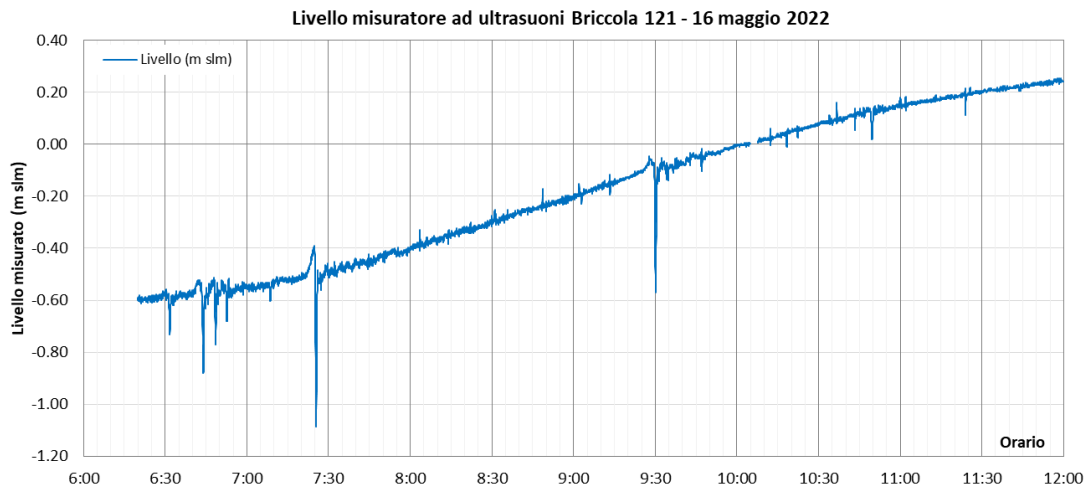


Fig. 4.1 - Level measured by the ultrasonic tide gauge at bricola 121 on May 16th

DRAFTED: BM	COMM HSM864-21	REV.: 00	Page 15 of 32
VERIFIED: MT, NS	FILE: 008-Appendix B.docx	DATE: June 2022	

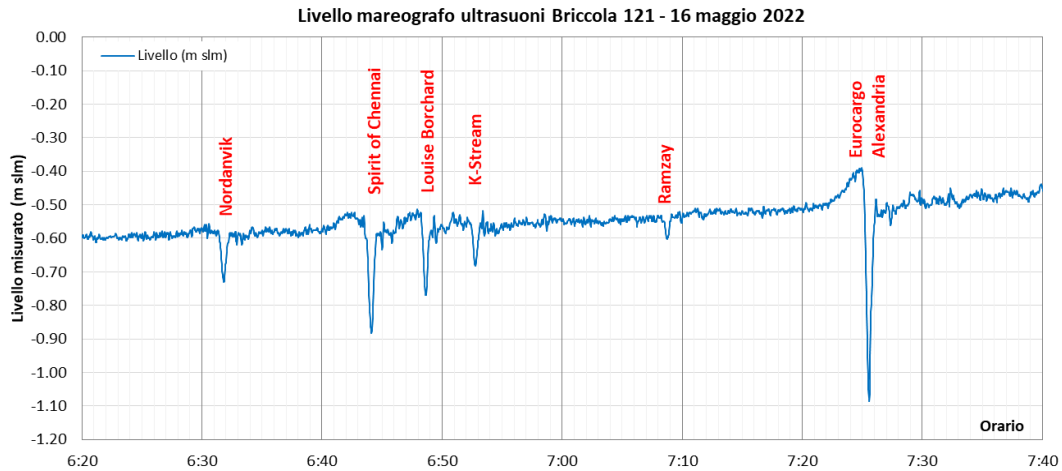


Fig. 4.2 - Detail of water levels measured at briccola 121 during the passage of the first convoy

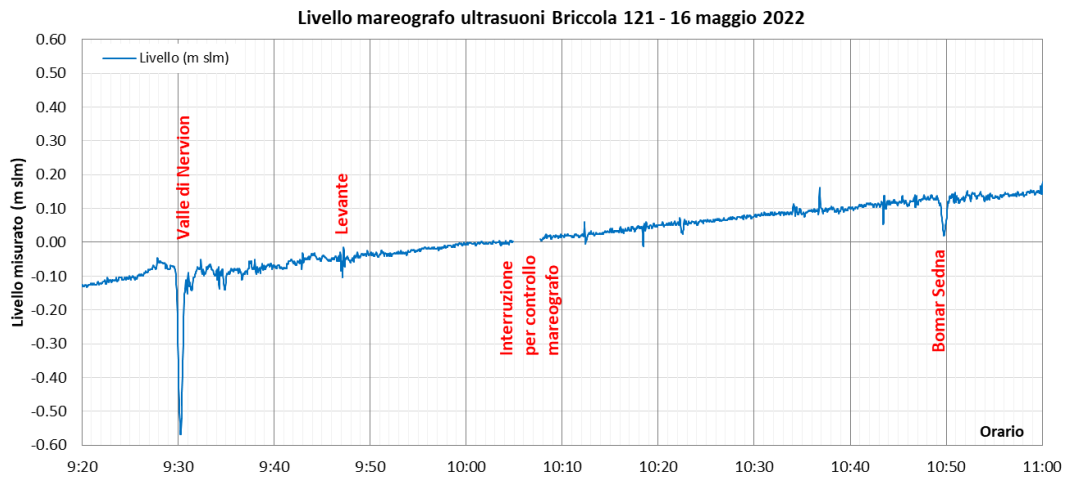


Fig. 4.3 - Detail of the water levels measured at briccola 121 during the passage of the second convoy

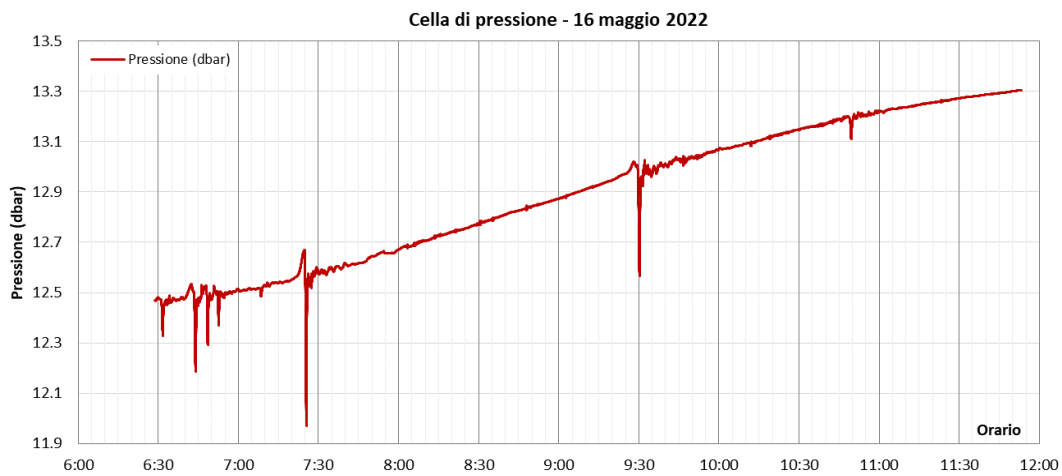




Fig. 4.4 - Pressure measured by the pressure gauge on May 16th

DRAFTED: BM	COMM HSM864-21 ..	REV.: 00	Page 16 of 32
VERIFIED: MT, NS	FILE: 008-Appendix B.docx	DATE: June 2022	

	TITLE:	SHIP GENERATED WAVES AND CURRENT SPEED MEASUREMENTS CAMPAIGN AT MALAMOCCO -MARGHERA CHANNEL	
	ELAB .:	TECHNICAL REPORT	

4.3 Current speed measurement

Current speed and direction during ship transits were obtained from processing of ADCP profiler measurements. For each passage, the vertical distribution of current speed as a function of time is reported (see for example Fig. 4.6). In the following Fig. 4.7, the average current speed and direction as a function of time are displayed, while in Fig. 4.8 the same data are shown as vectors. Fig. 4.9 shows the depression wave, as measured by the instruments located at different distances from the channel.

The highest measured speed was 1.18 m/s for the “Eurocargo Alexandria” ship, while the lowest was 0.27 m / s for the “K- Stream”. For the ships “Ramzay”, “Levante” and “Bomar Sedna” it was not possible to measure the current speed, as it couldn’t be separated from the environmental speed fluctuations due to tide and wind, which are in the order of 10÷15 cm / s. These ships generated very small depression waves, less than 10 cm high, and definitely insignificant for the “Levante”.

As already highlighted in the test campaign, from the velocity vectors it is possible to observe the water circulation forced by the bow wave (Kelvin wave), where vectors first directed in the opposite direction of the ship (all ships but “Valle di Nervion” and “Levante”) are heading North.

Tab. 4.2 summarizes the characteristics of the monitored vessels and the results of the measurements in terms of wave amplitude and maximum current speed. The following paragraphs show the detailed graphs of each monitored vessel.

Now	Ship	Length (m)	Length (m)	Draft (m)	Speed ship (kn)	Wave height at Briccola 121 (m)	Wave height at pressure gauge (m)	Maximum current speed (m/s)
6:31	Nordanvik	97.0	17.3	7.3	9.1	0.15	0.14	0.42
6:42	Spirit of Chennai	159.98	24.81	6.9	9.2	0.35	0.32	0.76
6:50 am	Louise Borchard	132.6	19.2	6.3	9.9	0.24	0.23	0.44
6:54	K- Stream	121.93	18.45	4.5	10.3	0.14	0.13	0.27
7:08	Ramzay	88.74	16.70	5.0	7.9	0.07	0.04	NM
7:27	Eurocargo Alexandria	200.85	26.50	7.5	10.5	0.70	0.70	1.18
9:31	Valle di Nervion	176.0	31.0	7.3	9.0	0.49	0.43	1.10
9:43	Levante	58.04	9.5	2.0	10.2	NM	NM	NM
10:51	Bomar Sedna	101.39	19.05	7.6	8.6	0.10	0.08	NM

Tab. 4.2 - Amplitude of the depression wave generated by passing ships, as measured at Briccola 121 and in the pressure cell, and maximum current speed measured by the ADCP. Red text refers to insignificant events, which are not reported in detail in the following paragraphs. "NM" indicates that the parameter was not measurable (ship effects below environmental fluctuations).

DRAFTED: BM	COMM HSM864-21 ..	REV.: 00	Page 17 of 32
VERIFIED: MT, NS	FILE: 008-Appendix B.docx	DATE: June 2022	

4.3.1 Spirit of Chennai

"Spirit of Chennai" is a container ship heading to Porto Marghera. The draft was 6.9 m and the speed 9.2 knots. As it passed through the monitoring range, the ship generated a depression wave of 0.35 m at briccola 121 and 0.32 dbar at the pressure cell. The maximum current speed was 0.76 m/s.



Fig. 4.5 - Spirit of Chennai ship passing through the measuring range

DRAFTED: BM	COMM HSM864-21 ..	REV.: 00	Page 18 of 32
VERIFIED: MT, NS	FILE: 008-Appendix B.docx	DATE: June 2022	

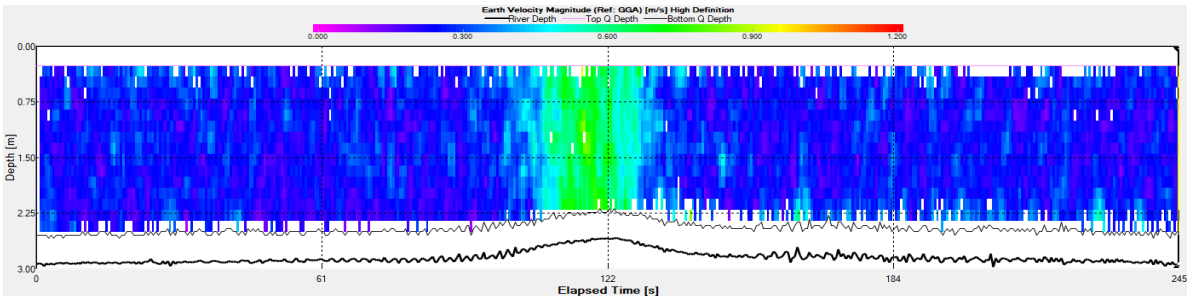


Fig. 4.6 - Vertical distribution of current speed as a function of time (ADCP)

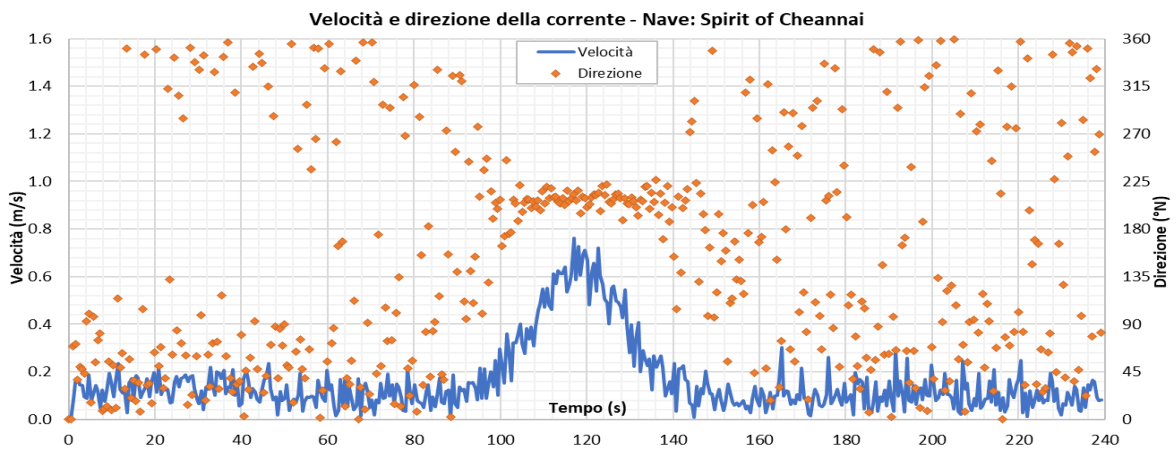


Fig. 4.7 - Average current speed and direction as a function of time (ADCP)

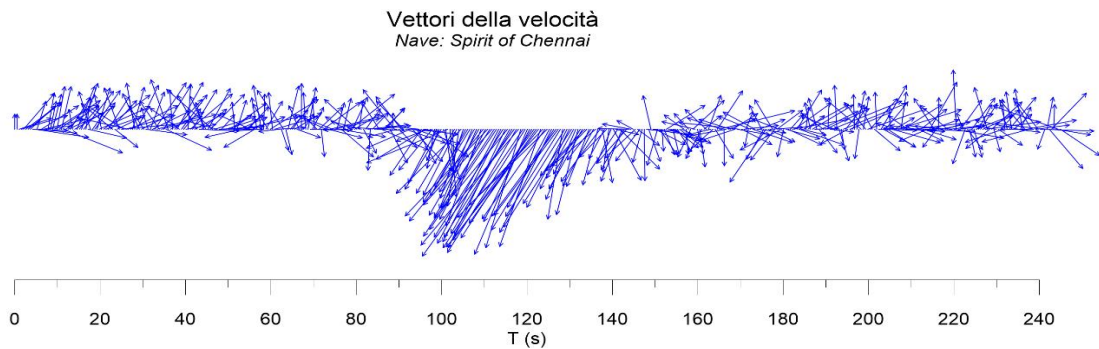
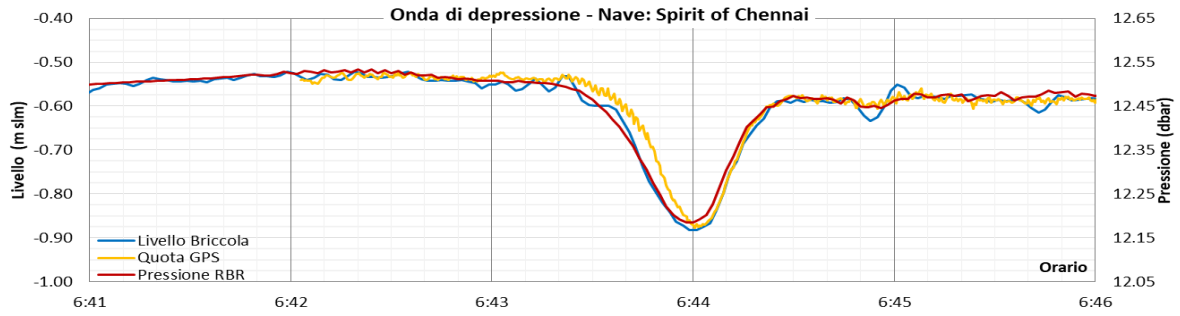


Fig. 4.8 - Current speed vectors measured by ADCP



**Fig. 4.9 - Depression wave measured at different instruments
(ultrasonic gauge at Briccola 121, GPS on drone boat and seabed pressure gauge)**

DRAFTED: BM	COMM HSM864-21 ..	REV.: 00	Page 20 of 32
VERIFIED: MT, NS	FILE: 008-Appendix B.docx	DATE: June 2022	

4.3.2 Louise Borchard

The "Louise Borchard " is a container ship heading to Porto Marghera. The draft was 6.3m and the speed 9.9 knots. As it passed through the monitoring range it generated a 0.24 m high wave at bricola 121 and 0.23 dbar at the pressure gauge. The maximum current speed was 0.44 m/s.



Fig. 4.10 - Louise Borchard ship passing through the measuring range

DRAFTED: BM	COMM HSM864-21 ..	REV.: 00	Page 21 of 32
VERIFIED: MT, NS	FILE: 008-Appendix B.docx	DATE: June 2022	

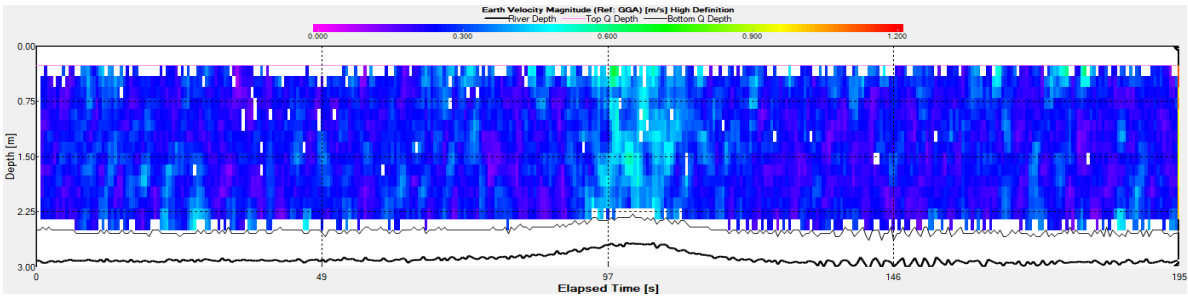


Fig. 4.11 - Vertical distribution of current speed as a function of time (ADCP)

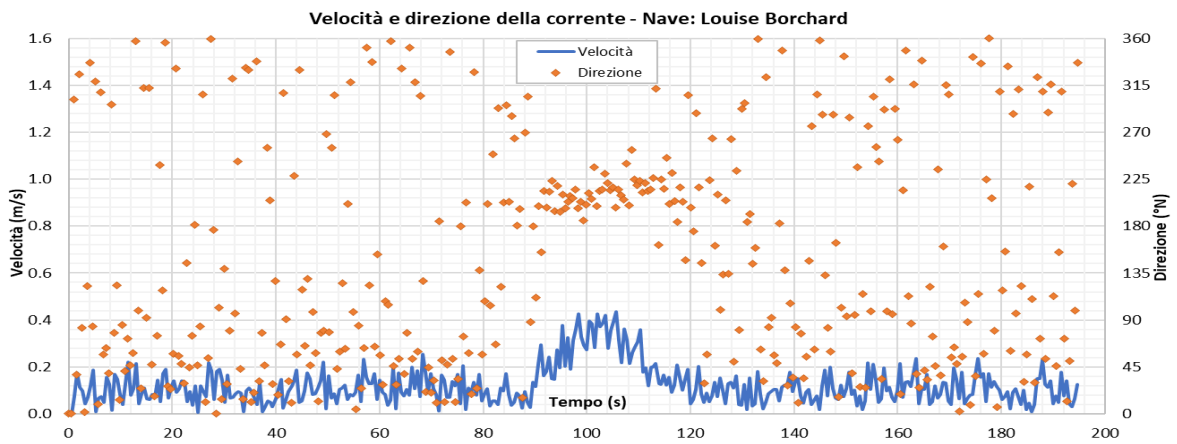


Fig. 4.12 - Average current speed and direction as a function of time (ADCP)

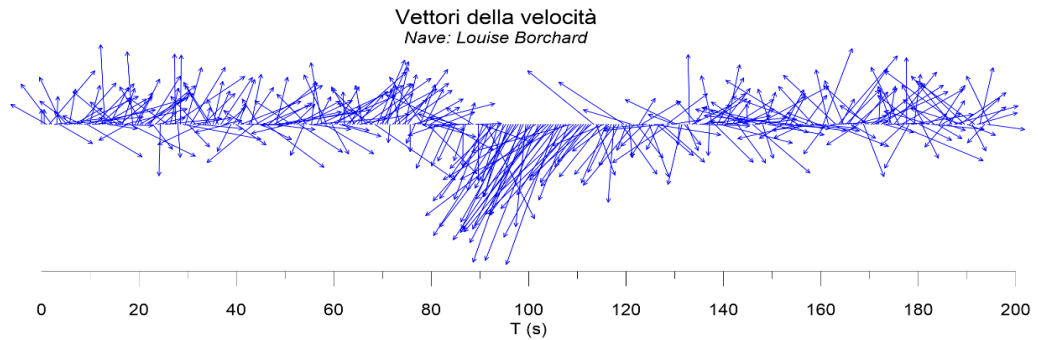


Fig. 4.13 - Current speed vectors measured by ADCP

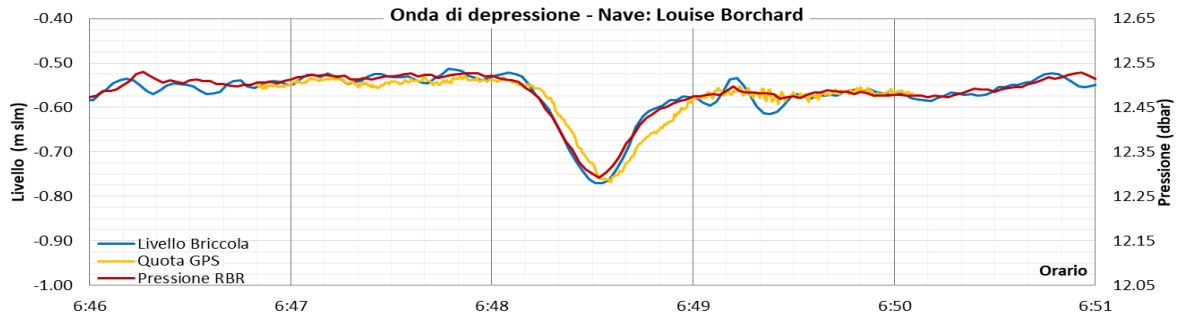


Fig. 4.14 - Depression wave measured at different instruments (ultrasonic gauge at Briccola 121, GPS on drone boat and seabed pressure gauge)

DRAFTED: BM	COMM HSM864-21 ..	REV.: 00	Page 23of 32
VERIFIED: MT, NS	FILE: 008-Appendix B.docx	DATE: June 2022	

4.3.3 Eurocargo Alexandria

The Eurocargo Alexandria is a Ro-Ro ship heading to Porto Marghera. The draft was 7.5 m and the speed 10.5 knots. As it passed through the monitoring, it generated a depression wave of 0.70 m at briccola 121 and of 0.70 dbar at the pressure cell.

The maximum current speed was 1.18 m/s.



Fig. 4.15 - Eurocargo Alexandria ship passing through the measuring range

DRAFTED: BM	COMM HSM864-21 ..	REV.: 00	Page 24 of 32
VERIFIED: MT, NS	FILE: 008-Appendix B.docx	DATE: June 2022	

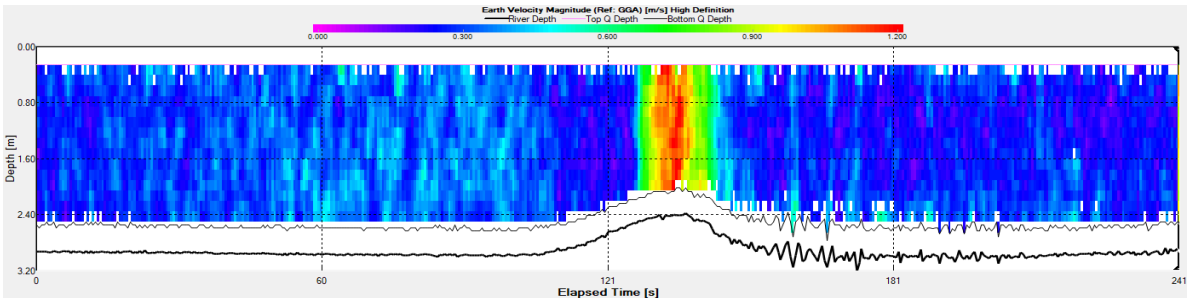


Fig. 4.16 - Vertical distribution of current speed as a function of time (ADCP)

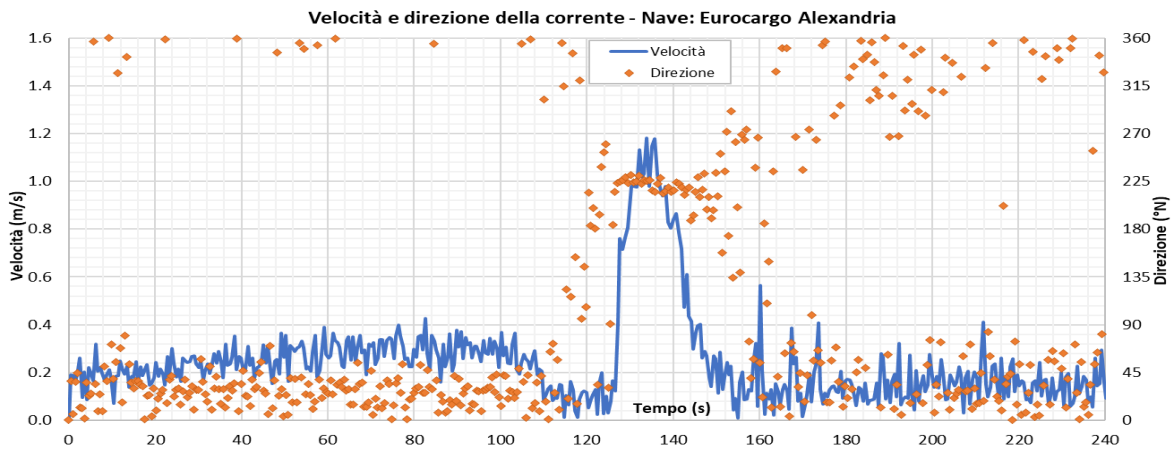


Fig. 4.17 - Average current speed and direction as a function of time (ADCP)

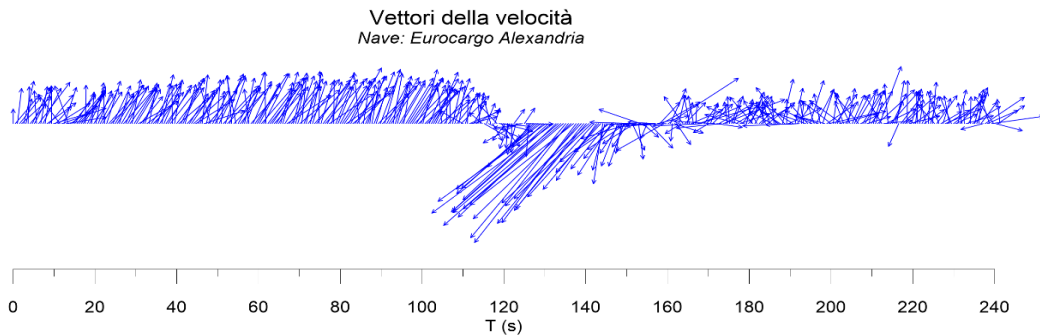


Fig. 4.18 - Current speed vectors measured by ADCP

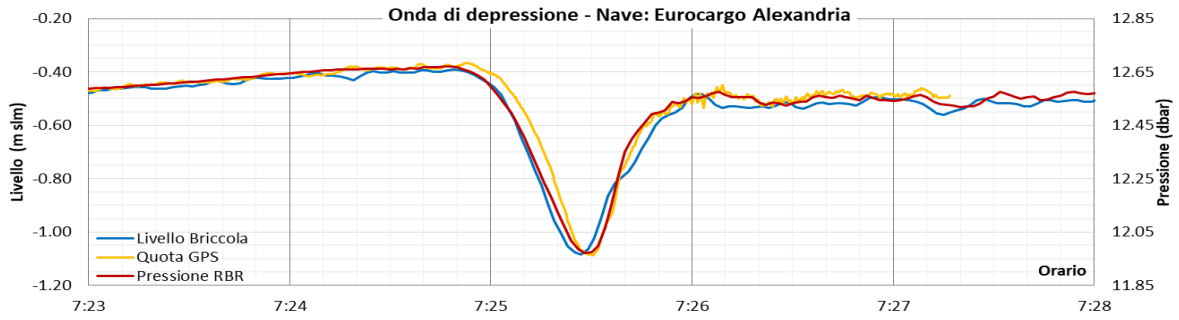


Fig. 4.19 - Depression wave measured at different instruments (ultrasonic gauge at Briccola 121, GPS on drone boat and seabed pressure gauge)

DRAFTED: BM	COMM HSM864-21 ..	REV.: 00	Page 26 of 32
VERIFIED: MT, NS	FILE: 008-Appendix B.docx	DATE: June 2022	

4.3.4 Nervion Valley

The Eurocargo Alexandria ship is a tanker heading to Bocca di Malamocco. The draft was 7.3 m and the speed is 9.0 knots. As it passed through the monitoring range, it generated a depression wave of 0.49 m at bricola 121 and 0.43 dbar at the pressure cell. The maximum current speed was 1.10 m/s.



Fig. 4.20 - Nervion Valley ship passing through the measurement range

DRAFTED: BM	COMM HSM864-21 ..	REV.: 00	Page 27 of 32
VERIFIED: MT, NS	FILE: 008-Appendix B.docx	DATE: June 2022	

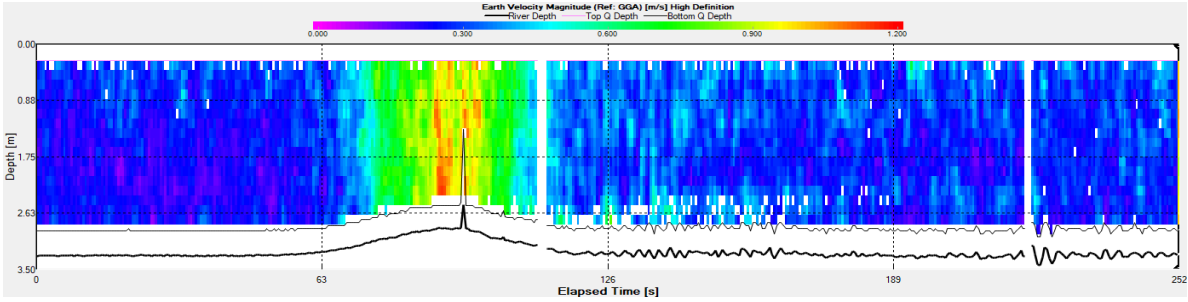


Fig. 4.21 - Vertical distribution of current speed as a function of time (ADCP)

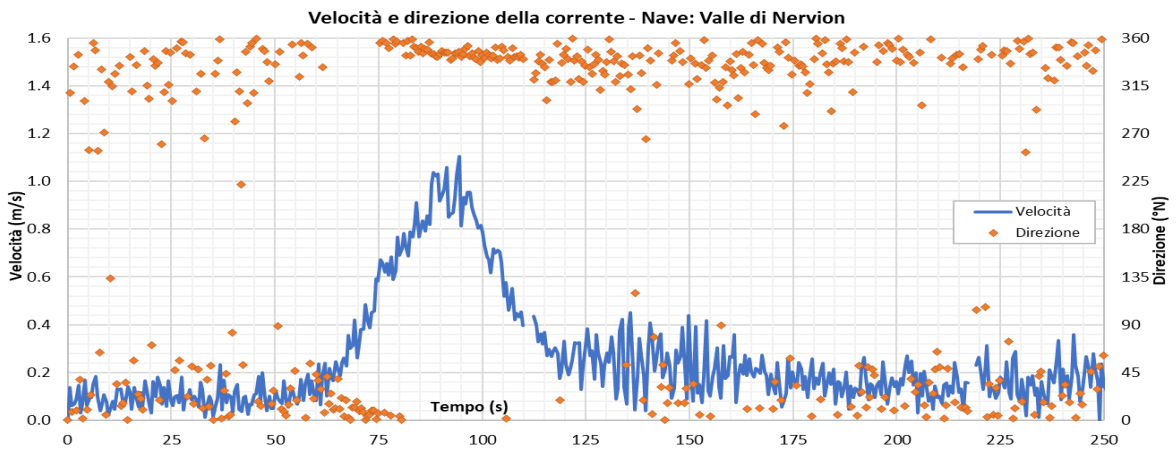


Fig. 4.22 - Average current speed and direction as a function of time (ADCP)

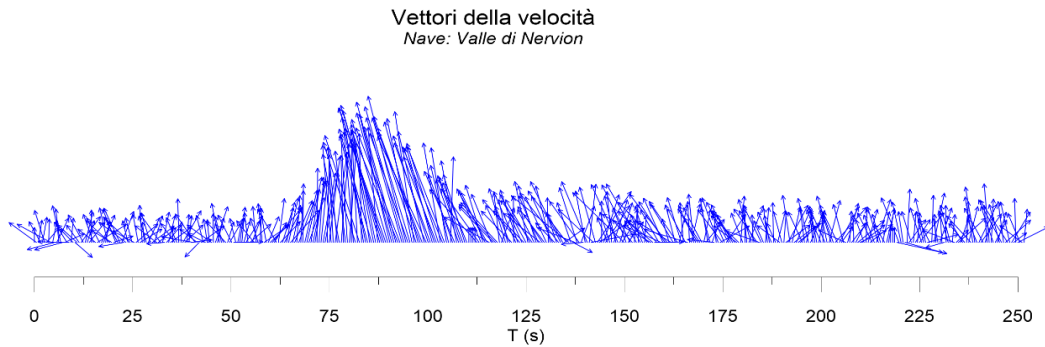


Fig. 4.23 - Current speed vectors measured by ADCP

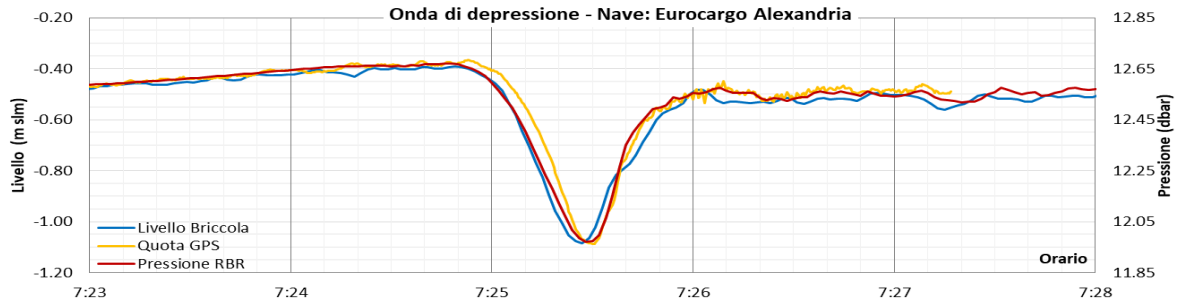


Fig. 4.24 - Depression wave measured at different instruments (ultrasonic gauge at Briccola 121, GPS on drone boat and seabed pressure gauge)

DRAFTED: BM	COMM HSM864-21	REV.: 00	Page 29 of 32
VERIFIED: MT, NS	FILE: 008-Appendix B.docx	DATE: June 2022	

4.4 Current transects across the channel

During the May 16th campaign, 2 current transects were measured next to briccola 121, towing the ADCP drone boat across the channel (Fig. 4.25). The aim was to measure the undisturbed current speed at two different tidal phases (Fig. 4.26). Tab. 4.3 shows the summary of speed measurements at the transect: the average speed in the section, the maximum speed with the related depth and the surface speed (average speed in the first 3 m).

Fig. 4.27 and Fig. 4.28 show the velocity distributions measured by the ADCP current profiler in terms of vectors and maps.



Fig. 4.25 - Position of the survey area and of the ADCP transect near the Briccola 121

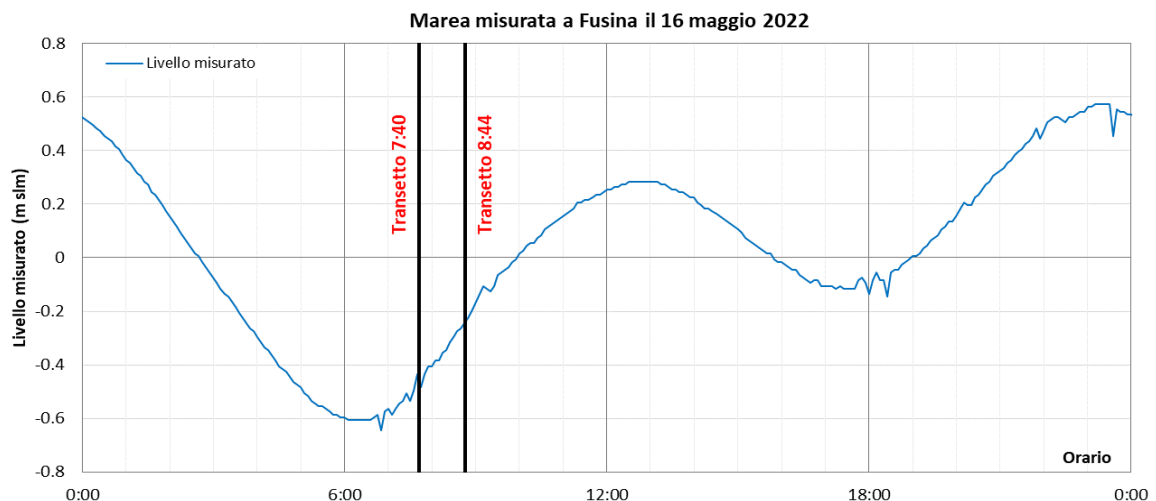


Fig. 4.26 - Tide measurement at Fusina quay (may 16th campaign) and points of transect measurements

DRAFTED: BM	COMM HSM864-21	REV.: 00	Page 30 of 32
VERIFIED: MT, NS	FILE: 008-Appendix B.docx	DATE: June 2022	

The measurements show that the current is directed straight along the channel (see vector plots in Fig. 4.27 and Fig. 4.28).

The measurement performed at 7:40, at the beginning of flood tide, showed the lower current speed. The average speed in the section was equal to 0.25 m/s, while the maximum was 0.66 m/s at -0.76 m depth. The speed is evenly distributed in the section, with an average surface speed of 0.28 m/s (from 0 to -3 depth).

The measurement performed at 8:44, at full flood tide, showed the highest current speed. The average speed in the section was 0.35 m/s, while the maximum was 0.84 m/s at -0.56 m depth. The speed was not evenly distributed and was higher at the surface. The average surface speed was 0.44 m/s (from 0 to -3 depth).

Parameter	Transect (7:40)	Transect (8:44)
Total DAQ length (m)	250	235
Transect length (m)	243.45	238.51
Average speed (m/s)	0.25	0.35
Maximum speed (at depth "d") (m/s)	0.66 (d = -0.76 m)	0.84 (d = -0.56 m)
Surface speed (average 0-3 m) (m/s)	0.28	0.44

Tab. 4.3 - Summary of current speeds measured at the transect

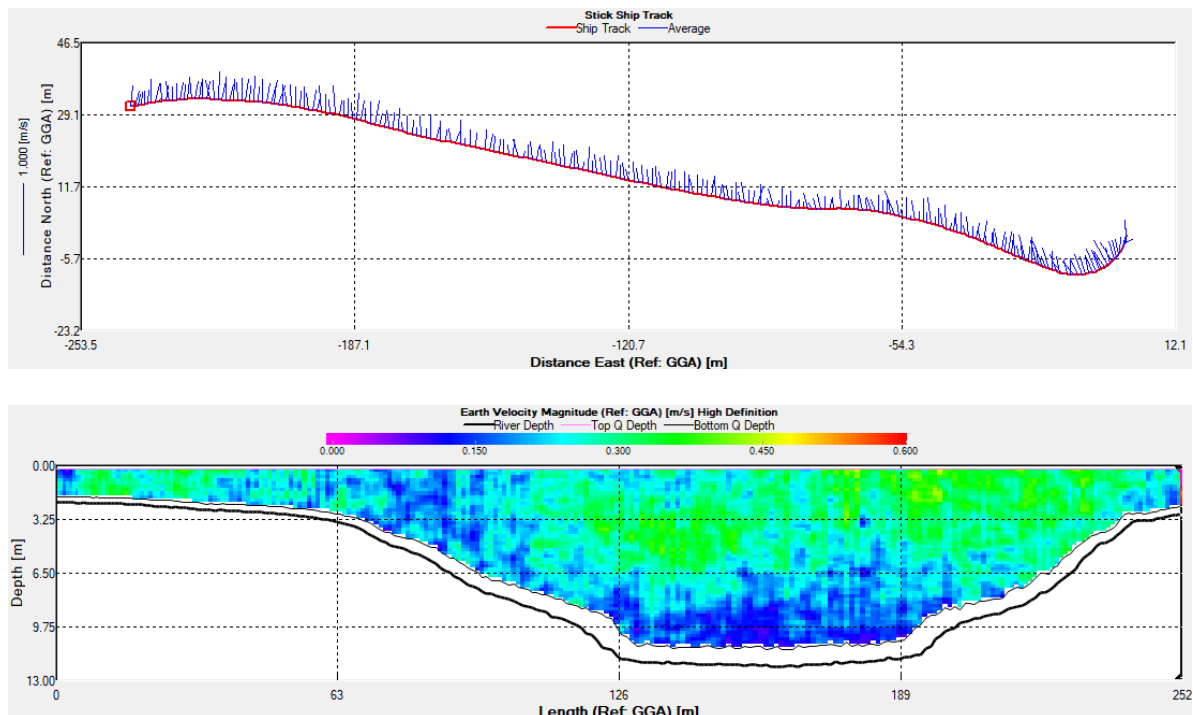


Fig. 4.27 - Speed distribution along the transect at 7:40 in the channel

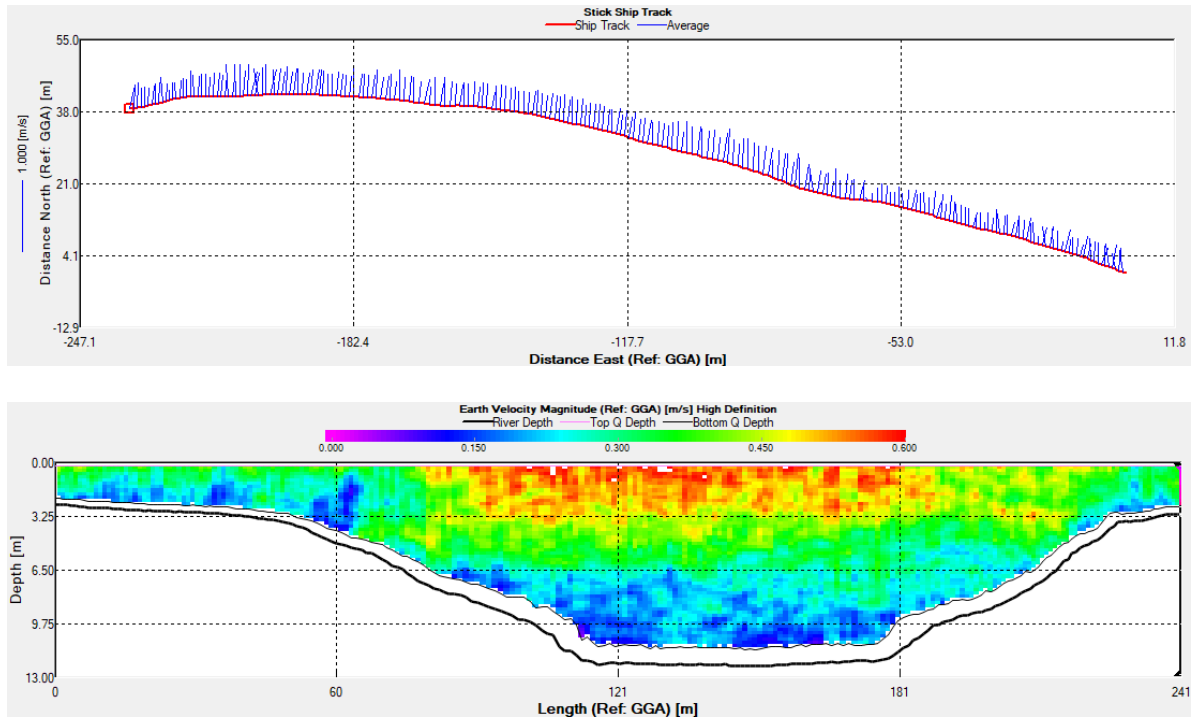


Fig. 4.28 - Speed distribution along the transect at 8:44 in the channel

DRAFTED: BM	COMM HSM864-21 ..	REV.: 00	Page 32 of 32
VERIFIED: MT, NS	FILE: 008-Appendix B.docx	DATE: June 2022	



Authorized by the European Commission
Priority of the Trans-European



AROUND WATER
di Andrea Zamariolo, Ph.D. Geol.





APPENDIX C

CRITICAL SHEAR STRESS DISTRIBUTION FOR THE MODEL'S SETUP



AROUND WATER
di Andrea Zamariolo, Ph.D. Geol.





Authorized by the European Commission
Priority of the Trans-European



AROUND WATER
di Andrea Zamariolo, Ph.D. Geol.



Critical shear stress distribution for the model's setup

The available information and dataset summary

The critical shear stress of the lagoon sediments is dependent on a number of physical, biological, and human stressors. The only available maps (Fig. 1) that report the distribution of the variable for the Venice Lagoon are those reported by Amos et al. (2010), based on two surveys conducted in the summer of 1998 and the following winter using two benthic annular flumes (Amos et al., 2004).

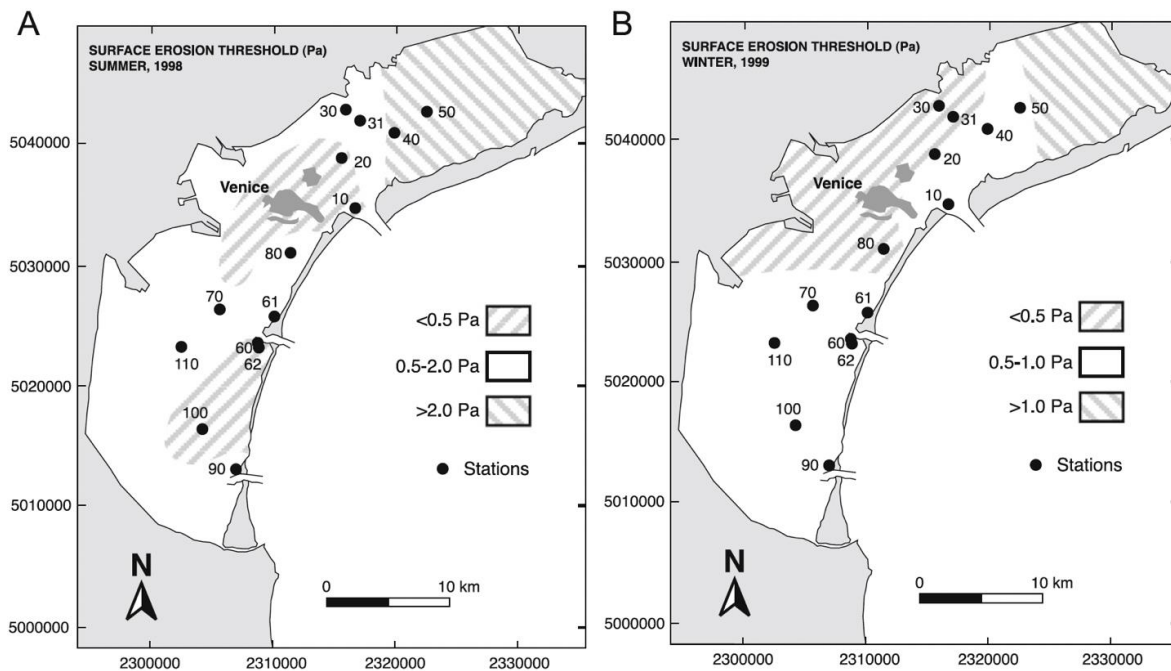


Figure 1 - The sites occupied during the summer (A) and winter (B) surveys of Amos et al. (2004). Also shown are the regions of surface erosion threshold (τ_c) interpolated across the entire lagoon. Notice that in both periods, the highest threshold is found in the northern lagoon, and the lowest in a broad region around the city of Venice (after Amos et al., 2010).

These data have already been deeply presented and discussed in the *Technical and Methodological Report* of phase 1 (see Chapter 4). As a synthesis, we can assign the average critical shear stress to different morphological zones, as follows:

- $\tau_c < 0.5\text{ Pa}$ in areas involved in boat traffic and intense Manila clam fishing;
- $\tau_c = 1.62 \pm 1.07\text{ Pa}$ in intertidal areas with a great heterogeneity (or patchiness); variability is greater during summertime than winter, and strongly influenced by seabed habitat type and depth;
- $\tau_c = 0.76 \pm 0.45\text{ Pa}$ in bare subtidal mud flats;
- $\tau_c = 1.23 \pm 0.62\text{ Pa}$ along channel margins;

An additional information regards the effects of seagrass cover and microphytobenthos, which tend to stabilize the lagoon bottom, thus increasing the critical shear stress. Re-arranging the data of Amos et al. (2004; 2010) we obtain:

- $\tau_c = 0.90 \pm 0.53\text{ Pa}$ in tidal flat with microphytobenthos cover;
- $\tau_c = 1.18 \pm 0.64\text{ Pa}$ in tidal and subtidal flat with seagrass cover (20-60% of *Zoostera noltii*).

The variability of the critical shear stress measured on the lagoon bottom, as well as the large scatter of the values when compared to the bulk density (dependent on water content and grainsize), do not

appear to indicate the need to investigate grainsize further as a primary controlling factor. Particularly for the Malamocco basin.

To validate this assumption, the more recent lagoon grainsize dataset reported by Zonta et al. (2018) was examined. The majority of sites showed a significant depletion of finer particles in the surface (10 cm) sediment layer compared to the deeper ones. For the Malamocco basin, three main outcomes are worth noting:

- 1) the grain size variability of surficial sediments is quite limited, due to the dominance of sandy silt and silty sand, according to the Shepard's (1954) nomenclature.
- 2) the surficial sediment layer is significantly depleted of fine mud (20-40%) compared to the deeper layer.
- 3) The fine mud depletion is the result of a selective process involving the sortable silt, progressively eroded by the wind waves, which are more effective over the deepest (erosional) lagoon basin.

These results confirm the well-known erosional tendency that affected the Malamocco basin during the morphological evolution from 1927 to 2002 (Sarretta et al., 2010), thus supposing a certain stabilization reached after the major morphological changes due to lagoon submergence reported by the same authors.

Although limited to a small area close to the Malamocco-Marghera canal near Fusina, Scarpa (2019)'s comparison of grainsize, water content, and computer tomography (CT) number provides an indirect observation of the critical shear stress invariance with respect to the grainsize for the Malamocco basin. CT number is a proxy of bulk density, which is inversely correlated to water content and the finest mud (<16 μm) content (Zonta et al., 2021). If we extrapolate the bulk density from the original water content and CT number reported by Scarpa (2019), the correlation between the median of sediment and bulk density is weak, due to the very high variability of density (1.4 – 1.9 g cm^{-3}) for sediments with median < 100 μm (typical of the silty sand-sandy silt sedimentary matrix of the Malamocco basin). This variability is likely to be related to the variable degree of compaction of the sediment, which in turn depends on the presence-absence of microfilm, seagrass cover, and intense winnowing due to clam harvesting and boat transit.

Accordingly, Petti et al. (2018) adopted the morphological and forcing similarity criterion without any assumptions on grainsize, in modeling the siltation processes of tidal channels in the Marano-Grado Lagoons. They consider representative mean values for the critical erosion shear stress, chosen from the experimental results by Amos et al. (2004), in the range from 0.5 Pa to 1.8 Pa, as follow:

- $\tau_c = 1.8 \text{ Pa}$: marshes and highest intertidal flats, wet only by the high tide;
- $\tau_c = 1.2 \text{ Pa}$: tidal flats occupied by the seagrass in patches that covered 20–60% of the seabed, assumed partially stabilized;
- $\tau_c = 0.7 \text{ Pa}$: permanently submerged lowest mudflats and subtidal flats, with the mean critical shear stress already adopted in the Venice Lagoon;
- $\tau_c = 0.5 \text{ Pa}$: mudflats subject to greater sediment mobility and reworking due to shellfish farming.

The adopted approach and critical shear stress distribution

According to the above-mentioned assumptions, we decided to adopt the same approach of Petti et al. (2018), in order to assess the effects of various Malamocco-Marghera canal configuration and marine traffic on the surrounding intertidal and subtidal muddy flats. Considering both the original findings by Amos et al. (2004; 2010) and the simplification of Petti et al. (2018), the final parametrization for the critical shear stress distribution is as follows:

CRITICAL SHEAR STRESS

MORPHOLOGY - CHARACTERISTICS

Stable (no erosion)	marshes and highest intertidal flats, wet only by the high tide
$\tau_c = 1.2 \text{ Pa}$	channels, canals and their margins, using the average value of Amos et al. (2004; 2010), as well in the assumption that their configuration is nowadays quite stable after the major morphological changes during the interval 1930-2000
$\tau_c = 0.9 \text{ Pa}$	tidal flats occupied by the seagrass, assumed partially stabilized; we adopted a value lower than that used by Petti et al. (2019) in order to consider patchiness and uncertainty in the species identification
$\tau_c = 0.7 \text{ Pa}$	permanently submerged lowest tidal flats and subtidal flats, with the mean critical shear stress already adopted in the Venice Lagoon and Marano-Grado Lagoons
$\tau_c = 0.5 \text{ Pa}$	bare tidal flats subject to greater sediment mobility and reworking due to clam harvesting (either concession and nursery)

The following is a summary of the information collected to define the critical shear stress area distribution. Data were recovered in GIS to cover the entire geographic space for modeling, using a 200x200 m grid for tidal flats and 50x50 m for channels.

- Channels, canals and margins ($\tau_c = 1.2 \text{ Pa}$)

Values of shear stress of 1.2 Pa were assigned to all the channelized system, as reported in Figure 2. The grid is 50x50 m.



Figure 2 – The channel system of the Malamocco basin, where it has been assigned a critical shear stress of sediment of 1.2 Pa. The grid is 50x50 m.

- Tidal flats covered by the seagrass ($\tau_c = 0.9$ Pa)

Dataset on seagrass distribution has been furnished by Port Authority. Other information is available in the *Atlante della Laguna WebGIS* (<http://www.atlantedellalaguna.it>).

Before assigning the critical shear stress attribute in GIS, we controlled the most recent aerial photos in Google Earth (March 2021) for matching the available dataset (unknown update) with the photographic evidence. We found some differences, since a lot of seagrasses has disappeared in the northern half of the basin, as reported in Fig. 3.

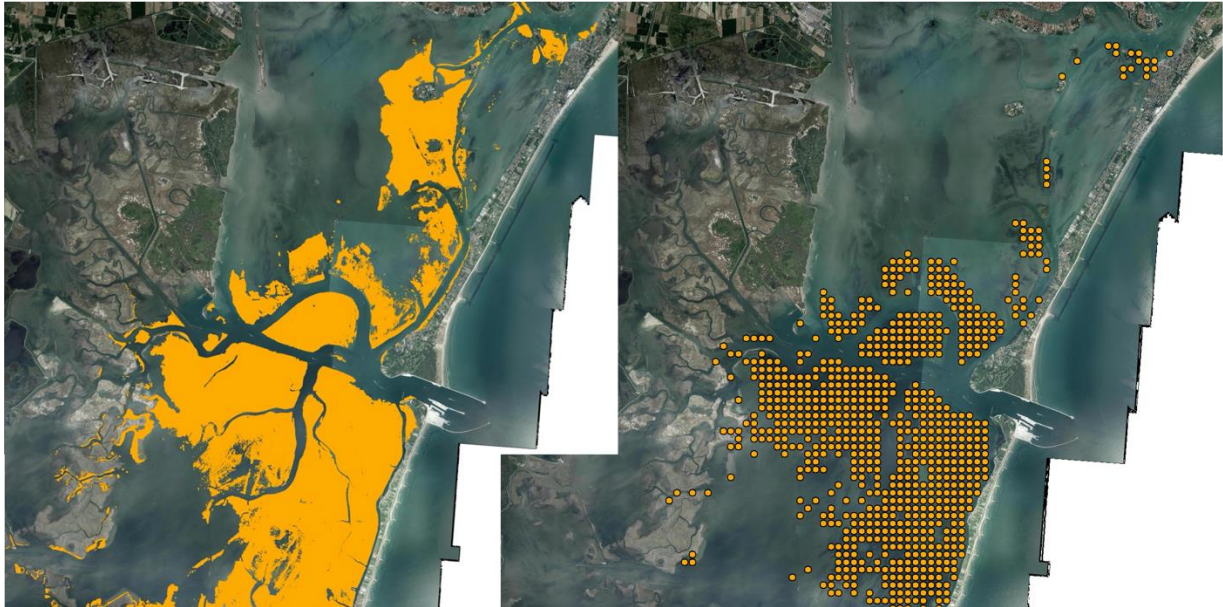


Figure 3 – Distribution of sea grass in the Malamocco basin (GIS layer furnished by the Port Authority) compared to the grid with the assigned value of critical shear stress of 0.9 Pa. Differences are due to disappearance of seagrass cover, as controlled using the most recent Google Earth aerial photos (March 2021). The grid is 200x200 m.

A detail of the grid points and aerial photo is reported in Figure 4.



Figure 4 – Detail of the distribution of sea grass in the Malamocco basin, close to the inlet. On the left the grid adopted after controlling the GIS layer furnished by the Port Authority with the aerial photo of Google Earth (March, 2021) on the right. The grid is 200x200 m.

- Permanently submerged tidal flats ($\tau_c = 0.7$ Pa)

These morphologies are easily mapped as the results of the remnant tidal flats after the exclusion of the other categories (Figure 5). The values are representative of the mean critical shear stress of the Venice Lagoon (Amos et al., 2004; 2010).

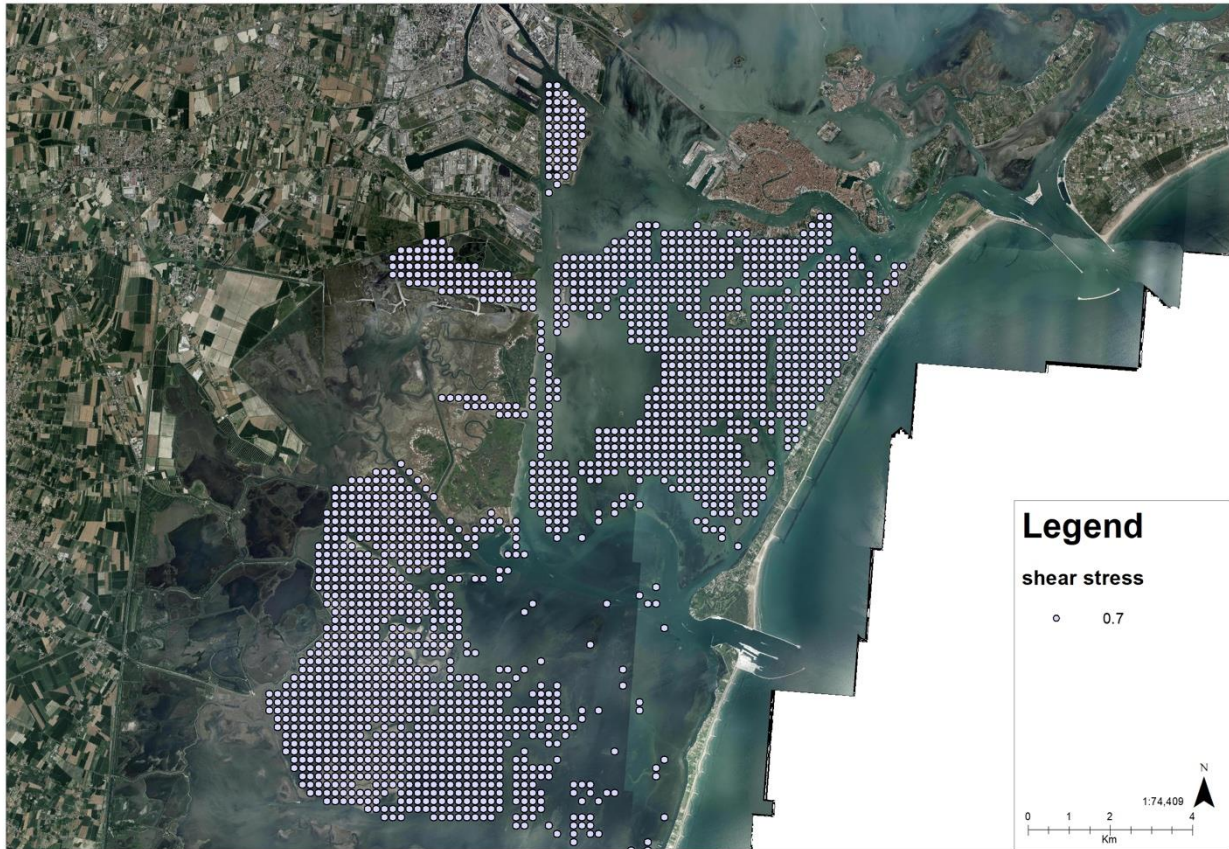


Figure 5 – Distribution of the tidal flats with the assigned value of critical shear stress of 0.7 Pa. The grid is 200x200 m.

- Reworked tidal flats due to clam harvesting ($\tau_c = 0.5$ Pa)

We used all available information to verify the capability of current and past activities to induce relevant changes to the lagoon bottom in order to accurately map the areas involved in fishing activities. Finally, we controlled the aerial photograph available in Google Earth to see if any effect was still visible in the clam harvesting tidal flats.

A first general overview of the past activity is reported in the *Morphological Plan* and in the *Atlante della Laguna WebGIS* (Figure 6). The more recent report by Pessa et al. (2018) confirms part of the past concessions and provides details on the new proposals for concessions and nursery areas (Figure 7). These latter are important as well, since the nursery areas are used to breed the Manila clam seeds that are mechanically collected, thus having a significant impact on the sedimentary layer. We decided to attribute the same critical shear stress for concessions and nursery areas after controlling with aerial photographs, because mechanical dredging is confirmed to induce relevant morphological and sedimentary structure changes (Figure 8).

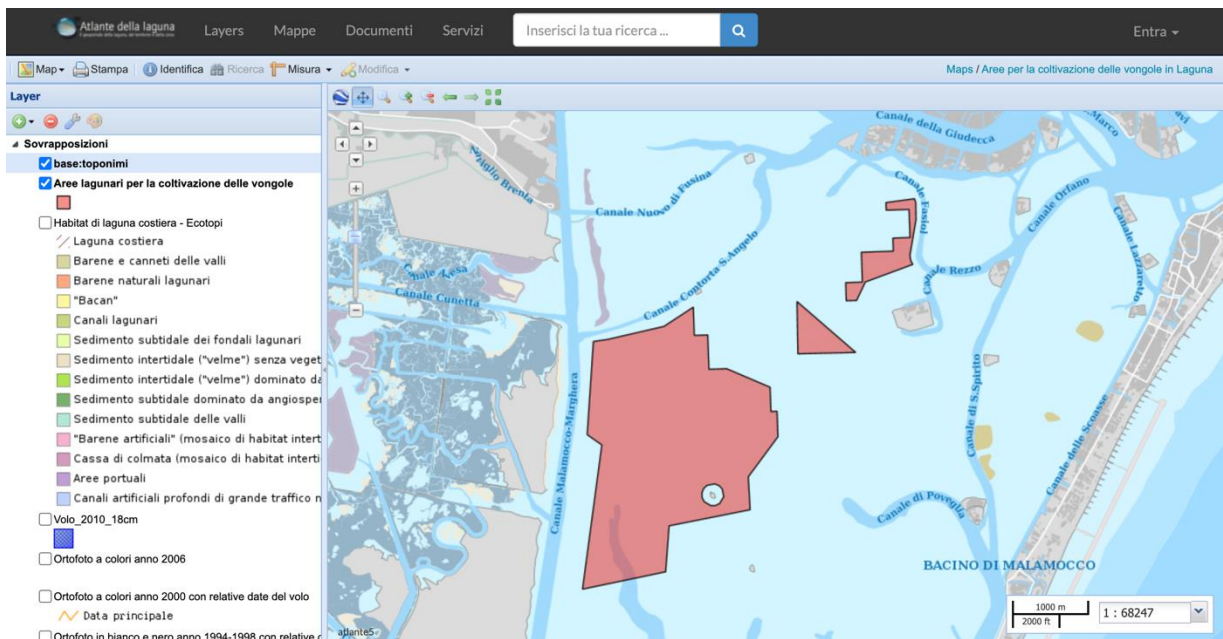


Figure 6 – Distribution of the tidal flats involved in the clam fishing activities (<http://www.atlantedellalaguna.it>).

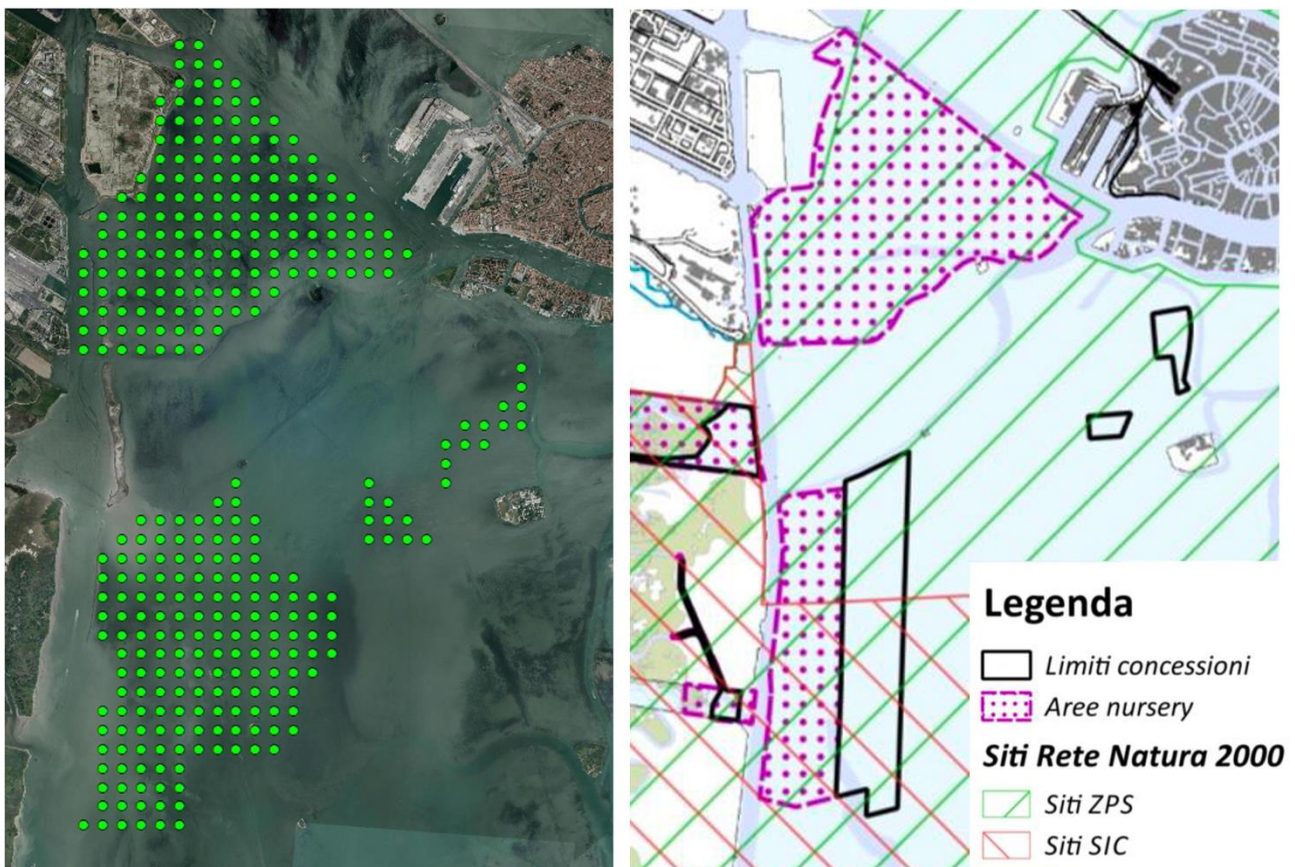


Figure 7 – Distribution of the tidal flats with the assigned value of critical shear stress of 0.5 Pa. The grid is 200x200 m. On the right the control of the data reported in the more recent and update report on the fishing activity (Pessa et al., 2018).

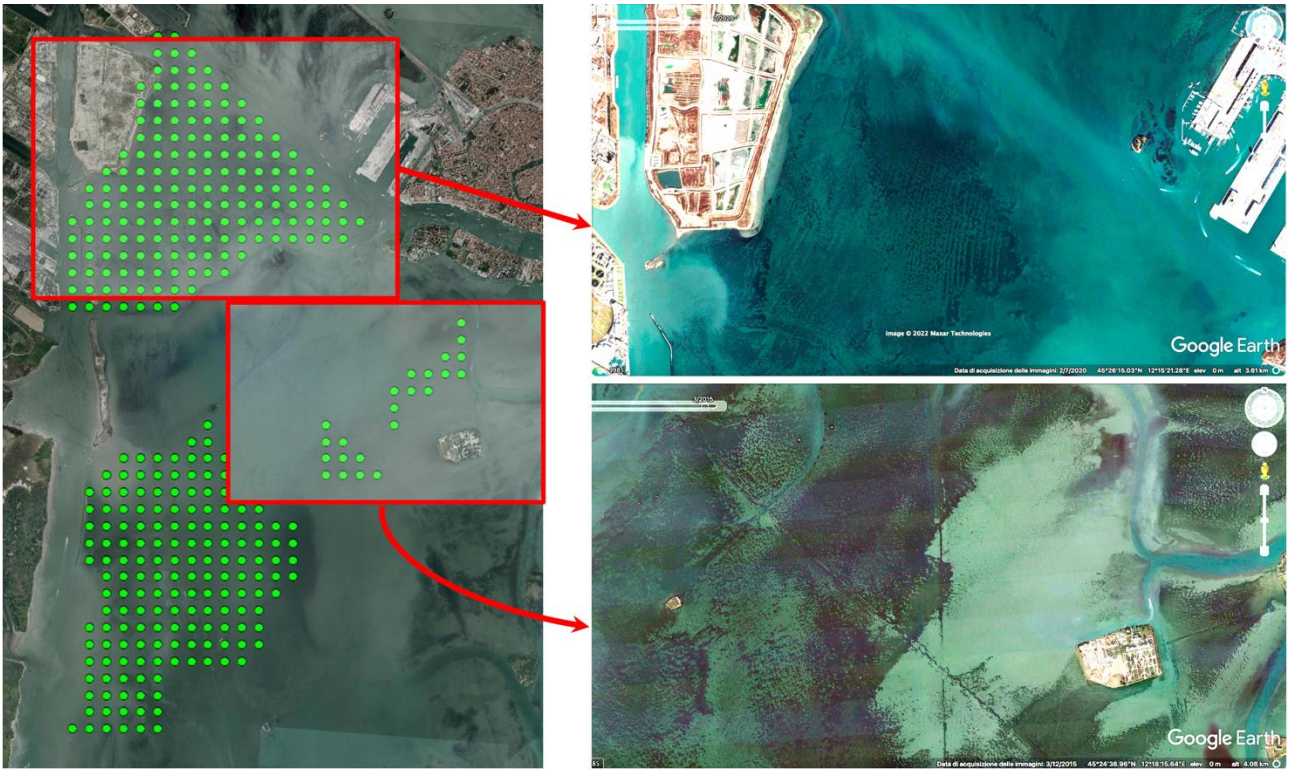


Figure 8 – Effects of the mechanical dredging on the tidal flats used as clam fishing concessions and nursery areas. On the left are the areas where the 0.5 Pa attribute has been assigned for critical shear stress at the bottom. On the right are the tidal flats exploited for clam harvesting, where there are visible the regular alignments of runnels and microtopography with differential current lineations caused by the mechanical seed collection (upper box) and the bare mudflat as the result of the dredging for clam exploitation (Google Earth photos, 2015 and 2020).

- The final grid

The final grid adopted with the different critical shear stresses used for the modeling purposes of the Malamocco basin is reported in Figure 9.

Figure 10 reports the detail of the grid in terms of spatial density: 200x200 m for the entire basin, 50x50 m for the channel network.

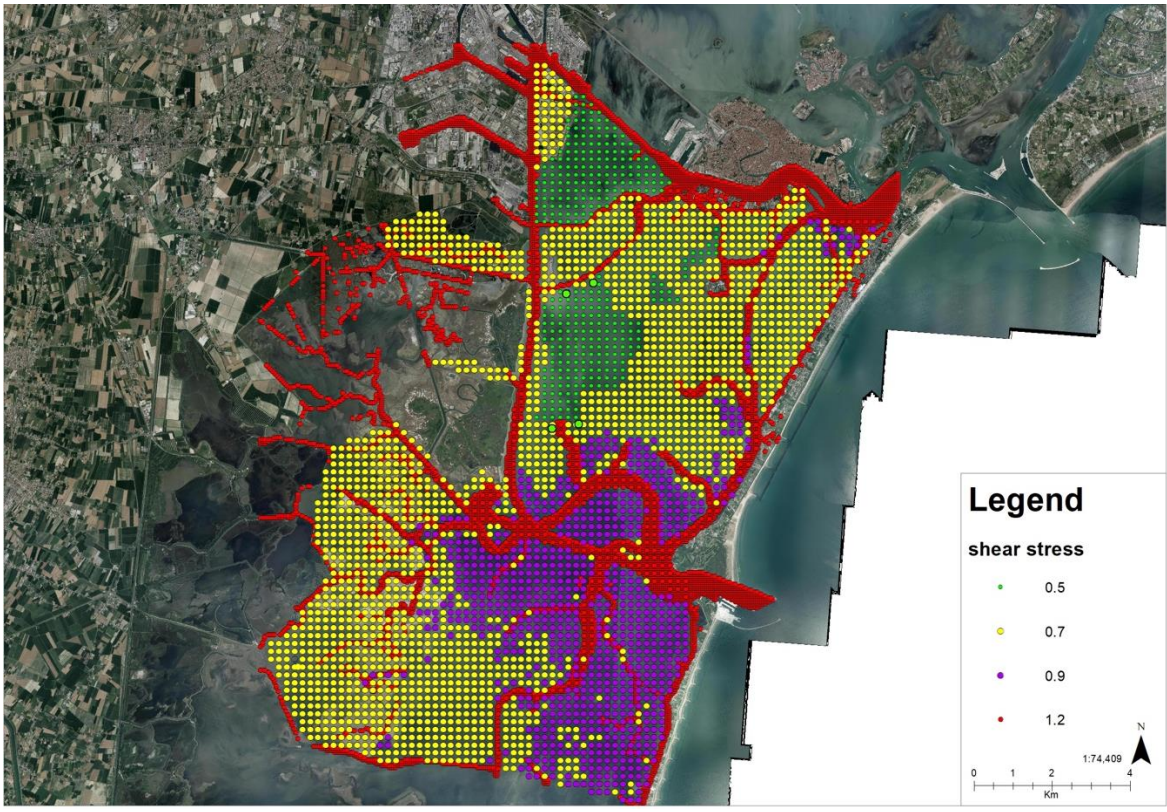


Figure 9 – The final grid with the different critical shear stresses adopted for the modeling purposes

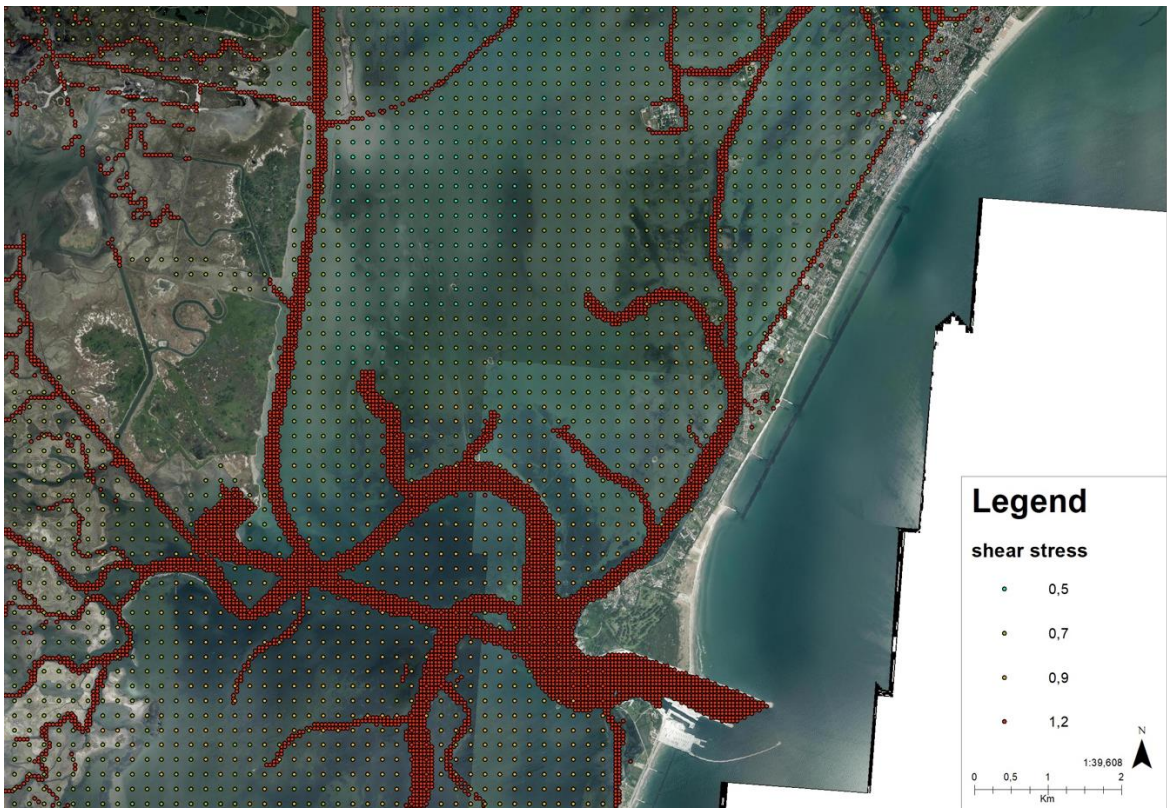


Figure 10 – Detail of the GRID density.

References

- Amos C.L., Bergamasco A., Umgiesser G., Cappucci S., Cloutier D., DeNat L., Flindt M., Bonardi M., Cristante S. (2004) The stability of tidal flats in Venice lagoon – the results of in-situ measurements using two benthic, annular flumes. *Journal Marine Systems* 51: 211–241.
- Amos C.L., Umgiesser G., Ferrarin C., Thompson C.E.L., Whitehouse R.J.S., Sutherland T.F., Bergamasco A. (2010) The erosion rates of cohesive sediments in Venice lagoon, Italy. *Continental Shelf Research* 30: 859-870.
- Pessa G., Fischetti D., Saggese A. (2018) Piano d'uso delle aree in concessione per la venericoltura. San Servolo s.r.l. Servizi Metropolitan di Venezia, Gestione Risorse Lagunari. Technical Report: 99 pp.
- Petti M., Bosa S., Pascolo, S. (2018) Lagoon Sediment Dynamics: A Coupled Model to Study a Medium-Term Silting of Tidal Channels. *Water* 10, 569. <https://doi.org/10.3390/w10050569>.
- Sarretta A., Pillon S., Molinaroli E., Guerzoni S., Fontolan G., (2010) Sediment budget in the Lagoon of Venice. *Continental Shelf Research*, 30: 934-949.
- Scarpa G.M., 2019. Impatti del traffico navale ed effetti della risospensione indotta nelle aree spondali e sulle piane di marea della Laguna di Venezia. Tesi di dottorato in Scienze Ambientali, Università Ca' Foscari Venezia, Ciclo XXXI, 150 pp.
- Shepard F.P. (1954) Nomenclature based on sand-silt-clay ratios. *Journal of Sedimentary Research* 24: 151-158.
- Zonta R., Botter M., Cassin D., Bellucci L.G., Pini R., Dominik J. (2018) Sediment texture and metal contamination in the Venice Lagoon (Italy): A snapshot before the installation of the MOSE system. *Estuarine Coastal and Shelf Science*, 205: 131-151.
- Zonta R., Fontolan G., Cassin D., Dominik J. (2021) X-ray computed tomography as a tool for screening sediment cores: an application to the lagoons of the Po River Delta (Italy). *MDPI Journal of Marine Science and Engineering*, 2021, 9, 323. <https://doi.org/10.3390/jmse9030323>.



AROUND WATER
di Andrea Zamariolo, Ph.D. Geol.





APPENDIX D

CFD SIMULATIONS OF THE WAVE PATTERN GENERATED BY A SHIP HULL IN SHALLOW WATER



AROUND WATER
di Andrea Zamariolo, Ph.D. Geol.





AROUND WATER
di Andrea Zamariolo, Ph.D. Geol.



Report n. 14891

Rev. 00




CFD simulations of the wave pattern generated by a ship hull in shallow water

Autori / Authors: Francesco Furcas Davide Grassi

Data emissione / Issue date:

14/03/2023

Pagina intenzionalmente bianca / *This page intentionally left blank*

Report n. 14891	Rev. 00	Data emissione / Issue date 14/03/2023
<p>Titolo / Title</p> <p>CFD simulations of the wave pattern generated by a ship hull in shallow water</p>		
<p>Autori / Authors</p> <p>Francesco Furcas Davide Grassi</p>		
<p>Sommario / Abstract</p> <p><i>The present technical report describes the numerical activities performed to simulate the model scaled flow field and the wave pattern generated by a ship transit in shallow water and at low speed. The aim of the CFD computation is to capture the wave elevation located at a defined measurement point and compare it with the available experimental data. After a detailed description of the test case vessel, the environment and the numerical CFD (RANS-based) model, the illustration of the results and the comparison with the experiments will be given and critically discussed. All the computations are performed through the commercial RANS solved STAR-CCM+ (v. 15.06.008)</i></p>		
<p>Autori / Authors</p> 	<p>Verificato / Verified</p> 	<p>Approvato / Approved</p> 
<p>Circolazione / Circulation</p> <p>Interna / Internal Only</p> <p>Libera / Free</p> <p><input checked="" type="checkbox"/> Riservata Industriale / Commercial in confidence</p> <p>Classificata / Classified</p>	<p>Codici di distribuzione / Distribution codes</p> <p>DHI S.r.l.</p>	
<p>Pagine / Sheets</p> <p>17</p>	<p>Commessa / Job</p> <p>69160421194</p>	<p>Note / Notes</p> <p>STAR-CCM+ (v. 15.06.008)</p>

Questo Documento è di proprietà di CETENA S.p.A. Non può essere riprodotto, trasmesso con qualsiasi mezzo, inserito in altri documenti, svelato ad altri o comunque usato per qualsiasi scopo diverso da quello per il quale è stato prodotto, senza esplicita autorizzazione scritta di CETENA S.p.A. L'utente del documento ha l'onere di verificare di essere in possesso dell'edizione corrente.

This document is the property of CETENA S.p.A. It may not be reproduced, transmitted by any means, inserted into other documents, disclosed to others or otherwise used for any purpose other than for which it was produced without the express written permission of CETENA S.p.A. The user of the document has the responsibility of verifying of being in possession of the current edition.

Revisioni Precedenti / Previous Revisions

<i>Rev.</i>	<i>Data / Date</i>	<i>Contenuto della Revisione / Revision Content</i>	<i>Autori / Authors</i>

Contenuto della revisione corrente / Current revision content

INDICE

1	Introduction.....	6
2	Description of the test case.....	6
3	Description of the numerical model.....	9
4	Description of the results	15
5	Conclusions	16
6	References	17

1 Introduction

The present technical report describes the numerical simulations carried out to characterize the flow field and the wave pattern generated by the transit of an oil/chemical tanker reference vessel in shallow water. Aim of the computations is to reproduce the measurements performed at sea during the passage of the vessel through the Malamocco-Marghera channel on 16/05/2022 [2].

Since the wave pattern generated by the ship transit is not expected to be influenced by any significant Reynolds-related effect, the numerical computations have been made in model scale to reduce the computational effort.

All the numerical simulations have been carried out through the commercial RANSE solver STAR-CCM+ (v. 15.06.008).

After a brief description of the test case and the numerical model, the results of the numerical analysis will be described in detail and compared with the experiments to draw conclusions and derive a validation of the applied methodology.

2 Description of the test case

The test case is an oil/chemical tanker (Valle di Nervion) whose main data are listed in the following Table 1 and Figure 1.

Table 1: test case main data

Vessel Name	Valle di Nervion
Vessel Type	Oil/Chemical Tanker
Flag	Italy
Gross Tonnage	25063
Summer DWT [t]	39999
Length Overall L_{OA} [m]	176
Breadth [m]	31
Draft [m]	7.3
Vessel speed SOG (V_s) [kts]	9
Current [kts]	+0.5
Direction	Outbound (to Malamocco)

Figure 1: test case (Valle di Nervion)



Since the original hull 3D CAD model is not available for the numerical model, a parent vessel (Figure 2) has been selected and scaled to match the test case main geometrical features (Table 2).

Figure 2: parent vessel 3D CAD geometry

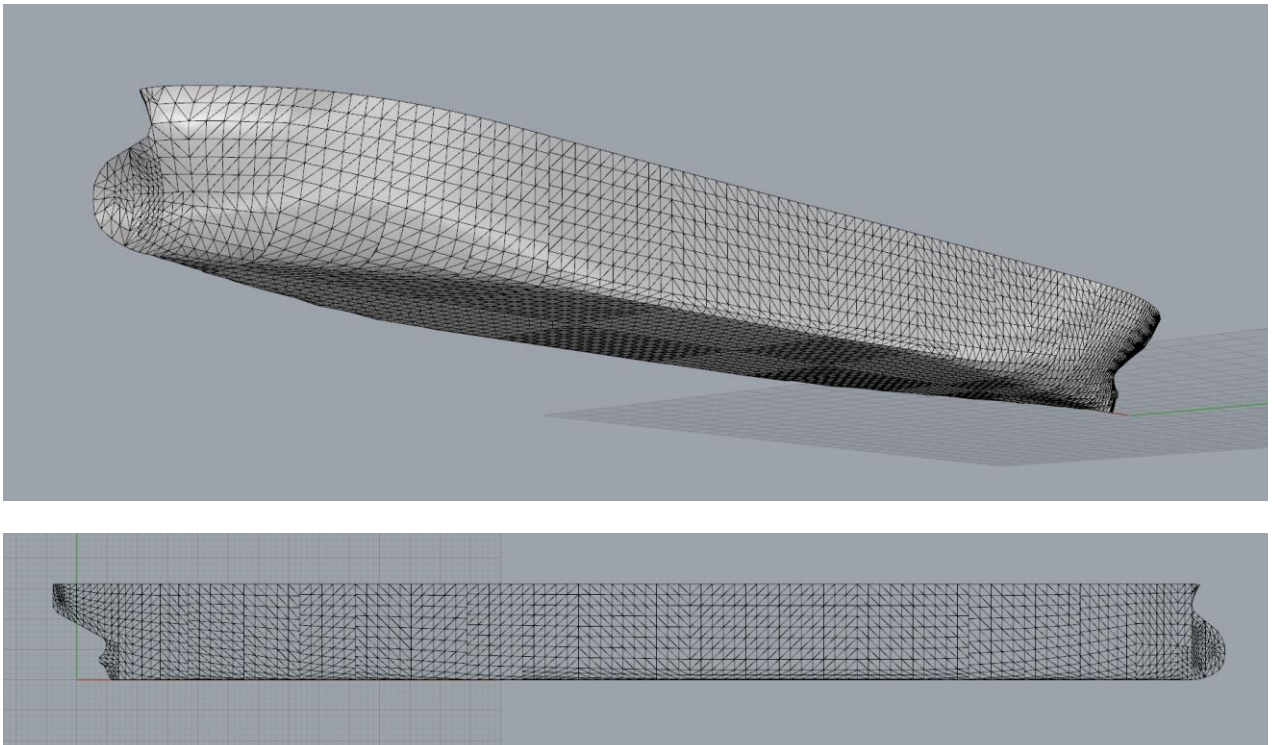


Table 2: scaling factors for the parent vessel

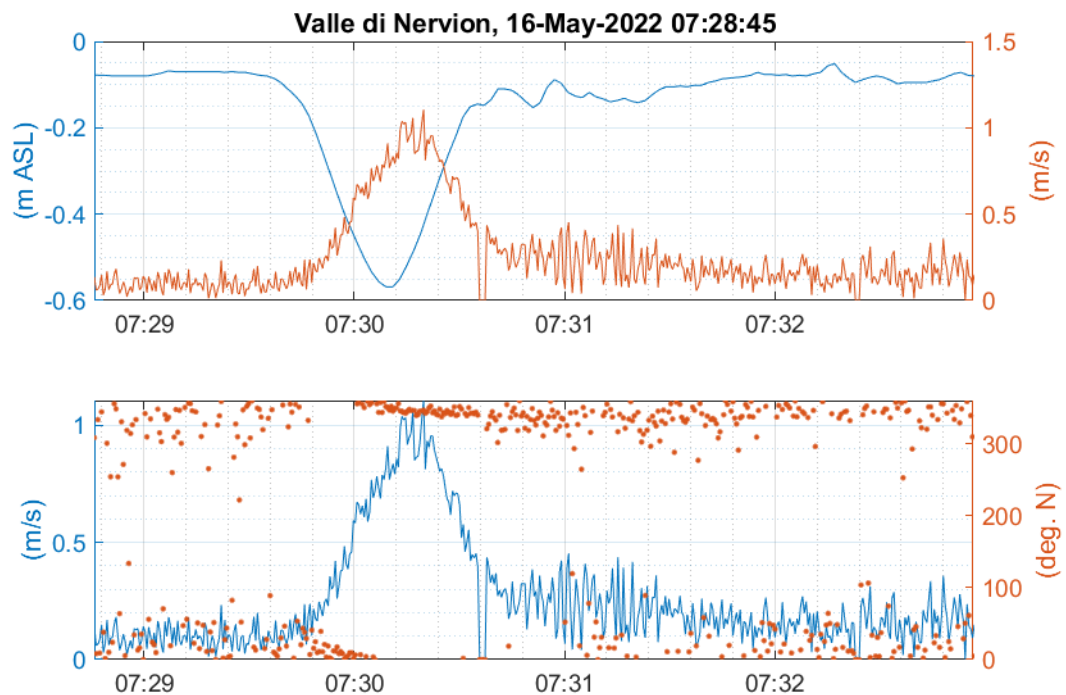
X (length)	0.910
Y (width)	1.006
Z (height)	1.089

The vessel passage has been monitored during its path toward the Malamocco Channel at the location described in the following Figure 3. The measurement point located at the “Briccola 121” has been provided with a water level probe with a sampling frequency of 1 Hz.

Figure 3: location of the measurement point

The water level and its vertical velocity is plotted in the following (Figure 4) in function of the time scale. The ship and measurement point relative position has not been recorded.

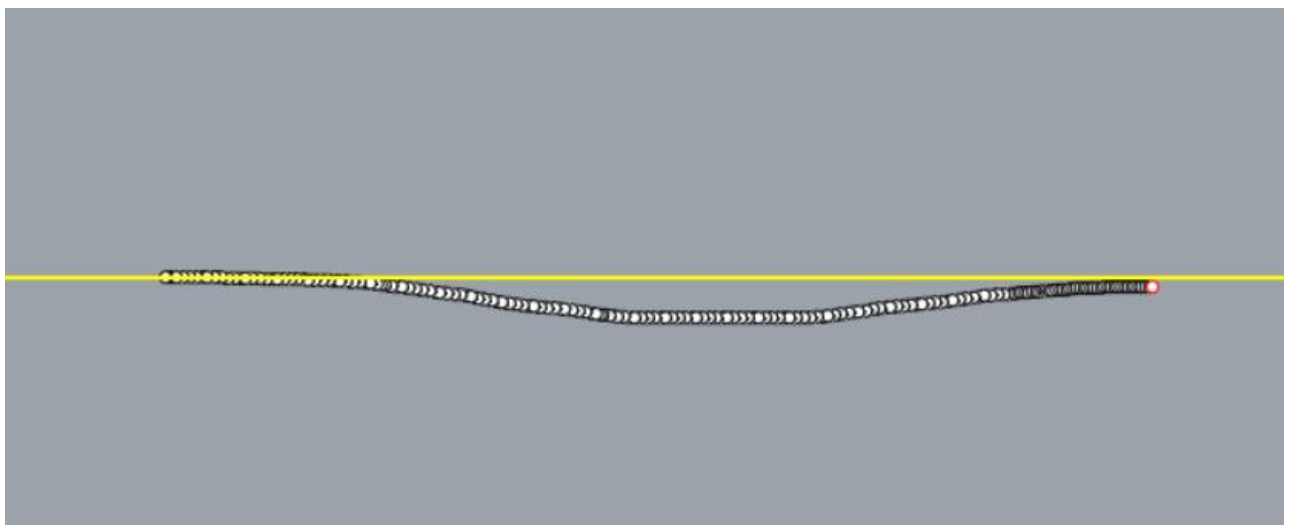
Figure 4: water level and vertical velocity for the measuring point (Briccola 121)



3 Description of the numerical model

The fluid domain has been generated starting from the 2D profile of the seabed provided by the Customer (Figure 5) in .csv format.

Figure 5: 2D profile of the seabed with the measurement point (in red) and the water level (in yellow)



The ship has been located in the middle of the channel and the seabed extended toward the open water (right-hand in Figure 5) by around 4.2 ship lengths. In order to get the final 3D CAD geometry for the CFD simulation, the 2D modified profile has been extruded in both directions by around 4.5

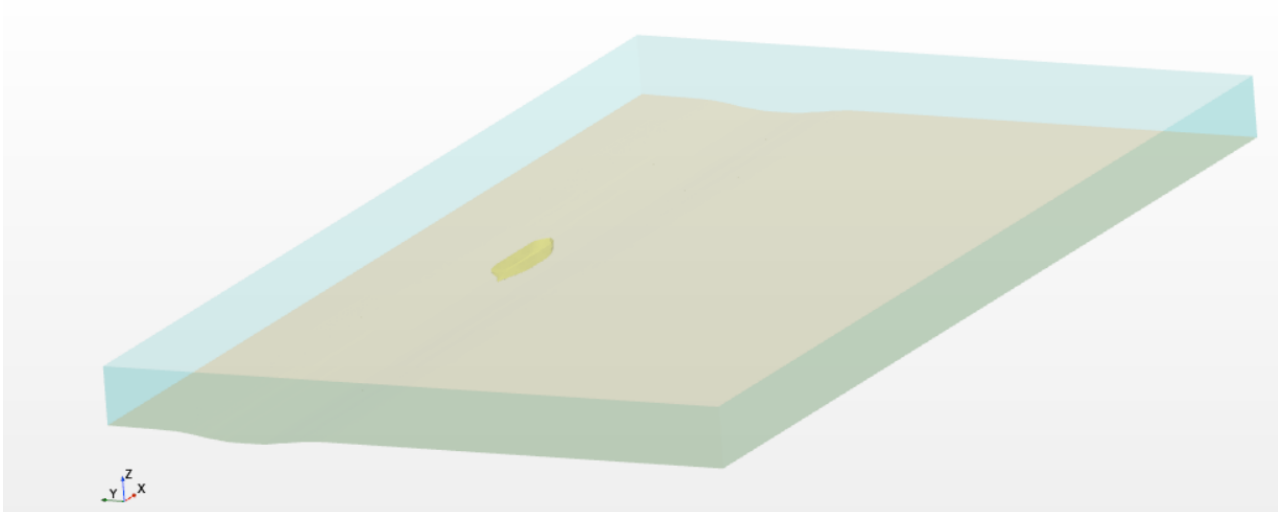
ship lengths and scaled by a factor of 32. The final fluid domain size is illustrated in the following Table 3 and Figure 6 where the overall dimensions have been selected according to CETENA's experience for wave elevation computation in shallow waters that requires larger sizes than required for the usual deep water CFD analysis.

Table 3: fluid domain size

Scale factor λ	32
Length (X direction) [m]	1650
Width (Y direction) [m]	950
Height (Z direction) [m]	100

Figure 6: 3D fluid domain

Simcenter STAR-CCM+



Boundary conditions are prescribed at the different fluid domain patches according to the following (Figure 7):

Seabed: *slip wall*

Top and shore: *symmetry plane*

Outlet: *pressure outlet*

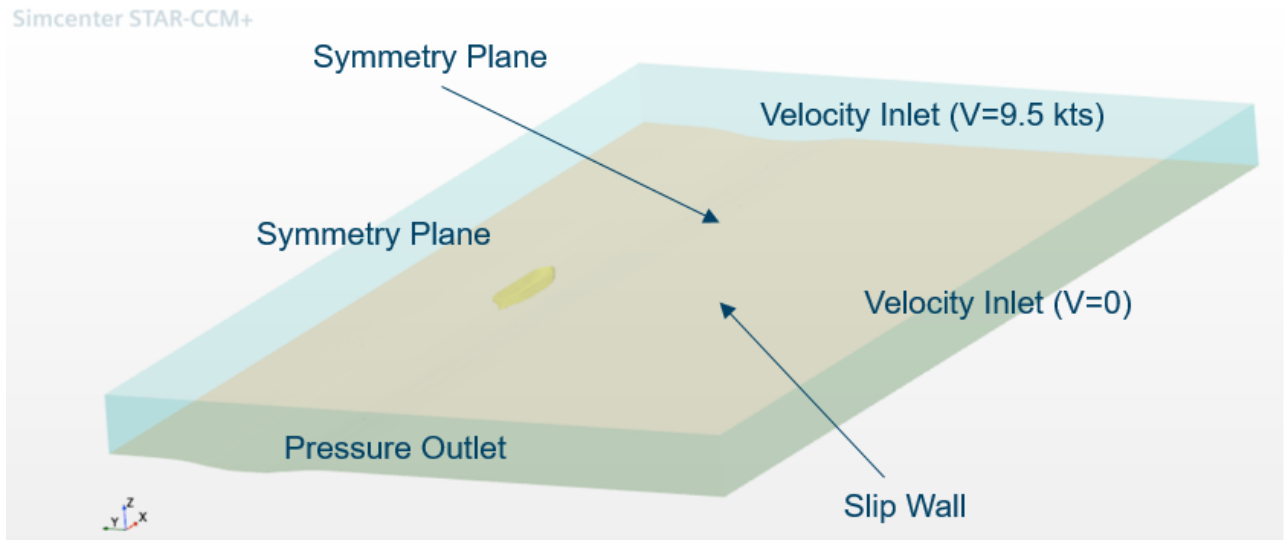
Inlet: *velocity inlet* (velocity = 9.5 kts in full scale)

Water side: *velocity inlet* (velocity = 0 kts)

Ship: *no slip wall*

The value for the velocity inlet has been selected as the sum of the ship speed over ground (9 kts) plus the current (0.5 kts), in order to account for the effect of the water current on the wave pattern generated by the hull passage.

Figure 7: boundary conditions



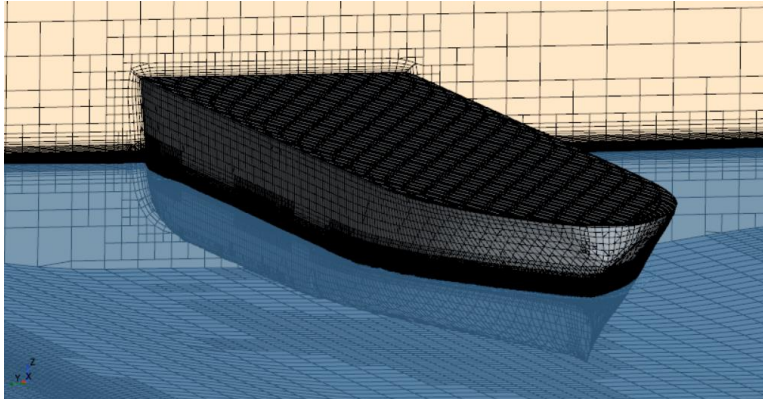
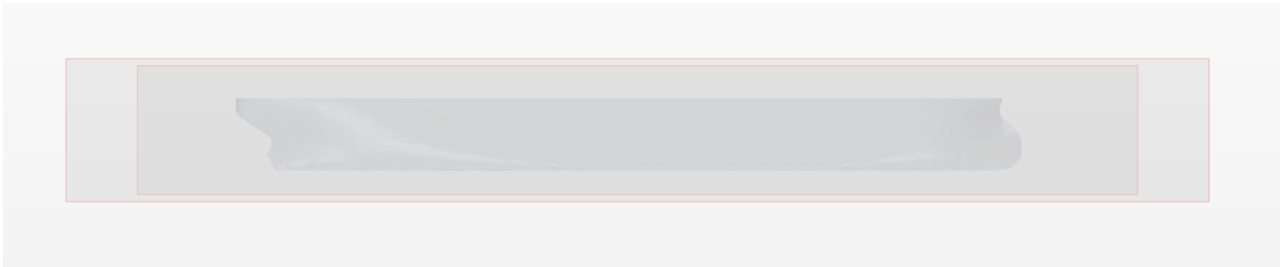
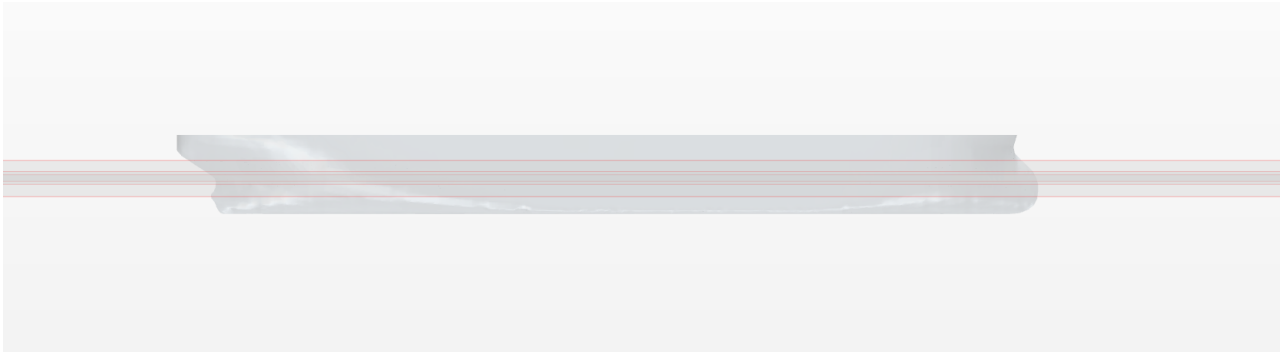
Once defined the fluid domain, a numerical grid has been generated; the characteristics of the surface and volume mesh are underlined in the following Figure 8 and Table 4.

Table 4: numerical mesh characteristics

Mesher	Trimmed
Number of volume cells [M]	46
Prism layer (PL) total thickness [mm]	49
Number of PL layers	5
PL stretching	1.3
Average Wall Y+ (hull boundary)	50

The trimmed mesher has been selected to ensure a flat free surface upstream of the ship hull where the alignment of the vertical position of the cell centroid provides a planar free surface.

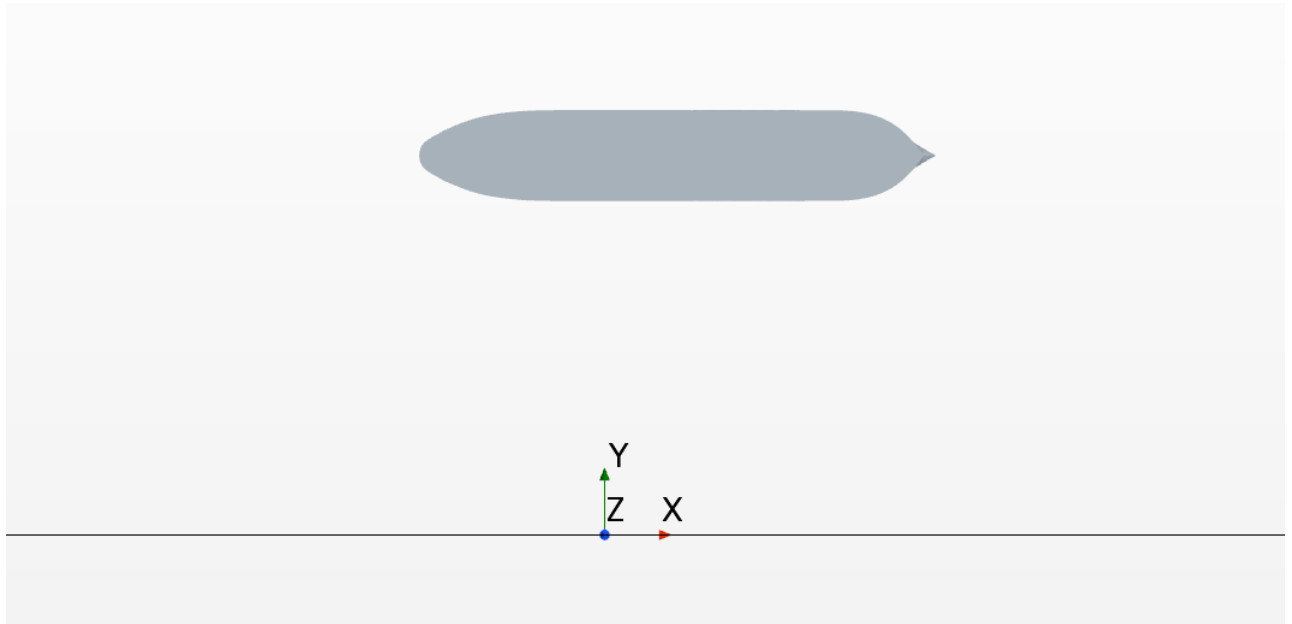
A set of volume refinement boxes is located near the hull surface (Figure 9) and around the free surface (Figure 10) in order to describe accurately the wave elevation near the hull and on the measurement point.

Figure 8: volume mesh*Figure 9: refinement volumes on the hull surface**Figure 10: refinement volumes around the free surface*

According to the prismatic fluid domain geometry, a steady (implicit unsteady) computation is selected to reduce the computational effort. The steady state wave pattern is then converted into a time dependent wave elevation at the measurement point through the following expression

$$t_{MP} = \frac{X_{MP}}{V_S}$$

Figure 11: reference system for the wave elevation measurement point



Where:

t_{MP} : time scale of the wave elevation at the measuring point

X_{MP} : X coordinate of the wave elevation measurement point in a Cartesian system located as described in Figure 11 with the origin on a vertical plane passing through the location of the Briccola 121

As mentioned in 2, the relative longitudinal location of the vessel and the measurement point (Briccola 121) during the experimental campaign was not known. Therefore, the computed wave elevation in function of time will be shifted along the time scale to match the numerical and experimental draught points (both at $t = 0$ s).

The other physical quantities and setup parameters of the numerical model are described in the following Table 5.

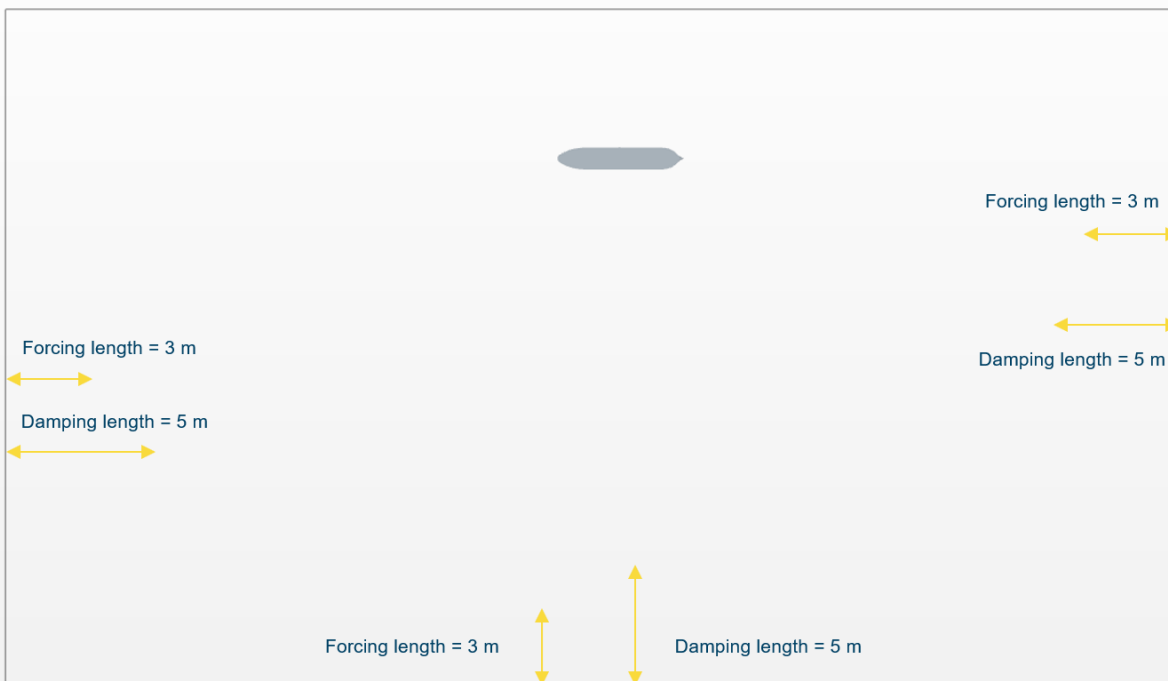
In order to reduce the computational domain of the simulation while not compromising the accuracy and reliability of the solution, the wave forcing and damping at particular boundaries has been applied. The VOF waves are damped and forced in the vicinity of selected boundaries to reduce wave oscillation near those boundaries through a vertical resistance to the vertical motion.

Damped and forced boundaries are Velocity Inlet, the water side and the Pressure Outlet (Figure 14).

Table 5: numerical model – physical properties

Phases	Salt water and air
Saltwater density [kg/m ³]	1025.56
Saltwater dynamic viscosity [Pa*s]	0.00116
Air density [kg/m ³]	1.18415
Turbulence model	Realizable k-ε
Convection discretization	2 nd order
Temporal discretization	1 st order
Time step [s]	0.01

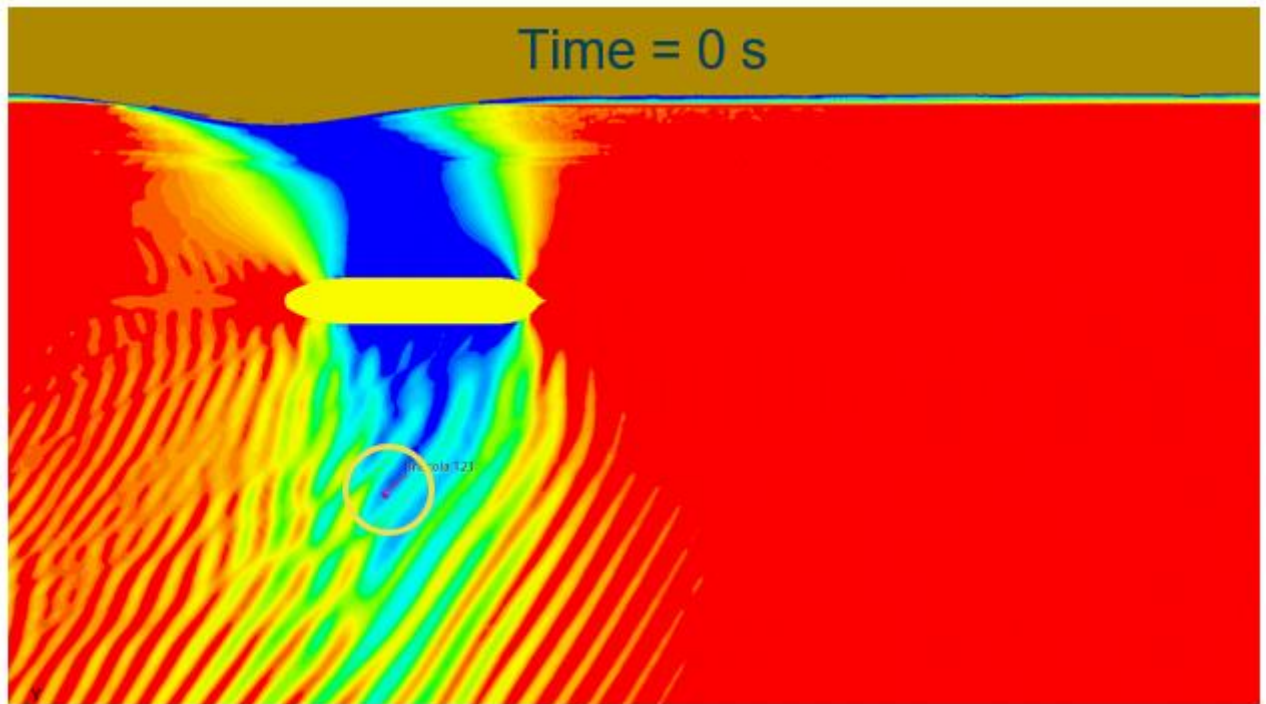
Figure 12: forcing and damping length at the boundaries



4 Description of the results

Results in terms of wave pattern are depicted in the following Figure 13 where the location of the measurement point is underlined by a yellow circle.

Figure 13: wave elevation and location of the measurement point



A zoom of the computed wave elevation near the ship bow is illustrated in the following Figure 14 and compared with a picture taken from the test case vessel.

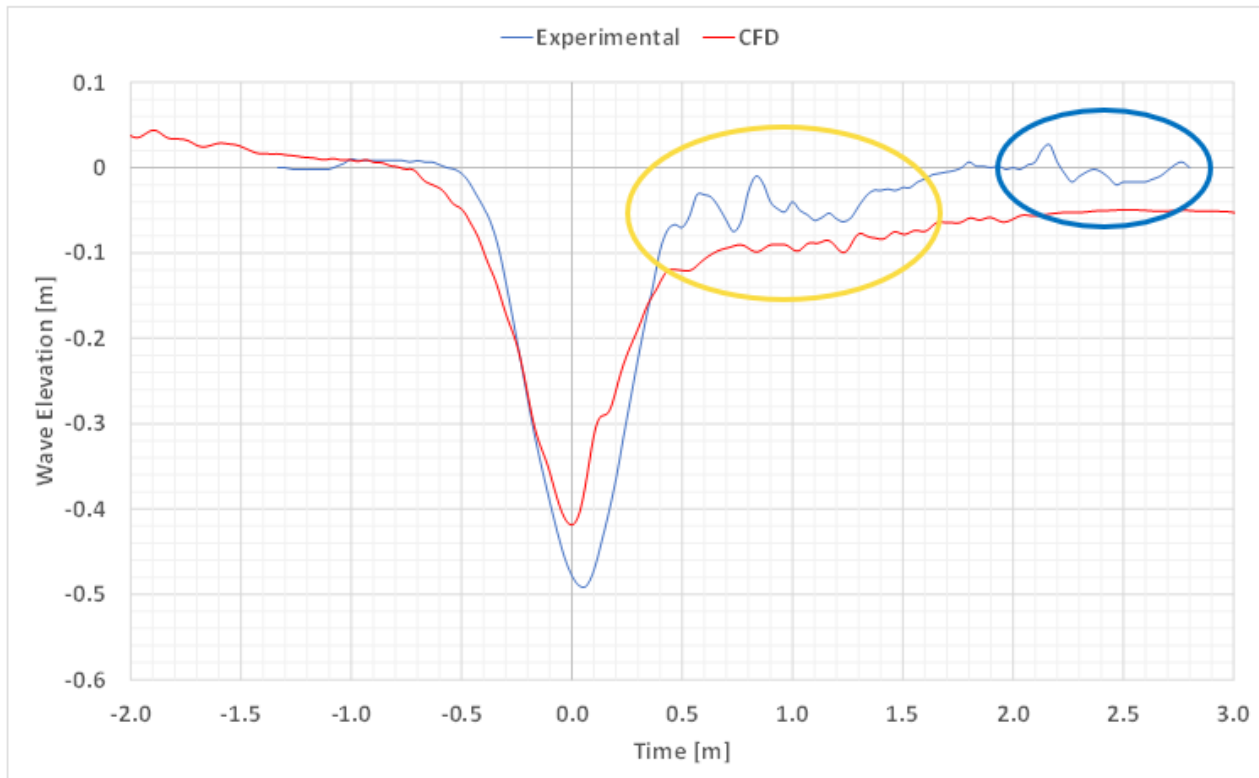
Figure 14: computed and experimental wave elevation near the bow



Given the geometrical differences between the test case and the parent vessel, the numerical computed wave elevation appears to be reasonably similar to the experimental picture.

The time dependent wave elevation (numerical and experimental) in full scale at the measurement point located on Briccola 121 are depicted in the following Figure 15.

Figure 15: numerical (red) and experimental (blue) wave elevation at the measurement point (bricola 121)



The experimental wave elevation shows a deeper maximum draught (-0.49 m vs. -0.42 m) with a numerical error of about 10%. Furthermore, the temporal extension of this first draught (around 1 s) is captured by the RANS-based model with a satisfactory accuracy.

The CFD computation has proven to capture the high frequency waves located after the first draught (underlined through a yellow circle in Figure 15) with a reduced amplitude, whereas the secondary wave group disturbance (underlined through a blue circle) is not reproduced by the numerical analysis. The latter is probably due to the wave forcing and damping length applied to the near boundaries; a reduced value of this length would have allowed to better capture the secondary wave disturbance but with some undue wave reflections.

5 Conclusions

The present technical report describes the numerical activities performed to simulate the flow and the wave elevation around an oil/chemical tanker passing through the Malamocco/Marghera channel. A CFD, RANS-based approach (through the commercial solver STAR-CCM+) has been applied to the selected test case demonstrating an effective and accurate capability of predicting the first maximum draught in terms of amplitude and temporal extension. The secondary high frequency wave group disturbance is predicted by the numerical approach with a reduced amplitude whereas the second wave group is not reproduced because of the wave forcing/damping applied to the boundaries of the CFD model to reduce the wave reflecting phenomena.

6 References

- [1] STARCCM+ - <https://www.plm.automation.siemens.com/global/it/products/simcenter/STAR-CCM.html>
- [2] Tondello M., Matticchio B., "Campagna di misure di velocità, corrente e moto ondoso generati dal transito di navi mercantili nel canale Malamocco-Marghera", Report HS Marine S.r.l., June 2022.